Crystallization and Phase Separation in Thin Film Polymers



Long Jiang

Corpus Christi College

A thesis submitted for the Degree of

D.Phil. in Materials

University of Oxford

Abstract

Properties of polymers in thin films are distinct from those in the bulk due to the significant effects of free or substrate surfaces. The presence of a free surface allows an increased mobility of polymer chains in the near-surface region, therefore, a lower glass transition temperature (T_g). With this lower surface T_g, a surface-specific crystallization phenomenon occurring at temperatures much lower than the bulk crystallization temperature (T_c) in polymers including PET, PEN and PVOH has previously been observed. However, whether or not this surface-specific crystallization is a phenomenon observable in all crystallizable polymers is still a question. Similarly, due to this greater mobility, phase separation may also be able to take place in the near-surface region of a polymer blend at a temperature much lower than the bulk phase separation temperature. Yet, no such investigation on polymer blends has been carried out. In addition, it is interesting to study the thin-film behaviours of a block copolymer that undergoes both phase separation and crystallization and compare these with corresponding bulk behaviour.

In this thesis, the thin-film crystallization behaviour of polyamide 12 (PA12) in spin-cast films is presented together with some investigation of crystallization of polyamide 6 (PA6) and polystyrene. Polystyrene and poly(methyl methacrylate) (PS/PMMA) systems are used to illustrate the phase behaviours specific to the near-surface region. Finally, the microstructural evolution in high hard block content thermoplastic polyurethane (TPU) thin films on annealing has also been investigated. These TPUs have hard segments (HS) extended by 2-methyl-1,3-propanediol (2M13PD) or 1,5-pentanediol (15PD).

With its flexible chains, PA12 crystallizes during spin coating forming as-spin-cast crystals with morphology that varies with solvent evaporation rate and film thickness. Despite the as-spin-cast crystals, the free surface allows secondary surface crystallization of PA12 at an annealing temperature (T_a) roughly 20 ℃ below the bulk T_c. The secondary surface crystals were indicated to exist in the most stable crystalline phase of PA12. Similar

secondary surface crystallization has also been observed in the PA6 films but at a higher T_a due to the higher T_g of PA6. In addition, surface-specific crystals have been observed in PS (semicrystalline, likely due to some stereoregularity of composition), a polymer with bulky side groups. The PS surface crystals are, however, flat-on oriented showing the important effect of side groups on the morphology or growth shape of surface crystals. The discovery of these surface crystals supports the universality of surface-specific crystallization.

Using fast solvent quenching, it is possible to “freeze in” a structure containing both PS and PMMA in the near surface region. On annealing, surface-specific phase behaviours (observable as pits, undulations and aggregations) confined to the near-surface region take place first at temperatures around or just below the bulk polymer T_g, while bulk vertical phase separation and dewetting of PS to PMMA, forming holes, network structures and islands, occur at temperatures well above T_g. This surface-specific phenomenon, being a result of the free surface, should be applicable to other phase separation systems with a free surface as well. An increase in the crystallinity of PS was found to promote the phase separation process, but the free surface effect is independent of the interplay between the crystallization and phase separation.

Rather than having a two-phase morphology, as was previously observed in melt-quenched bulk samples, 2M13PD-extended TPU spin-cast films showed a single-phase morphology as-spin-cast. However, the HS ordering, the formation of mesophase, the melting of HS ordered regions, and microphase mixing observed in thin films are consistent with the bulk results but with slightly different transition temperatures due to spatial confinement. With a more flexible chain extender, e.g. 15PD, the hard and soft phase separation is more limited. The thin film investigations have allowed a better understanding of the microstructural evolution in these high hard block content TPUs on annealing by imaging the morphology directly. A thin-film specific phenomenon: formation of large multilayer flat-on crystals, was also observed in these TPU thin films. These

crystals are initially developed from preformed aggregations and are believed to be induced by the significant substrate effect in thin films and the free surface effect.

Acknowledgements

There are many people that helped me in my DPhil. research life and contributed to this thesis. I would like to take this opportunity to acknowledge them:

Firstly, I want to give my sincere thanks to my supervisor Prof. Hazel Assender for her constant support, patient guidance and precious suggestions throughout this research project and the period of thesis writing. It is precious to have her being my supervisor. Many thanks and my best wishes to her again. I would also want to thanks all the other people in our group for their help and support. My appreciation to Dr. Matthew Thomas for the basic experimental trainings for thin film investigations, e.g. spin coating, and for his precious advices and encouragement. Many thanks to Dr Vincent Chan, Dr. Andy Cook, Dr. Gamal Abbas, Dr. Phil Butler, Mr. Ziqian Ding and Mr. Vincent for their useful discussions and suggestions on my work. My sincere thanks to our group technician Mr. Richard Turner for his technical support. Without him my experiments would not go smoothly. I enjoy my DPhil. life very much with all these people in the group.

Special thanks to the members in the Solar Cell Group. The combined group meeting of their and our groups helped me a lot and allowed me to have chances to practice my presentation skills and discuss research with others. I am grateful to Prof. Andrew Watt for his constructive suggestions and help on TEM and for the permission of using their chemical lab for sample preparation. Many thanks to all these people working around the lab: Dr. Simon Fairclough, Dr. Peter Kovacik, Dr. Elva Zou, Dr. Cheng Cheng, Dr. Jenna Holder, Dr. Laura Droessler, Dr. Shawn Willis, Mr. Chris Cattley, Miss. Assia Kasdi, Miss. Maria Nelson, Mr. Matthew Wincott, Miss. Natasha Hjerrild, Mr. Darren Neo, Miss. Inji Yeom, Miss. Nina Klein, and Mr. Camden Ford. They are helpful and lovely and the time with them is precious.

For experimental techniques, I would like to thank Oxford Materials Characterisation Service (OMCS) for the use of their characterisation equipment. I am grateful to

Dr. Sverre Myhra for the AFM training and useful discussion on AFM results. My great appreciation and thanks to Dr. Alison Crossley and Dr. Hugh Bishop for XPS characterization and the precious discussion. Many thanks to Dr. Phil Holdway and Dr. Susan Warren for XRD and DSC, respectively. Thank you to Dr. Colin Johnston for advices on FTIR and Raman microscopy. I would also want to express my thanks to the staff in EM group: Mrs. Gabriella Chapman, Dr. Adam Papworth, Mr. Greg Cook, and especially to Dr. Neil Young for training and helping TEM.

My acknowledgements to Dr. John Morrison from the School of Chemistry, University of Manchester for the GPC experiments of PS and PMMA. I am also thankful to the collaborators from the School of Materials, University of Manchester for providing the TPU samples and the corresponding DSC data.

There are also other people in the Materials Department that I want to thanks: Mrs. Lyn Richmond, Mrs. Marion Beckett, Mrs. Jan Pearson, Mr. Barry Fellows, Dr. Paul Warren, Mr. Ian Sutton, Mr. Dr. Alex Cock, Mrs. Rebecca Bradford. Their efforts make life easier in the department. I would like to show my special thanks to Mrs. Lyn Richmond for her sincere help. This lady is kind and worth respecting. I want to wish her a good retired life

I would also want to acknowledge my college advisor Prof. Peter Nellist for his care and advices. Many thanks to Ms. Rachel Pearson, the college graduate secretary, for her help.

Finally, I want to express my gratitude to my parents for their invaluable love and support.

Declaration

This thesis is based on the work carried out by the author in the Department of Materials, University of Oxford under the supervision of Prof. Hazel Assender. Any work of others has been acknowledged in the references. No part of this thesis has been submitted for any degree, diploma or certificate or other qualification in the University of Oxford or elsewhere. Some part of this thesis has been used for the preparation of papers:

L. Jiang, H. E. Assender, Crystallization of polyamides in thin films: free surface effects, in preparation

L. Jiang, H. E. Assender, Phase behaviours from near-surface to bulk in thin films of PS/PMMA blends, in preparation

L. Jiang, H. E. Assender, C. Nedolisa, J. Wu, A. Saiani, Phase separation and crystallization in high hard block content polyurethane thin films, in preparation

Table of Contents

ABSTRACT I

ACKNOWLEDGEMENTS IV

DECLARATION VI

TABLE OF CONTENTS VII

LIST OF ABBREVIATIONS, ACRONYMS AND SYMBOLS X

1 INTRODUCTION 1

2 CRYSTALLIZATION AND PHASE SEPARATION IN THIN FILMS 5

2.1 CRYSTALLIZATION IN POLYMERS 6
- **2.1.1 Thermodynamics of Polymer Crystallization** 7
- **2.1.2 Morphology** 9
  - **2.1.2.1 Fringed micelle model** 9
  - **2.1.2.2 Chain folded model** 9

2.2 PHASE SEPARATION IN POLYMERS 12
- **2.2.1 Incompatibility of Polymer Blends** 12
- **2.2.2 Thermally Induced Phase Separation** 13

2.3 POLYMER THIN FILMS 15
- **2.3.1 Glass Transition in Polymer Thin Films** 15
  - **2.3.1.1 T_g in supported polymer films** 16
    - *Polymer-substrate interfacial interactions* 17
    - *Polymer-air interface* 17
    - *Molecular weight and chain conformation* 19
  - **2.3.1.2 T_g in free-standing polymer films** 19
  - **2.3.1.3 Chain mobility in polymer thin films** 21
- **2.3.2 AFM in Characterizations of Polymer Thin Films** 21

2.4 CRYSTALLIZATION IN POLYMER THIN FILMS 23
- **2.4.1 Surface Crystallization** 23
  - **2.4.1.1 Edge-on lamellae** 24
  - **2.4.1.2 Flat-on Lamellae** 31
  - **2.4.1.3 Parameters affecting surface crystallization** 35
- **2.4.2 Crystallization Kinetics in Thin Films** 38

2.5 PHASE SEPARATION IN POLYMER THIN FILMS 41
- **2.5.1 Phase Separation during Spin Coating** 41
  - **2.5.1.1 Solvent quench** 42
  - **2.5.1.2 Non-equilibrium phase separation** 44
- **2.5.2 Phase Separation Induced by Annealing** 46
- **2.5.3 Parameters Affecting Phase Separation in Thin Films** 47
  - **2.5.3.1 Film thickness** 48
  - **2.5.3.2 Molecular structure and molecular weight** 48

2.5.3.3 Substrate effect 49
2.5.4 Crystallization in Copolymers or Polymer Blends 50

2.6 CONCLUSIONS 52

3 CRYSTALLIZATION OF POLYAMIDES IN THIN FILMS 53

3.1 BACKGROUND 54

3.2 EXPERIMENTAL 56

3.3 RESULTS AND DISCUSSION 59
3.3.1 As-Spin-Cast Morphologies 59
3.3.1.1 2D crystals in as-spin-cast films 60
3.3.1.2 Confinement induced crystalline polymorphism 62
3.3.1.3 Solvent-crystallization in ultrathin PA12 films 66
3.3.1.4 A model for surface crystallization during solvent evaporation 67
3.3.2 Morphological Evolution on Annealing 70
3.3.2.1 Secondary surface crystallization 70
3.3.2.2 Effects of annealing temperature and film thickness 73
3.3.3 The Near-Substrate Layer 77
3.3.4 The Substrate Effect 81
3.3.5 Crystallization in PA6 Thin Films 82

3.4 CONCLUSIONS 84

4 NEAR-SURFACE PHASE BEHAVIOURS IN PS/PMMA THIN FILMS 85

4.1 BACKGROUND 86

4.2 EXPERIMENTAL 87

4.3 RESULTS AND DISCUSSION 90
4.3.1 Near-Surface Phase Separation 91
4.3.1.1 Confined PS/PMMA phase separation in thin films 91
4.3.1.2 Bulk phase separation in 151-nanometer films 94
4.3.1.3 Surface phase separation in 64-nanometer films 95
4.3.1.4 Thickness and substrate effects 102
4.3.2 Effects of Crystallization 109
4.3.2.1 Crystallization in PS films 109
- *Surface crystallization and crystalline aggregation* 109
- *Diffusion-limited surface crystallization of PS* 112
4.3.2.2 Effects of PS crystallization on PS/PMMA phase separation 113
- *Bulk aggregations on annealing* 116
- *Surface crystals in PS/PMMA films* 117

4.4 CONCLUSIONS 119

5 MICROSTRUCTURAL EVOLUTION IN HIGH HARD BLOCK CONTENT TPU THIN FILMS ON ANNEALING 120

5.1 BACKGROUND 121

5.2 EXPERIMENTAL 123

5.3 RESULTS AND DISCUSSION **125**
5.3.1 2M13PD-Extended TPU Thin Films 125
5.3.1.1 Morphological evolution on annealing 126
5.3.1.2 Influence of HS content 134
5.3.1.3 Microphase mixing 137
5.3.1.4 Thickness effects 138
5.3.2 15PD-Extended TPU Thin Films 140
5.3.3 Multilayer Crystal Blocks 143
5.3.3.1 Crystal development 144
5.3.3.2 Crystal morphology 146
- *Influence of chain extender* 148
- *Influence of soft block* 149
- *Influence of interfaces* 151
- *Influence of annealing temperature* 152
- *Influence of film thickness* 154

5.4 CONCLUSIONS **156**

6 CONCLUSIONS **158**

6.1 SURFACE-SPECIFIC CRYSTALLIZATION **158**

6.2 SURFACE-SPECIFIC PHASE SEPARATION **159**

6.3 CRYSTALLIZATION AND PHASE SEPARATION IN TPU THIN FILMS **160**

REFERENCES **162**

APPENDIX **175**

List of Abbreviations, Acronyms and Symbols

AFM	Atomic force microscopy
BA-Cn	Poly(bisphenol A alkyl ether)
BDO	1,4-butanediol
CD	Compact dendrite
CE	Chain extender
CS	Compact seaweed
DMAC	Dimethylacetamide
DMC	Dichloromethane
dPMMA	Deuterated poly(methyl methacrylate)
dPS	Deuterated polystyrene
DSC	Differential scanning calorimetry
ED	Electron diffraction
EO-PPO-EO	Poly(propylene oxide) end-capped with ethylene oxide
EVA	Poly(ethylene-vinyl acetate)
FA	Formic acid
F_{adh}	Adhesion force
F_{att}	Attractive van der Waals force
FD	Fractal dendrite
FS	Fractal seaweed
FTIR	Fourier transform infrared spectroscopy
G	Gibbs free energy
GPC	Gel permeation chromatography
H	Enthalpy
HDPE	High density polyethylene
HFIP	Hexafluoroisopropanol
HS	Hard segment
iPS	Isotactic polystyrene
LCST	Lower critical solution temperature
LDPE	Low density polyethylene
MDI	4,4’-methylene diphenyldiisocyanate
M_n	Number average molecular weight
M_w	Meight average molecular weight
OLEDs	Organic light-emitting diodes
OM	Optical microscopy
PA	Polyamide
PA6	Polyamide 6
PA12	Polyamide 12
PAA	Poly(acrylic acid)
PCL	Poly(ε-caprolactone)
PDHS	Poly(di-n-hexylsilane)
PE	Polyethylene
PEDOT	Poly(3,4-ethylenedioxythiophene)
PEEK	Poly(aryl ether ether ketone)
PEI	Poly(ether imide)
PEO	Poly(ethylene oxide)
PEN	Poly(ethylene naphthalate)
PET	Poly(ethylene terephthalate)
PHB	Polyhydroxybutyrate
PI	Polyisoprene

PDLA	Poly(D-lactide)
PLLA	Poly(L-lactide)
PMMA	Poly(methyl methacrylate)
PP	Polypropylene
PpMS	Poly(p-methylstyrene)
PS	Polystyrene
PTFE	Polytetrafluoroethylene
PVAc	Poly(vinyl acetate)
PVC	Poly(vinyl chloride)
PVDF	Poly(vinylidene fluoride)
PVME	Poly(vinyl methyl ether)
PVOH	Poly(vinyl alcohol)
R_{EE}	End-to-end distance of unperturbed polymer chains
R_g	Radius of gyration
RMS	Root mean square
S	Entropy
SAN	Poly(styrene-*ran*-acrylonitrile)
SEM	Scanning electron microscopy
SIMS	Secondary ion mass spectroscopy
sPS	Syndiotactic polystyrene
SS	Soft segment
T_A	Annealing endotherm
Ta	Annealing temperature
T_c	Crystallization temperature
TEM	Transmission electron microscopy
T_g	Glass transition temperature
T_{gHP}	T_g of the hard phase
T_{room}	Room temperature
T_m	Melting point
T_M	Melting of the HS orders
T_{MMT}	Microphase mixing transition
TPE	Thermoplastic elastomer
TPU	Thermoplastic polyurethane
UCST	Upper critical solution temperature
UV	Ultraviolet spectroscopy
XPS	X-ray photoelectron spectroscopy
15PD	1,5-pentanediol
2CP	2-chlorophenol
2D	Two-dimensional
2M13PD	2-methyl-1,3-propanediol

1 INTRODUCTION

With a large volume of polymers produced for film applications every year, the field of polymer thin films is one of the most successful and important applications of polymers [1]. Polymer thin films have an increasingly wide range of applications in not only traditional markets such as packaging, adhesives and protective coatings, but also some novel technologies like biomedical products, flexible electronics and photovoltaics [2, 3]. Polymer thin films normally play the function of “surfaces” in biometric systems and are favoured for their excellent biocompatibility and relatively low cost. These biometric applications involving polymer thin films include: (a) implant coatings, which allow implants to be compatible with the tissues around and may also play an antibacterial function; (b) tissue engineering substrate coatings, inducing biocompatibility and biofunctionality to substrates; (c) films for drug and gene delivery, which control the release of drugs or DNA [4]. Organic electronics and solar cells have been emerging areas in the last two decades [5-9]. Predominating in organic materials, polymers are used in a wide range of devices including: organic light-emitting diodes (OLEDs) [10-13], transistors [14, 15], photovoltaic cells [16-19] and so on. The roles of polymer thin films in these devices can be generally classified as permanent conductors or insulators, semiconductors, barrier layers and substrates [5-7, 13].

Since polymer thin films play an important role in such a wide range of applications, it is essential to have a good understanding of polymer thin film systems. It is well known that the properties of polymers in surface or interface regions are distinct from the bulk properties of corresponding polymers [20-22]. Considerable research [22-25] has demonstrated that the presence of a free surface (or an air-polymer interface) allows polymer chains in the near-surface region to have a higher mobility, hence, a lower glass transition temperature (T_g). Comparing T_g of PS films in air, dry nitrogen and vacuum,

Raegen *et al.* [26] found that this free-surface effect is the result of the intrinsic properties of the confined polymers rather than being due to the composition of surrounding atmospheres.

With a lower surface T_g, a polymer in the near-surface region is expected to show a different crystallization or phase separation behaviour from that of the polymer in the bulk. Despite the great amount of research that has been done to investigate the properties of polymers in thin film systems, more work is needed for a better understanding of crystallization and phase separation in polymer thin film systems.

The aim of this project is to investigate crystallization and phase separation in different polymer thin film systems with particular interests in the effect of the free surface.

The first part of this project is the study of the crystallization of polyamides in thin films. Experiments were done on Nylon 12 and 6 to see whether it is possible for them to form surface-specific crystals. Previous work [27] showed that amorphous as-spin-cast poly(ethylene terephthalate) (PET) can bear surface-specific crystals after annealing at temperatures even below the bulk T_g. This phenomenon was observed in films in excess of 1 µm thick and for films thicker than 70 nm it was not thickness dependent. This indicates that the surface crystallization is not an exclusively thin film phenomenon, but is probably a surface-specific phenomenon in polymers. So far, this effect has been observed in PET and poly(ethylene naphthalate) (PEN) [28] with a rather stiff monomer, and poly(vinyl alcohol) (PVOH) [29], a flexible chain with a high density of hydrogen bonding. Polyamides represent a group of flexible-chained polymers with some degree of hydrogen bonding. In chapter 3 of this thesis, the free surface effect on crystallization of polyamides in thin films is revealed.

The second part of this project is the investigation of near-surface phase separation in polystyrene/poly(methyl methacrylate) (PS/PMMA) thin films, described in chapter 4. On account of the effect of the free surface, polymer phase separation is also expected to

show a surface-specific behaviour similar to that of polymer crystallization: a surface phase separation confined in near-surface regions may occur at a lower temperature than bulk phase separation temperature. To date, most surface work on phase separation in polymer blend films is actually the investigation of the surface part of the phase separation of the whole film and the annealing temperatures for phase separation are normally well above the bulk T_g of the polymers in the blend [30-34], which means that any phase separation confined to the near-surface region that may occur at lower temperatures is unobserved. The PS/PMMA system was chosen since much work [32-36] has already been done on this system showing the phase separation mechanism of the blend in the bulk of the thin films, which would help interpretation of phase behaviours specific to the near-surface regions. In this part, great attention is paid to the near-surface behaviours of the thin-film blend system annealed at temperatures around bulk T_g of the two polymers. The possibility of surface-specific phase separation in a polymer blend has been proved and the surface-specific phase separation and the bulk phase separation of PS/PMMA are compared.

The last part of this project focuses on crystallization and phase separation in thermoplastic polyurethane (TPU) thin films. Thermoplastic elastomers (TPEs) are versatile copolymers consisting of flexible soft (SS) and rigid hard (HS) segments which provide rubbery properties and act as physical crosslinks respectively. Among TPEs, thermoplastic polyurethanes (TPUs) are a representative group and have received much attention due to their wide range of applications. It is believed that the intriguing properties of TPUs are due to their microphase-separated structures resulting from the thermodynamic immiscibility between the SS and HS [37]. One of the most extensively investigated TPU classes is that of polyurethanes with HS based on a 4,4'-methylene diphenyldiisocyanate (MDI) extended by 1,4-butanediol (BDO). Previous work of co-workers investigated the crystallization and phase separation behaviour of a set of linear TPUs with a high content of HS: from 50 to 100 wt%, in bulk samples and related these

transitions to the origin of multiple endotherms. These TPUs have poly(propylene oxide) end-capped with ethylene oxide (EO-PPO-EO) as the SS and MDI chain extended with a short diol chain as the HS. The chain extenders (CE) involved in this project were 2-methyl-1,3-propanediol (2M13PD) and 1,5-pentanediol (15PD). Replacement of BDO with these diols lowers the melting temperature, thus, allows annealing studies at higher temperatures, e.g. above melting, without significant degradation [38]. In chapter 5, the morphological evolution in thin films of linear TPUs with high content of HS, from 70 to 100 wt%, on annealing is studied. The crystallization and phase separation of these TPUs in thin films are presented and compared to the bulk. Effects of annealing, HS content, film thickness and chain extender are extensively investigated.

2 CRYSTALLIZATION AND PHASE SEPARATION IN THIN FILMS

In this chapter, some fundamental aspects of crystallization and phase separation in bulk polymers are presented first. After that, polymer properties in confined conditions are reviewed with emphasis on the T_g in polymer thin films. Because the molecules become significantly more mobile above T_g, the T_g will affect crystallization and phase separation behaviours directly. The main part of this review describes previous observations of crystallization and phase separation in polymer thin films or near-surface regions, summarising the parameters that affect these two physical behaviours.

2.1 CRYSTALLIZATION IN POLYMERS

Polymers are large molecules made up of many smaller monomers which are covalently bonded together. With their structural irregularity and high melt viscosity, polymers are never fully crystalline [39-42]. Semicrystalline polymers are composed of amorphous (or liquid) and crystalline phases, as confirmed directly by X-ray diffraction showing both diffuse amorphous haloes as well as sharp crystalline rings [39, 40, 43]. However, the degree of crystallization of different polymers varies a lot. Polymer structure and intermolecular forces, as well as sample history and processing, decide the extent of crystallinity. Regular structures are always favourable to polymer crystallization [40, 43], thus, the degree of chain branching is one important factor that affects crystallinity. A typical example is polyethylene (PE): the crystallinity of linear PE can reach as high as 95%, whereas highly branched PE may be only around 30% crystalline [44]. For polymers with side groups, tacticity influences crystallization as it determines the regularity of a polymer. In general, isotactic and syndiotactic polymers are able to pack together more easily than atactic polymers, especially for those polymers with bulky side groups [43]. For instance, syndiotactic polystyrene (sPS) with large phenyl groups arranged on alternating sides of the chain is semicrystalline, while atactic PS is irregular and amorphous. In addition, geometric isomerism is also an important factor influencing polymer crystallization, as exemplified by amorphous cis-polyisoprene and crystalline trans-polyisoprene [40, 43].

Together with the intramolecular factors, intermolecular forces also affect the crystallization in polymers. As polymer chains are closely packed together in crystallites, polymer crystals are strengthened by van der Waals forces. However, stronger intermolecular forces, which allow polymer chains to be attracted to each other and line up, are hydrogen bonding and dipole-dipole interactions which normally appear in polymers with polar groups, e.g. OH or Cl [43]. Nylon 66, for example, can crystallize

easily due to the hydrogen bonds formed between the carbonyl oxygens and amide hydrogens [43], shown in Fig. 2.1.

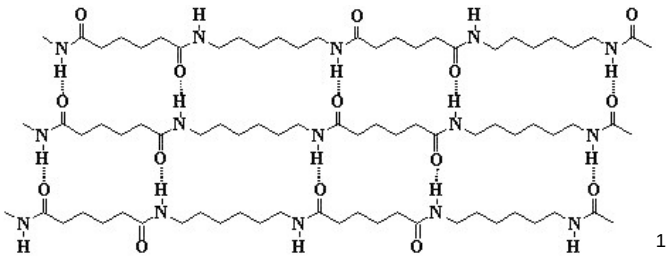
[1]

Fig. 2.1 Zigzag structures for Nylon 66, showing the hydrogen bonds between the carbonyl oxygens and amide hydrogens.

2.1.1 Thermodynamics of Polymer Crystallization

The thermodynamics of crystallization and melting can be explained by the changes in the Gibbs free energy during polymer melting, which is defined by the thermodynamic equation [40, 43, 45]:

$$\Delta G = \Delta H - T\Delta S \qquad \text{(Eq. 2-1)}$$

where ΔG is the difference in the Gibbs free energy, $\Delta G = G_{crystal} - G_{amorphous}$, ΔH is the enthalpy of fusion, and ΔS is the entropy of fusion.

At the equilibrium melting point, T_m, an equilibrium between the crystal and melt phases exists, where $\Delta G_m = 0$. So,

$$T_m = \frac{\Delta H_m}{\Delta S_m} \qquad \text{(Eq. 2-2)}$$

Since a lower free energy state is preferable for polymer chains, crystallization is spontaneous at temperatures below T_m, while melting of crystals happens when the temperature is above, shown in Fig. 2.2 [45, 46].

[1] http://pslc.ws/macrog/crystal.htm

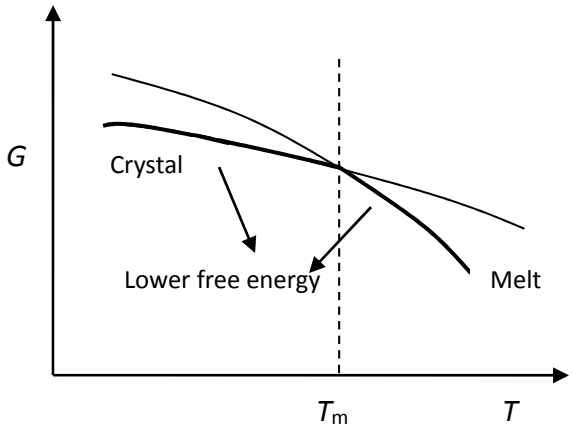


Fig. 2.2 Gibbs free energy as a function of temperature for a liquid and a crystal [45].

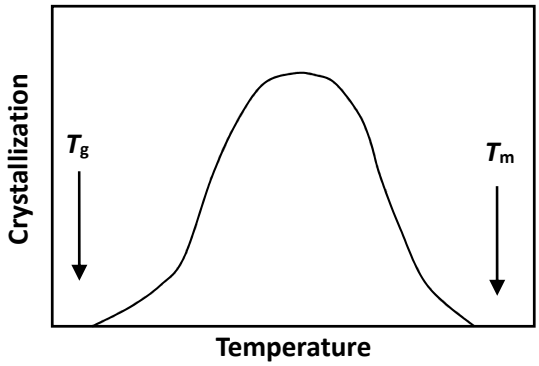


Fig. 2.3 Overall crystallization rate of a polymer. A maximum crystallization rate is found at the temperature between T_g and T_m [47].

The crystallization rate of a polymer depends on the diffusion rate of polymer chains to the growing crystal and crystal nucleation, which are both governed by temperature. When the temperature is near T_g, the viscosity of a polymer is high, so transport of polymer chains to the crystal growing ends is restrained. As temperature increases, polymer viscosity decreases and the mobility of polymer chains is improved dramatically. However, as the temperature approaches T_m, the kinetic energy of the molecules increases, which results in a lower nucleation rate and, hence, a reduced crystallization rate [40, 43, 47]. Thus, a maximum crystallization peak exists when the temperature increases from T_g to T_m, as displayed in Fig. 2.3 [47].

2.1.2 Morphology

Various explanations have been put forward to understand how long polymer chain molecules grow into small crystals. The morphology of polymer crystallites can be broadly classified into two groups: the fringed micelle model and the chain folded model [40, 43, 46].

2.1.2.1 Fringed micelle model

The fringed micelle model was first proposed in the 1930s to account for small crystalline regions in semicrystalline polymers and was advanced by Bryant [48] and Flory [49] later. In this model, a single polymer chain passes through several crystalline and amorphous regions. Crystalline regions are suggested to be aligned polymer segments and be joined together by amorphous regions which are made up of disordered segments [40, 46], illustrated in Fig. 2.4 [48]:

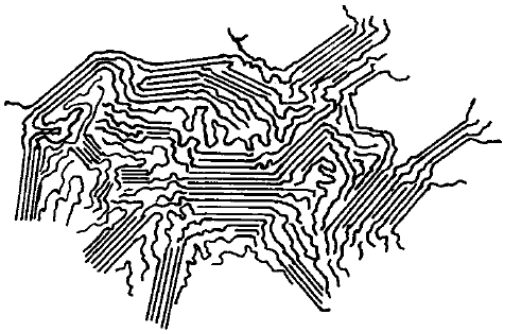


Fig. 2.4 Fringed micelle model for semicrystalline polymers. Parallel lines represent crystalline regions connected by amorphous regions. Reproduced from [48] with permission of the copyright holder.

Although this model accounts for crystal size and could describe polymers with very low levels of crystallinity, e.g. poly(vinyl chloride) (PVC), it cannot explain crystal structures like spherulites and was replaced by the chain folded model during the 1950s [40].

2.1.2.2 Chain folded model

The chain folded model was widely applied for describing polymer crystallization and

morphology after the discovery of single crystals from very dilute linear PE solution [41, 50-53], a typical example of which is shown in Fig. 2.5 [41]. As polymer chains may be around 1000 nm long and the single crystal lamellae are only 10 to 20 nm thick, the observation of a single crystal is strong evidence for a folded chain configuration [40, 43, 51].

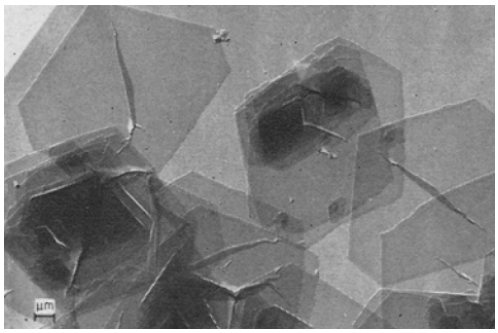


Fig. 2.5 Polyethylene single crystals from dilute xylene solution. Reproduced from [41] with permission of the copyright holder.

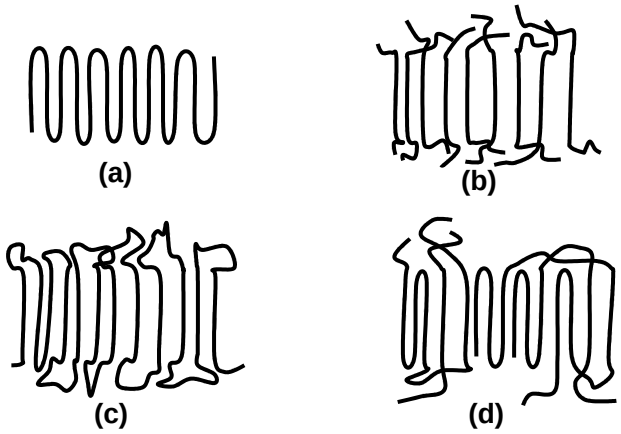


Fig. 2.6 Schematic diagram of models for polymer lamellae [40]: (a) regular folding model, (b) “switchboard” model, (c) irregular folding with adjacent re-entry, (d) a combination of the three models.

Nowadays, the lamellar structure is generally accepted as the usual polymer crystal morphology. The most commonly accepted models for the lamellar structure of polymer crystals are presented in Fig. 2.6. The regular or sharp folded model is successful in explaining polymer crystals with smooth surfaces such as single crystal lamellae [51].

However, when situations are moved to single crystals with folded surfaces or polymer systems with rough surfaces, this model shows its weakness. An irregular or loose folded model, and a “switchboard” model were proposed by Flory [54] later for better understanding of morphology of crystalline polymers. A combination of the three models has also been suggested for better understanding of polymer morphology [40].

If the discovery of single crystals is a milestone in the field of polymer crystalline science, the identification of spherulites is, definitely, another one. Spherulites were first investigated and reported by Bunn and Alcock [55] in 1945. Along with lamellae, spherulites lay down the foundation of current polymer crystalline theory and are expected to exist in most semicrystalline polymers. The hierarchy of polymer crystalline structures is illustrated in Fig. 2.7 [46].

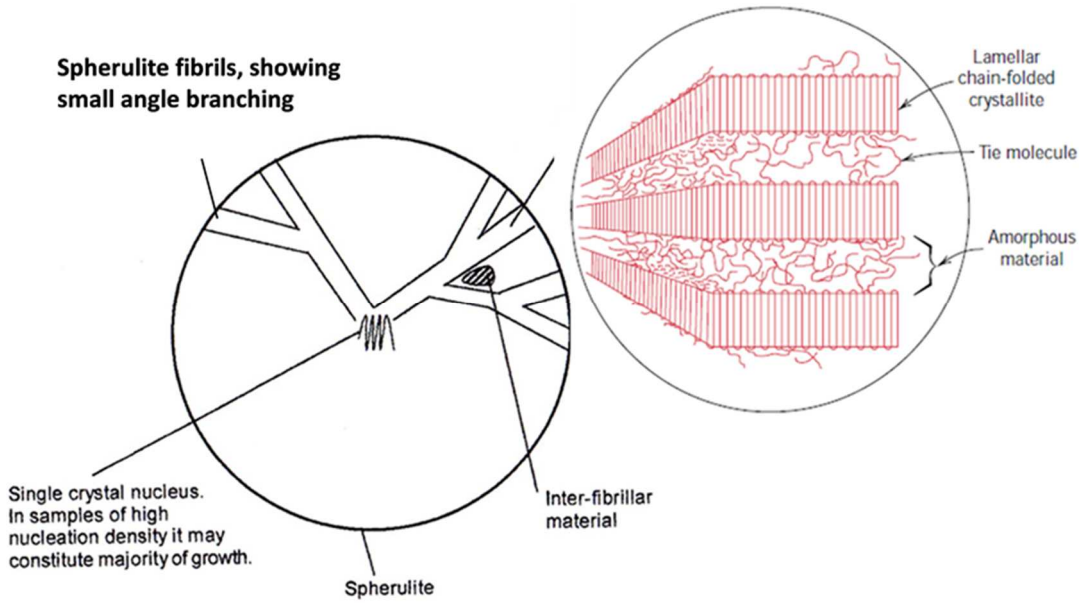


Fig. 2.7 Schematic representation of a polymer spherulite. Spherulites develop from nuclei and are made up of lamellar fibrils. Amorphous regions exist both within and without the spherulites [46].

A spherulite develops from a nucleus. During nucleation, initial growth arises either through chain folding or from additives or impurities. Folded chains form lamellae, which then make up lamellar fibrils. Small angle branching of lamellar fibrils occurs at the points where a growing crystal end meets a nucleus or an impurity. With three dimensional branching, lamellar fibrils grow into a spherulitic structure, which contains amorphous

regions both between the branches of fibrils and between the lamellae within the fibrils [40, 43, 46]. In addition to the bulk crystallization mentioned above, surface-specific crystallization has also been found in polymer thin films, reviewed in section 2.4.

2.2 PHASE SEPARATION IN POLYMERS

Blending and copolymerisation are common techniques in the polymer industry to combine features from different polymers, which allow the production of a composite with desirable properties and low cost [56, 57]. Phase separation is a critical phenomenon in polymer systems as polymeric materials with different phases may exhibit two or more glass transitions and completely different bulk properties [58]. Some representative schematic diagrams of polymer-polymer phase separation in a binary system are presented below [59]:

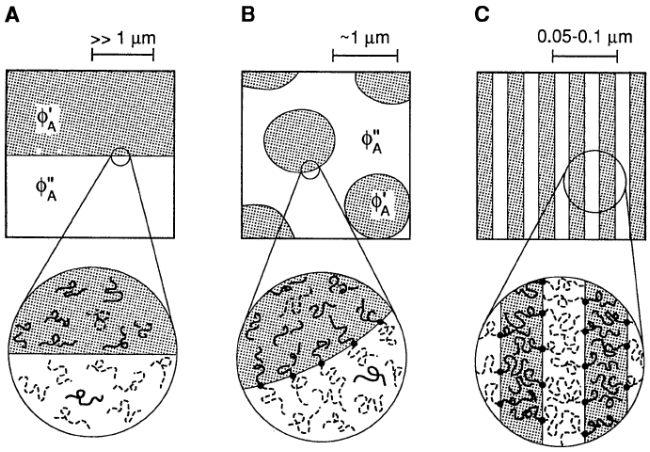


Fig. 2.8 Examples of polymer-polymer phase separation. (a) macrophase separation between linear homopolymers; (b) intermediate-scale phase separation in a mixture of diblock copolymer and the constituent homopolymers; (c) microphase segregation in a diblock copolymer. Reproduced from [59] with permission of the copyright holder.

2.2.1 Incompatibility of Polymer Blends

Polymer blends can be defined as mixtures of polymer/polymer or polymer/small molecules. They can be actually described as polymer solutions [47, 60]. The miscibility of

polymer blends, i.e. mixing on the segmental level, is determined by the changes in the Gibbs free energy during mixing:

$$\Delta G_{mix} = \Delta H_{mix} - T\Delta S_{mix} \qquad \text{(Eq. 2-3)}$$

where ΔG_{mix} is the free energy change during mixing, and ΔH_{mix} and ΔS_{mix} are the enthalpy and entropy of mixing, respectively. A negative ΔG_{mix} value is required for full miscibility, while a positive ΔG_{mix} value results in unstable state of polymer blends and will tend to lead to phase separation at some compositions and temperatures. When ΔG_{mix} = 0, the miscibility is controlled by processing conditions [45, 47, 56].

Assuming an incompressible lattice system, Flory [61] and Huggins [62] gave the ΔG_{mix} of homopolymers (polymer A and B) as:

$$\frac{\Delta G_{mix}}{kT} = \phi_A \phi_B \chi + \left(\frac{1}{N_A}\phi_A \ln \phi_A + \frac{1}{N_B}\phi_B \ln \phi_B\right) \qquad \text{(Eq. 2-4)}$$

where k is the Boltzmann constant, ϕ is segment volume fraction, $\phi_A + \phi_B = 1$, N is the number of monomers per chain, χ is the Flory-Huggins interaction parameter. The first term at the right-hand side accounts for ΔH_{mix}, while the last two terms represent ΔS_{mix}. Hence, for polymers, which have high N values, ΔS_{mix} is small. Although ΔH_{mix} is normally positive, it could be negative when there are specific intermolecular interactions.

2.2.2 Thermally Induced Phase Separation

As the Flory-Huggins interaction parameter is a function of temperature, polymer phase separation is temperature dependent [56], and this dependency can be illustrated in a phase diagram. Partially miscible polymer blends can show two features on the phase diagram: lower critical solution temperature (LCST) and upper critical solution temperature (UCST), Fig. 2.9 [43, 47, 60].

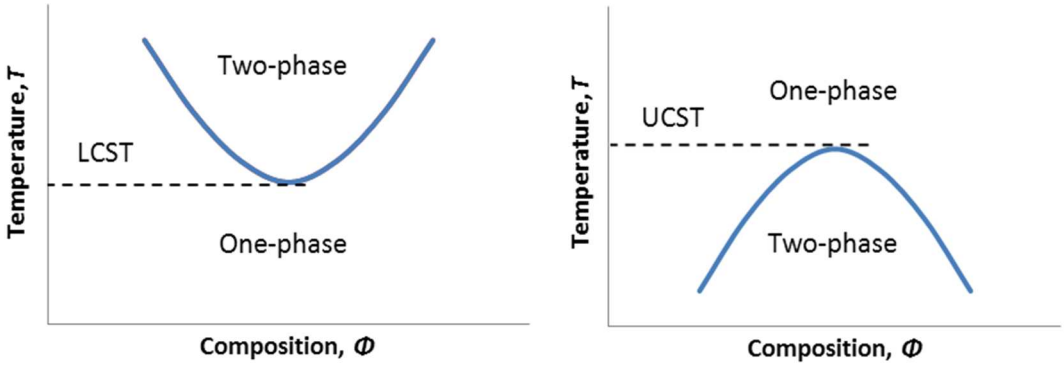


Fig. 2.9 Schematics of the lower and upper critical solution temperature. Reproduced from [47].

In polymer blends with strong polar interactions, phase separation normally takes place when the temperature is increased to a certain point, showing LCST phase behaviour. This is mainly due to the fact that polar interactions, e.g. hydrogen bonding, give a good bonding between the two components and may allow the mixed phase to have a better ordered structure, hence, lower entropy. However, these polar interactions will be destroyed as temperature goes up and the difference in thermal expansion will also be enlarged, and consequently, phase separation occurs. On the other hand, UCST behaviour mostly appears in systems with non-polar solutions, in which the solubility of polymers increases with temperature and a single phase appears at certain higher temperature [43, 47, 60, 63].

2.3 POLYMER THIN FILMS

A polymer thin film can be generally recognized as a polymer film with thickness between hundreds of nanometres and several microns. Frank *et al.* [20] suggested that, considering the radius of gyration (R_g) for typical polymers, which is around 10 nm, confined polymer films could be separated as ultrathin and thin films with thickness less than 100 nm and between 100 nm and 1000 nm, respectively. Polymer thin films are widely applied in many areas including packaging, protective coatings, biomedical engineering, flexible electronics and photovoltaics [1-3, 64].

With enormous constraint in one dimension compared with bulk polymers, polymer thin films show distinct properties from bulk properties of the corresponding polymers. This has already been confirmed by a great amount of research on polymer thin films, free standing or on substrates [2, 3, 20-22, 64-72]. Obviously, a good understanding of properties in polymer thin films is important for all the applications mentioned above. In the following sections, the properties of polymer thin films and the differences from bulk will be reviewed.

2.3.1 Glass Transition in Polymer Thin Films

T_g can be simply defined as the onset of segment motion in polymer chains, at which the properties of a polymer undergo dramatic changes. For instance, the modulus may decrease by three orders of magnitude around T_g for many polymers. Polymers show a transition from a glassy state to a liquid-like state as the temperature increases from below T_g to above [40]. The effect of confinement on T_g was first reported by Jackson and McKenna [73], who discovered a depression of T_g in o-terphenyl. This initiated various studies of T_g under confined conditions including the investigation of T_g in polymer thin films, which in general is different than that in the bulk [21-24, 26, 65-69, 71-118].

2.3.1.1 T_g in supported polymer films

Although polymer thin films have been widely applied in many areas, it was not until 1993 that Beaucage *et al*. [105] first reported work on T_g in polymer thin films. They performed measurements of T_g of spin cast thin polystyrene films on silicon wafers using ellipsometry. This technique is able to detect the thickness of a polymer film on a reflective substrate. Since polymer thermal expansion changes around T_g, T_g is able to be recognized in the plot of film thickness versus temperature [21, 105]. The relationship of T_g and film thickness was described by Keddie *et al*. [74]. They found that, for PS films on hydrogen-passivated silicon wafers with thickness below 40 nm, T_g decreases when film thickness decreases, in the same manner for three different molecular weights, shown in Fig. 2.10.

Figure removed due to the copyright issue

Fig. 2.10 T_g as function of film thickness for polystyrene with different molecular weights. △: M_w = 120000, ○: M_w =500800, ◇: M_w = 2900000. Fig.3 in ref. [74].

To explain this, Keddie *et al.* [74] suggested a liquid-like layer at the air-polymer interface:

$$T_g(d) = T_g(\infty)\left[1 - \left(\frac{A}{d}\right)^{\delta}\right] \qquad \text{(Eq. 2-5)}$$

where $T_g(d)$ is T_g of film with thickness d, $T_g(\infty)$ is the bulk T_g, A is the characteristic length of the surface layer, A = 3.2 nm and δ = 1.8.

Assuming a polymer film has a surface region of constant thickness with a lower T_g, the thinner the polymer film, the higher proportion of surface region in the film, hence, the lower the overall T_g [28]. The depression of T_g in polymer thin films has been confirmed by

extensive research using different techniques including: ellipsometry, X-ray reflectivity, positron annihilation lifetime spectroscopy and Brillouin light scattering [76, 78, 83-86, 97]. However, this depression is not observed in all situations. Later work of Keddie *et al*. [75] demonstrated that T_g of PMMA films on silicon wafers with a native oxide layer increases slightly with decreased film thickness. Similar phenomena have also been observed by other researchers [92-95].

Several parameters have been suggested and investigated to account for the shift of T_g in polymer thin films:

- *Polymer-substrate interfacial interactions*

Keddie *et al.* [75] initially indicated that interactions between polymers and substrates, e.g. hydrogen bonding, can explain the observed increase in T_g, in their case of PMMA films (with thickness below 100 nm) on silicon oxide substrates. The idea that strong substrate interactions may lead to T_g increasing in polymer thin films with decreased thickness was, subsequently, supported by research of Wallace *et al.* [94, 95]. They examined increased T_g firstly in PS thin films on hydrogen-passivated silicon and then in poly(2-vinylpyridine) on acid-cleaned silicon oxide by X-ray reflectivity, emphasising the importance of substrate interactions. Further work has been carried out on polymer-substrate interactions by Tsui *et al.* [91]. They measured T_g of PS film, 33 nm thick, on random copolymers of styrene and methyl methacrylate with different polymer-substrate interactions and found that that T_g varies with different interaction energy. This work demonstrated a significant effect of substrate on the mobility of polymer chains, hence the T_g, in ultrathin films, those with thickness of a few tens of nanometres.

- *Polymer-air interface*

The significance of free surfaces is most clearly revealed in free standing polymer films, reviewed in section 2.3.1.2. Comparing T_g of thin PS films with one free surface, Fig. 2.11b, and films capped by a metal layer, Fig. 2.11c, Sharp *et al*. [24] discovered that

the T_g of original PS films on substrates decreases when the film thickness is reduced below 40 nm, while, for capped PS films, T_g values are the same as the bulk T_g. This is strong evidence for the contribution of free surfaces to the T_g reduction in polymer thin films.

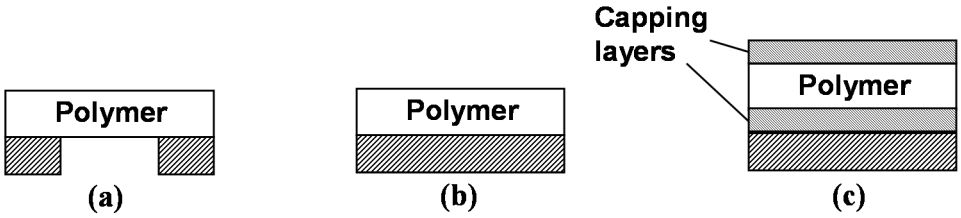


Fig. 2.11 Schematic diagram of three polymer thin film systems: (a) free standing; (b) supported; (c) capped films. With different polymer-air and polymer-substrate interfaces, these configurations allow the study of the two kinds of interfaces [2].

To exclude the effect of atmosphere, Raegen *et al.* [26] investigated T_g of PS thin films in ambient, in dry nitrogen and in vacuum, respectively, and found that for all the atmospheres, T_g values were depressed with reduced film thickness. The conclusion that may be drawn from their experiments is that the presence of this phenomenon of T_g reductions in polymer thin films is not affected by ambient environment, e.g. moisture content, but the existence of the free surface and the intrinsic properties of the confined polymers. However, the T_g of a polymer at the surface should be affected by the atmosphere.

The application of atomic force microscopy (AFM) provides a new insight for studies of T_g in polymer thin films. With AFM, it is possible to directly measure the T_g of a surface layer, which is lower than the bulk T_g [88]. The lower surface T_g is of course a result of the enhanced free volume in the near-surface region.

- *Molecular weight and chain conformation*

Early research by Keddie *et al.* [74-76] implied that T_g in polymer thin films is almost independent of molecular weight (e.g. Fig. 2.10). However, later work has demonstrated that glass transition behaviour in polymer thin films is actually both molecular weight and film thickness dependent [81, 106]. Singh *et al*. [81] discovered that, for PS thin films, the critical film thickness, below which T_g decreases with film thickness, is around 10 times the radius of gyration. They expressed the influence of molecular weight and film thickness as:

$$T_g = f(M_w) \times f\left(\frac{h}{\langle s^2 \rangle^{1/2}}\right) \qquad \text{(Eq. 2-6)}$$

where $f(M_w)$ accounts for the bulk T_g variations due to different molecular weight and $f\left(\frac{h}{\langle s^2 \rangle^{1/2}}\right)$ describes the confinement effects related to the radius of gyration. Furthermore, Grohens *et al*. [80] reported a significant influence of polymer structure, e.g. tacticity and chain conformation on T_g of PMMA films, which may be induced by strong adsorption and fast solvent evaporation during spin coating.

2.3.1.2 T_g in free-standing polymer films

Studies of free-standing polymer thin films provided powerful evidence for a depression of T_g in the presence of the free surface. In free standing polymer thin films, the effect of substrate on T_g can be eliminated and it has been demonstrated that, with the additional free surface, the depression of T_g is greatly enlarged compared to that in thin films on substrates [22, 23, 72, 106-108]. The study of T_g in free standing polymer thin films was first performed by Forrest *et al*. [22] using Brillouin light scattering. Their work showed that for free standing PS thin films, T_g decreases linearly when film thickness is reduced below the critical thickness, approximately 70 nm, which is 30 nm greater than that in PS thin films on substrates, displayed in Fig. 2.12a [22].

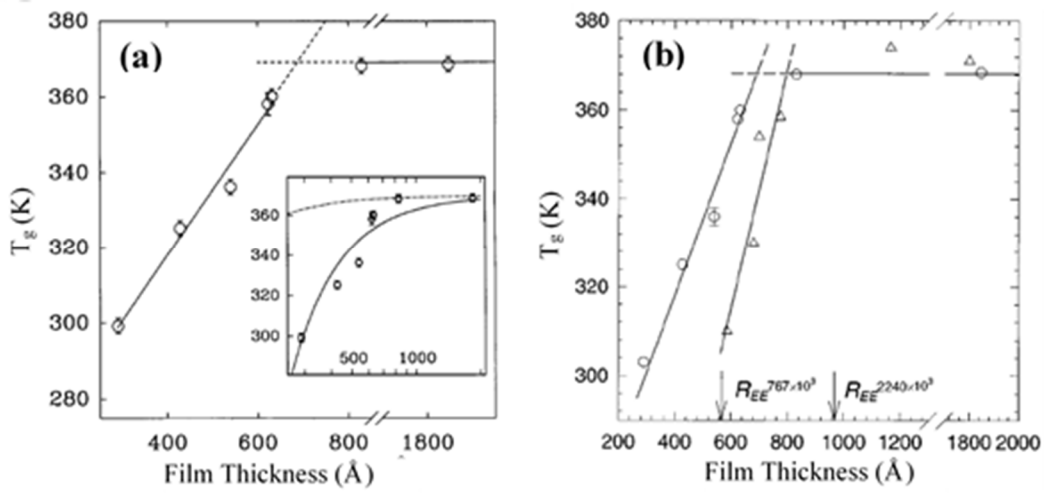


Fig. 2.12 Depression of T_g in free standing PS thin films. (a) T_g decreases linearly with film thickness when film thickness is below 70 nm. The insert shows the fit of the data by Eq. 2-5 (solid line) and the data from PS films on Si wafer by Keddie *et al.* [74] (dashed line). (b) T_g as a function of film thickness with different molecular weights: ○: $M_w = 7.67 \times 10^5$, △: $M_w = 2.24 \times 10^6$. (a) and (b) are reproduced from [22] and [23] respectively with permissions of the copyright holder.

Another significance of free standing films is the identification of the molecular weight dependence of T_g reduction in polymer thin films. After investigation of T_g as a function of film thickness for two PS with different molecular weights, Forrest, Dalnoki-Veress and Dutcher [23] revealed an obvious influence of molecular weight on T_g in PS thin films, shown in Fig. 2.12b. They suggested that the average end-to-end distance of unperturbed polymer chains, R_{EE}, is controlling the critical thickness for observing a reduction in T_g. This discovery could imply a significant contribution of chain confinement effects to T_g depressions. With a higher molecular weight, hence a higher R_{EE} value, the film thickness required for the depression of T_g to be observed is increased. Detailed work on the influence of molecular weight on T_g depressions in free standing PS films were carried out by Dalnoki-Veress *et al.* [106] later and confirmed this molecular weight dependence.

2.3.1.3 Chain mobility in polymer thin films

The T_g reduction in polymer thin films is a direct identification of the improved polymer chain mobility at the surface of thin films. Chain mobility is indicated to be relatively high in the near surface region since a surface T_g with a much lower value than that of the bulk has been observed [28, 86-89, 116]. However, increased mobility in polymer thin films was first suggested by Reiter [69] when it was found that dewetting of thin PS films on float glass substrates was able to be detected at temperatures below bulk T_g. With the "asymmetric rim" mode proposed by Reiter [114], this near T_g dewetting was further studied by Saulniter *et al*. [115]. Subsequent research on relaxation in polymer thin films has also confirmed the enhanced chain mobility [109]. However, when the film is extremely thin, the mobility of polymer chains will decrease due to the relatively high spatial confinement, and possibly due to substrate interactions. Frank *et al*. [110] reported that the lateral diffusion coefficient in PS films decreases substantially as the film thickness is less than 150 nm and is reduced by a factor of two when the film thickness is around 50 nm.

2.3.2 AFM in Characterizations of Polymer Thin Films

AFM characterizes the forces between a sharp tip and the sample surface and is a powerful technique for the characterisation of topography, adhesion, friction, modulus and relevant properties of surface or near-surface regions for polymers [119-121]. The development of tapping or non-contact mode AFM allows these characterisation of polymers with minimal damage and contaminations to sample surfaces [119, 120]. AFM can present the direct morphology development of the polymer surface during crystallization [122-124] and can also be used to measure surface T_g [88], since the viscoelasticity of polymers changes greatly around T_g. Taking the tip-surface interaction force as a function of tip displacement, a force-distance hysteresis curve can be recorded,

an example of which is displayed in Fig. 2.13a [125]. As polymers become soft at temperatures over T_g, a marked enhancement of the displacement hysteresis can be observed around T_g, which can be used for T_g detection [88]. Typical examples of force-distance curve for low molecular weight PS are given in Fig. 2.13b, illustrating the substantial change in hysteresis with temperature.

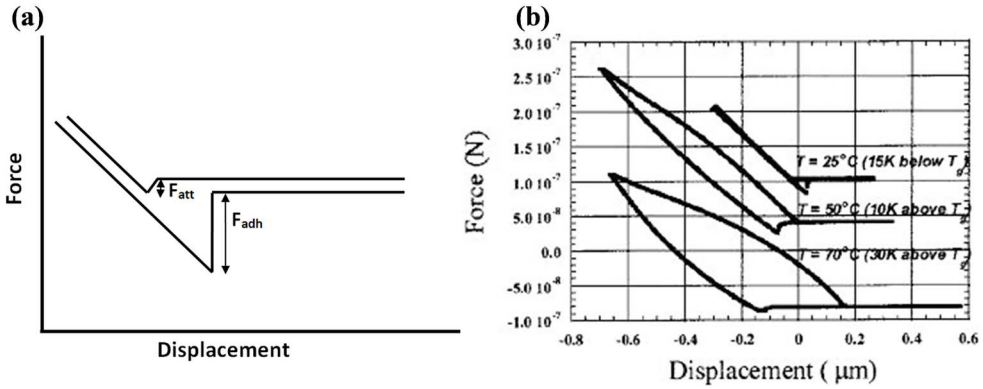


Fig. 2.13 (a) Schematic of a force-distance curve, where F_{att} is the attractive van der Waals force at the tip-sample contact point, F_{adh} is the adhesion force when the tip is pulling out [125]; (b) Force-distance curves for PS of molecular weight 3900, T_g = 40°C, reproduced from [88] with permission of the copyright holder. The hysteresis of pull out increases dramatically when temperature goes higher than T_g.

2.4 CRYSTALLIZATION IN POLYMER THIN FILMS

With higher mobility of polymer segments and chains, manifesting in a lower T_g, crystallization of a polymer in near-surface regions, surface-specific crystallization is expected to occur at a temperature lower than the bulk crystallization temperature. Confined in thin films, polymer crystals exhibit surface-specific morphologies (not just a change in surface morphology due to bulk crystallization in a thin film), which are very different from those in the bulk [2, 126-128]. Reflecting the experimental approaches, the focus of this review is placed on spin cast or drop cast films on substrates instead of films from commercial industrial processing. Referring to the lamellar orientation, polymer crystals in sub-micron films can be, generally, classified into two groups: edge-on lamellar crystals with fold surface perpendicular to the substrate and flat-on lamellar crystals with their fold surface parallel to the substrate [128, 129], illustrated in Fig. 2.14 [129].

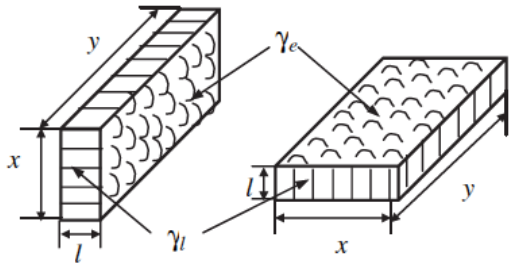


Fig. 2.14 Schematic of edge-on (left) and flat-on lamellar orientations, where x, y, l are lamellar width, length and thickness, respectively. γ_e is the free surface energy of fold surface which is much higher than that of lateral surface γ_l. Reproduced from [129] with permission of the copyright holder.

2.4.1 Surface Crystallization

Edge-on lamellae are, normally, in the form of two-dimensional (2D) spherulites or lamellar bundles, which are made up of lamellar fibrils, while flat-on lamellae can show morphologies like dendrites or seaweed, which are single-crystalline-like structures, or regular single crystal lamellae [2, 126]. Various techniques are available for the characterisation of crystallization in polymer thin films, including: (a) imaging techniques,

like optical microscopy (OM), AFM, scanning electron microscopy (SEM) and transmission electron microscopy (TEM), among which AFM is preferred due to its capabilities such as: non-destructive tapping mode, crystal thickness detection with excellent height resolution and in-situ crystallization studies with a wide temperature range [123, 126, 130], and (b) crystallinity and crystalline lattice characterization techniques, such as electron diffraction (ED), grazing incidence X-ray diffraction, Fourier transform infrared spectroscopy (FTIR) and ultraviolet spectroscopy (UV). Between them, these techniques are able to determine the lamellar orientation, crystallinity and crystallization kinetics in polymer thin films [126, 131, 132].

2.4.1.1 Edge-on lamellae

Previous research has found edge-on lamellae in thin films of different semicrystalline polymers including: homopolymers such as PE (high and low density polyethylene HDPE and LDPE) [133-138], polypropylene (isotactic PP and elastomeric PP) [139-141], PS (isotactic and syndiotactic PS) [142-144], poly(ethylene oxide) (PEO) [145], PVOH [146], PET [122, 147-149], PEN [28], polyamide (PA) (PA6 and PA66) [150, 151], polylactide (poly(L-lactide) (PLLA) and poly(D-lactide) (PDLA)) [152, 153], poly(ε-caprolactone) (PCL) [154]; poly(vinylidene fluoride) (PVDF) [155], and polyhydroxybutyrate (PHB) [156]; copolymers like poly(ethylene-vinyl acetate) (EVA) [157], poly(L/D-latide) [153], and poly(bisphenol A alkyl ether) (BA-Cn) [158-161]; and polymer blends such as poly(aryl ether ether ketone)/poly(ether imide) (PEEK/PEI) blend [162] and blends containing PVDF [155].

Surface lamellae of spherulitic morphology were observed by Bassett and Vaughan [142] as early as 1985. Using electron microscopy, they performed extensive work on melt-crystallized isotactic polystyrene (iPS) and found the existence of sheaf-like lamellae, an array of separated lamellae and spherulitic lamellae on the surface of iPS samples, shown in Fig. 2.15. The sheaf-like lamellae, which were around 20 nm thick, packed

closely at the centre and spread at the edges. This phenomenon showed that it is possible for spherulitic morphologies to grow in two-dimensions in surface layers. However, the iPS films involved above were as thick as 1 to 2 mm and cannot show the effects of confinement on crystallization in thin films. Following this, work on submicron polymer films has been carried out and revealed that two dimensional spherulitic structures can develop from sheaf-like structures [28, 133, 145].

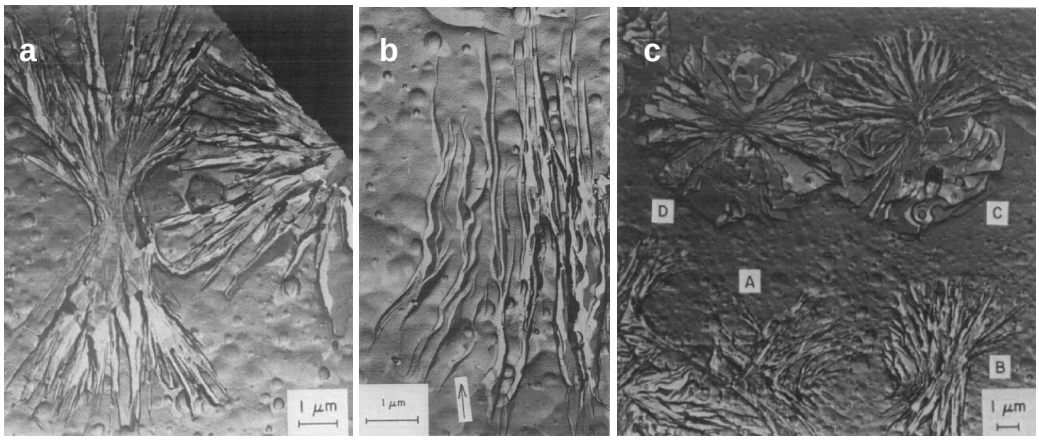


Fig. 2.15 Electron micrographs of isotactic polystyrene crystallized at 220 ℃ for 24 hr: (a) sheaf-like lamellae; (b) an array of separated parallel lamellae; (c) lamellae splaying in three dimensions. Reproduced from [142] with permission of the copyright holder.

Pearce and Vancso [145] first performed the imaging of melt crystallized PEO using hot-stage AFM. They obtained PEO films by casting PEO solutions (2 wt% PEO in chloroform) directly onto the copper electrode of the heating stage. PEO films were first melted at 75 ℃ for 1 min and then crystallized at the desired temperature producing hedritic structures. Growth of the PEO hedrites is displayed in Fig. 2.16, with typical edge-on lamellae. These edge-on crystals obtained from melt-crystallization, however, are observed long after the start of crystallization and cannot tell us about the very early morphology of the crystals immediately after their birth.

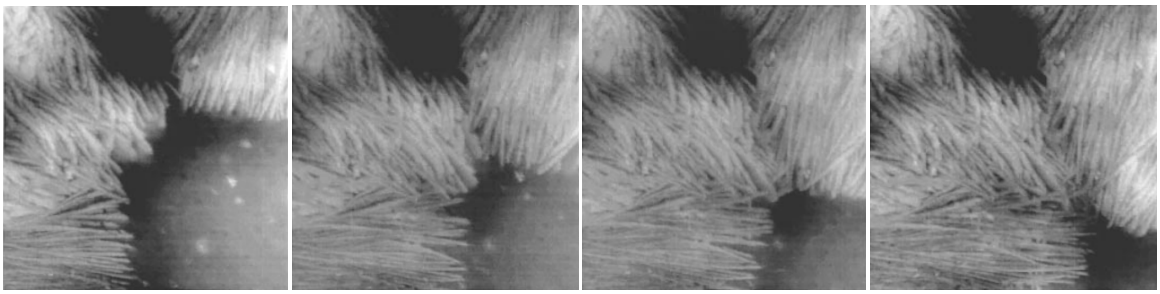


Fig. 2.16 AFM height images of PEO spherulites growing at 57 ℃. The time gap between the nearby images is 3 min and the scale from dark to bright is 800 nm. All the images are 12.5 μm × 12.5 μm large, reproduced from [145] with permission of the copyright holder.

In spite of the fact that crystals in polymer thin films are mostly introduced by thermal processes, either melt-crystallizing or annealing, polymer thin films without any thermal treatment may also exhibit crystalline morphologies. A typical example is HDPE. Bartczak *et al*. [133] found that, for a spin-coated HDPE film (15 nm thick) on a calcite substrate, 2D spherulites with sheaf-like lamellae can be examined using contact mode AFM, shown in Table 2.1. A possible explanation is that the crystallization rate of HDPE was faster than the solvent evaporation rate, thus, crystallization happened during sample drying.

Li *et al*. [158] performed the first systematic study of the birth and growth of surface-specific lamellae and spherulites in polymer thin films using AFM. In their work, poly(bisphenol A octane ether) (BA-C8) films with thickness around 300 nm on a silicon wafer were investigated. Results indicated that the branching of lamellae in polymer thin films is the result of secondary nucleation, which forms secondary lamellae. It was observed that primary lamellae, which develop from nuclei, splay apart at the two ends and form more lamellae through secondary nucleation, which leads to the formation of lamellar sheaves, shown in Fig. 2.17. Similarly, through further secondary nucleation and splaying, a lamellar sheaf can gradually grow into a 2D spherulite, exhibited in Fig. 2.18. Therefore, the edge-on surface-specific crystal growth is, actually, a nucleation-limited process. Li *et al*. also found that AFM probe influences the development of lamellae. They proved that the growth direction of lamellae tips are actually changed when the set point amplitude ratio for AFM is reduced, which means the AFM probe is pressed deeper. This

point is vital in the AFM investigation of polymer surface behaviour especially for the situations where morphology changes are slight.

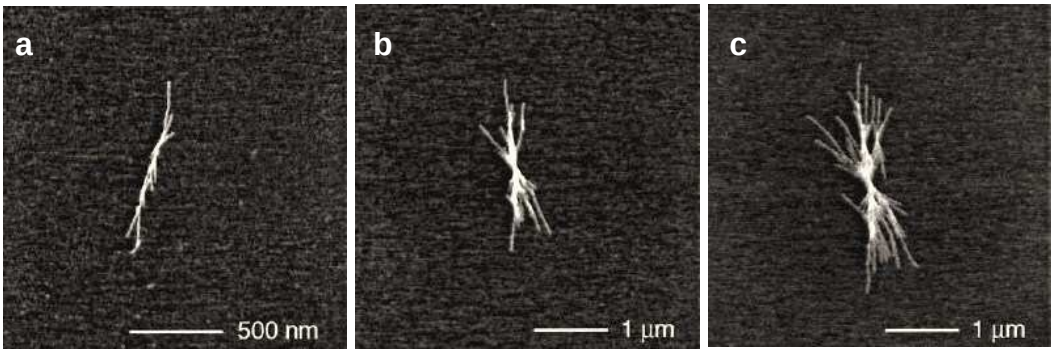


Fig. 2.17 AFM phase images showing lamellar sheaf development (reproduced from [158] with permission of the copyright holder): (a) birth of lamellae from a single nucleus; (b) lamellae splaying and forming of new lamellae; (c) sheaf-like lamellar formation.

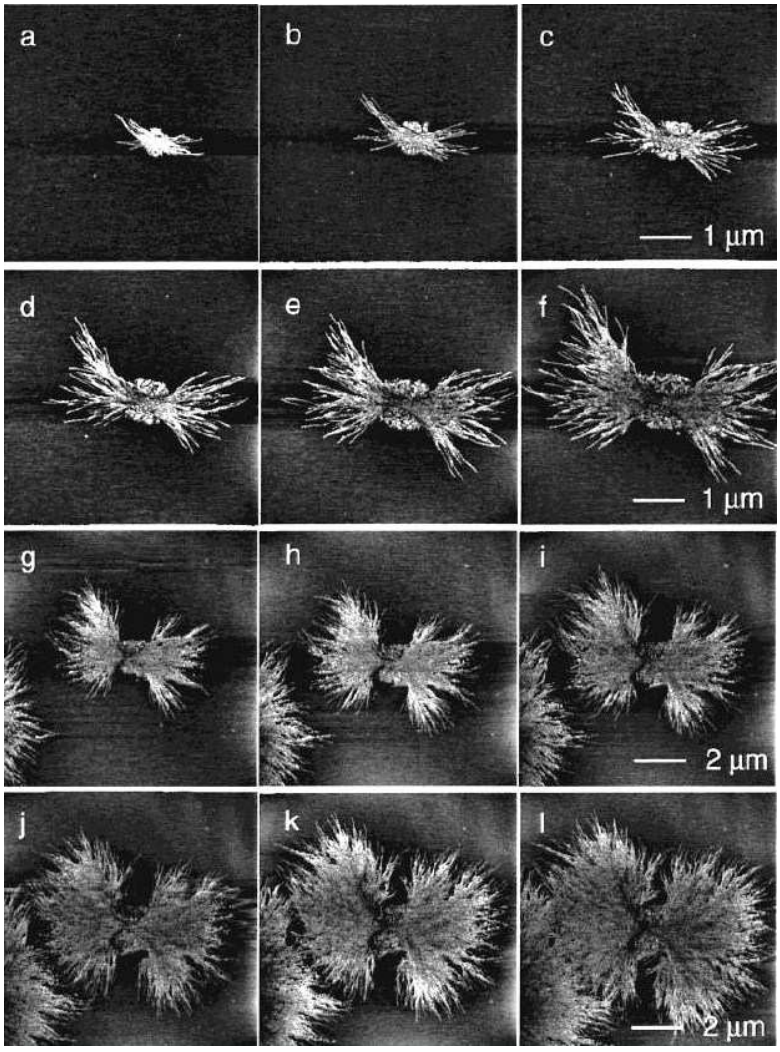


Fig. 2.18 AFM images displaying the development of a spherulite. Reproduced from [158] with permission of the copyright holder.

Another good example showing surface-specific 2D spherulites is with PET thin films. Research in our group [28] found that surface sheaf-like lamellae of PET can be induced by annealing amorphous films at temperatures much lower than the bulk crystallization temperature. These lamellar sheaves grow and form 2D spherulites as the annealing temperature is increased (Fig. 2.19a-d). However, as the temperature continues to go up, bulk crystallization in the underlying part occurs and disrupts the surface-specific crystallization (Fig. 2.19e&f). The development of the crystallization in PET thin films displayed in Fig. 2.19 clearly shows a surface and a bulk crystallization stage.

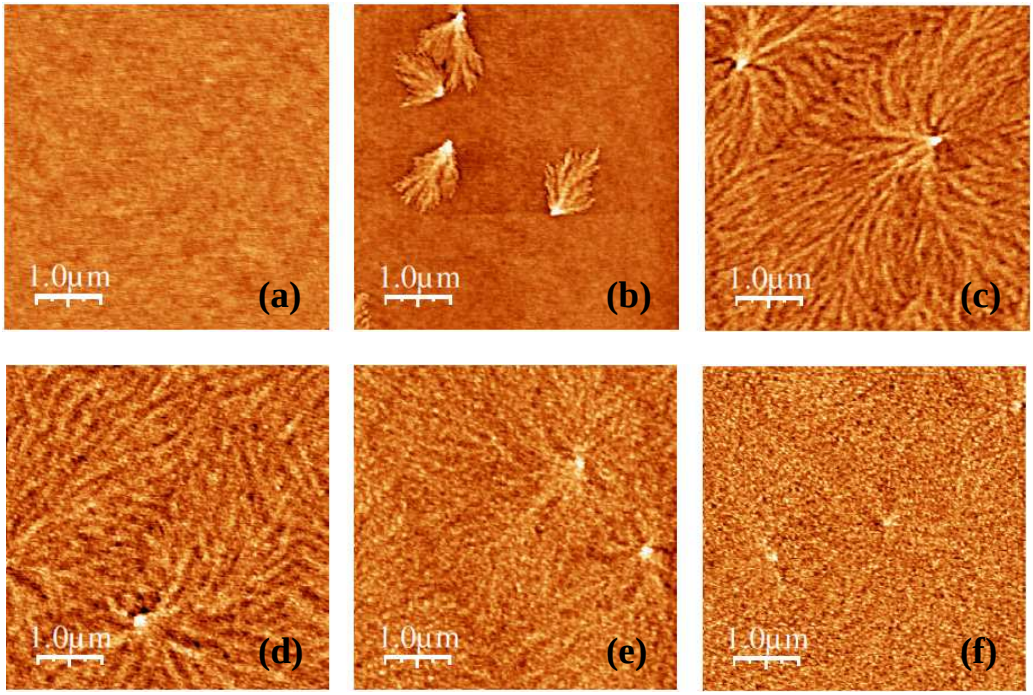
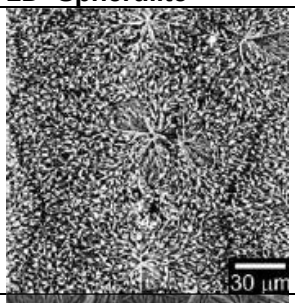
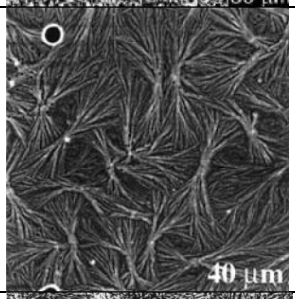
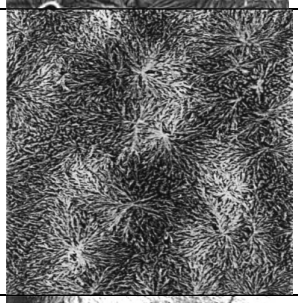
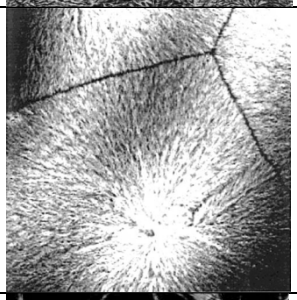
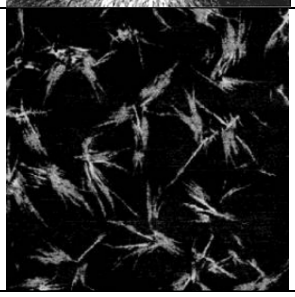
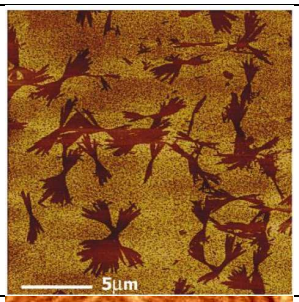
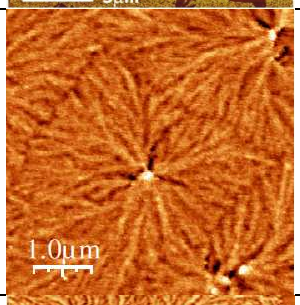
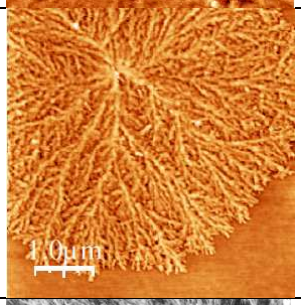
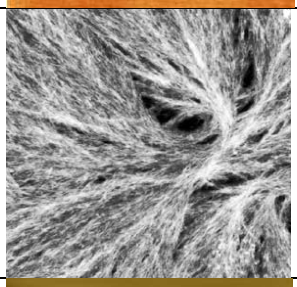
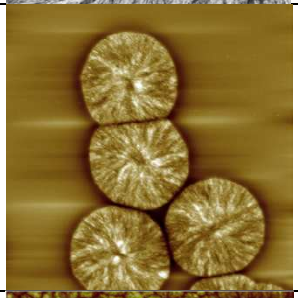
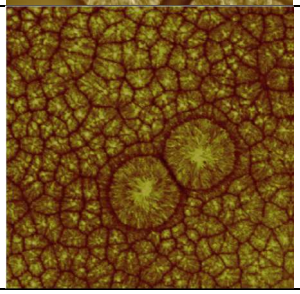


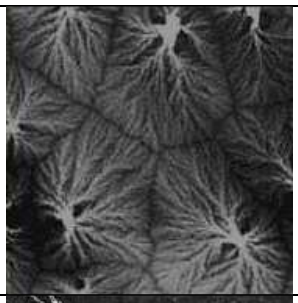
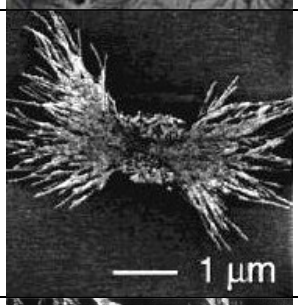
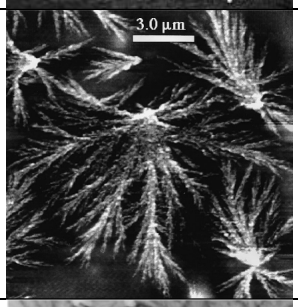
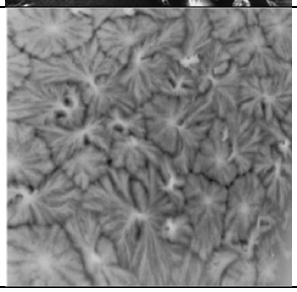
Fig. 2.19 AFM height images showing the growth of 2D spherulites in 28 nm thick PET films by annealing at: (a) 60 ℃ ; (b) 75 ℃ ; (c) 85 ℃ ; (d) 90 ℃ ; (e) 95 ℃ ; (f) 150 ℃. Reproduced from [28].

Examples of edge-on 2D spherulites in various polymer thin films revealed by AFM are summarized in Table 2.1. It could be found here that, in most cases, the 2D edge-on crystals are obtained by crystallization from a melt or at an annealing temperature well above T_g. These crystallization studies are actually different from the surface-specific crystallization that occurs in samples annealed below the bulk crystallization temperatures of corresponding polymers. Work on polymer thin films is still needed for a better understanding of the surface-specific crystallization.

Table 2.1 Summary of 2D spherulites in polymer thin films detected by AFM. Figures reproduced with permission of the copyright holders.

Polymer		2D- Spherulite	Interpretation	Author(s)
Homopolymer	LLDPE		194nm thick LLDPE film, melt first and then crystallized at 115 ℃ for 10 hr	Jeon *et al*. [138]
	LDPE		20nm thick dip-crystallized (dip substrate into hot solution) LDPE film heated to 70 ℃ at 5 ℃/s	Godovsky *et al*. [134]
	HDPE		15nm thick spin-casted HDPE film on a calcite substrate, 75×75 µm	Bartczak *et al*. [133]
	HDPE		220nm thick HDPE spin coated on silicon at 180 ℃, 80×80 µm	Mellbring *et al*. [136]
	ePP		Phase image of single lamellae on the surface of an ePP film (70 µm) at 34 ℃ (melt first) 4×4 µm	Schonherr *et al*. [141]

Homopolymer	PVOH		Lateral force image of a PVOH film by solution casting (10 µm thick)	Strawhecer *et al*. [146]
	PET		As-spin-cast amorphous 39 nm thick PET film annealed at 80 °C	Shinotsuk [28]
	PEN		As-spin-cast amorphous 16nm thick PEN film annealed at 125 °C	Shinotsuk [28]
	PA66		As-spin-cast PA66 on gold, 5×5 µm	Elzein [151]
	PLLA		2D crystals of PLLA form at 120°C for 4 min, solution-cast film 500-600 nm thick, 100×100 µm	Yuryev [153]
Copolymer	Copolymer of PLLA/PDLA		Crystallized at 110°C for 4 min, solution-cast film 500-600 nm thick, 100×100 µm	Yuryev [153]

	EVA		70nm thick EVA films spin coated onto silicon at 150℃ (T_m = 95 ℃), 50×50 μm	Wang *et al*. [157]
	BA-C8		Surface crystals in a spin-cast BA-C8 film (300 nm thick) at 25 ℃	Li *et al.* [158]
Polymer Blend	PEEK		PEEK spherulites in a PEEK/PEI (55/45) thin film (20-200 nm) melt-quenched and annealed at 190 ℃ for 210 min	Ivanov *et al*. [162]
	PVAc/PVDF		PVAc/PVDF (50/50) film from solvent casting, 30×30 μm	Lee *et al*. [155]

2.4.1.2 Flat-on Lamellae

In contrast to edge-on lamellae, flat-on lamellae normally exist in ultrathin films or monolayer polymer samples. Surface morphologies in these situations result from crystallization in a highly confined state. Due to the enhanced confinement, the formation of flat-on lamellae is a diffusion-limited process rather than the surface nucleation controlled process for edge-on lamellae development [126-128]. Examples of polymers observed to form flat-on lamellae morphologies include: PE [138, 163], PP (isotactic and syndiotactic PP) [164-166], iPS [167-169], PCL [154, 170], PEO and its copolymers or blends with other polymers [171-179], poly(di-n-alkylsilanes) [180, 181],

poly(trifluoroethylene) [182], poly(oxymethylene) [183], and PLLA [152, 184].

According to theoretical work of Brener *et al*. [185, 186], crystal patterns of polymers under diffusion-limited conditions can be divided into dendritic, with evident geometrical order, and seaweed morphologies. Each of these crystal growth patterns can also be classified as compact and fractal patterns, where a fractal pattern has structures with self-similarity. For better understanding of the different diffusion-limited crystal morphologies, they developed a morphology phase diagram of growth patterns by plotting supercooling (Δ) versus anisotropy (ε) (of surface tension in the plane of growth, e.g. due to crystalline anisotropy), presented in Fig. 2.20. In addition to the degree of supercooling and anisotropy, they also recognize the influence of fluctuation at the growth front in the two-dimensional diffusional growth of crystalline structures [186, 187]. Although the theory of Brener *et al*. is not applied to all the flat-on lamellae in polymer thin films, e.g. regular single crystals, it is able to explain most diffusion-limited crystal growth observed.

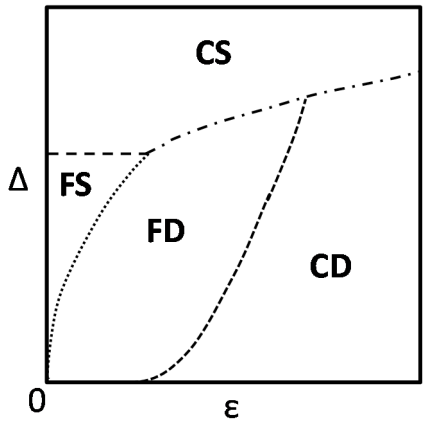


Fig. 2.20 Morphology phase diagram of growth patterns for diffusion-limited crystallization, where Δ represents supercooling and ε stands for crystalline anisotropy. CS: compact seaweed; FS: fractal seaweed; FD: fractal dendrite; CD: compact dendrites. Reproduced from [186].

An isotactic PS ultrathin film is one of the best understood systems to exhibit special flat-on lamellar crystals. Extensive experiments were carried out by Taguchi *et al*. showing special iPS crystal growth in ultrathin films [167-169]. In their early work [167], 11 nm thick iPS films were melted at 250 °C for 3 min and then quenched to room temperature before

isothermal crystallization at different temperatures. AFM images of the crystals formed are displayed in Fig. 2.21. It shows that iPS film crystallized at 210 ℃ produces a hexagonal single crystal. As the crystallization temperature decreases (which means increasing supercooling), a compact dendrite pattern (snowflake-like) (Fig. 2.21c) is formed and a number of branches grow on the dendrite (Fig. 2.21d&e). When the temperature decreases below 180℃, a compact seaweed pattern ap pears with many random branches (Fig. 2.21f). This series of crystal growth pattern agrees well with the morphology diagram by Brener *et al*., where the surface pattern changes from CD to CS with increasing supercooling at high anisotropy.

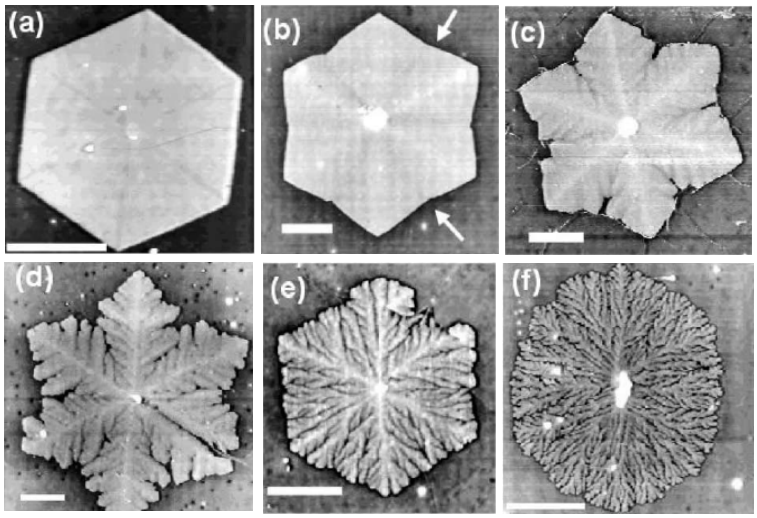


Fig. 2.21 AFM images showing isotactic PS crystal growth in 11nm thick film at (a) 210 ℃ for 4 hr; (b) 205 ℃ for 4 hr; (c) 200 ℃ for 4 hr; (d) 195 ℃ for 3 hr; (e) 190 ℃ for 1 hr; (f) 180 ℃ for 1 hr. Scale bars represent 5 μm. Reproduced from [167] with permission of the copyright holder.

Figure removed due to the copyright issue

Fig. 2.22 AFM images showing crystal growth of isotactic PS at 180 ℃ in ultrathin films: (a) 17 nm thick for 30 min; (b) 14 nm, 1 hr; (c) 11 nm, 1.5 hr; (d) 9.7 nm, 3.25 hr; (e) 8.7 nm, 3.25 hr; (f) 6.1 nm, 14 hr. Scale bars represent 5 μm. Fig. 1 in [168].

Following work on the crystal growth of iPS, an investigation of the influence of film thickness were soon carried out by Taguchi *et al*. [168]. Using the same crystallization method mentioned above, iPS ultrathin films with different thickness were crystallized at 180 ℃. The results in Fig. 2.22 show that diffusion-limited crystal growth appears when the film thickness is reduced below 15 nm. With decreasing film thickness and increasing annealing time, the crystal morphology of iPS undergoes changes from a compact seaweed structure (Fig. 2.22b), to compact dendrite (Fig. 2.22c) and then to fractal seaweed or dendrite (Fig. 2.22d-f). This indicates a thickness dependence of crystal growth rate and morphology. The morphological change also suggests a thickness effect on the anisotropy of surface tension in the diffusion-limited situations.

PCL, which is able to form fractal dendritic crystals in ultrathin films, is another typical system. Mareau *et al*. [170] found that the morphologies of the flat-on crystals for PCL films (6 nm thick) are affected by the thermal history of the samples. As is shown in Fig. 2.23, the width of the PCL dendritic branches formed at 30 ℃ decreases when the pre-heating time at 64 ℃, which is above the melting point of PCL, increases. They also detected a decrease in the crystal growth rate for the films heated at 64 ℃. The changes in the crystal morphology and growth rate were attributed to the residual solvent, which acted as a plasticizer and increased the mobility of PCL chains (by reducing the T_g of the system). As the heating time before crystallization increases, the amount of solvent remaining in the film decreases, which results in a lowered diffusion rate, thus, a reduced crystal growth rate. For a constant crystallization temperature, a slower diffusion may cause an increased number of nuclei at the growth front, which leads to decreased dendritic width.

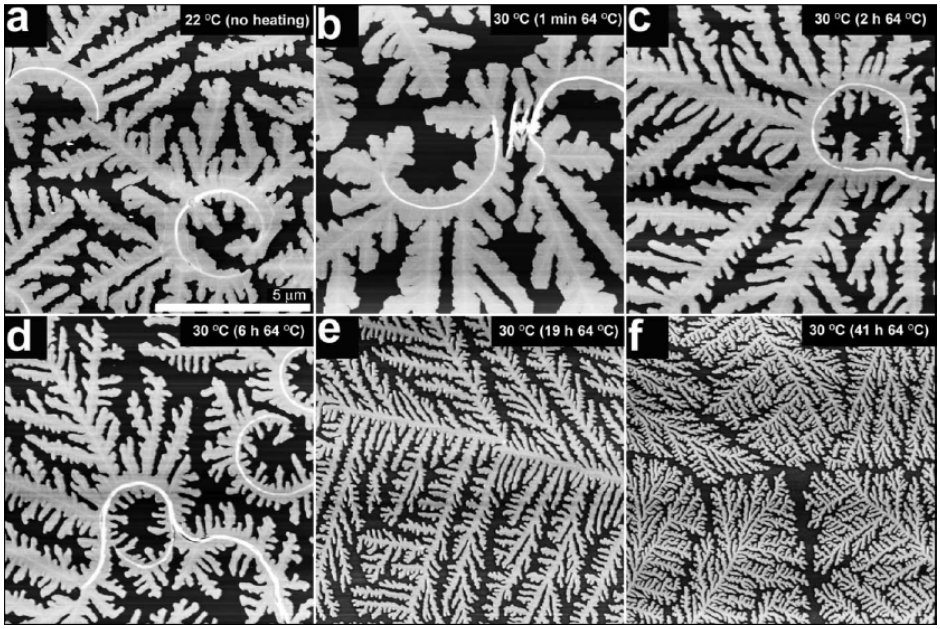


Fig. 2.23 AFM images (10 µm × 10 µm) of 6 ± 1 nm thick PCL films isothermally crystallized: (a) at room temperature (22℃) without heat treatment; crystallized at 30℃ after heating at 64℃ for (b) 1min; (c) 2 hr; (d) 6 hr; (e)19 hr; (f) 41 hr. Reproduced from [170] with permission of the copyright holder.

In addition to the surface morphologies induced by melt-crystallization, flat-on crystallites can also be produced by annealing spin-coated amorphous films (cold-crystallization). Reiter and Sommer [171] discovered that isothermal crystallization of a PEO monolayer is able to give a fractal seaweed (finger-like) pattern. Their experimental results indicated that crystallization temperature as well as molecular weight is crucial to the morphology of diffusion-limited crystals.

2.4.1.3 Parameters affecting surface crystallization

Referring to the literature reviewed above, the main parameters that control the morphology of surface crystals in polymer thin films are film thickness, polymer-substrate interactions, molecular weight, and crystallization temperature. The first three parameters determine the T_g in polymer thin films (mentioned in section 2.3.1), hence, affect the mobility of polymer chains in thin films directly. Along with surface T_g, crystallization temperature controls the diffusion of polymer chains and nucleation rate, thus, influences the morphological pattern of surface crystals.

Work on various polymer thin films has demonstrated that the lamellar orientation at the surface of polymer films turns from edge-on to flat-on as the film thickness decreases [28, 127, 129, 138, 154]. A good example for this transition is PCL investigated by Mareau *et al*. [154]. They used AFM and TEM to examine the surface crystals of PCL induced by crystallizing films with different thicknesses, from 200 nm to 6 nm, at room temperature for 24 hr. Although crystals in films with thickness 200, 120 and 60 nm show similar spherulitic structures, the fuzzy diffraction spots in Fig. 2.24a&b proved the existence of edge-on lamellae in 200 and 120 nm thick films. As film thickness continues to decrease, flat-on lamellae dominate and surface crystal morphology changes from compact seaweed (Fig. 2.24e) to fractal dendrite (Fig. 2.24f).

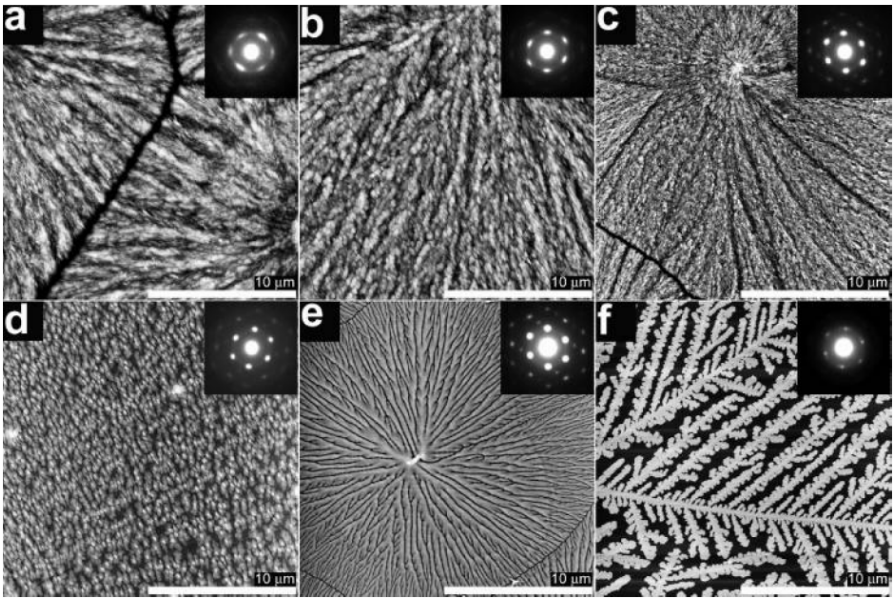


Fig. 2.24 AFM height images of PCL films crystallized at room temperature for 24 hr with corresponding electron diffraction patterns. The film thickness: (a) 200 nm; (b) 120 nm; (c) 60 nm; (d) 30 nm; (e) 15 nm; and (f) 6 nm. Reproduced from [154] with permission of the copyright holder.

Ma *et al*. [128] suggested that film thickness can be categorized into three groups including: (a) films thicker than several hundreds of nanometres, where edge-on lamellae predominate; (b) films thicker than polymer coil size but thinner than 100 nm, where both edge-on and flat-on may exist; (c) films thinner than the polymer coil size (monolayer) with typical diffusion-limited morphology.

The effect of substrate on crystal orientation and morphology has been confirmed as well. Through investigation of the surface crystals in PE films on different substrates, Wang *et al*. [129] showed that PE films on silicon have ordered surface crystals, while those on Al and polyimide substrates do not (all films were prepared by spin coating above 100 ℃ and then slow cooled from 140 ℃ to ro om temperature in a vacuum oven). With reduced film thickness, surface crystals in films on silicon turn from spherulitic morphology (edge-on) to a fractal seaweed pattern (flat-on), Fig. 2.25. However, this crystalline orientation transfer with decreased thickness was not found in films on Al and polyimide. Wang *et al*. worked out that the interfacial energy of PE on silicon is the lowest, whereas it is the highest on polyimide.

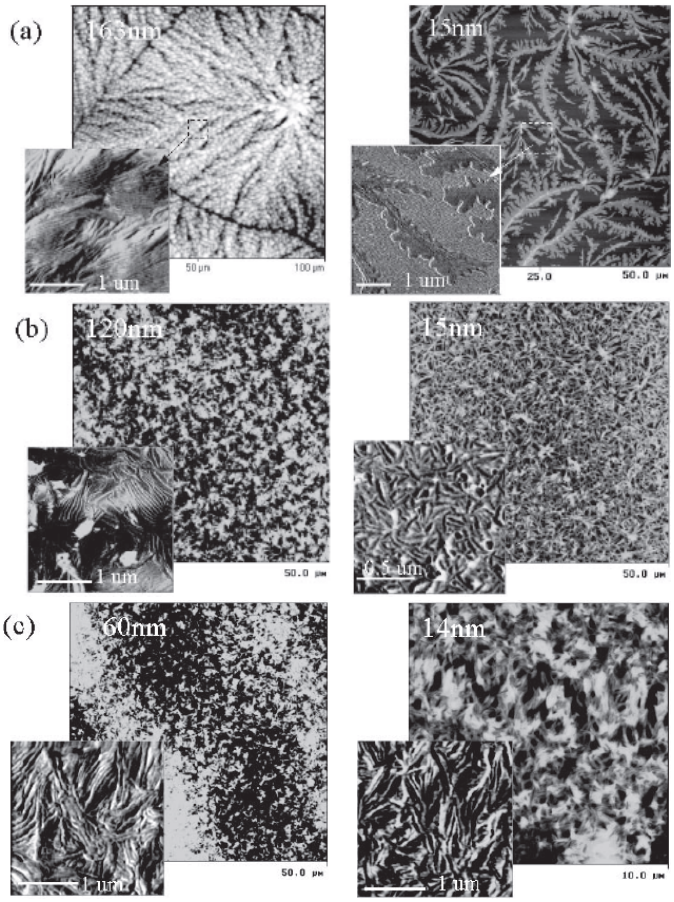


Fig. 2.25 AFM height (large ones) and phase (small insets) images of B-3 (polyethylene with hexane as co-monomer, 20 branches per 1000 backbone atoms) films on (a) silicon, (b) aluminium, and (c) polyimide substrates, with thicknesses marked in the images. Reproduced from [129] with permission of the copyright holder.

Furthermore, research by Wang *et al.* [127] also reported that, for ultrathin films (33 nm) of poly(bisphenol A hexane ether) (BA-C6), the formation of edge-on lamellae predominated at temperatures near T_g (~ 35 ℃), while flat-on lamellae appeared when the temperature approaches T_m (~ 98 ℃). This was explained by the higher rate of homogeneous nucleation at the surface at low temperatures resulting in the edge-on lamellae, and the faster heterogeneous nucleation at the polymer-substrate interface which produces flat-on lamellae. The preference of lamellar orientation at different temperatures shows the critical role of temperature in the crystallization in ultrathin films.

2.4.2 Crystallization Kinetics in Thin Films

To explain the crystallization kinetics in polymer thin films, Avrami-Evans theory is the most widely applied model. This kinetic approach established a relation between crystallinity and crystallization time and provided a method for crystal growth rate:

$$V^c = 1 - e^{-Kt^n} \qquad \text{(Eq. 2-7)}$$

where V^c is the volume percent crystallinity, t is the crystallization time, K is a rate constant depending on experimental conditions, nucleation type and crystal shape, n is the Avrami exponent depending on the dimensionality of growth [2, 20, 131, 188].

With poly(di-n-hexylsilane) (PDHS) films, Despotopoulou *et al*. [188] fitted the Avrami equation to experimental data for films with different thicknesses crystallized at 0 ℃ and 50 nm films crystallized at different temperatures, shown in Fig. 2.26. It was found to be difficult to determine the influence of film thickness and temperature on K. However, similar K values were obtained for films with various thicknesses crystallized at different temperature. Results also demonstrated that the Avrami exponent, n, decreased and approached 1, which means one-dimensional and athermal crystal growth, as the film thickness decreased. Moreover, n was observed to increase with decreasing crystallization temperature, implying the effect of supercooling, which is in good

agreement with the theory by Brener *et al*. [186] in section 2.4.1.2.

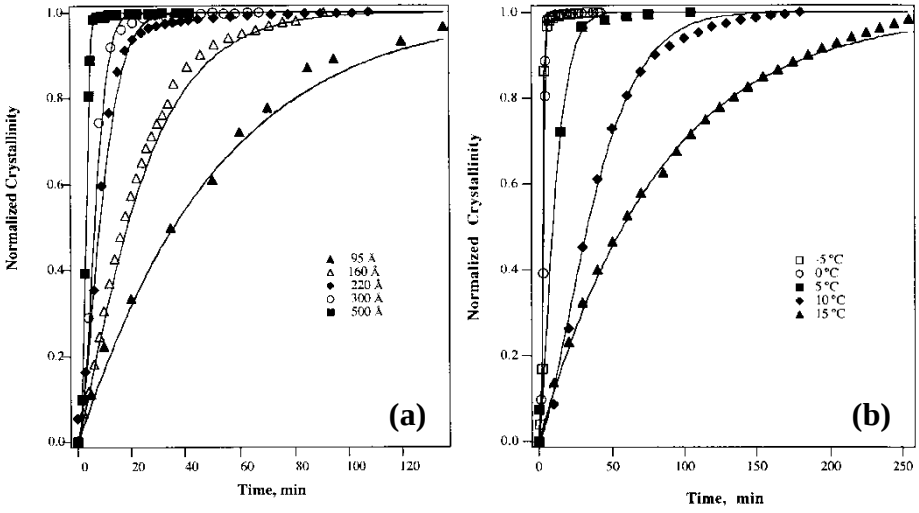


Fig. 2.26 Non-linear fits of the Avrami equation to experimental data for (a) crystallization at 0 ℃ ; (b) crystallization of a 50 nm thick film. Reproduced from [188] with permission of the copyright holder.

Nevertheless, different results were obtained in PEO films by Schonherr and Frank [131], where K decreased with decreasing film thickness. The Avrami exponent for crystallization in PEO films stayed between 3 and 4, which indicates two- and three-dimensional crystallization. A possible explanation for the differences between PEO and PDHS is the different preferred chain orientation for the two polymers in thin films.

The demonstration of decreased growth rate with reduced film thickness for PEO supports the early work on iPS by Sawamura *et al*. [189]. To explain the thickness dependent crystal growth rate of iPS, they developed the equation:

$$G(d) = G(\infty)(1 - \frac{a}{d}) \qquad \text{(Eq. 2-8)}$$

where G(d) and $G(\infty)$ are the crystal growth rate in a film of thickness d and in the bulk, respectively. The constant, a, is independent of substrate, molecular weight and temperature.

However, Taguchi *et al*. [168, 169] pointed out later that this equation is limited to thickness larger than the lamellar thickness, d_c. An example is presented in Fig. 2.27

illustrating the change of thickness dependence of iPS crystal growth. For films thicker than d_c, the thickness dependence of growth rate may be interpreted by the decreased chain mobility due to the enhanced entanglements of polymer chains in the highly confined state. When the film thickness is down to the lamellar thickness, crystal growth rate is limited by the diffusion of polymer chains to the crystal growth front [169].

Figure removed due to the copyright issue

Fig. 2.27 Plot of $G(d)$ versus $1/d$ for iPS ultrathin films crystallized at 180 ℃. Fig . 5 in [168].

2.5 PHASE SEPARATION IN POLYMER THIN FILMS

Similar to crystallization, phase separation of polymers in thin films is also different from that in the bulk due to the differences in mobility of the polymer chains. With techniques such as AFM [190-193], SEM [194], TEM [195-197], OM [197], and mapping mode of secondary ion mass spectroscopy (SIMS) [198], the morphology of phase separation in thin films is able to be imaged. There are also some depth profiling techniques involved for the studies of vertical phase separation including: nuclear reaction analysis [199, 200], dynamic SIMS [201, 202], forward recoil spectrometry [203-205], and neutron scattering and reflectivity [206-208].

2.5.1 Phase Separation during Spin Coating

In contrast to the spin coating of a single polymer, which produces a smooth and uniform film, spin coating of a blend of immiscible polymers is able to introduce a non-equilibrium phase separation producing some special morphologies like islands, holes and bicontinuous morphology. These have been extensively investigated by many researchers [36, 208-218]. To study the morphology of phase separation in a thin film formed from an immiscible polymer blend, a polymer blend is quenched from the temperature where a stable one-phase region is formed, to the temperature where metastable or unstable regions are formed, leading to phase separation (Fig. 2.28a). However, when the T_g of the components in a two-component system are significantly different, the temperature quench method may not be suitable anymore as a temperature over the softening temperature of the polymer with higher T_g may cause the degradation of the polymer with lower T_g [209, 210].

2.5.1.1 Solvent quench

Dalnoki-Veress and co-workers [209, 210] first researched the morphology of phase separation in thin films of polymer blends through a solvent quench method, where the polymer blend was quenched by fast solvent evaporation during spin coating.

With polystyrene/polyisoprene (PS/PI) blends of different mass fraction dissolved in toluene, they produced films (~ 100 nm thick) with typical patterns by spin coating onto Si with an oxide layer (Si-SiO_x). It was found that small circular PS domains formed when the PS mass fraction (Φ_m) was low, e.g. 0.40. As Φ_m increased to a critical point, around 0.43, a bicontinuous morphology was observed. With even higher Φ_m, e.g. over 0.6, PI domains appeared. These morphology changes were explained by Dalnoki-Veress *et al*. using the phase diagram in Fig. 2.28b. They also reported that the quench time, which is controlled by spin speed, can affect the morphology of phase separation in thin blend films. By plotting domain area versus spin speed (Fig. 2.29), they found that domain size decreases as the spin speed increases and dramatic changes occur in the range of spin speeds from 1000 to 3000 rpm for a PS/PI (Φ_m = 0.63) blend [210]. This implies a less developed phase separation with increased spin speed, hence a higher rate of solvent quenching.

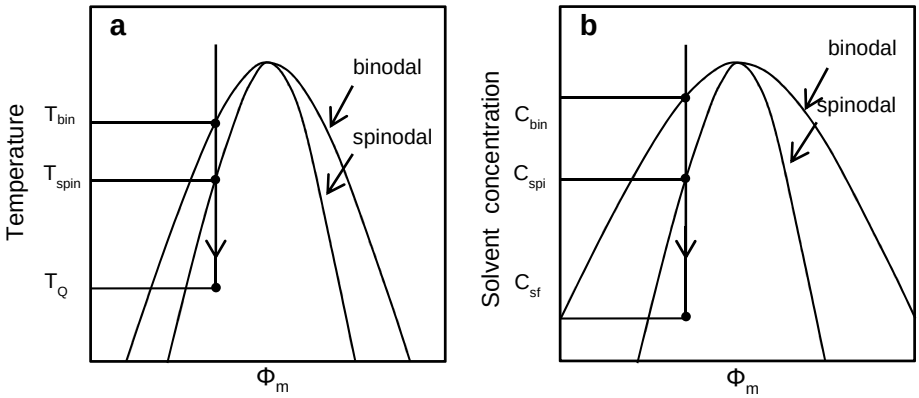


Fig. 2.28 Schematic phase diagram for (a) a temperature quench and (b) a solvent quench, where ϕ_m is mass fraction of one component, T_{bin}, T_{spin}, and T_Q are the binodal, spinodal, and quench temperature, respectively, C is the solvent concentration [209].

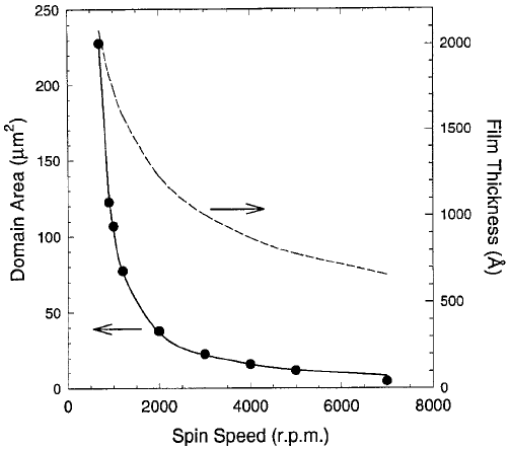


Fig. 2.29 Domain area (solid line) and film thickness (dashed line) as function of spin speed for PS/PI blends (PS mass fraction Φ_m is 0.63). Reproduced from [210] with permission of the copyright holder.

Although the results presented by Dalnoki-Veress *et al*. showed the importance of solvent evaporation rate, they did not carry out a direct investigation of the effect of solvent evaporation on phase separation. Soon after, Kumacheva *et al*. [212] studied the influence of solvent evaporation rate, which was controlled by solvent vapour pressure, on surface morphology using a PMMA/PS (weight ratio 1/9) film system. Using laser confocal fluorescent microscopy, they discovered that PMMA-rich domains were formed with random shapes and different scales at a high solvent evaporation rate (Fig. 2.30a). As the evaporation rate decreased, PMMA-rich domains tended to be circular (Fig. 2.30b). When the solvent evaporation rate was slowed down to a certain value (0.022 g/h in this work), an ordered pattern of PMMA-rich domains was obtained (Fig. 2.30c&d).

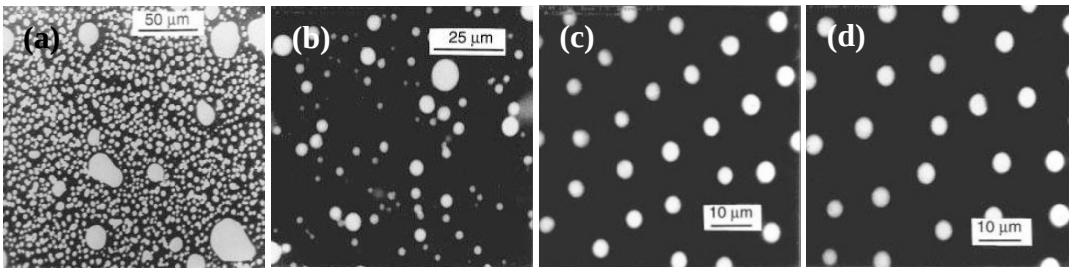


Fig. 2.30 LCFM images showing surface morphology of PMMA/PS films cast from toluene with different toluene evaporation rates, g/h: (a) 0.52; (b) 0.16; (c) 0.022; (d) 0.013. Bright domains are the dye-labelled PMMA-rich phase. Reproduced from [212] with permission of the copyright holder.

These results indicate that a slower solvent evaporation rate may result in a better ordered phase separation pattern. Considering the different evaporation rates of different solvents, the effect of the solvent needs to be taken into account when considering phase separation during spin coating. This was demonstrated by the later work of Walheim *et al*. [211].

2.5.1.2 Non-equilibrium phase separation

Since spin coating is a rapid film preparation technique, the fast solvent quench does not allow polymers to relax fully. Therefore, any phase separation that happens during spin coating is far from the equilibrium state. This can be confirmed by the further morphological changes that can occur during annealing. Investigating a blend system of deuterated polystyrene (dPS) and poly(p-methylstyrene) (PpMS), Muller-Buschbaum *et al*. [208] found that the surface pattern of phase separation of a spin coated film could change markedly after annealing, as shown in Fig. 2.31. AFM images show that phase separation scale increases with the increasing annealing time accompanied by an increasing variation in height.

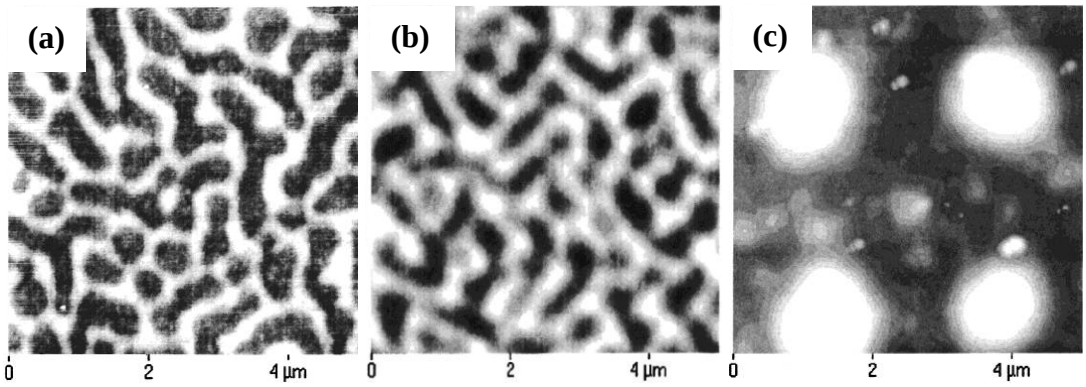


Fig. 2.31 AFM height images of dPS/PpMS (60/40 by weight) blend thin films (46 ± 2.5 nm thick): (a) as spin coated; (b) annealed at 161 ℃ for 8 hr; (c) annealed at 161 ℃ for 261 hr. The z-scale increases during annealing: (a) 3.6 nm; (b) 5.3 nm; (c) 94.6 nm. Reproduced from [208] with permission of the copyright holder.

To explain the phase separation in films of F8BT/TFB blend (poly(2,7-(9,9-di-n-

octylfluorene-alt-benzothiadia-zole)/poly(2,7-(9,9-di-n-octylfluorene)-alt-(1,4-phenylene-((4-sec-butylphenyl)imino)-1,4-phenylene)), Kim *et al*. [214] proposed a "morphology frozen-in" model, illustrated in Fig. 2.32. In this model, a layer of polymer solution (around 10 μm thick), with the same concentration as the bulk solution, is formed first. As the solvent evaporates, phase separation occurs through either nucleation and growth or spinodal decomposition, while the T_g of the mixture increases until entrapped domains are formed. This model gives a good explanation of the phase-separated patterns in as-spin-cast blend films and illustrates the freezing of the spin-cast system well in term of T_g elevation through the evaporation of solvent, the plasticizer in the system.

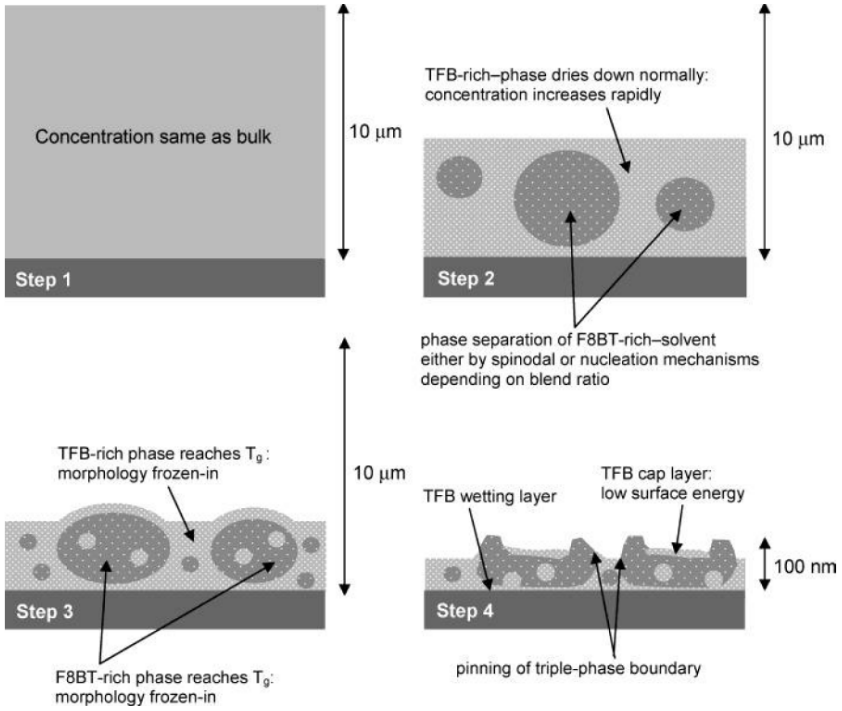


Fig. 2.32 Phase separation development of F8BT/TFB blends in thin films: step (i) spin-off; (ii) solvent evaporation; (iii) freezing of morphology; (iv) final thin film formed. Reproduced from [214] with permission of the copyright holder.

However, the model suggested by Kim *et al*. does not fit well to the situation where there is a large difference in the wetting abilities of components. Through the investigation of a PS/PMMA (50/50) system, Heriot and Jones [36] concluded that, for the spin coating of a blend of two polymers, vertical phase separation occurs forming two layers soon after the

spin-off of spare solution (Fig. 2.33 (i-iii)) due to the different wetting abilities of different components, either wetting substrate or wetting air. As solvent evaporation continues, the interface between the two polymer layers becomes unstable, which is attributed to the different interfacial tensions caused by the lower solvent concentration in the upper layer since solvent in the near-surface regions evaporates quicker. This instability of the polymer-polymer interface increases with solvent evaporation and results in the final phase separation in thin films, displayed in Fig. 2.33 (iv-vi).

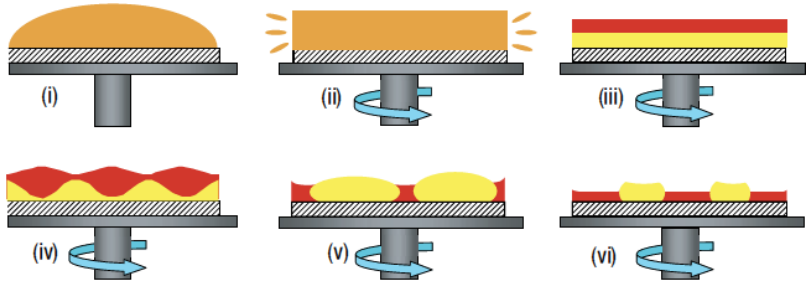


Fig. 2.33 schematic of phase separation of a polymer blend during spin coating: vertical stratification (i-iii), phase separation due to the unstable polymer-polymer interface (iv-vi). Reproduced from [36] with permission of the copyright holder.

2.5.2 Phase Separation Induced by Annealing

Another common method used to induce phase separation in thin films of polymer blends or copolymers is annealing. During this process, an equilibrium phase separation can be achieved for a blend or copolymer showing lower critical solution behaviour or in a thermodynamic non-equilibrium state [202-204, 219-222].

With research on phase separation on a blend thin film of deuterated poly(methyl methacrylate) (dPMMA) and poly(styrene-*ran*-acrylonitrile) (SAN), Wang and Composto [203, 204] proposed a three-stage model for phase separation evolution in thin films during annealing, displayed in Fig. 2.34. They suggested that, for the early stage of annealing, layers wetting the surface and substrate are formed with a bicontinuous

structure between them and, subsequently, grow according to a hydrodynamic flow mechanism. During the intermediate stage, domains (dPMMA in the experiment) which span surface and substrate wetting layers develop. At the final stage, the component forming wetting layers encapsulates the other component to form droplets. Although, the as-spin-cast morphology may vary in different blend systems and the development of film morphology could be influenced by different parameters (section 2.5.3), this model implies the general evolution trend of immiscible polymer blends on annealing and shows the influence of the wetting at the surface and the substrate on phase separation.

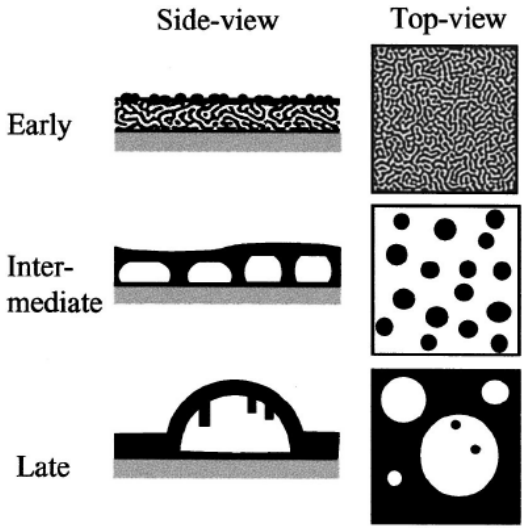


Fig. 2.34 Schematic of three-stage model for phase evolution in a blend thin film of dPMMA (dark regions) and SAN (bright regions). Reproduced from [204] with permission of the copyright holder.

2.5.3 Parameters Affecting Phase Separation in Thin Films

All the parameters determining the polymer chain mobility in a thin film or the miscibility of polymers are able to influence the phase separation in thin films of polymer blends or copolymers. In addition to these factors, including component composition, solvent evaporation rate, spin speed, annealing temperature and time, phase separation in thin films is also significantly affected by film thickness [34, 201, 223-226], molecular structure [227-230] and molecular weight [231-233], the substrates [211, 234, 235], and impurities

or fillers [236-238]. The main factors predominating phase separation in polymer thin films are summarized below:

2.5.3.1 Film thickness

As early as the beginning of 1980s, Reich *et al*. [223] pointed out the thickness dependence of phase separation. By studying PS and poly(vinyl methyl ether) (PVME) blend films, they found that phase separation happened through spinodal decomposition and the phase separation temperature exhibited a thickness dependence when film thickness was decreased below 1 μm. They also revealed that this effect varied with the nature of the substrate. Their experimental results showed that, for films on glass, phase separation temperature decreases with film thickness, while, the opposite situation occurs in films on a gold substrate.

Later work showed [201, 224] that, with film thicknesses below 100 nm, phase separation is actually suppressed, which may be caused by the increasing substrate effects. Liao *et al*. [224] reported that the apparent compatibility of PMMA and SAN increases as film thickness decreases for film thickness $d > 5R_g$ (radius of gyration). In this thickness range only phase separation takes place. When $d < 5R_g$, both phase separation and dewetting occur. Similar work on phase separation and dewetting in PS/PVME blend films has also been carried out by Ogawa *et al*. [225, 226]. However, the results of their research showed that dewetting induced by phase separation can be observed in thin films of several hundred nanometres and they suggested that the annealing time for the appearance of dewetting is thickness dependent. Thus, the thickness dependence of phase separation in polymer thin films is clear despite the fact that it is not fully understood yet.

2.5.3.2 Molecular structure and molecular weight

As polymer chains with different molecular structure and molecular weight (M_w) have different mobilities, it is possible to use molecular structure and M_w to control phase

separation in polymer thin films. A typical example of phase separation control of polymer blend by M_w is given in Fig. 2.35 [232], showing that, for PS/PMMA blend (50/50) films, surface morphology displays nano-phase separation, hole formation, and island forming as the M_w of PS increases from 2.9k to 129k.

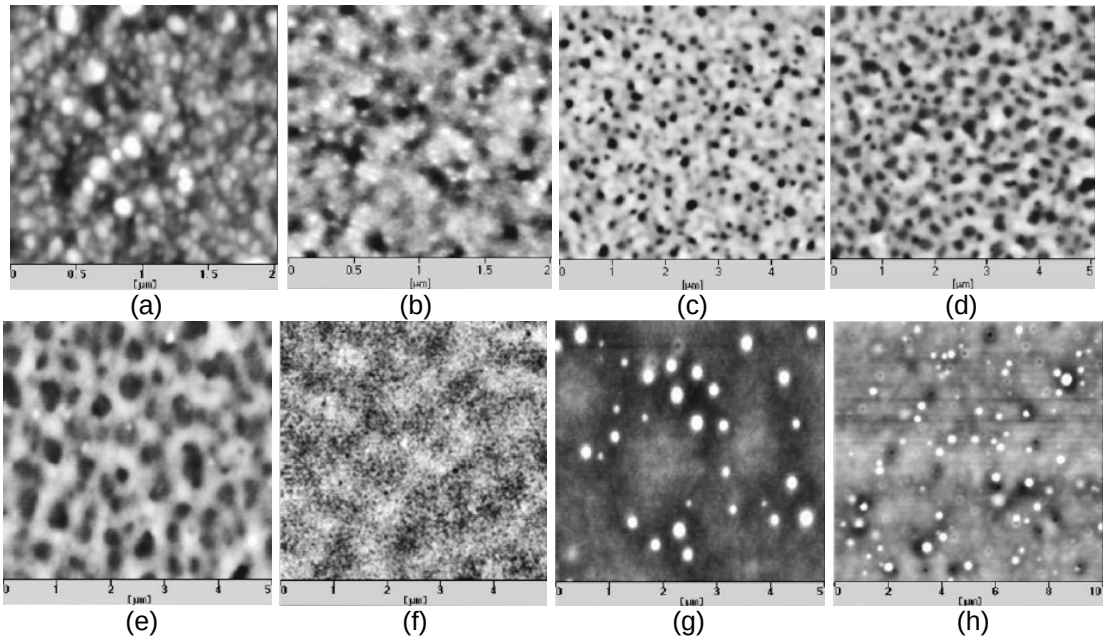


Fig. 2.35 AFM height images of PS/PMMA (weight ratio 50/50) blend films (70-90 nm) with different PS M_w: (a) 2.9k; (b) 4.0k; (c) 5.6k; (d) 7.1k; (e) 10k; (f) 31.6k; (g) 65k; (h) 129k. Reproduced from [232] with permission of the copyright holder.

2.5.3.3 Substrate effect

Research on phase separation in polymer thin films has also demonstrated the important role of substrates [211, 217, 233, 234]. As reviewed in section 2.3, substrates with different surface energy lead to different chain mobilities in polymer thin films, which, subsequently, affect phase separation. Boltau *et al*. [234] suggested that it is possible to control the phase separated structure by controlling surface patterns of a substrate. Work on PS/PMMA systems [211, 239] showed that a substrate plays a crucial role in the forming of the phase-separated structure due to the different substrate preferences of the polymers in a blend, which is intrinsically determined by the surface energy of the substrate and the polymers.

2.5.4 Crystallization in Copolymers or Polymer Blends

For binary systems with one or two semicrystalline polymers, crystallization usually cooperates with phase separation, and much research [240-245] has been carried out to identify how crystallization and phase separation interact with each other in confined systems.

Normally, crystallization in binary systems can lead to phase separation. For instance, annealing of poly(L-lactide)-block-poly(oxyethylene) (PLLA-PEG) is able to allow PLLA to form fibril crystals and produce phase separated morphology, shown in Fig. 2.36 [240].

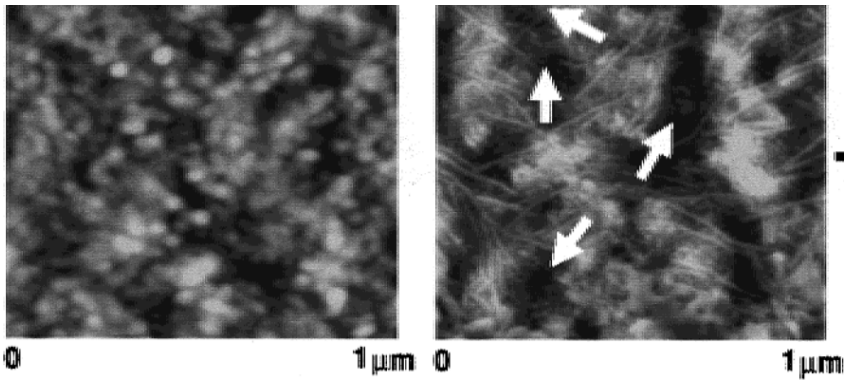


Fig. 2.36 AFM height images of PLLA-PEG nanoparticles on a mica substrate: (a) as spin cast; (b) annealed at 60 ℃ for 2 hr. Reproduced from [240] with permission of the copyright holder.

However, there are also some situations in which crystallization is affected by phase separation. Work done by Zhang *et al*. [241, 242] showed that crystallization tends to start from the interfaces of a phase-separated structure (islands or holes) and develops into the interior areas. In their work, a poly(styrene-b-ε-caprolactone) system, where PS is amorphous and PCL crystallizes at room temperature, was chosen and crystallization was investigated after phase separation induced by annealing. A typical boundary effect on crystal growth is illustrated in Fig. 2.37. To interpret this boundary effect, Zhang *et al*. suggested that PCL blocks are stretched at the edges produced by phase separation and so the interface can be recognized as a nucleation agent.

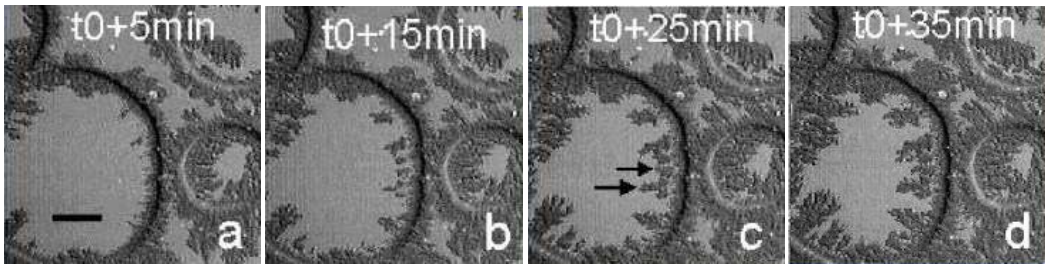


Fig. 2.37 AFM phase images of crystal growth in PS-b-PCL films (15-20 nm). All samples were annealed at 120 ℃ for 3 min and then crystallized at room temperature (22 ℃). t0 is 20 min and the scale bar is 2 μm. Reproduced from [242] with permission of the copyright holder.

Parameters affecting crystallization in copolymer or polymer blend thin films are almost the same as the ones which affect thin film crystallization of homopolymers and phase separation in thin films, reviewed in section 2.4.1.3 and 2.5.3, and so are not repeated here.

2.6 CONCLUSIONS

From the literature reviewed above, it can be shown that a great amount of research has been carried out to investigate polymer behaviour, both crystallization and phase separation, in thin film systems already. However, crystallization and phase separation in thin films are still far from being fully understood. For surface-specific crystallization in polymer thin films, there is yet no conclusion as to whether surface crystallization due to enhanced chain mobility at the surface is a universal phenomenon or whether there are any specific molecular-characteristics that contribute to it. In addition, currently, the 2D crystallization found for many polymers is obtained through a melt-crystallization process, rather than an investigation of crystal growth rising from the solid amorphous phase, meaning the lowest crystallization temperatures at which these 2D crystals occur are unknown, and any crystallization specific to the free surface cannot be confirmed. Hence, more work is required for an advanced understanding of crystallization in thin films, particularly the surface-specific crystallization. For phase separation in polymer thin films, even though much work has been done to explore different binary systems, the understanding of how phase separation in thin film systems is different from bulk systems is not very clear yet, especially when this problem is combined with surface-specific crystallization. Whether phase separation is able to occur in the near-surface region at a lower temperature than the bulk phase separation temperature remains a question to answer. All these unsolved questions are addressed in this thesis: to investigate surface-specific crystallization in various polymers and examine phase separation in some typical blend or copolymer systems to see how phase separation in thin films varies from bulk systems.

3 CRYSTALLIZATION OF POLYAMIDES IN THIN FILMS

Despite the fact that much research has been carried out to investigate crystallization in polymer thin films, surface-specific crystallization has still not been observed for many polymers. A typical example is polyamide. So far this surface-specific crystallization phenomenon occurring at temperatures well below bulk crystallization temperature has only been observed in PET and PEN [28] derived from rather stiff monomers, and PVOH [29], a flexible chain with a high density of hydrogen bonding. In contrast to PET, polyamides represent a group of flexible-chained polymers with some degree of hydrogen bonding that crystallize readily. A large amount of research has been done on crystallization of polyamides, but surface crystallization phenomena have not yet been studied.

3.1 BACKGROUND

Polyamides are recognized by the amide group (NH−CO) and can be generally divided into (a) homopolymers of an amino acid or lactam, and (b) copolymers of a diamine and a diacid:

(a) PA n: $-(-(NH-CO)-(-CH_2)_{n-1}-)-$

(b) PA m,n: $-(-(NH-CO)-(CH_2)_{n-2}-(CO-NH)-(CH_2)_m-)-$

Crystalline structures of polyamides are generally recognized as ether α form, where molecular chains are arranged anti-parallel and exhibit a fully extended configuration, or γ form, where molecular chains are parallel and twist to maximize the number of hydrogen bonds. It was reported that, for even polyamides (PA2n), the α crystalline structure is more stable when 2n ≤ 6, while γ structure is preferred when 2n > 6 [246]. The transition between different crystals in polyamides has been extensively studied using, small- and wide-angle X-Ray scattering [247-250] and FTIR [251, 252], demonstrating that both heat treatment and mechanical deformation may contribute to the crystalline transition, normally from the crystalline phase with higher stability to a lower one with energy absorbed. Fig. 3.1 shows such a crystalline transition in PA12 during a stepwise heating process: from γ form at 60 ℃ (one scattering peak) to α' form, a stable monoclinic structure at high temperature, at temperatures over 140 ℃ (two peaks) [249].

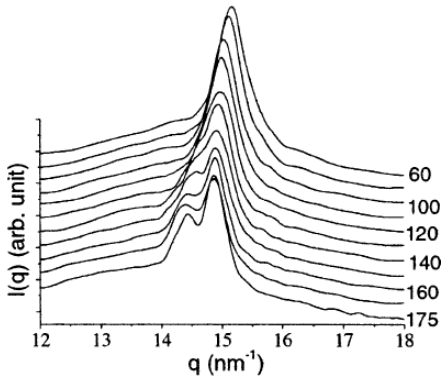


Fig. 3.1 WAXS profiles of a PA12 sample (with initial crystals in γ form) during stepwise heating. Reproduced from [249] with permission of the copyright holder.

AFM has proved to be a good technique to reveal the crystal morphology of polyamides at

the microscopic scale [253]. Using AFM, spherulitic structures on the surfaces of both as-cast and melt-crystallized cast PA 6 films have been found [124, 253-255], displayed in Fig. 3.2. However, the thicknesses of the films involved were greater than 50 μm, and so it is not known whether these crystals arise from confined crystallization at the surface or whether they are bulk crystals. No work has yet been carried out to perform a good investigation of surface-specific crystallization in polyamide films with sub-micron thickness, and the effect of the crystalline transition, which is found in even or even-even PA [256-258], on surface morphology is still not clear for PA thin films.

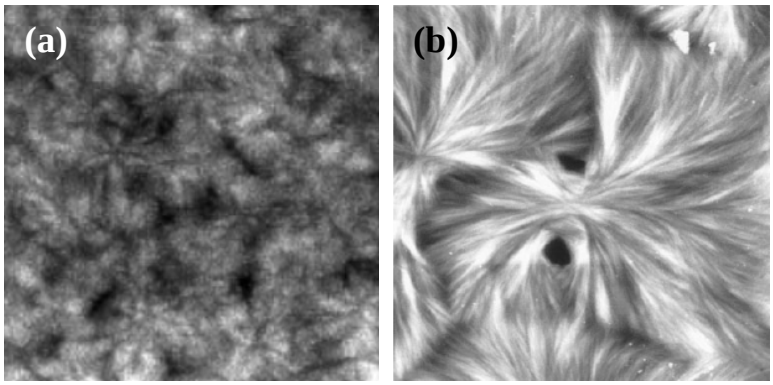


Fig. 3.2 AFM height images of cast PA 6 films: (a) 15 μm × 15 μm, as cast film 50 μm thick; (b) 30 μm × 30 μm, 80 μm thick film melt at 250 ℃ for 5 min, then isother mally crystallized at 188 ℃ for 1 hr. (a) and (b) are reproduced from [124] and [254] respectively with permission of the copyright holders.

In general, most of the polyamide work has been on the surface morphology of bulk spherulites in as-cast or melt-crystallized polyamide films with a thickness of several microns, i.e. greater than the diameter of the spherulites. Crystallization of polyamides in thin films or specific to the near-surface region is still uncharacterized. In this chapter, the thin-film crystallization behaviour of PA12 in spin-cast films is presented, together with some investigation of crystallization of PA6, indicating the characteristics of crystallization behaviour in polymers with differing hydrogen bonding densities. Various 2D crystals, which have distinct morphologies from bulk crystals, are reported in both as-spin-cast and

in annealed polyamide films. The effects of annealing and film thickness on polyamide crystals are discussed.

3.2 EXPERIMENTAL

PA6 and PA12 were used as-purchased from Sigma-Aldrich. The T_g, the crystallization temperature, T_c, and the T_m, as provided by the manufacturer and obtained from differential scanning calorimetry (DSC) are listed in Table 3.1.

Table 3.1 Transition temperatures of polyamides. The DSC scan rate was 5 ℃/min and measurements were taken from the first heating (T_g and T_m) and cooling cycle (T_c). An error of ± 1 ℃ is expected for the results by DSC.

	PA	T_g ℃	T_c ℃	T_m ℃
Manufacturer	6	62	-	228
	12	37	-	178
DSC	6	-	188	223
	12	47	146	179

Thermal analysis was performed by a Diamond DSC (Perkin Elmer). A scan rate of 5 ℃/min was used. With this low scan rate, a very high crystallinity was obtained during cooling, thus, the T_g signal from the amorphous part was too weak to be detected during the second heating trace and the data were collected from the first heating. The failure of collecting the T_g of PA6 is also attributed to the high crystallinity of the material. (T_g of PA6 was detected to be 61 ℃ when the scan rate was increased to 80 ℃/min). For the T_g of PA12, the difference between the data from the manufacturer and from our measurement is possibly due to different testing rates. Discussion in this chapter is based on the data from DSC.

Spin coating is a favoured method to produce a uniform polymer thin film due to its reasonably good thickness control and easy operation [259]. All the polyamide films were obtained by spin coating solutions of the polyamides in 2-chlorophenol (2CP) (Aldrich) that had been stirred for a long period, usually overnight, to ensure good dissolution. For a comparison of the effect of solvents on the spin-casting process, solutions were also

made using hexafluoroisopropanol (HFIP) (Fluka) and a mixture of formic acid (FA) (Fluka) and dichloromethane (DMC) (Romil Ltd.). The solutions were cast onto glass substrates using a spin coater (Laurell Technologies Corporation) operated at 3000 rpm (acceleration rate 200 rpm/s) for 1 min, with film thickness controlled by varying the solution concentration (where a different spin speed or acceleration rate is used for a particular experiment, this will be recorded in the appropriate section). Fig. 3.3 shows the relationship of PA concentration in 2-chlorophenol to the resulting thickness of PA12 films. Prior to deposition, the glass substrates were sonicated in detergent, i.e. several drops of Decon in 600 ml deionized water, and then deionized water for 10 min each, and then cleaned in each of acetone and isopropanol on a hotplate reading 125 ℃ for 3 min in turn. The as-spin-coated samples were dried in a fume cupboard at room temperature (T_{room}) for 60 hr.

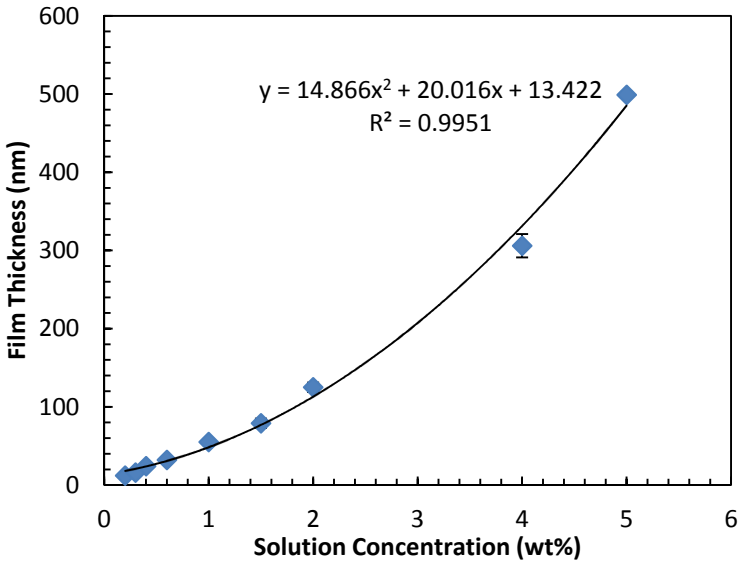


Fig. 3.3 Film thickness as a function of solution concentration (PA12 in 2-chlorophenol) measured by Dektak.

The thicknesses of the polyamide films were measured by a Dektak profilometer (Veeco). Depth profiles were performed with 1 milligram stylus force and scan direction from polymer covered side to naked substrate side. Normally, a scan rate around 150 μm/s was used, e.g. a length of 2000 μm and duration of 13 s. For films below 50 nm thick, the scan

length was decreased for better accuracy.

The surface morphology of polyamide films was investigated using tapping mode AFM (Park Scientific Instruments) recording both topography and phase images under ambient conditions (For AFM, imaging, standard SPM probes with tips (height 20-25 μm, cone angle < 40°, tip radius < 10 nm) mounted on a recta ngular silicon chip were used. The resonant frequency of the tip is roughly in the range 150-210 kHz and the force constant 4.5-7.5 N/m. A constant scan rate of 1 Hz was used in all AFM experiments. AFM images were obtained by the Nanotec Electronica WSxM software [260]). As-spin-coated polyamide films were annealed at different temperatures roughly ranging from below T_g to T_m, normally for 2 hr, and then the samples were cooled rapidly on an aluminium block cooled with acetone before characterization. The as-spin-cast morphology of each of the samples was characterized before annealing. The tip size was normally calibrated using as-spin-cast samples where the morphology is fine.

TEM analysis was carried out using a JEOL-JEM 4000EX LaB_6 microscope operated at 80 kV. To prepare the samples for TEM, a poly(acrylic acid) (PAA) detachment method was used [261]. A small drop of PAA solution (35 wt% PAA in water) was placed on a polyamide film sample and dried at room temperature for 2 days. The solidified PAA can then be detached from the substrate, taking with it the polyamide film (note that this method catches only the upper layers of a PA film with a thickness around a few tens of nanometres and is not available for very thin films, e.g. with thickness below 24 nm). When the PAA is dissolved in deionized water, a floating polyamide film can be obtained. After being picked up onto a TEM grid and dried, the sample is ready for TEM analysis.

3.3 RESULTS AND DISCUSSION

3.3.1 As-Spin-Cast Morphologies

Polyamides show high crystallization rates, comparable with the associated solvent evaporation rate, thus, crystallization was found inevitably to occur during the spin coating and sample drying stages. The solvent choice can affect the as-spin-cast morphology. Fig. 3.4, illustrates that with the same PA12 concentration and spin coating conditions, a solvent with a high evaporation rate, e.g. FA/DCM, can lead to a PA12 film with root mean square (RMS) roughness as high as 162.6 nm (Fig. 3.4a), while a solvent that evaporates more slowly, such as HFIP (Fig. 3.4b) or HFIP/2CP (Fig. 3.4c) brings this value down to several nanometres. This indicates that, with a high crystallization rate, rapid evaporation of the solvent may prevent a PA12 solution layer from shrinking to a compacted film, which leaves a foamy structure with a very rough surface. Also the pits shown in the AFM topography images show that, with low evaporation rate solvents, the crystallization of PA12 enables some shrinkage and creates paths for solvent evaporation. In spite of the fact that PA12 is able to crystallize during the solvent evaporation, the degree of crystallization is limited as the diffusion of molecular chains slows down as the solvent evaporates.

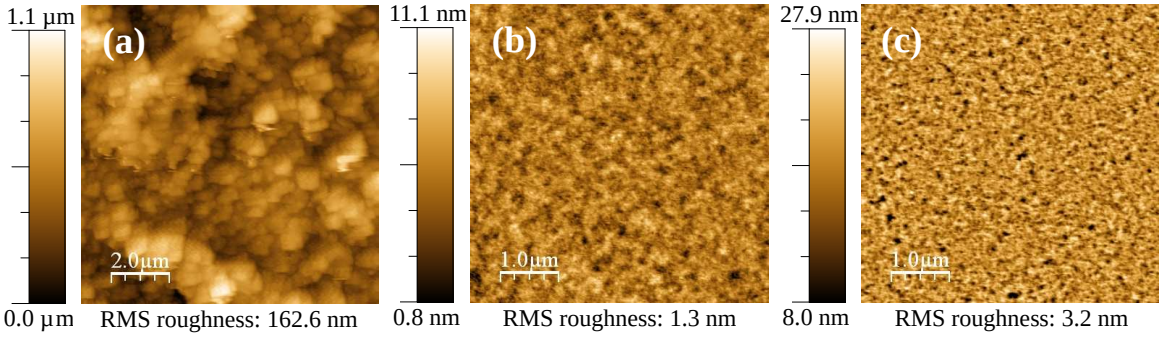


Fig. 3.4 PA12 on glass slides from solutions of 1wt% PA12 in (a) FA/DCM with 1/1 volume ratio; (b) HFIP; (c) 30wt%HFIP/70wt%2CP. Here, the acceleration rate for spin coating is 3000 rpm/s.

3.3.1.1 2D crystals in as-spin-cast films

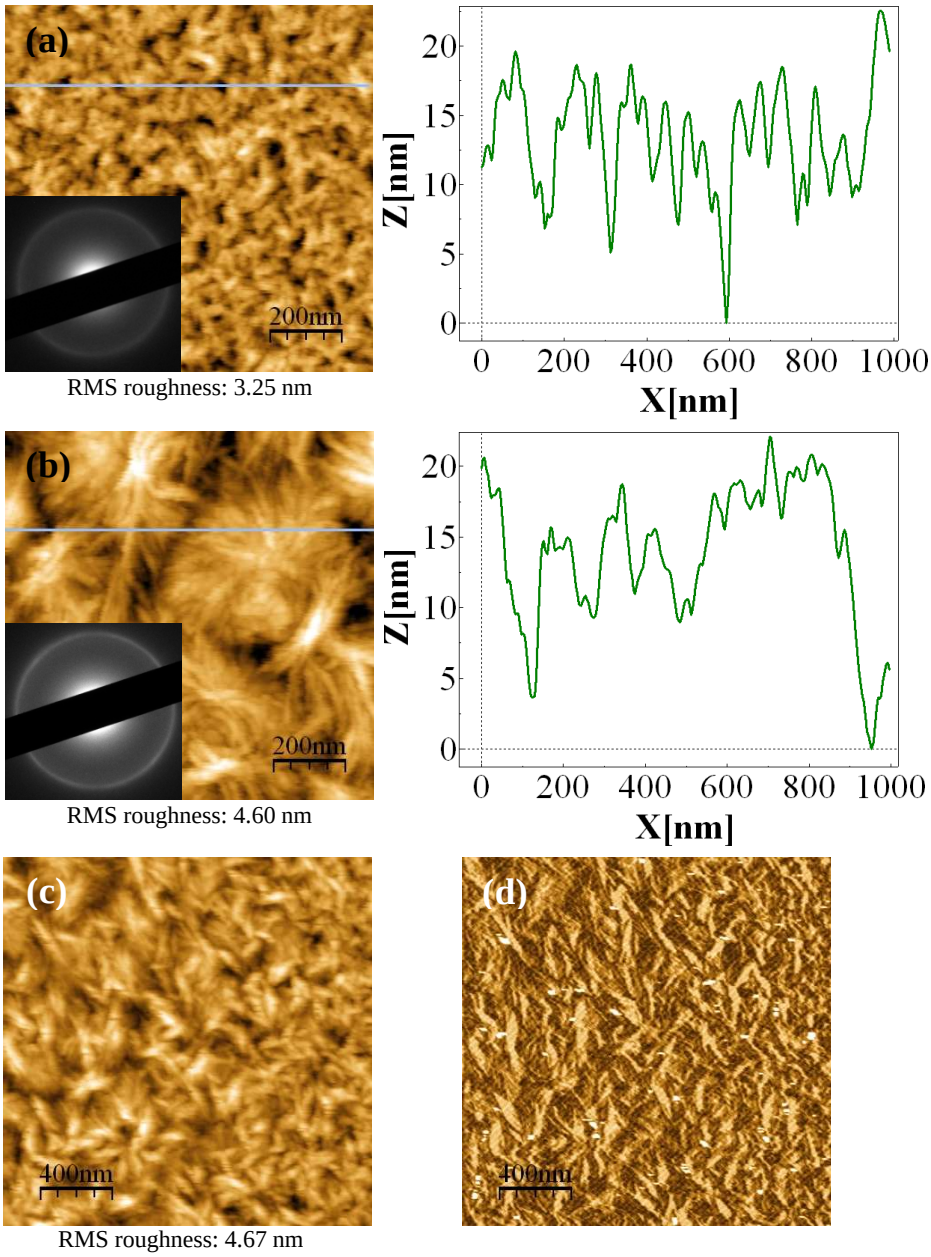


Fig. 3.5 AFM topography images of as-spin-coated PA12 films from 2CP solution with corresponding ED patterns and line profiles of surface height: (a) shuttle-like crystals in a network structure; (b) 2D spherulites of crystal lamellae. (c) Topography and (d) phase images of the inter-penetrating morphology. Both topographic and phase images display the crystalline morphology transition from 2D spherulites on the left of the image, to shuttle-like on the right of the image. The films are around 55 ± 4 nm thick.

AFM results of as-spin-cast PA12 films from 2CP solutions show that there are generally

two kinds of morphologies of crystals in these as-spin-cast PA12 films: one in the form of shuttle-like crystals building a network structure (Fig. 3.5a) and the other lamellar crystals in the form of 2D spherulites together with some sheaf-like crystals, which are the precursors of the spherulites (Fig. 3.5b). These two morphologies can, in some cases, be observed in one sample, showing some interpenetration of the two types (Fig. 3.5c&d). This morphology difference can probably be attributed to subtly different rates of solvent evaporation during spin coating and the following sample drying. There may be a morphology transition, from shuttle-like to lamellar, in the solvent-rich environment. Yang and Han [262] reported a crystal growth transition in polymer thin films treated in saturated solvent vapour demonstrating that a high solvent concentration could lead to such a transition. Within the confinement of the thin film, instead of forming spherulites with diameters reaching tens of microns, as observed in the bulk [263], polyamide lamellae arrange into 2D spherulites (Fig. 3.5b) with diameters around 400 nm, but only a few lamellae in thickness. Being composed of small shuttle-like crystals along different directions, the network crystal structure (Fig. 3.5a) exhibits isotropy at the surface layer and most likely developed through a diffusion-limited crystallization. The generation of the spherulitic morphologies (Fig. 3.5b), however, is a nucleation-controlled process confirmed by the coexistence of lamellar sheaves and 2D spherulites.

Both of these morphologies are found to be of γ crystalline form since both their electron diffraction (ED) patterns (Fig. 3.5) show a single strong diffraction ring. However, the ED pattern of the lamellar crystals shows a greater sharpness than that of the shuttle-like crystals, which could indicate that molecular ordering in the lamellar crystals is greater than that in the shuttle-like crystalline network, or that the crystallite size is greater. Furthermore, the results in Fig. 3.5 show that films with spherulites at the surface have a higher surface roughness than those with the network structure of shuttle-like crystals observed at the surface. With its higher stability, the γ crystalline structure is normally predominant in PA12 [246], however Ishikawa *et al*. [264] in the early work on solution

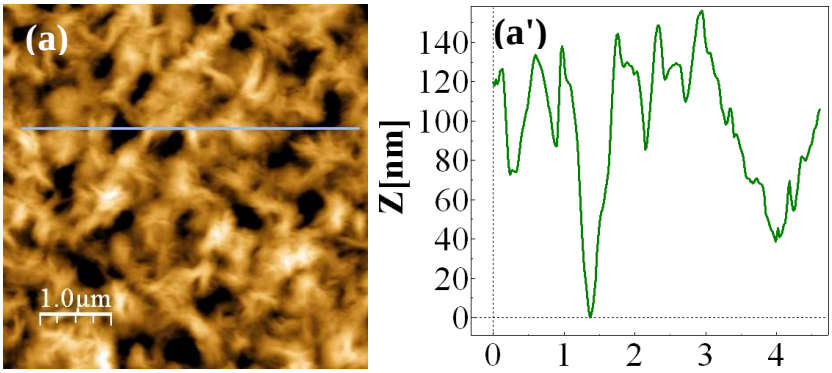
(PA12 in phenol/ethanol) cast PA12, found that it tended to form α crystals at temperatures below 30 ℃ or with a slow solvent evaporation rate, while a temperature above 90 ℃ or a rapid solvent evaporation, a typical example of which is casting from formic acid solution [265], may lead to the γ form. However, the PA12 films prepared by this casting method only represent the bulk situation. (Although the thickness of the cast samples was not reported, their thickness should be over 1 μm as they were available for IR analysis.) In near-surface regions of polyamide solution layers, molecular chains exhibit a much higher mobility which might be expected to significantly lower the temperature required for the formation of γ crystals. This explains why the as-spin-cast crystals at the surface formed during solvent evaporation tend to be γ form.

Line profiles of the topography images (Fig. 3.5a&b) suggest that these as-spin-cast crystals in films around 55 nm thick are present over a depth of at least 15 nm. This crystal thickness value is higher than that for PET surface crystals obtained by annealing, which is around 10 nm or even less. However, some defects in PA12 samples (presented in section 3.3.3) indicate that these crystals exist in the upper layers rather than penetrating through the bulk of the film.

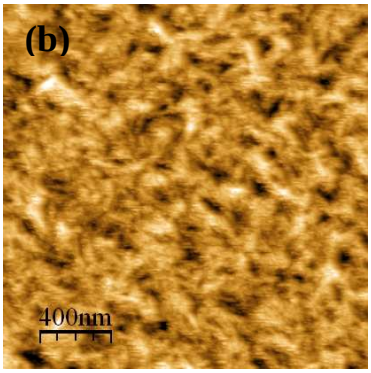
3.3.1.2 Confinement induced crystalline polymorphism

For very thin films, the morphology of 2D crystals can be influenced by film thickness [27, 168, 169]. Taguchi *et al*. [168] suggested that when film thickness is decreased to become comparable to the lamellar thickness, crystallization would become a diffusion-limited process, hence, a change in crystalline morphology would occur. Previous work [27] also showed that the width of branches of surface crystals demonstrate a roughly linear relation with film thickness over thin films. AFM topography images of PA12 films of different thicknesses with shuttle-like or lamellae structured crystals are presented in Fig. 3.6. With decreasing film thickness, the morphologies of both surface crystals in the as-spin-coated PA12 films changes significantly. However, since there is still a large

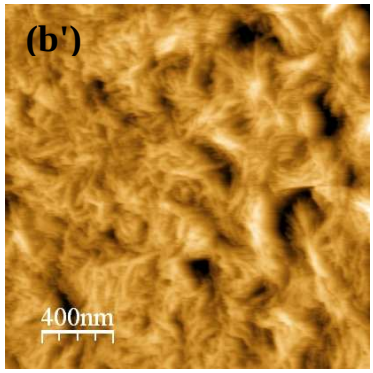
amount of residual solvent in a polyamide film during the period of crystallization, solvent evaporation channels are still observed to form.



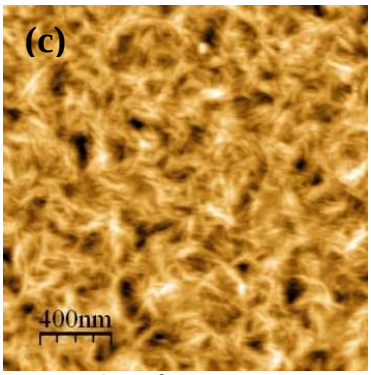
RMS roughness: 24.84 nm



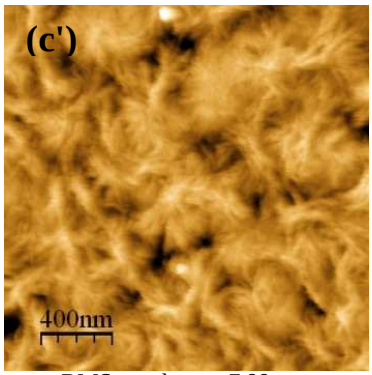
RMS roughness: 4.67 nm



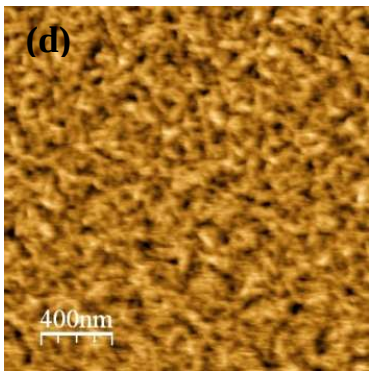
RMS roughness: 9.94 nm



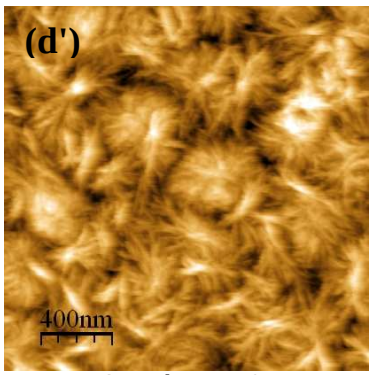
RMS roughness: 7.22 nm



RMS roughness: 7.99 nm



RMS roughness: 3.06 nm



RMS roughness: 4.92 nm

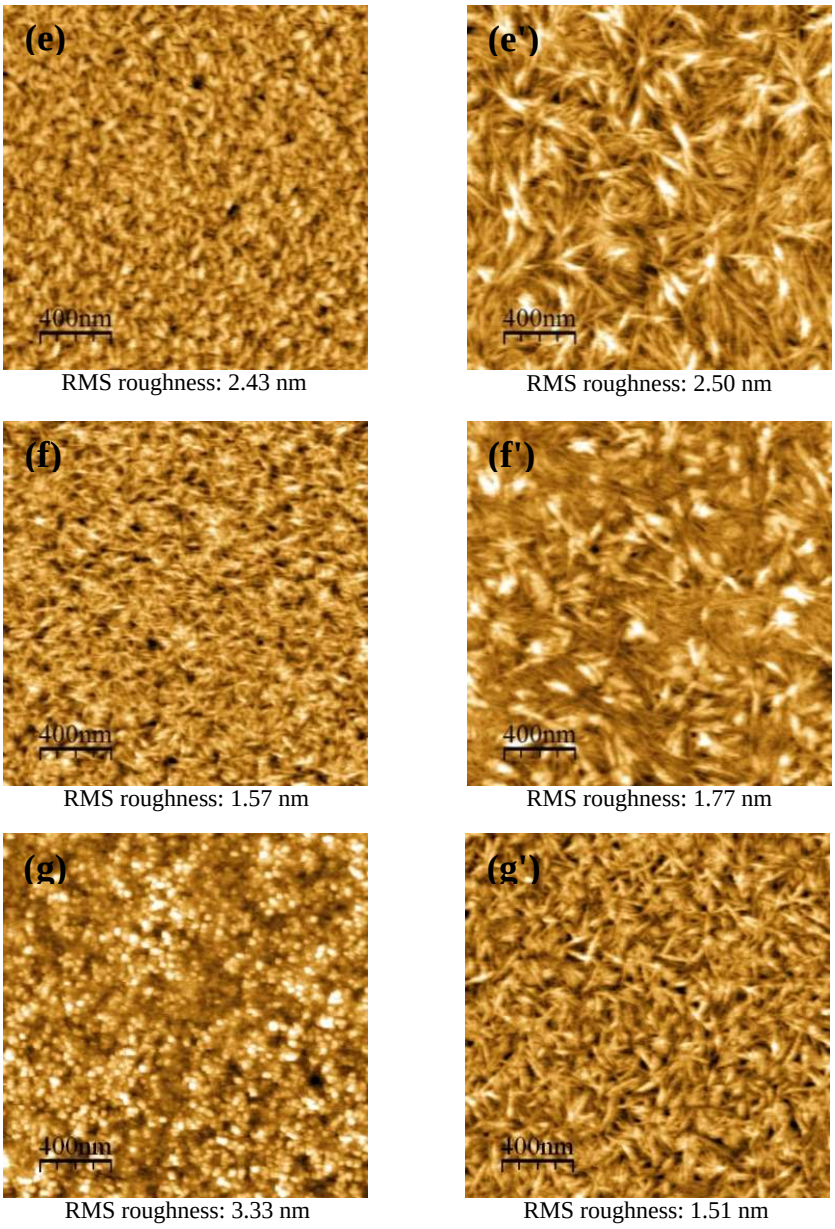


Fig. 3.6 AFM topography of as-spin-coated PA12 films with different thicknesses: (a) 499 ± 4 nm; (b)(b') 125 ± 6 nm; (c)(c') 79 ± 6 nm; (d)(d') 55 ± 4 nm; (e)(e') 32 ± 2 nm; (f)(f') 24 ± 3 nm; (g)(g') 12 ± 2 nm. (a') is a line depth profile of rough surface crystals in films with thickness around 500 nm. (b)(c)(d)(e)(f)(g) display the morphology change of shuttle-like crystals with film thickness, while (b')(c')(d')(e')(f')(g') shows the situation for lamellar crystals.

The measured surface roughness is in part due to the solvent evaporation channels, therefore, for as-spin-coated PA12 films the thicker the film thickness, the rougher the film surface. A typical example is displayed in Fig. 3.6a, where a PA12 film around 500 nm thick has a surface RMS roughness as high as 24.8 nm. The line profile (Fig. 3.6a') shows

the existence of peaks and holes with dimensions over 50 nm. With this extremely rough surface, the two different structures of surface crystals become indistinguishable. In general, for both cases, surface roughness has a decreasing trend as the film thickness is reduced. As film thickness decreases, the scale of the shuttle-like crystals decreases, demonstrated in Fig. 3.6 (left column), which could contribute to the decreasing roughness. Considering the surface morphologies of the crystals in Fig. 3.6, it is most likely that, for films thicker than 100 nm, the changes in surface roughness are mainly due to the formation of solvent evaporation channels (in the form of holes), while for PA12 films below 100 nm, the surface roughness enhancement with film thickness is predominately due to the size of the polymer crystals. Shuttle-like crystals with a very fine scale could be obtained when the film thickness is below 50 nm (Fig. 3.6e&f). The slight roughness enhancement of non-lamellar crystals in films around 10 nm thick is possibly due to the fact that the amount of material in this case is so small that molecular aggregations, either crystalline or non-crystalline, cannot even cover the whole substrate layer leaving fossae in the surface layer, illustrated in Fig. 3.6g.

Similar scale changes with film thickness have also been found in lamellar as-spin-cast crystals (Fig. 3.6 right column). However, the morphology transformations in lamellar crystals are more obvious. With decreasing film thickness, the development of 2D spherulites is hindered, thus, what becomes a mixed morphology (Fig. 3.6d') of 2D spherulites and lamellar sheaves transforms into a morphology of lamellar sheaves alone (Fig. 3.6e') with decreasing thickness. For even thinner films, rather than forming lamellar sheaves, a lamellar network structure (Fig. 3.6f') with ridges is preferred. These ridges are probably short-range lamellar crystals with some molecular aggregations attached, which are shown clearly in Fig. 3.7a. When the film thickness is below 20 nm, the crystals now exist largely in the form of lamellar ridges (Fig. 3.6g'), details of which are presented in Fig. 3.7b. In this situation, the growth of lamellae is restricted and molecular chains are only able to form lamellar fibres together with some crystalline aggregations before further

growth is prevented by solvent evaporation.

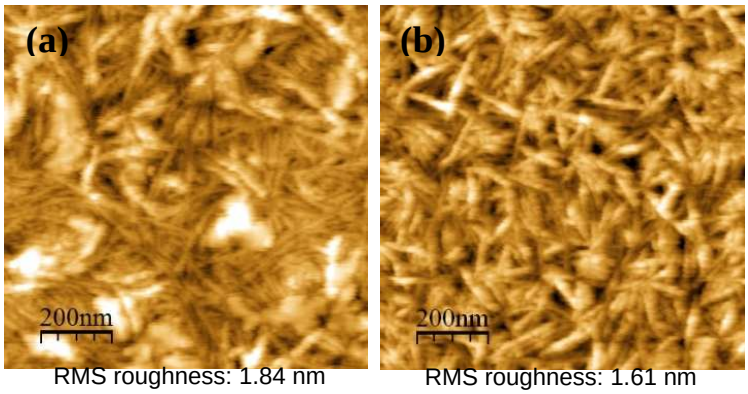


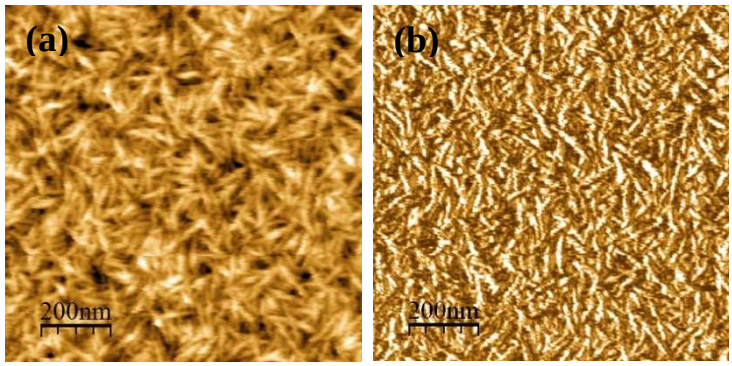
Fig. 3.7 AFM images of as-spin-coated PA12 films with thickness around (a) 24 nm and (b) 12 nm.

The morphology difference with thickness, especially in the case of lamellar crystals, can mainly be attributed to the diffusion rate of molecular chains and the time for solvent evaporation during which crystallization can occur. With a low film thickness, confinement of molecular chains along the thickness direction is increased, and there could be an additional hindrance to molecular motion due to interactions with the substrate [23], therefore, molecular chains have a lower diffusion rate. Meanwhile, with less residual solvent, the duration of solvent evaporation in a thinner film decreases, which means less diffusion time for polyamide chains. The confinement-induced crystalline morphology for PA12 lamellar surface crystals reveals a typical hierarchy of crystalline morphology in polymers showing that lamellae form lamellar fibrils which make up lamellar sheaves and then 2D spherulites. With diffusion time and mobility limited, the development from nuclei to full crystalline morphologies is restricted, leaving distinct structures at different growing stages as the results of different film thicknesses.

3.3.1.3 Solvent-crystallization in ultrathin PA12 films

The growth of lamellar spherulites in bulk polymers was successfully explained by Hoffman and Lauritzen [266] with a secondary nucleation and growth theory, which has been utilized as the usual method to analyse polymer crystallization. Similarly, early work on the growth of surface lamellae and spherulites [158] also suggested a secondary

nucleation and growth process from primary lamella to form 2D spherulites. The linear growth rate of surface spherulites also agrees with Hoffman-Lauritzen theory.



RMS roughness: 1.81 nm

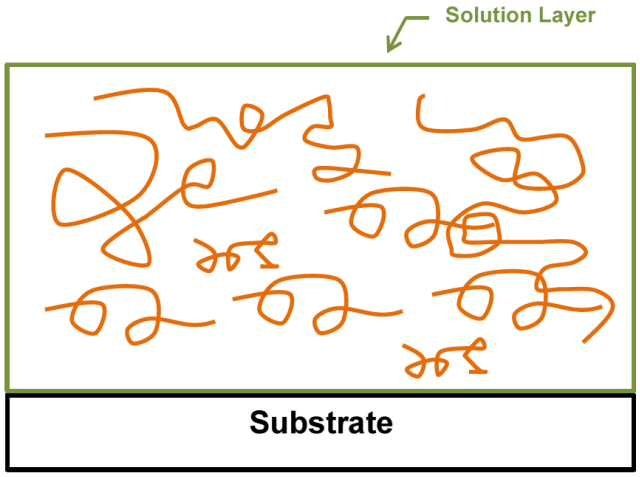
Fig. 3.8 An example of surface shuttle-like crystals in PA12 films with thickness around 20 nm.

However, this growth mechanism shows weaknesses in explaining the very small crystal size and low crystallinity in polymers, a typical example of which is presented in Fig. 3.8, which shows shuttle-like PA12 crystals with a scale smaller than expected for lamellar crystals. In this situation, a mesomorphic state theory [267] would be helpful, where small crystalline clusters are believed to form prior to lamellae. Supported by recent research [267-271], this theory allows a better understanding of lamellar crystals and indicates that a smaller crystalline morphology is preferred at a lower temperature, where the mobility of a polymer chain is limited. Although this theory was initially proposed for melt-crystallization, it fits well in the situation of crystallization with fast solvent evaporation. Providing that this network layer of shuttle-like crystals is formed during spin coating, it is then reasonable that the rapid solvent evaporation at surface during spin coating restricts the chain mobility in surface regions which, subsequently, leads to crystalline clusters rather than lamellar crystals.

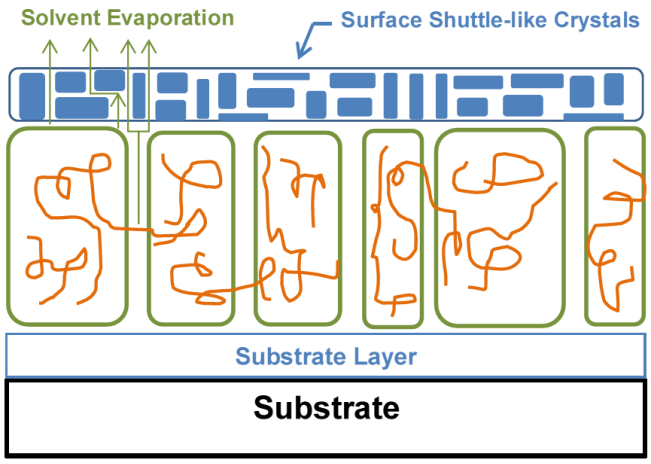
3.3.1.4 A model for surface crystallization during solvent evaporation

Referring to the results on the crystals in the as-spin-cast PA12 films presented above and previous thin film work on polyesters [28], a model for polyamide crystallization accompanied with solvent evaporation in thin films can be conceived (Fig. 3.9). During

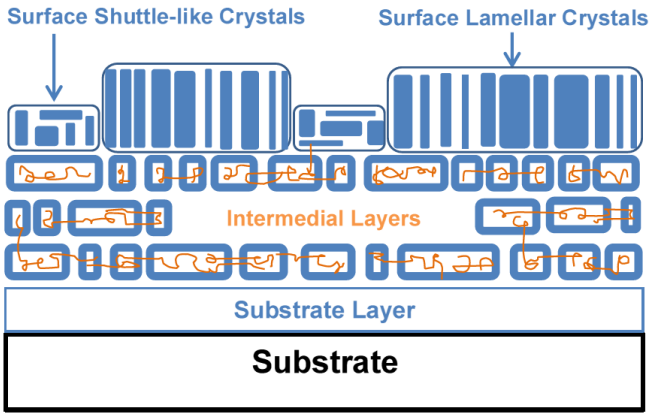
spin coating, a homogeneous amorphous polyamide solution layer is formed initially (Fig. 3.9a). However, as crystallization of a polyamide takes place very easily due to chain flexibility and H-bonding, the morphology of a polyamide film soon alters with solvent evaporation. When crystallization happens, the associated decrease in volume enables the generation of solvent evaporation channels through the thickness of the film.



(a) Solution layer produced during spin coating.



(b) A network of shuttle-like crystals in the near-surface region associated with solvent evaporation forms during spin coating. Solvent evaporation channels also form in the film.



(c) A dried PA12 film with shuttle-like or lamellar crystals in the surface region. The lamellar crystals are formed from recrystallization of the shuttle-like crystals during the solvent evaporation stage after spin coating. The intermedial layers (bulk) of the film are thought to have relatively low crystallinity.

Fig. 3.9 A model for solvent evaporation associated crystallization of PA12 in ultrathin films.

A network structure of shuttle-like crystals (examples can be found in the left column of Fig. 3.6), which provide sufficient channels for solvent evaporation, is believed to form in the upper layers (near-surface region) of the films during the early stages of spin coating, where the rate of solvent evaporation is high (Fig. 3.9b). Also, a wetting layer is expected to form at the substrate surface at this stage and dries to ultimately become a near-substrate layer. The formation of the substrate layer is attributed to the strong interaction at the substrate-polymer interface, which is most likely due to the possibility for H-bonding between the polyamide chains and the substrate since the cleaned substrate is hydrophilic with some hydroxyl groups. In between the near-surface and near-substrate layers is a solution layer, (the solvent concentration in this layer is much higher than when the solution is first cast), with solvent evaporation channels (Fig. 3.9b). As the solvent eventually evaporates from this intermediate layer it may transform to contain a network of small crystallites, although no direct evidence of the crystallinity or otherwise of this layer is available.

Lamellar crystals, however, are thought to develop during the drying state after spin coating, where solvent evaporation rate is slow and crystallization time is enhanced (Fig. 3.9c). During this stage, a morphology transition from shuttle-like to lamellar crystals may occur due to the solvent-rich environment, where the initially-formed shuttle-like crystals dissolve and recrystallize into lamellar crystals. This is consistent with the inter-penetrating morphology (Fig. 3.5c&d) at the boundary of the two different crystals. However, this dissolution-recrystallization may not occur for all the shuttle-like crystals due to the limited residual solvent. The different crystallization processes during the spin coating stage and the drying stage result in the two distinct crystalline morphologies as displayed in Fig. 3.6.

A schematic illustration of a dried as-spin-cast polyamide film is given in Fig. 3.9c including a surface crystalline layer, a network-structured intermediate layer as the bulk of a polyamide film and a near-substrate layer.

3.3.2 Morphological Evolution on Annealing

3.3.2.1 Secondary surface crystallization

On annealing from an amorphous state, polymers may crystallize in surface regions at lower temperatures than that in bulk regions. Dramatic transformations in both surface morphology and roughness were observed when bulk crystallization takes place [27]. In the case of polyamides, this situation is more complex as there is already some crystallization during spin coating. These crystalline structures affect further crystallization processes during annealing and the morphological changes are less obvious. In contrast to the situation in amorphous polymer films, the surface roughness of polyamide films with surface lamellar crystals only varies within a few nanometres during annealing (Fig. 3.10).

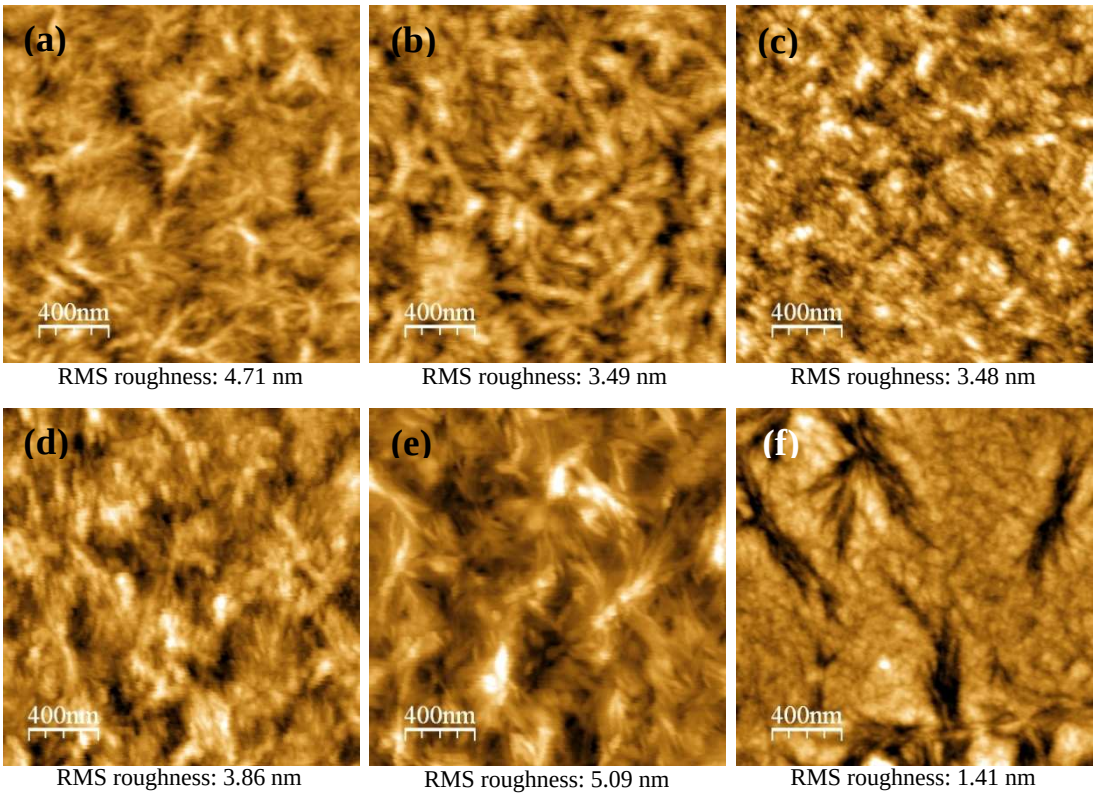


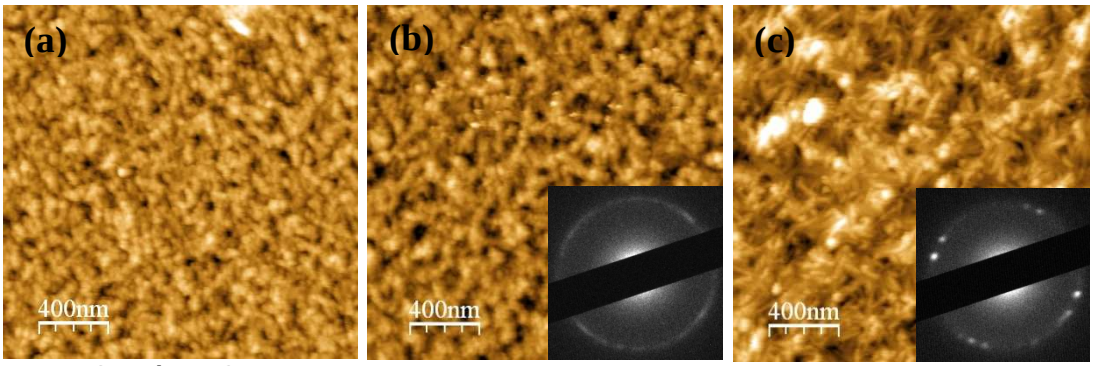
Fig. 3.10 Crystalline development in PA12 films 55 ± 4 nm thick on annealing. Samples are annealed at different temperatures: (a) 120 °C; (b) 130 °C; (c) 140°C; (d) 150 °C; (e) 160 °C; (f) 170 ℃ for 2 hr from as-spin-cast films with 2D sph erulitic morphology (Fig. 3.6d').

A significant change in surface morphology takes place at annealing temperatures as low

as 120 ℃ due to crystallization of amorphous regions (Fig. 3.10a). The morphology change here indicates that crystallization during annealing starts from the existing lamellar structures and develops into the gaps in-between: the morphology of the 2D spherulites and sheaf-like crystals grows fuzzy. This effect becomes even more obvious when the annealing temperature (T_a) increases (Fig. 3.10b). With new crystals filling the gaps between original crystals, the surface roughness of PA12 after annealing may even decrease (compare RMS in Fig. 3.6d' and 3.10a&b). Previous work [249, 272] on the crystallization in PA12 (bulk samples) indicated the possibility of a secondary crystallization on annealing around 120 ℃, which resulted in an increase of about 3-5% in crystallinity, and an increase in Bragg's long spacing (L_B, sum of the average thicknesses of the crystal lamellae and the interlamellar amorphous regions), induced by the melting and recrystallization of secondary lamellae or a crystalline transition from γ to α' (mentioned in section 3.1). However, this possible secondary bulk crystallization is too small an effect to explain the evident crystallization process displayed in Fig. 3.10a&b. The bulk crystallization temperature for PA12 obtained from DSC is between 136 ℃ and 160 ℃, close to the reported range from 140 ℃ to 155 ℃ [273], and so the morphology changes at 120 ℃ and 130 ℃ are associated with the enhanced mobility (lower T_g) at the surface leading to changes in the crystallinity in the near-surface region. The more significant morphology change with T_a between 140 ℃ and 155 ℃, however, is attributed to bulk crystallization.

After annealing at around 160 ℃, PA12 crystals (Fig. 3.10e) show a structure more similar to the lamellar crystals in as-spin-cast films (Fig. 3.6d'). At this T_a the very fine secondary crystals observed at the surface are unlikely to form, being very close to the melting temperature of the larger bulk crystals. For even higher T_a, e.g. 170 ℃ (Fig. 3.10f), melting and recrystallization of the whole PA12 film starts (i.e. at a temperature consistent with DSC measurements), which breaks down the initial lamellar structure and leaves a relatively uniform surface with some sheaf-like cracks. This brings the RMS roughness

value below 1.5 nm.



RMS roughness: 3.11 nm RMS roughness: 3.48 nm RMS roughness: 5.25 nm

Fig. 3.11 AFM images for PA12 films (55 ± 4 nm) with shuttle-like crystals annealed for 2 hr at (a) 130 ℃, (b) 140 ℃ and (c) 160 ℃ respectively. The insets are the c orresponding ED patterns.

Similar crystalline development upon annealing has also been observed for the as-spin-cast shuttle-like PA12 crystals. However, in addition to the transformation of secondary surface crystals (Fig. 3.11a), there appears to be a peak-forming process in PA12 films with shuttle-like crystals (bright small discs in Fig. 3.11c, Fig. 3.12a&b). In contrast to as-spin-cast lamellar crystals with better developed structures, the shuttle-like crystals are much smaller and could easily act as nucleation centres during further crystallization processes, which might result in crystalline aggregations penetrating into the free surface. Corresponding ED patterns for PA12 crystals before and after annealing at different temperatures (Fig. 3.5a, Fig. 3.11b&c) show a constant γ crystalline contribution. The crystalline transition from γ to α' phase, reported for bulk PA12 crystals measured by scattering annealed and measured at temperatures above 120 ℃ [248, 249] is not observed here as any transitions to the α' phase clearly transit back to γ form on cooling, as has been reported previously [248]. However, when the annealing temperature increases, diffraction spots are observed (Fig. 3.11), which indicates the generation of a few crystals with particular flat-on orientations during annealing within the region of the selected-area diffraction. This is consistent with Wang *et al*.'s work [127] on the lamellar orientation at the surface that the flat-on lamellae tend to form in very thin polymer films when T_a approaches T_m.

Annealing for longer periods, as exemplified in Fig. 3.12, which compares PA12 films annealed at 150 ℃ for 2 hr and for 64 hr, shows th at the morphology of the film with longer annealing is fundamentally similar, but is larger-scale with higher roughness and bigger aggregation peaks, as indicated by shifting of the height distribution peak to a higher value and the appearance of the small second peak in the red histogram at about 45 nm associated with the aggregation peaks.

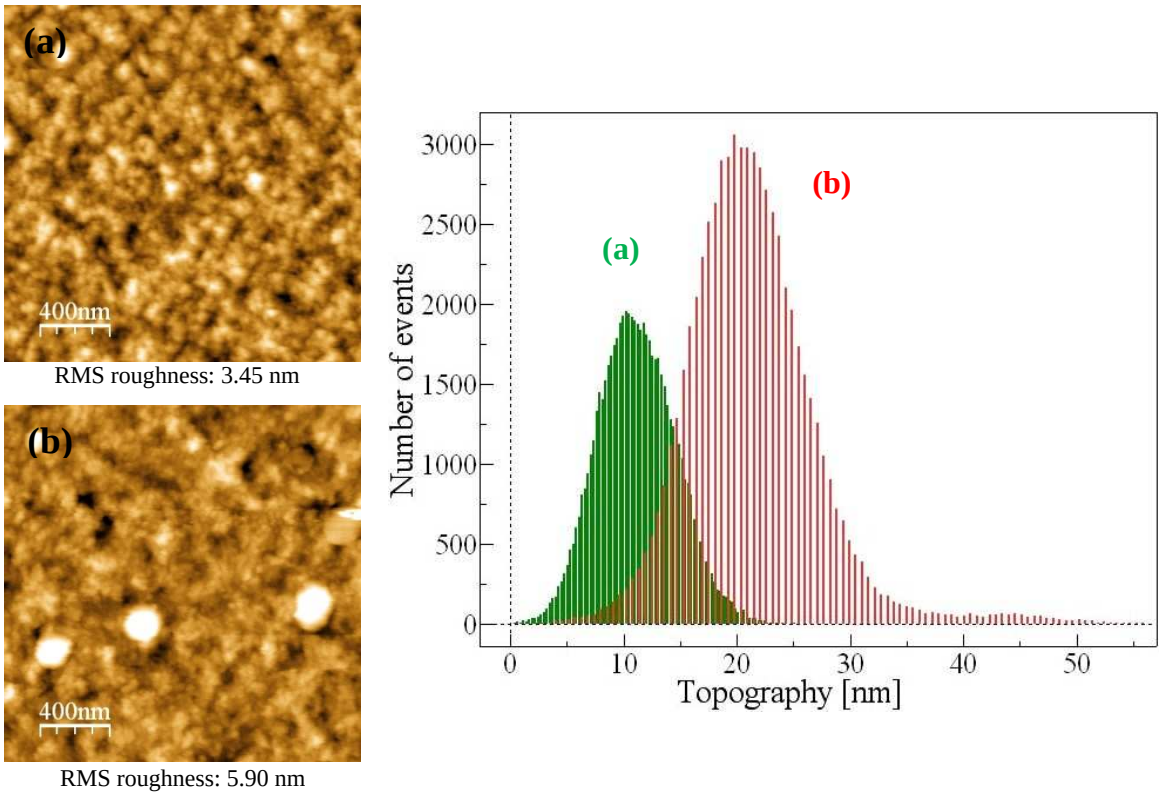


Fig. 3.12 AFM topography images for PA 12 films (55 ± 4 nm) with surface network crystals annealing at 150 ℃ for (a) 2 hr and (b) 64 hr with histograms beside.

3.3.2.2 Effects of annealing temperature and film thickness

Using the AFM results, the PA12 crystal morphologies in thin films are mapped in Fig. 3.13, illustrating the effects of both T_a and film thickness on the crystalline structures. As the surface roughness of PA12 films increases quickly with film thickness, it becomes difficult to distinguish any morphological changes on annealing, especially for surface crystallization, where normally nano-scale changes take place. Thus, the stability diagrams of shuttle-like (Fig. 3.13a) and lamellar (Fig. 3.13b) crystals are limited to films

with thickness up to 79 nm and 55 nm respectively.

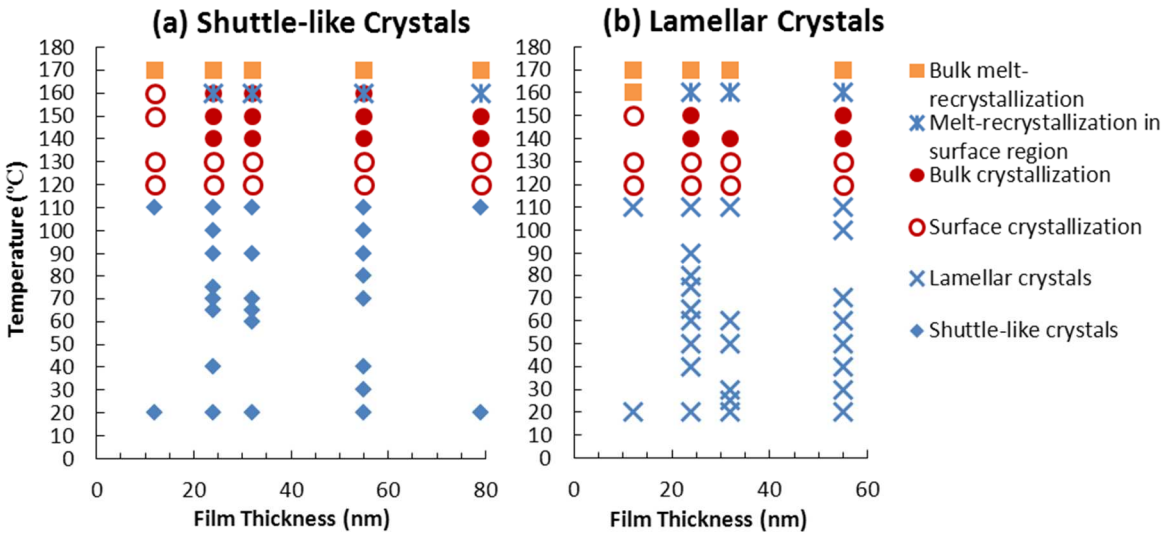


Fig. 3.13 Stability diagrams of surface shuttle-like crystals (a) and lamellar crystals (b) in PA12 films with different thicknesses. Samples were annealed at different temperatures for 2 hr. As annealing temperature increases, secondary surface crystallization occurs first and then bulk crystallization. At even higher temperature, melt and recrystallization of secondary surface crystals take place and finally bulk melting and recrystallization occurs. T_{room} is assumed to be 20 °C.

With increasing T_a, the crystalline morphology could be divided into five stages: crystals with as-spin-cast morphology, secondary surface and then bulk crystallization induced by annealing, onset of melt-recrystallization of the fine crystals in the surface regions, and the full on-set of melt-crystallization. The morphology differences between the surface and bulk crystallization processes become slight as the film thickness decreases, and there is no substantial change in surface roughness on bulk crystallization due to the initial as-spun crystallinity. However, as the onset of the secondary crystallization is at temperatures substantially lower than the bulk crystallization temperature and clear morphological differences can be observed, such as in Fig. 3.10b&c, it is apparent that improved chain mobility near the sample surface does allow for surface crystallization (as discussed in section 3.3.2.1, although the possibility of bulk crystallization cannot be excluded, the surface crystallization should be dominant, and when bulk crystallization is observed at higher T_a, this is apparent from the surface morphology). The approximate

temperatures required for the melting of these surface crystals and the start of bulk melting are 160 ℃ and 170 ℃ respectively. In gene ral, the stabilities of both shuttle-like and lamellar crystals in surface regions are very similar, which indicates that the further crystallization processes on annealing are not specifically defined by the as-spin-cast morphology (shuttle-like or lamellar crystalline structure).

The morphologies of the annealed PA films, however, varied dramatically with decreasing film thickness due to the increased confinement with decreasing film thickness, as illustrated in the as-spin-cast morphologies of Fig. 3.6. Another example showing the surface morphology development of PA12 films with surface lamellar crystals is presented in Fig. 3.14. These films, around 32 nm thick, are thinner than those displayed in Fig. 3.10 and have crystals mainly in the form of lamellar sheaves before annealing (Fig. 3.6e').

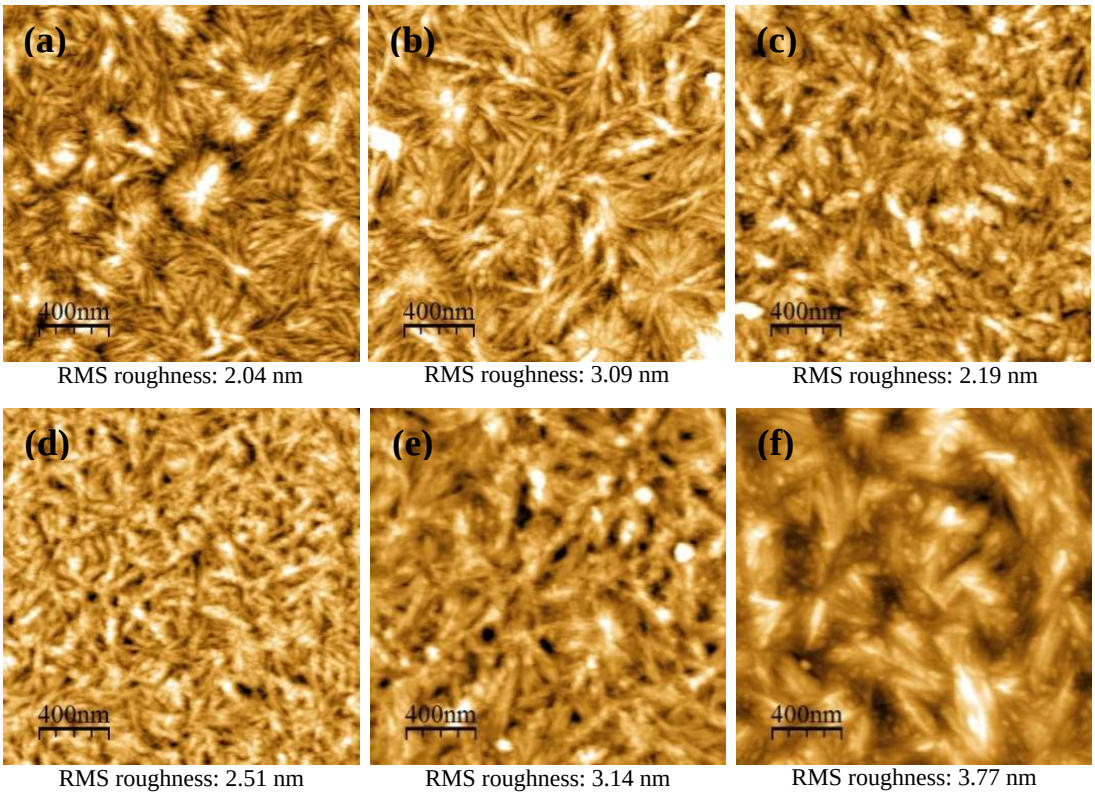
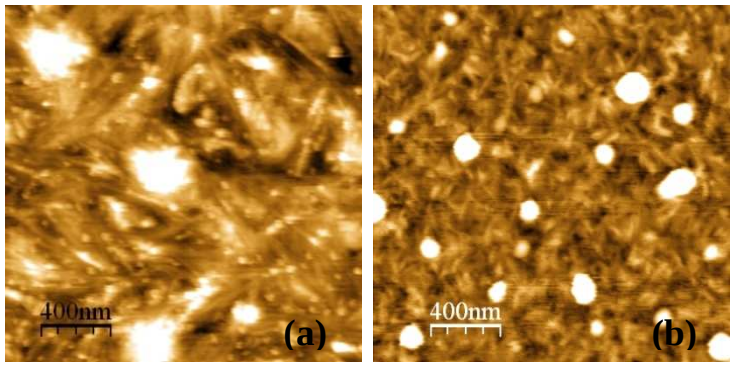


Fig. 3.14 Crystalline development in PA12 films 32 ± 2 nm thick on annealing. Samples are annealed at different temperatures: (a) 110 ℃, (b) 120 ℃, (c) 130 ℃, (d) 140 ℃, (e) 160 ℃, and (f) 170 ℃ for 2 hr from as-spin-cast films with la mellar sheaves morphology (Fig. 3.6e').

Instead of having an apparent growing-fuzzy process of lamellar crystals in thicker PA12 films (around 55 nm) after a 2 hr anneal at 120 ℃, only barely distinguishable aggregations grow around the lamellar fibrils (Fig. 3.14b) indicating the presence of the secondary surface crystallization in these films. As the surface crystallization advances, the lamellar fibrils become difficult to recognize, e.g. as seen in a sample annealed at 130 ℃ (Fig. 3.14c). Since the thicknesses of these films are merely around 32 nm, the bulk region (intermediate layer) in the film is very thin. Hence, during the bulk crystallization stage, the significant bulk morphology change observed in the films around 55 nm (Fig. 3.10c&d) annealed at temperatures above 140 ℃ was not observed in these thinner films. The bulk crystallization is markedly limited in these film and just results in a slightly modified network structure (Fig. 3.14d). The melt and recrystallization of secondary crystals in the near-surface region happened at 160 ℃ allowing the formation of a coarser network structure. In this case, the network is generated through the joining of the lamellar fibrils within a lamellar sheaf since the lamellar sheaves can still be subtly recognized with similar size to that in the as-spin-cast films (Fig. 3.6e'). The effect of molecular confinement due to film thickness on the crystallization of PA12 can also be observed in samples after bulk melt and crystallization at 170 ℃: a typical melt-quenched crystalline morphology with sheaf-like depressions was observed in the 55 nm film (Fig. 3.10f) with RMS roughness as low as 1.41 nm, while, for the 32 nm thick film, a much less developed morphology was discovered (Fig. 3.14f) with a relatively high RMS roughness of 3.77 nm.

The overall thickness of the film can also influence the detail of the morphological development on annealing. Fig. 3.15 shows that, as observed for PET [27], at a greater film thickness, e.g. 79 nm, PA12 shuttle-like crystals (Fig. 3.6c) have the opportunity to grow into coarser, lamellar, crystals (Fig. 3.15a) on annealing at 160 ℃. However, for films of lower thickness (e.g. Fig. 3.6f, Fig. 3.15b), the large lamellar crystals are not formed, and the primary effect of annealing is that large protrusions are observed, thought to be

associated with constrained crystallization penetrating into the surface.



RMS roughness: 4.65 nm RMS roughness: 5.49 nm

Fig. 3.15 AFM images showing the morphology of surface shuttle-like crystals after annealing at 160℃ for PA12 films with thickness (a) 79 ± 6 nm, (b) 24 ± 3 nm.

3.3.3 The Near-Substrate Layer

Our characterisation of the PA12 thin films has led to some direct observations of the near-substrate region of the polymer, consistent with Wang *et al*.'s [127] three-layer model (near-surface layer, bulk layer and near-substrate layer). In a 24 nm film after annealing, some defects were revealed showing the lamellar surface crystals to be covering a distinct substrate-polymer layer (the dark patches in Fig. 3.16a), perhaps about 10-15 nm thick, without an overlayer of crystals around 10 nm thick in these regions. Fig. 3.16b shows the topography of the PA12 film around 12 nm thick with aggregations from several nanometres to around 10 nm high. The morphology in the pitted areas here is similar to that in Fig. 3.16a, indicating the existence of a special near-substrate polymer layer at the substrate-polyamide interface.

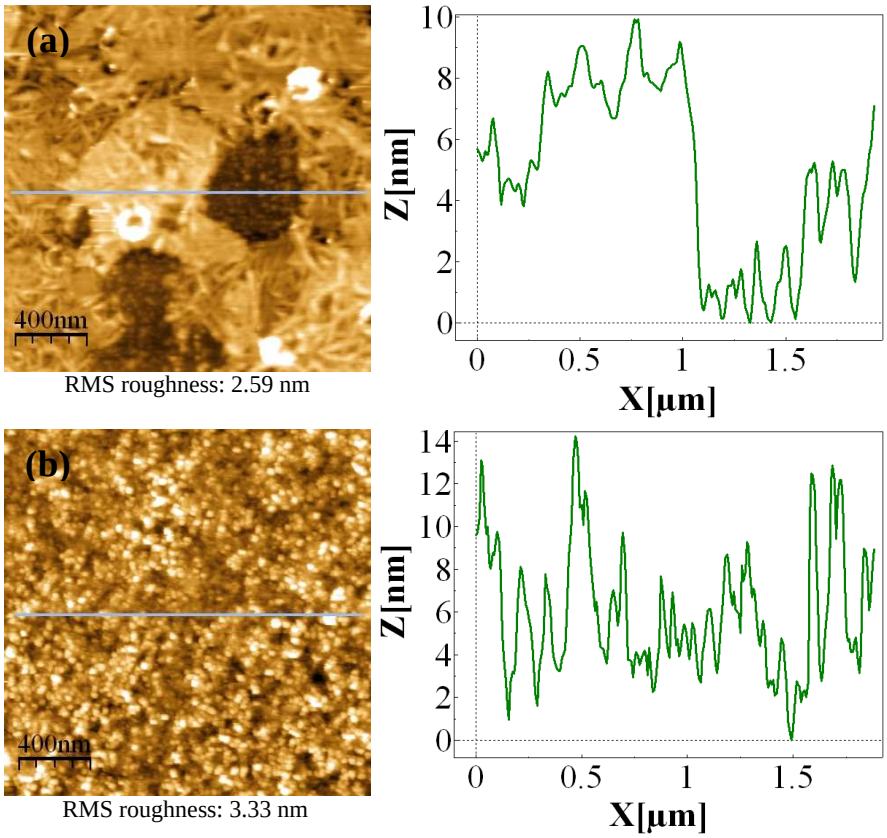


Fig. 3.16 AFM topography images and line profiles of surface height show (a) surface lamellar crystals on the substrate layer in PA12 film around 24 nm thick annealed at 120 ℃ for 2 hr; (b) molecular aggregations on the substrate layer in as-spin-cast PA12 films around 12 nm thick.

After high temperature annealing of thicker films (e.g. annealed at 170 ℃ for 2 hr), during which significant melting has happened, under low magnification optical microscopy, it is possible to observe a “dewetting” behaviour (not the dewet of PA12 on substrate, but the dewet of PA12 on the substrate-polymer layer): some areas in the film appear to significantly thin leaving other thicker regions (Fig. 3.17). It was found that this phenomenon tended to occur in thicker films (Fig. 3.17a&b) and disappeared when the film thickness was below a certain value, e.g. 24 nm (Fig. 3.17c). Moreover, the thin areas of the thicker film (Fig. 3.17a"&b"), when examined with the AFM, showed a morphology similar to that of the very thin, 24 nm, film (Fig. 3.17c') after the same annealing, and distinct from that of uncoated glass (Fig. 3.18c). Since the cleaned glass surface is hydrophilic, there is a strong bonding between the substrate and the attached PA12 restricting motion of the chains in this region, whereas the bulk and surface PA12 in the

regions above this can melt and dewet from the sublayer to release the horizontal stretching forces of molecular chains induced during spin casting.

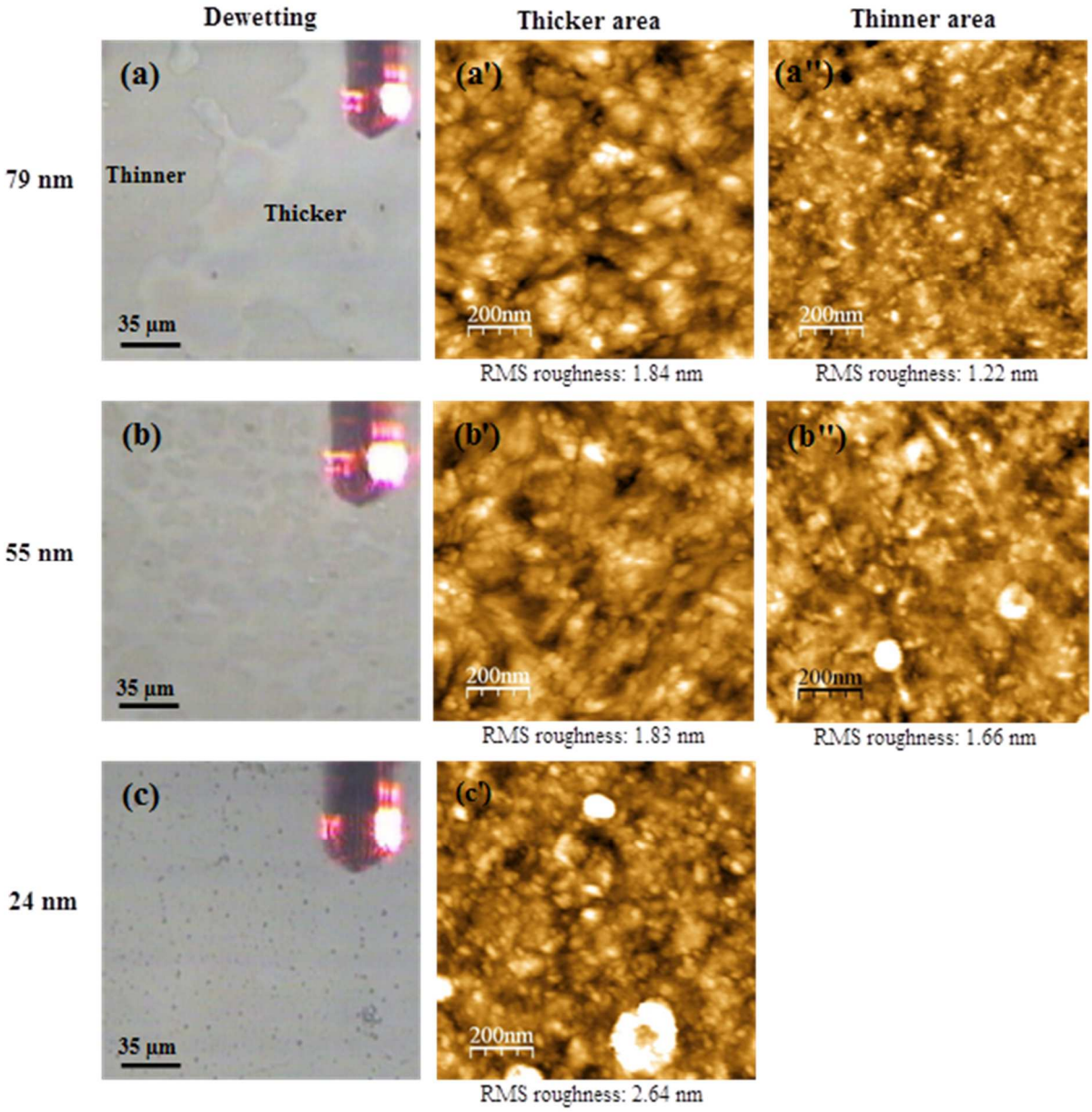
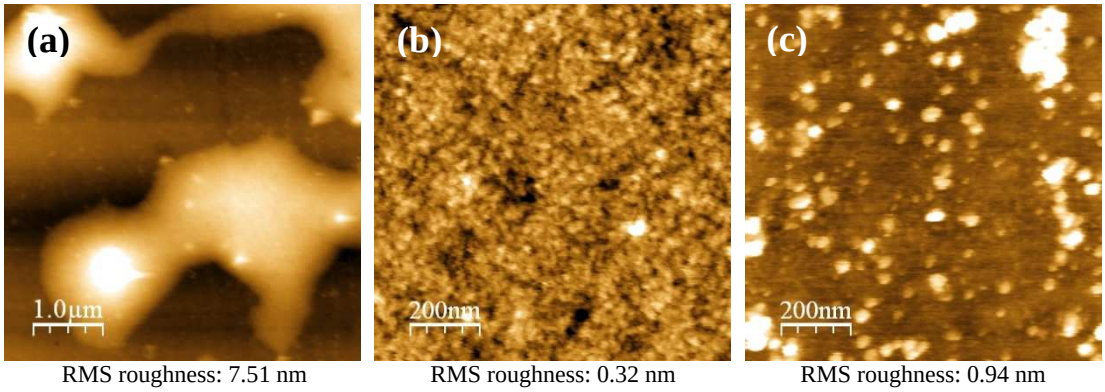


Fig. 3.17 Optical and AFM images showing bulk melt-recrystallization and dewetting of upper layers on the near-substrate layers in PA12 thin films. All the samples were obtained by annealing PA12 films with shuttle-like surface crystals at 170 °C for 2 hr and the thickness values are from the corresponding initial films.

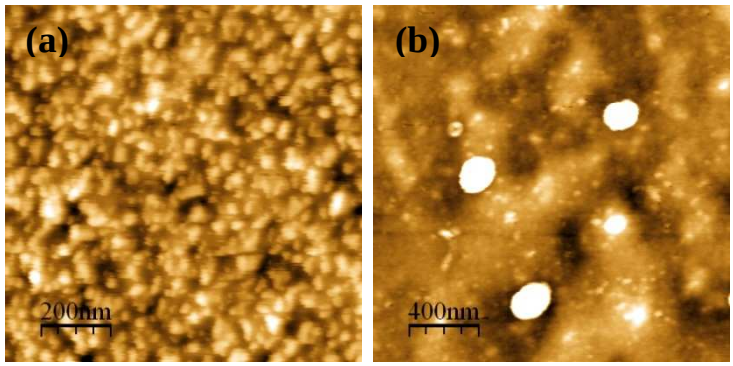
For ultrathin films (thickness 24 nm) that in the spin-cast state had surface lamellar crystals, this dewetting phenomenon can still be observed, but on a much smaller scale (Fig. 3.18a), observable only with AFM. In this case the morphology of the lower levels is

homogeneous with a RMS roughness value only around 0.32 nm (Fig. 3.18b), which is even lower than that of a glass substrate (Fig. 3.18c), reminiscent of the substrate layer at polymer-substrate interface (the dark patches in Fig. 3.16a). This suggests that this dewetting phenomenon is a pseudo-dewetting between the upper layers and the near-substrate polymer layer. The melt behaviours of the two kinds of surface crystals suggest a better connectedness between the substrate layer and the upper layer showing shuttle-like crystals compared to those that show the lamellar crystals.



RMS roughness: 7.51 nm RMS roughness: 0.32 nm RMS roughness: 0.94 nm

Fig. 3.18 AFM images for PA12 film (24 ± 3 nm) with surface lamellar crystals annealed at 170 ℃ for 2 hr: (a) dewetting and (b) surface morphology of thinner area; and glass substrate (c).



RMS roughness: 3.64 nm RMS roughness: 4.38 nm

Fig. 3.19 Morphology of PA12 films (12 ± 2 nm) with (a) molecular aggregations (Fig. 3.6g) and (b) lamellar crystals (Fig. 3.6g') annealed at 170 ℃ fo r 2 hr.

The dewetting during the melting process disappears when the films become even thinner (around 12 nm), where the horizontal movement of molecular chains is restricted (Fig. 3.16b and Fig. 3.19a). Nevertheless, when annealed at 170 ℃, a 12 nm thick PA12 film with lamellar crystals (Fig. 3.19b) shows similar morphology to that of a 24 nm thick

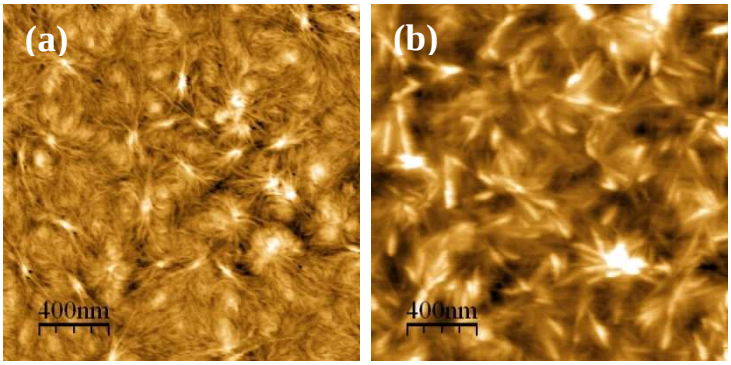
film with shuttle-like crystals (Fig. 3.17c'). This might be attributed to the similar crystal size of lamellar crystals in 12 nm thick film (Fig. 3.6g') and the shuttle-like crystals in the film around 24 nm (Fig. 3.6f), confirmed by their AFM images.

3.3.4 The Substrate Effect

The confinement of film thickness on the mobility of polymer chains may also be due to the hindrance from the substrate, especially in the situation discussed before where the polymer-substrate interaction is strong. This is confirmed by the surface morphology of PA12 on glass substrates coated by poly(3,4-ethylenedioxythiophene) (PEDOT) (Fig. 3.20). There will be strong interaction between the PA and the PEDOT, as there was between the PA and the glass due to the expected H-bonding in both cases, however the flexibility and chain mobility of the polymer underlayer in the case of the PEDOT, may lead to differences in behaviour. These PA/PEDOT films have the same preparation method as for the 32 nm PA12 films. The similar as-spin-cast morphology of the two kinds of films (comparing these with as-spin-cast lamellar crystals, Fig. 3.6e' and 3.20a), both mainly in lamellar sheaves, indicates close thickness values. Rather than having both shuttle-like and lamellar crystals, only the lamellar morphology was observed in these as-spin-cast films on PEDOT (Fig. 3.20a) (similar situation has also been found in PA12 films of roughly 24 nm thick on PEDOT). This indicated a complete transformation from shuttle-like crystals to lamellar crystals in these films on PEDOT rather than a partial transformation in the films on glass substrates before the PA chains were immobilized by solvent evaporation, which is the result of the higher mobility of PA chains in the films on PEDOT.

The enhanced chain mobility in films on PEDOT is also manifested by the morphology of the annealed samples. For instance, when annealed at 160 ℃ for 2 hr, the film on PEDOT showed a more advanced melt and recrystallization of secondary crystals in the

near-surface region (Fig. 3.20b) than the film on glass (Fig. 3.14e). The morphology agrees well with that of the 55 nm films on glass with 2D spherulites after melt and recrystallization of the secondary crystals (Fig. 3.10e). These observations confirm the significant influence of a substrate on the secondary crystallization in very thin films, e.g. below 32 nm, and hence, the melt and recrystallization process.



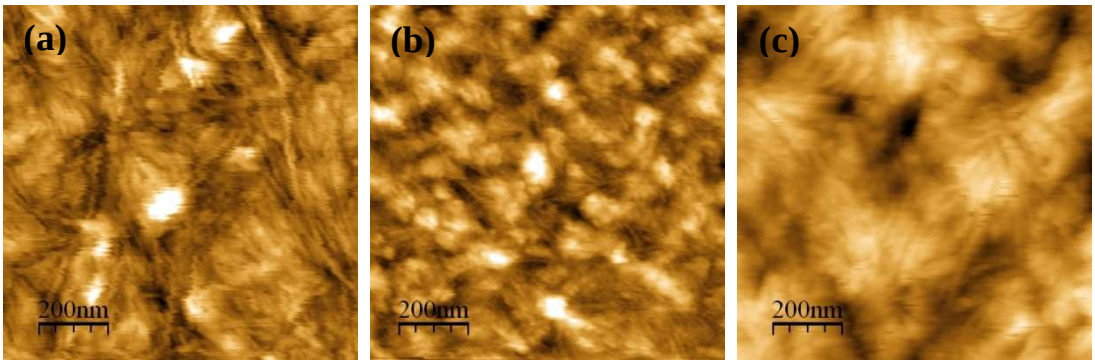
RMS roughness: 2.06 nm RMS roughness: 3.39 nm

Fig. 3.20 AFM topography of PA12 films on glass substrate coated by PEDOT: (a) as-spin-cast and (b) annealed at 160 ℃ for 2 hr. The solution concen tration and the operation conditions for spin coating is the same as that for the 32-nm PA12 films on glass.

3.3.5 Crystallization in PA6 Thin Films

Similar surface crystallization behaviour has also been found in PA6 films. However, experimental results show that PA6 has an even higher crystallization rate and forms as-spin-cast crystals mainly in the form of lamellar crystals. In comparison with PA12, PA6 has a greater density of H-bonding, which contributes to the enhanced crystallization rate. It is reasonable that, with the same solvent evaporation rate, a higher crystallization rate would lead polyamide chains to form the better structured lamellar crystals rather than shuttle-like crystals. Nonetheless, the increased nucleation rate in PA6 stops the formation of large 2D spherulites as observed in PA12, which relies on a secondary nucleation and growth mechanism. Examples of as-spin-coated PA6 films with different thicknesses are shown in Fig. 3.21. It is very clear that, with increasing film thickness, the as-spin-cast

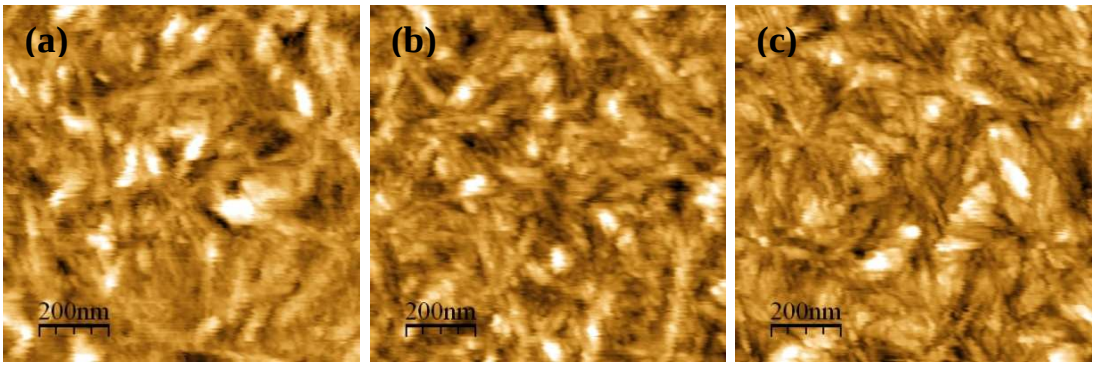
PA6 crystals become larger as in PA12 films



RMS roughness: 1.72 nm RMS roughness: 3.81 nm RMS roughness: 8.04 nm

Fig. 3.21 Morphology of as-spin-coated PA6 films (spin coated from solutions in 2CP) with thickness: (a) 72 ± 3 nm, (b)132 ± 3 nm, (c) 361 ± 16 nm.

Annealing induced secondary crystallization in amorphous regions in PA6 also results in the formation of aggregations around the lamellar fibrils and a decrease in surface roughness (Fig. 3.22). However, as PA6 has higher T_g and T_m values than that of PA12, the annealing temperatures for the appearance of the secondary surface crystallization and the surface melt-recrystallization phenomena in PA6 films were increased. AFM results in Fig. 3.22 show that obvious secondary surface crystallization took place when the PA6 films were annealed at 140 ℃, and the surf ace crystallization also explains the morphology changes at 150 ℃ and 160 ℃. The bulk c rystallization of PA6 took place at temperatures between 180 ℃ and 200 ℃ (by DSC).



RMS roughness: 2.53 nm RMS roughness: 1.84 nm RMS roughness: 1.75 nm

Fig. 3.22 Surface morphology of PA6 films (72 ± 3 nm) annealed at (a) 140 ℃, (b) 150 ℃, and (c) 160 ℃ for 2 hr, respectively.

3.4 CONCLUSIONS

Spin-coating PA12 leads to as-spin-cast semicrystalline morphologies that depend upon solvent evaporation rate and film thickness. Two different crystalline morphologies: shuttle-like and lamellar, could be produced due to the different solvent evaporation rate during the spin coating stage and the subsequent drying stage. These crystals are thought to exist in the upper layers of a film rather than penetrating through the whole film, although no direct measure of the degree of crystallinity in the bulk of the film has been achieved. Electron diffraction on PA12 showed both kinds of the as-spin-cast formed PA12 crystals in the γ form (rather than α form), which is the most stable crystalline phase for PA12. Despite the existence of as-spin-cast crystals, the free surface effect allows further (secondary) crystallization of PA12 at an annealing temperature (roughly 20 ℃) below the bulk crystallization temperature, which was confirmed by the significant change in surface morphology. Constant γ crystalline distribution was found for the annealed PA12 samples, indicating the γ structure of the secondary surface crystals, while secondary crystals in α or α' form are expected according to previous work [249, 272]. This gives the idea that surface crystals tend to form the most stable crystalline phase of a polymer. The annealing temperature for further crystallization is not influenced by film thickness due to the already existing confinement from the as-spun crystals. An interesting melting and recrystallization of secondary crystals prior to bulk melting was discovered in PA12 films reflecting the smaller size of the secondary crystals. There is a clear substrate-confined region about 10-15 nm thick that appears to give rise to the dewetting of upper layers from near-substrate layers during melting.

Due to the higher crystallization rate, only lamellar crystals were observed in as-spin-cast PA6 films. A similar free surface effect was also observed in the PA6 films allowing a secondary surface crystallization at a temperature lower than the bulk crystallization temperature. The secondary surface crystallization temperature for PA6 is higher than that for PA12 as a result of the higher T_g.

4 NEAR-SURFACE PHASE BEHAVIOURS IN PS/PMMA THIN FILMS

As crystallization exhibits surface-specific phenomena associated with an increased mobility of molecules near the free surface, it might also be possible for phase separation to develop in the near-surface region of a polymer blend at a temperature lower than the bulk phase separation temperature. To date, most surface work on phase separation in polymer blend films has actually been an investigation of the surface part of the phase separation of the whole film and the annealing temperatures for phase separation are normally well above the bulk T_g of the polymers in the blend [30-34], meaning that any phase separation confined to the near-surface region that may occur at lower temperatures is unobserved.

In this work, the phase behaviour in the near-surface region, typically around 10 nm in depth, of PS/PMMA thin films is presented. The surface-specific phase separation and dewetting between the two polymers were examined following annealing at temperatures below the bulk phase separation temperature, even at temperatures below the bulk T_g of both polymers. Although the surface-specific phase separation of PS/PMMA appeared in different forms, it showed remarkable similarity to the bulk phase behaviours that occur at much higher temperatures. The influence of both annealing time and film thickness were investigated. The PS/PMMA system was chosen since much work [32-36] has already been done on this system showing the phase separation mechanism of the blend in the bulk of the thin films, which would help interpretation of phase behaviours in the near-surface region.

4.1 BACKGROUND

Phase separation in thin films is greatly influenced by the presence of the free surface [26] and substrate [94, 95]. Polymer blend thin films are commonly prepared using spin coating in laboratory work for the investigation of phase separation. During this process, an immiscible polymer blend can be forced into the unstable or metastable phase through solvent quenching [209, 210], which normally induces a non-equilibrium phase separation that can transform towards the equilibrium state through further annealing [208, 274]. In contrast to the bulk, phase separation in blend thin films tends to be accompanied by dewetting between the component polymers due to their different wetting preference at the substrate-polymer or air-polymer interface [208, 211, 225] and this phenomenon becomes significant as the film thickness approaches the radius of gyration (R_g) of polymers, e.g. thinner than $5R_g$ [224]. Tanaka *et al.* [275] showed that, with film thickness less than $2R_g$, the dewetting between polymers could even lead to the phase separation of a blend that would be miscible in the bulk, such as polystyrene/poly(vinyl methyl ether) (PS/PVME). In addition, vertical phase separation tends to occur in polymer blend thin films with the polymer of lower surface energy aggregating at the polymer-air interface [32, 211].

4.2 EXPERIMENTAL

PS (M_w = 96000; M_w/M_n = 1.04) and PMMA (M_w = 99400; M_w/M_n = 1.08) were purchased from Sigma-Aldrich. With similar molecular weight values, the PS and PMMA show a similar T_g and, hence, comparable chain mobility on annealing. Also, the narrow molecular weight distribution of the polymers helps to minimize the range of properties. As two different batches of PS purchased at different times showed different crystallizabilities, two different situations are discussed: one PS with very low crystallizability (PS1, section 4.3.1) and the other with a higher crystallizability (showing surface crystallization) (PS2, section 4.3.2).

Blend films were prepared by spin coating solutions of PS/PMMA in toluene (Sigma-Aldrich) onto glass substrates. Prior to deposition, solutions were filtered with 200 nm pore sized polytetrafluoroethylene (PTFE) syringe filters to remove any impurities or undissolved polymer particles as they would change the surface and interfacial tensions around them, which would affect phase separation processes [274]. Substrate-cleaning and the operation of spin coating is the same as that in section 3.2. The blend ratio in this study was set as a constant 50/50 (weight%/weight%) to exclude the influence of blend composition. Pure PS or PMMA films were prepared in the same way.

Film thickness was controlled by solution concentration and was measured by a Dektak profilometer (Veeco) (details in section 3.2).

Characteristics of PS and PMMA are given in Table 1. The values of number-average molecular weight, M_n, and molecular weight distribution, M_w/M_n, are provided by the manufacturer, while the R_g of each of the polymers was calculated using the equation

$$R_g = (Nb^2/6)^{1/2} \qquad \text{(Eq. 4-1)}$$

where, N is the degree of polymerization and b is the statistical segment length. The values of b for PS and PMMA were reported to be 0.68 nm [276] and 0.74 nm [277] respectively.

Table 4.1 Characteristics of PS and PMMA.

	M_n	M_w/M_n	$2R_g$ nm	T_g ℃
PS1	92.0k	1.04	16.5	106
PS2				99
PMMA	92.1k	1.08	18.3	114

Using DSC, T_g values of the two polymers were measured at different scan rates (data were collected from the second heating trace). Plotting T_g as a function of scan rate, a trend line could be obtained for each polymer, and the quoted T_g can be determined from extrapolation to the point at which the scan rate becomes zero. T_g results of PS and PMMA are displayed in Fig. 4.1 and the T_g values in Table 4.1.

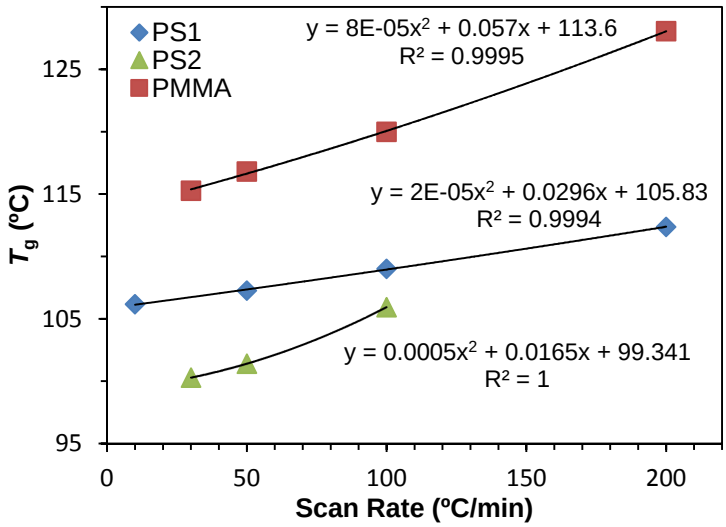


Fig. 4.1 T_g as a function of scan rate obtained by DSC. According to the equation of the trend line, the T_g values of the polymers could be obtained when the scanning rate is zero.

The surface morphology of PS/PMMA blend films was investigated using AFM (details in section 3.2). As-spin-coated blend films were annealed at different temperatures, ranging from about 30 K below T_g (80 ℃) to the bulk phase separation temperature, around 160 ℃, for different times, and then cooled rapidly on an clean aluminium block before characterization. All the temperature values were read directly from the (thermocouple) hotplate. (The actual annealing temperatures were examined by detecting the temperature at the surface of a glass slide on the hotplate. This calibration indicated an error of ± 2 ℃.) The as-spin-cast morphology of each of the samples was characterized

before annealing to ensure that any obtained surface morphology development is due to annealing rather than as-cast defects, since the initial surface behaviours have a tiny scale and could be easily neglected. Also, samples were examined soon after annealing to exclude any possible morphological changes at room temperature after annealing. Some samples were immersed in cyclohexane (Sigma-Aldrich) for 10 min to dissolve away the PS. After drying, the internal structure of these blend films could then be revealed by AFM.

The surface chemistry of some samples was also analysed by X-ray photoelectron spectroscopy (XPS) performed in an ion pumped VG Microtech CLAM 4 multi-channel detecting analyser system. 250 Watt unmonochromated Al X-ray excitation was used and the analyser was operated at constant pass energy of 100 eV for wide scans and 20 eV for detailed scans. The neutral carbon peak was set at binding energy of 284.8 eV to correct any sample charging.

4.3 RESULTS AND DISCUSSION

To investigate the development of near-surface phase separation, a two-component phase in the near-surface region is required at the start. Although phase separation of an immiscible polymer blend is often observed during spin coating, it is possible to 'freeze in' a surface morphology with both components rather than a single-component during solvent casting by rapid solvent evaporation. Early work on PS/PMMA films by Tanaka *et al.* [34] showed that the surface morphology of a spin-cast PS/PMMA film depends on film thickness and indicated the possibility of obtaining a blend film with phase separation extremely confined. In this project, solution concentration was decreased further to obtain thinner films and, hence, a faster solvent quenching.

It was reported by Walheim *et al.* [211] that, for PS/PMMA films spin-cast from a PS-better (i.e. PS is more soluble than PMMA) solvent, e.g. toluene, onto a hydrophilic substrate, a PMMA-rich phase tends to form a wetting layer on the substrate with islands penetrating through the upper PS-rich layer, which is consistent with the results of our blend films around 150 nm thick (Fig. 4.2a&b). Walheim *et al.* [211] attributed this spin-cast structure to the substrate preference of the two polymers, which substantially relies on the surface energy, and also to the different solubilities of PS and PMMA in the common solvent. Furthermore, in the non-equilibrium phase-separated state, the PMMA domains are possibly covered by a very thin PS layer due to the fast solvent quenching. This agrees well with the XPS results in Fig. 4.2c: the surface of the as-spin-cast samples apparently exhibits a PS signal with a main hydrocarbon (C−C/C−H) peak at binding energy of 284.8 eV and π−π* shake-up satellites at shifts of 6-8 eV from the hydrocarbon peak. Later investigation of *in-situ* phase separation of PS/PMMA during spin coating by Heriot and Jones [36] showed that the final phase-separated pattern is developed through the break-up of PS and PMMA wetting layers, at the free surface and substrate respectively, formed by previous vertical phase separation in the solution, (the model is displayed in Fig. 2.33). However, this model is limited to the as-spin-cast thin films with thickness over

a certain value, e.g. 100 nm, and is not what has been found in the thinner PS/PMMA films (displayed in section 4.3.1.1).

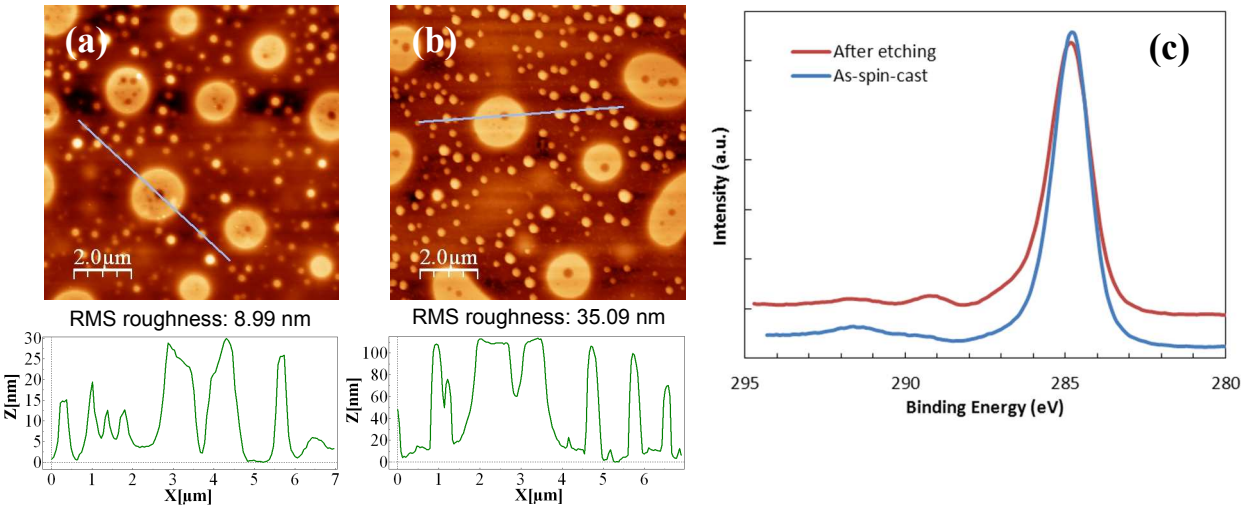


Fig. 4.2 AFM height images of (a) an as-spin-cast PS/PMMA film with thickness 151 ± 9 nm and (b) the film after the removal of upper PS-rich phase by cyclohexane. (c) XPS C1s spectra for thin films of as-spin-cast and etched samples. The apparent signal of the carbon in ester group at 289.2 eV is only observed after the removal of PS-rich phase, which indicate that the big PMMA islands have some PS attached.

4.3.1 Near-Surface Phase Separation

4.3.1.1 Confined PS/PMMA phase separation in thin films

Fig. 4.3 shows the as-spin-cast morphologies of the blends at a range of film thicknesses. Instead of forming mainly large PMMA islands as seen in the 151 nm thick films (Fig. 4.2a), in thinner films of 101 nm, the surface of PS/PMMA films shows only small peaks, which should also be PMMA, as confirmed by the phase image, (insert in Fig. 4.3a), with height mainly below 10 nm (Fig. 4.3a). These peaks almost disappear in blend films with thickness around 64 nm (Fig. 4.3b), indicating an increased confinement in lateral phase separation with decreasing film thickness, which has recently been studied in a PS/d-PMMA system [278]. However, in even thinner films (Fig. 4.3c), 31 nm, some pits with depth around 2 nm can be observed. These could be attributed to the

instability induced by a rapid change in solvent-concentration due to the fast solvent evaporation rate at the free surface. In this study, research focused on the mixed-phase films with the three different thicknesses.

Investigating spin-cast PS/dPMMA (50wt%/50wt%) films, Dunbar *et al.* [278] showed that when the film thickness is decreased to a certain value, rather than forming laterally phase-separated domains, a bi-layer structure will be developed with pockets of high dPMMA concentration trapped in the upper PS-rich layer and vice versa. These dPMMA pockets tend to aggregate at the top surface where they will be “frozen” by solvent evaporation or at the interface between the two layers where they could join the d-PMMA layer. This study is in good agreement with the observation that for the film of thickness 101 nm the density of the peaks decreases dramatically with the etching away of the upper PS-rich phase, (compare Fig. 4.3a and a'). Therefore, most of these small PMMA peaks in films around 101 nm thick are PMMA pockets trapped in the upper PS-rich layer, whereas some of them with height around 70 nm after etching, revealed in Fig. 4.3a', are PMMA peaks penetrating through the PS-rich layer. In even thinner films, 64 nm and 31 nm thick, no such localized etching is observed (Fig. 4.3b&b', Fig. 4.3c&c'), suggesting that the lateral phase separation in the bulk has not started and only some PMMA-rich pockets exist. However the increased surface roughness of the corresponding films after etching away the PS-rich material (Fig. 4.3a'-c') indicates some undulations resulting from the instability at PS-PMMA interface.

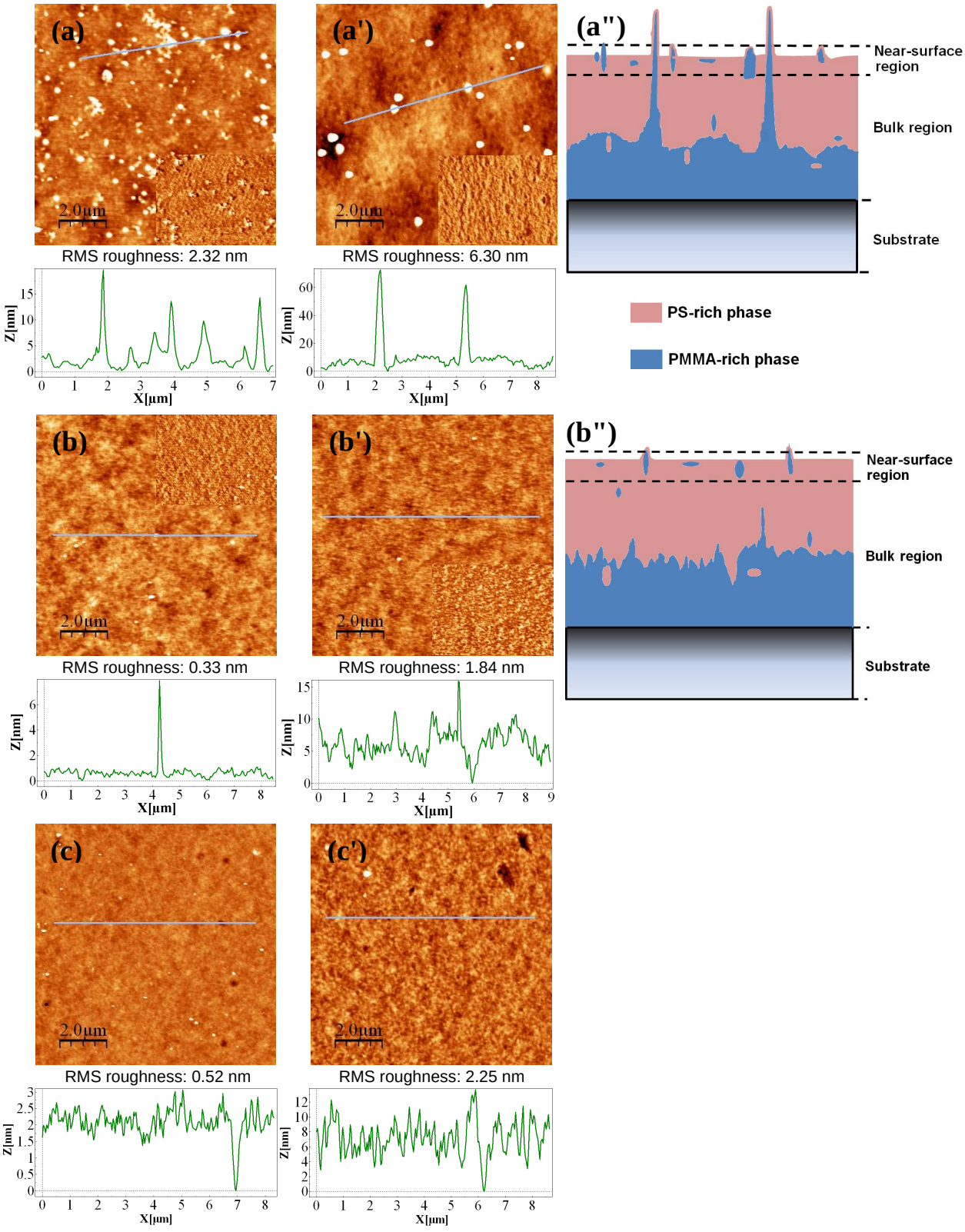


Fig. 4.3 AFM height images of as-spin-cast PS/PMMA films with thickness: (a) 101 ± 9 nm, (b) 64 ± 3 nm, and (c) 31 ± 4 nm, with corresponding images of the film after the removal of PS-rich phase by cyclohexane. (a")(b") are the schematic diagrams of the as-spin-cast structures with thickness around 101 nm and below 64 nm respectively.

Based on the literature and the AFM results, two schematic structures for the as-spin-cast PS/PMMA films are proposed in Fig. 4.3a" and 4.3b" respectively. For the 101-nm film, the as-spin-cast state is at the beginning stage of lateral phase separation with some peaks due to the lateral domains and others to the secondary phase-separated PMMA pockets concentrated at the free surface (Fig. 4.3a"). The as-spin-cast films around 64 nm and 31 nm thick have the structure before the break-up of the bi-layer (the two wetting layers) confirmed by the disappearance of the lateral PMMA peaks in the sample after PS-etching (Fig. 4.3b'&4.3c'). However, PMMA-rich pockets are still expected in the near-surface region (Fig. 4.3b"). The phase separation state of the PMMA-rich pockets is not clear since only a few small peaks were observed (Fig. 4.3b&c). The very surface of the as-spin-cast samples are almost PS covered due to the non-equilibrium phase separation during fast solvent quenching.

4.3.1.2 Bulk phase separation in 151-nanometer films

With a bulky as-spin-cast morphology, any surface changes in the films with thickness around 151 nm become very difficult to distinguish. However, these films gave a good example of PS/PMMA bulk phase separation on annealing as displayed in Fig. 4.4. As a result of the solvent quenching, the spin-cast immiscible polymers are frozen in a non-equilibrium state, which move towards thermodynamic equilibrium upon annealing. For PS/PMMA thin films on a hydrophilic substrate annealed well above the bulk T_g, the mixed films first undergo vertical phase separation with PS wetting the air and PMMA wetting the substrate followed by the dewet of PS on PMMA, first forming holes and a PS network and then PS droplets [211, 222, 232]. This progression can be observed in Fig. 4.4 in the thick films after annealing for 2 hr at temperatures above the bulk T_g.

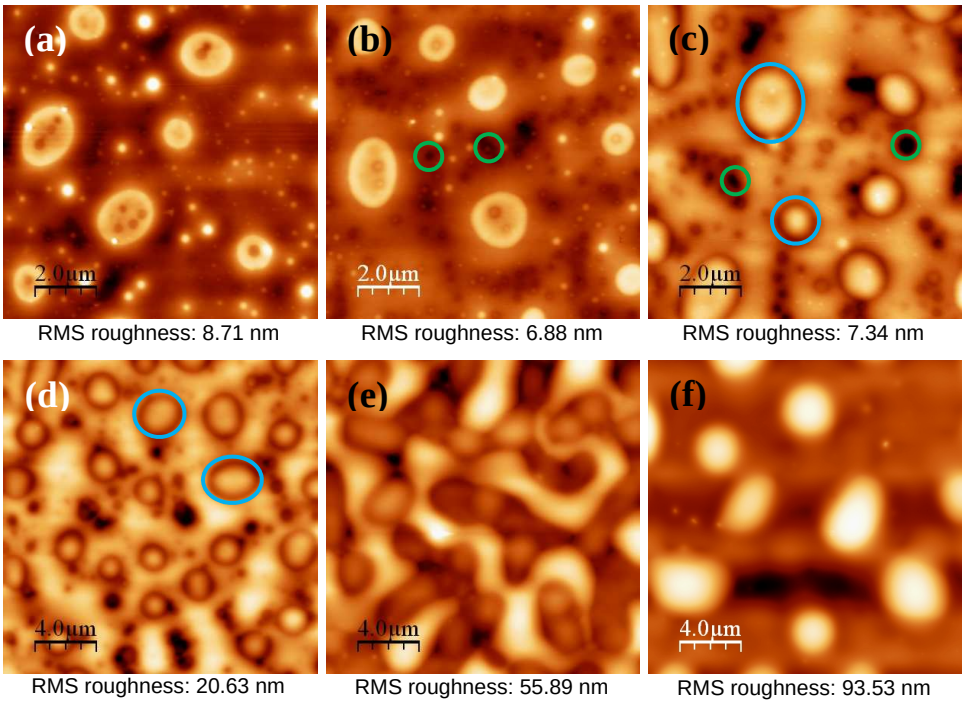


Fig. 4.4 AFM height images showing the phase morphological evolution of PS/PMMA (151 ± 8 nm) on annealing at (a) 130 ℃, (b) 140 ℃, (c) 150 ℃, (d) 160 ℃, (e) 170 ℃, and (f) 190 ℃ for 2 hr.

After 2 hr annealing at 130 ℃, surface undulations were observed in the sample (comparing Fig. 4.4a and 4.2a). Elevating T_a from 140 ℃ to 160 ℃ (Fig. 4.3b-d), the resulting morphologies clearly illustrated how a vertical phase separation takes place: the small PMMA peaks (note that they are small lateral domains rather than the pockets at the surface) sink first leaving pits (green circles in Fig. 4.4b&c) and then the larger islands transform to droplet shape (blue circles in Fig. 4.4c&d) and start to sink. At 170 ℃, a PS network formed through dewetting with PMMA aggregations beginning to "dissolve" in the PMMA-rich phase beneath. When annealed at 190 ℃ for 2 hr, the PS/PMMA bulk phase separation and dewetting has finished leaving PS droplets, with height around 300 nm, distributed on the PMMA layer.

4.3.1.3 Surface phase separation in 64-nanometer films

The evidence for surface phase separation was first found in PS/PMMA films around 64 nm thick after a short, 2 hr, anneal (Fig. 4.5). Pits in the surface were observed after annealing at 130-155 ℃, indicating a surface-phase-separation stage (Fig. 4.5a&b) at

lower annealing temperatures. Bulk phase separation took place (Fig. 4.5c&d) at higher temperatures, e.g. above 160 ℃. This is clearly ma nifested by the dimensional changes in Fig. 4.5e&f. Pits start to appear at 130 ℃ with diameters around 0.5 μm and depth around 1 nm. As the T_a was elevated from 130 ℃ to 155 ℃, only a slight enhancement in the dimensions of the pits was observed (Fig. 4.5e&f). The depth of these pits is less than 8 nm, which indicates that they are confined to the surface regions. By contrast, large dimensional changes take place when the temperature is above 160 ℃, which can be attributed to the bulk-phase-separation stage.

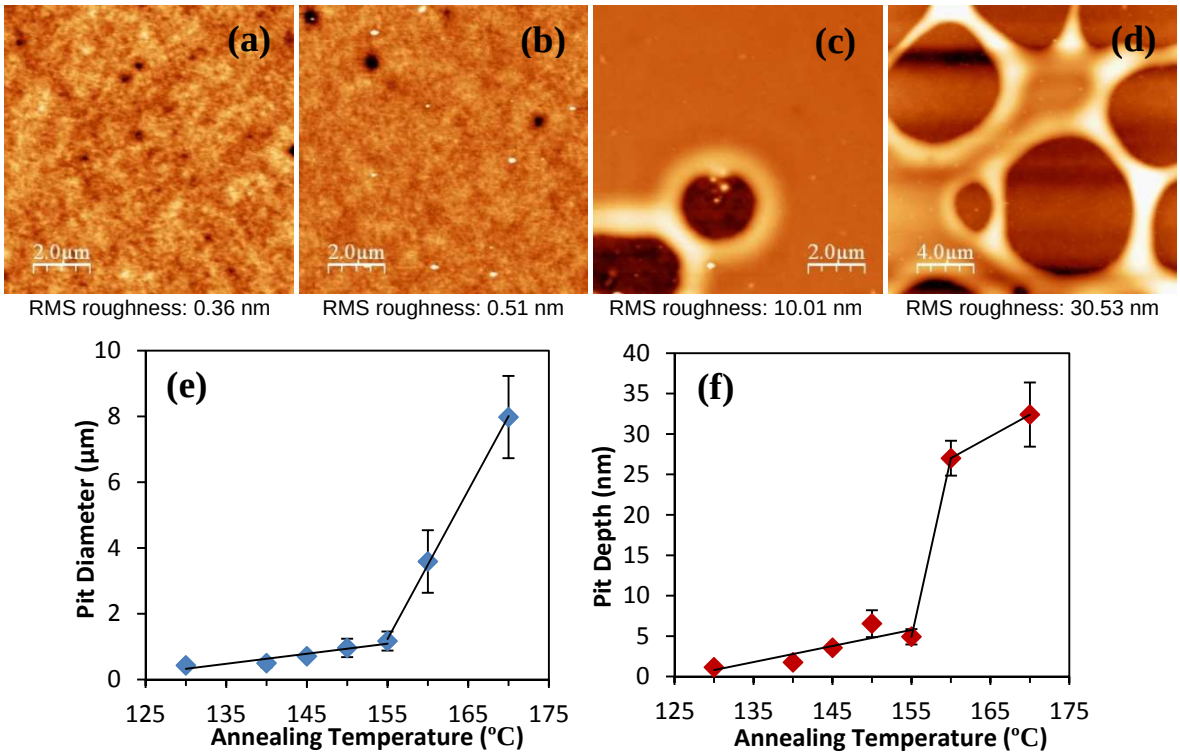


Fig. 4.5 Pit growing in PS/PMMA films (64 ± 3 nm) annealed at different temperatures for 2hr revealed by AFM height images: (a) 140 ℃, (b) 150 ° C, (c) 160 ℃, and (d) 170 ℃. (e) and (f) display the diameter and depth of these pits, respectively, as a function of annealing temperature.

These pits in the surface are attributed to the phase separation and dewetting between PS and PMMA confined to the more mobile near-surface region (Fig. 4.3b"), while the large dimensional changes are the result of the bulk phase separation of the whole film. The number of these pits, however, does not increase with increasing temperature possibly due to the heterogeneous distribution of the PMMA pockets in the near-surface

regions and their small proportion in the near-surface region layer.

Since the molecular weights of both polymers are over their characteristic molecular weights (W_c), which are 35k and 31k for PS and PMMA respectively [279], the entanglement of both polymers cannot be neglected. With increased annealing time, polymer chains have more time to arrange themselves and diffuse. Thus, phase separation can be observed at much lower temperatures. For 128 hr annealing, pits associated with near-surface phase separation with dimensions close to that of pits found in samples after 2 hr annealing at 140 ℃ appear at 80 ℃ (Fig. 4.6a). This onset of phase separation at the surface occurs at a temperature much lower than the bulk T_g of both polymers (105.8 ℃ for PS1, 113.6 ℃ for PMMA). Thi s is attributed to the much lower T_g in the surface region, which allows chain motion and phase separation in surface regions when the polymer chains in the bulk are still in the glassy state.

When the T_a increased from 90 ℃ to 100 ℃ at this longer anne aling time, rather than forming pits with enlarged dimensions as happened when T_a was elevated from 80 ℃ to 90 ℃ (profiles in Fig. 4.6a&b), undulations of sev eral nanometres height fluctuation (Fig. 4.6c) occurred showing a spinodal pattern. The pits indicate the phase separation in limited surface regions with a clear phase boundary, while the undulations indicate stress relaxation in near-surface regions. Since 100 ℃ is still below the bulk T_g of both polymers, the restriction from the glassy bulk layers beneath contributes much to the pattern formation. An interesting point is that the surface undulation here is very similar to the spinodal dewetting reported for low molecular weight PS (4k) thin films on a silicon substrate when the film thickness is below 10 nm [280]. This implies that for this near-surface PS-rich phase these undulations are the origin of dewetting in such systems, which agrees well with Tolan *et al.*'s work on polyethylene-propylene thin films [281]. Annealing at this temperature also revealed peaks with height of a few nanometres (within the green circle in Fig. 4.6c), which should be the PMMA pockets either from within the surface regions of as-cast films, or generated through surface phase separation.

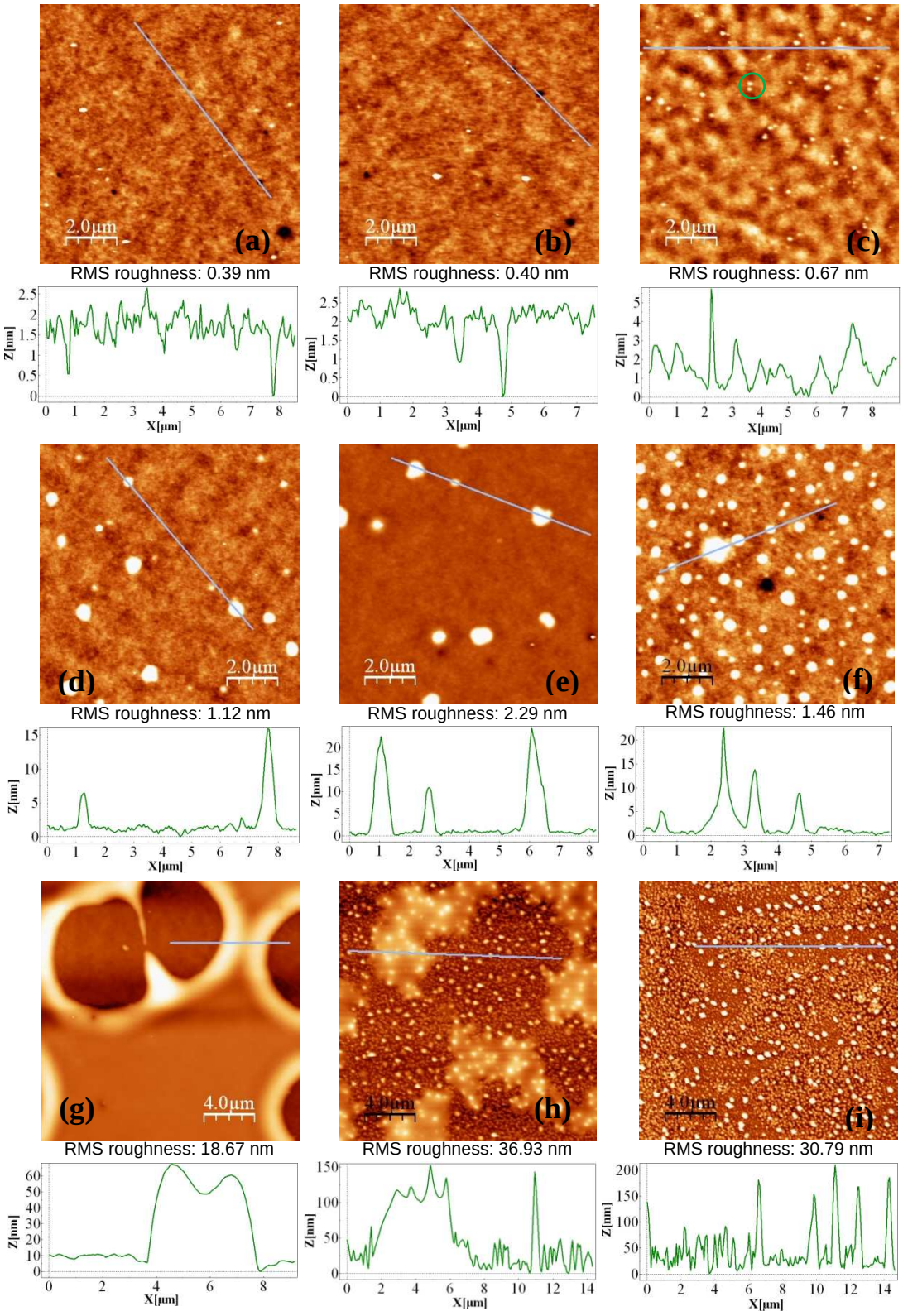


Fig. 4.6 AFM height images showing phase separation of PS/PMMA films (64 ± 3 nm) after annealing at (a) 80 ℃, (b) 90 ℃, (c) 100 ℃, (d) 110 ℃, (e) 120 ℃, (f) 130 ℃, (g) 140 ℃ and (h) 150 ℃ for 128 hr, with corresponding height pr ofiles; (i) Morphology after the removal of PS by cyclohexane of a sample annealed at 150 ℃ for 128 hr.

From 110 °C to 130 °C, phase separation developed through a nucleation and growth mechanism forming aggregations (Fig. 4.6d-f). Aggregations generated at 110 °C (Fig. 4.6d) are considered to be a near-surface phenomenon since the temperature is merely between the bulk T_g of PS and PMMA and the heights of these aggregations are only around 10 nm. XPS of the PS/PMMA film annealed at 110 °C for 128 hr showed no increase in PMMA concentration at the surface compared to the as-spin-cast sample (Fig. 4.7). Therefore, the aggregations appear to be PS or PS covered. Considering the large aggregations of PS on the substrate-wetting PMMA layer (Fig. 4.4f) developed through bulk phase separation and dewetting of the PS/PMMA thin films [211, 222, 232], it is then probable that these aggregations are the result of phase separation and the PS dewetting in the near-surface region.

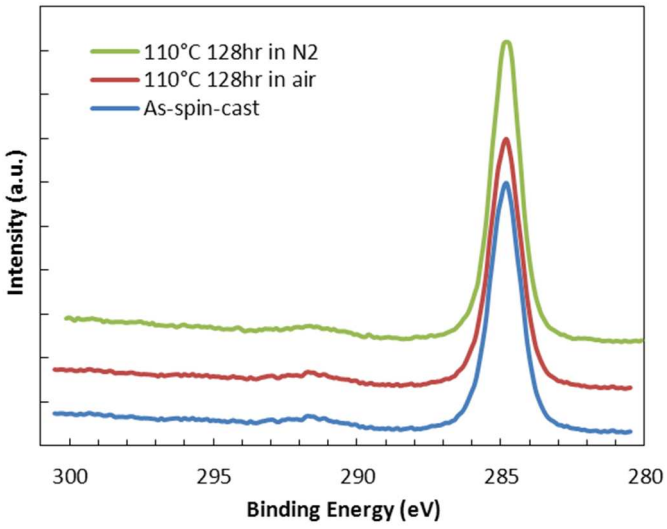


Fig. 4.7 XPS C1s spectra for thin films of as-spin-cast PS/PMMA films (64 ± 3 nm) and samples annealed at 110 °C for 128 hr in air and in nitrogen respectively. All the samples show a typical C1s spectrum of PS: a main hydrocarbon (C−C/C−H) peak at binding energy of 284.8 eV and π−π* shake-up satellites at shifts of 6-8 eV from the hydrocarbon peak.

The aggregations developed at higher temperatures, 120 °C and 130 °C, however, are due to bulk phase separation. As no small PMMA pockets were found in these films with (annealing induced) bulk aggregations, e.g. annealed at 120 °C (Fig. 4.6e), they are most likely to play the role of nuclei in the aggregation-forming process. Given the conclusions

above, we may conceive that the bulk aggregations over tens of nanometres have a core-shell structure: PMMA inside and PS outside. This has been confirmed by the increased height of the aggregations after cyclohexane etching. The increased density of the aggregations in the sample annealed at a higher temperature, 130 ℃, is attributed to an increased density of nuclei, which is very likely to result from the enhanced bulk mobility of the system at a higher temperature.

When the T_a reaches 140 ℃, typical bulk phase separation and dewetting occur forming holes with depth around 40 nm (Fig. 4.6g) and, with even higher temperature, PS islands were observed (Fig. 4.6h). Cyclohexane etching proved that these islands are PS, while the small peaks both penetrating through the PS islands and outside them are PMMA (Fig. 4.6i). The formation of the peaks seen in Fig. 4.6h, some of which are over 100 nm high, might be explained by PMMA crystallization after long time annealing, as DSC indicated some crystallinity of the original PMMA (Fig. 4.8, only in the 1st heating trace). The formation of peaks of PMMA on annealing was also confirmed in pure PMMA films with a similar thickness, around 62 nm. Fig. 4.9 shows that a two-hour anneal at 180 ℃ allows the generation of peaks around 10 nm high in PMMA films. Numerous peaks were also found in the PMMA film annealed at 160 ℃ for 96 hr. In this case, the density of peaks is much greater. However, after this long annealing at high temperature, only a few peaks have heights of tens of nanometres, while most are below 10 nm, implying that crystal growth is limited.

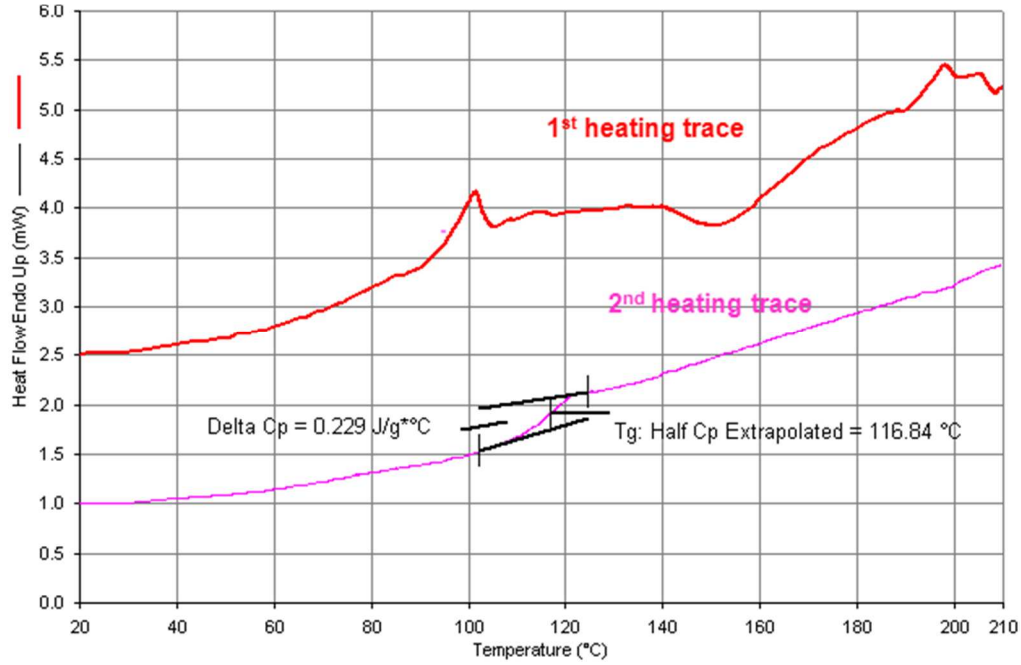


Fig. 4.8 DSC traces of PMMA with a scan rate of 50 ℃/min. Procedure: hold for 5 min at 0 ℃, heat from 0 ℃ to 210 ℃ at 50 ℃/min, hold for 1 min at 210 ℃, cool from 210 ℃ to 0 ℃ at 50 ℃/min; and then repeat.

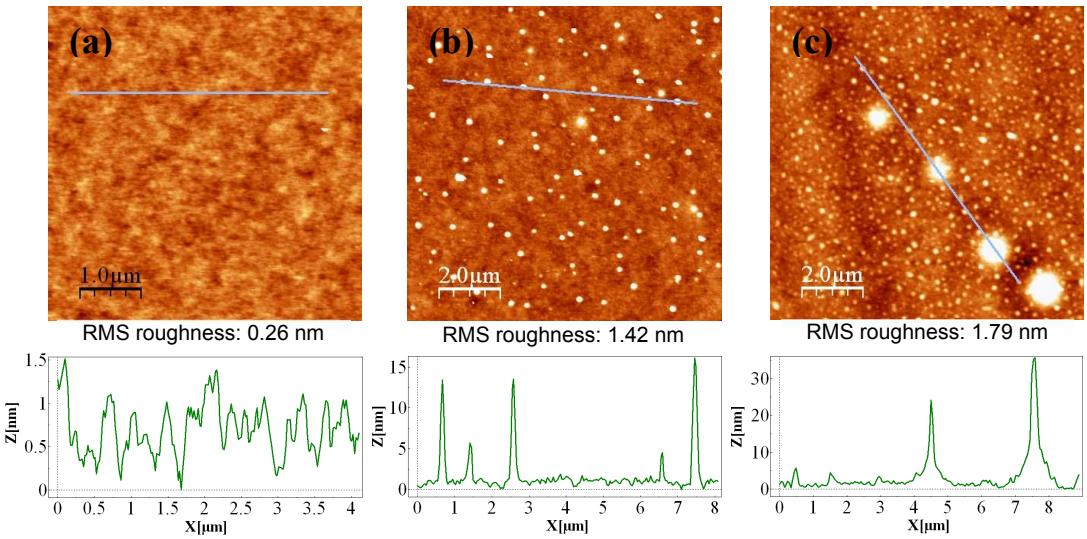


Fig. 4.9 AFM height images of PMMA films (62 ± 3 nm) annealed at: (a) 160 °C for 2 hr, (b) 180 °C for 2 hr, and (c) 160 °C for 96 hr, with corresponding depth profiles beneath.

Since repeating experiments of PS/PMMA annealed at 110 °C for 128 hr in a nitrogen environment (Fig. 4.10) showed similar aggregations to that annealed in air (Fig. 4.6d), GPC indicated only small changes in molar mass distribution (Appendix 1, Table A1), and XPS revealed a similar surface composition (Fig. 4.7), one can be confident that oxygen

has little effect on our results and the aggregations are not due to low molecular weight chains from polymer degradation.

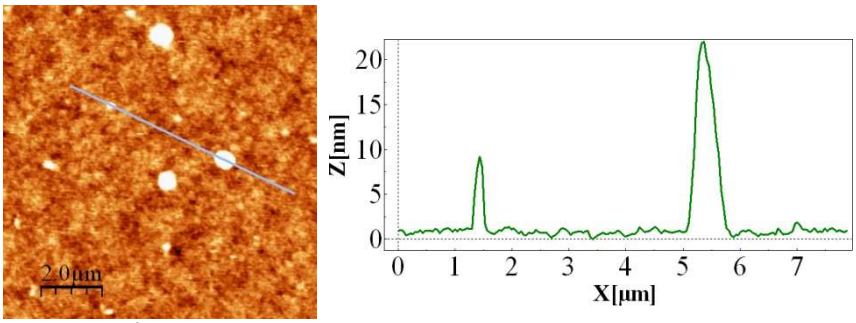


Fig. 4.10 Phase separation of PS/PMMA films (64 ± 3 nm) after annealing at 110 ℃ for 128 hr at a nitrogen environment (in a glove box). A different hotplate was involved and the actual T_a was slightly lower than 110 ℃ according to calibration .

4.3.1.4 Thickness and substrate effects

Although the as-spin-cast samples with different film thicknesses exhibit various surface morphologies (Fig. 4.3a-c), the phase separation stages of films with different starting points show the same behaviour after annealing (128 hr) as summarized in Fig. 4.11a: surface pits, surface undulations and aggregations, bulk aggregations and then bulk phase separation and dewetting. Distinct surface phase separations occur at lower temperatures (green region), while bulk phase separations at higher temperatures (red region).

With film thicknesses decreasing from 101 nm to 31 nm, the temperature for the onset of surface pits stays constant at 80 ℃. This confirms that the surface layer is independent of the confinement induced by the film thickness. Of course, if the film is extremely thin, this free surface may disappear, with all chains influenced by the underlying substrate, resulting in a higher temperature required for chain movement. A typical example is the increase in the starting temperature for surface-specific crystallization [27]. In the case of the PS/PMMA thin films, phase separation in the as-spin-cast films was observed when the film thickness was around the $2R_g$ of PS and PMMA (Fig. 4.12), and so the

surface-specific phase separation behaviour of these very thin films could not be observed.

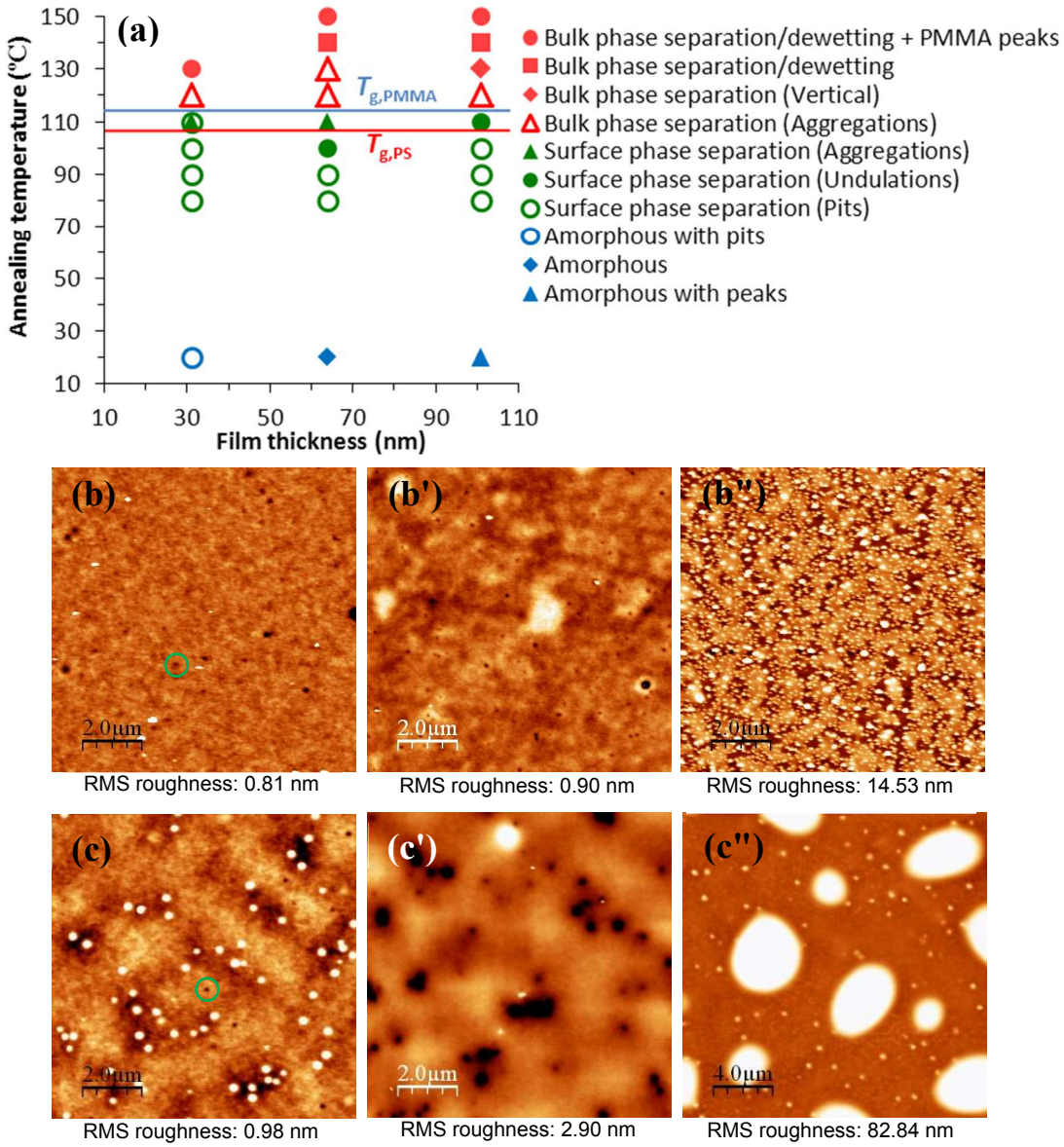
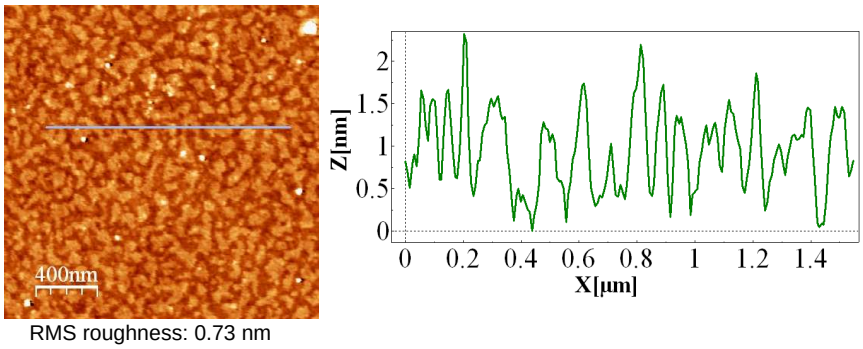


Fig. 4.11 Phase map of PS/PMMA films with different thicknesses annealed at different temperatures for 128hr (a) together with the AFM height images of some typical examples: films around 31 nm (b) 80 ℃, (b') 110 ℃ and (b") 130 ℃ ; films around 101 nm (c) 90 ℃, (c') 130 ℃ and (c") 150 ℃. (The images of the 64 nm films are in Fig. 4.6) Distinct surface phase separations occur at lower temperatures (green region), while bulk phase separations at higher temperatures (red region).



RMS roughness: 0.73 nm

Fig. 4.12 As-spin-cast morphology of a PS/PMMA film with a thickness of 16 ± 2 nm.

Examples showing the annealing induced surface pits in films with as-spin-cast pits and with as-spin-cast peaks are given in Fig. 4.11b and 4.11c respectively. When the surface pits are first generated (an example of which is circled in Fig. 4.11b), their dimensions are smaller than any pits seen in the as-spin-cast films (31 nm) (Fig. 4.3c), and hence could be distinguished. The surface pits in the film (101 nm) with as-spin-cast peaks (circled in Fig. 4.11c) are easy to recognize, but with smaller dimensions compared to the pits formed in thinner films without as-spin-cast peaks (Fig. 4.6b) with the same annealing conditions.

Annealing at temperatures below the bulk T_g of both polymers leads to surface phase separation in the form of pits, while annealing at temperatures around bulk T_g of PS, below bulk T_g of PMMA, allows surface segregations in the form of undulations and aggregations. This transition is attributed to the enhanced chain mobility, especially of PMMA, and disentanglement with elevated temperature in the near-surface regions. However, it is possible that there is an overlap between the different surface behaviours. A typical example is the 31 nm film annealed at 110 °C for 128 hr (Fig. 4.11b'), where both surface pits and surface segregations are observed. The segregations here are actually an interplay of the undulations and aggregations (several nanometres height). Bulk phase separation is limited to the temperatures above the T_g of both polymers.

In contrast to the surface phase separation, bulk phase separation of the whole film is strongly affected by film thickness. In the beginning stage of bulk phase separation,

annealing at 120 ℃, films with different thickness all show an aggregation-forming process. However, as the temperature is increased to 130 ℃, mixed films of thickness around 31 nm already show phase separation and dewetting together with PMMA peaks (Fig. 4.11b''), while similar processes in thicker films require a temperature around 150 ℃ (Fig. 4.6h&4.11c''). This is mainly on account of the fact that, on annealing, PS/PMMA phase separation is essentially dominated by the interfacial energies: polymer-air, polymer-polymer and polymer-substrate [32, 222]. A hydrophilic substrate would promote the formation of a PMMA wetting layer at the polymer-substrate, hence, direct the phase evolution [239, 282]. Thus, with decreased film thickness, instead of having an elevation in bulk-phase-separation temperature induced by confinement, the temperature required for bulk phase separation drops as the substrate effects become significant. Also, it could be observed that the density of PMMA peaks increases with decreased film thickness (Fig. 4.11c'', 4.6h&4.11b''). This implies that these PMMA peaks, arising from the PMMA layer at the polymer-substrate, are substrate-promoted as well. In addition, the bulk phase separation processes of PS/PMMA films (101 nm thick) with PMMA peaks in the as-spin-cast morphology (Fig. 4.3a) are slightly different and more like that in even thicker (152 nm) films (Fig. 4.2a). Before the dewetting of PS from PMMA, there is a vertical phase separation with PMMA aggregations sinking from the upper PS-rich layers leaving pits, which occurs around 130 ℃ for 128 hr anneali ng (Fig. 4.11c').

More results of surface and bulk phase separation in these PS/PMMA films as a function of annealing time are summarized in the phase maps in Fig. 4.13. As in Fig. 4.11a, the green regions in these maps stand for the surface phase separation and dewetting region, while the red regions for bulk phase separation. It can be clearly observed here that, with sufficient annealing time (128 hr), phase separation in the near-surface regions could occur even at a temperature more than 20 K below the bulk T_g of PS. This arises from enhanced mobility of polymer chains at the free surface and allows phase separation specifically limited to the near-surface region.

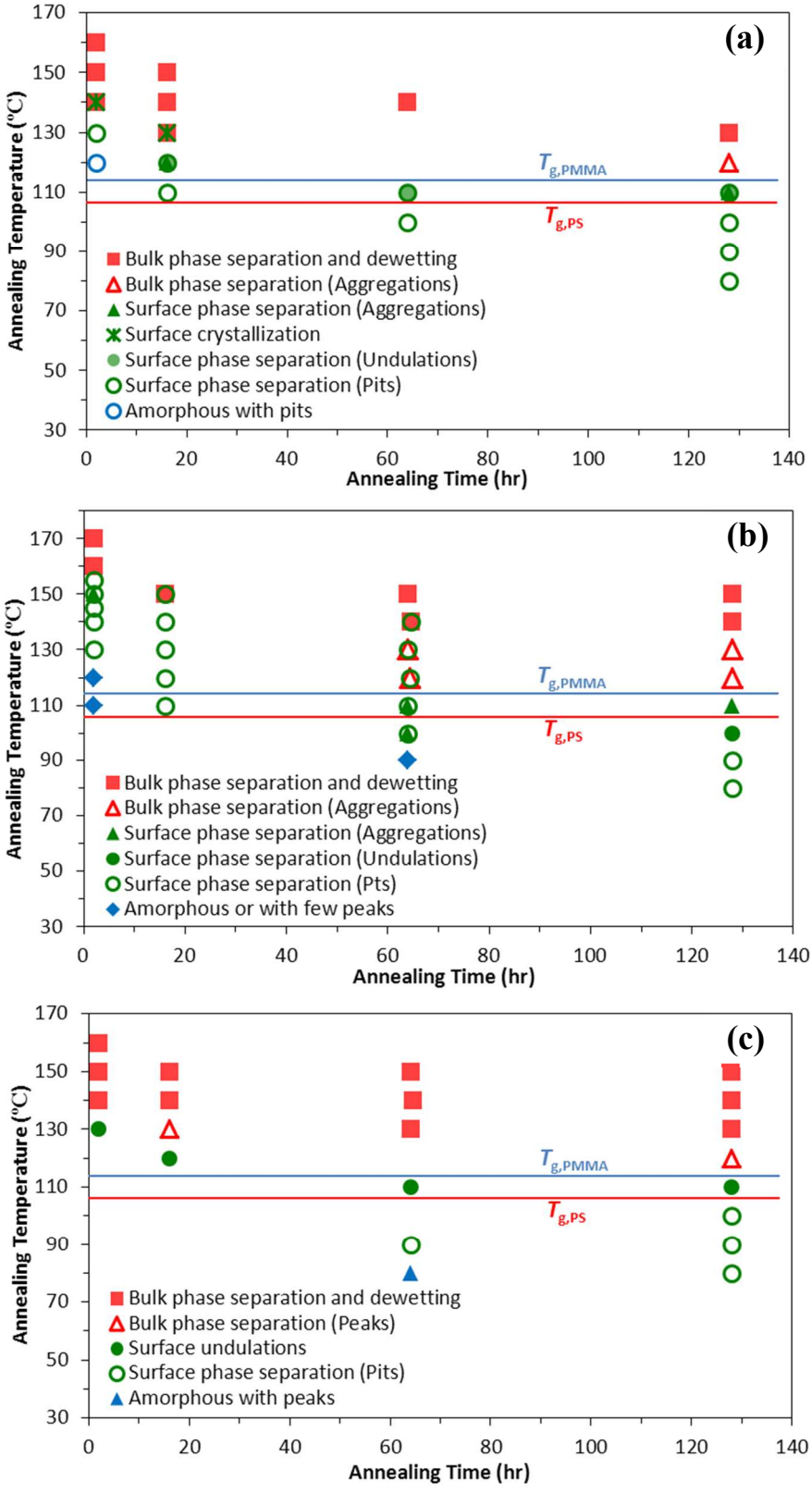


Fig. 4.13 Phase maps of PS/PMMA films: (a) 31 ± 4 nm thick with as-spin-cast pits (Fig. 4.3c), (b) 64 ± 3 nm thick with homogeneous as-spin-cast surface (Fig. 4.3b), and (c) 101 ± 9 nm thick with as-spin-cast peaks (Fig. 4.3a). The green region stands for the near-surface phase separation.

In the case of PS/PMMA (50/50 wt/wt) mixture films, the initial surface phase separation tends to appear in the form of pits, whereas phase separation and dewetting dominate the bulk-phase-separation stage. A coexistence of surface and bulk behaviours may be found, (mostly in samples with shorter annealing time), a typical example of which is displayed in Fig. 4.14 showing a pit with depth of a few nanometers from surface phase separation and a hole around 30 nm depth from bulk phase separation and dewetting. This is mainly attributed to the slow bulk phase separation due to the entanglement of polymer chains.

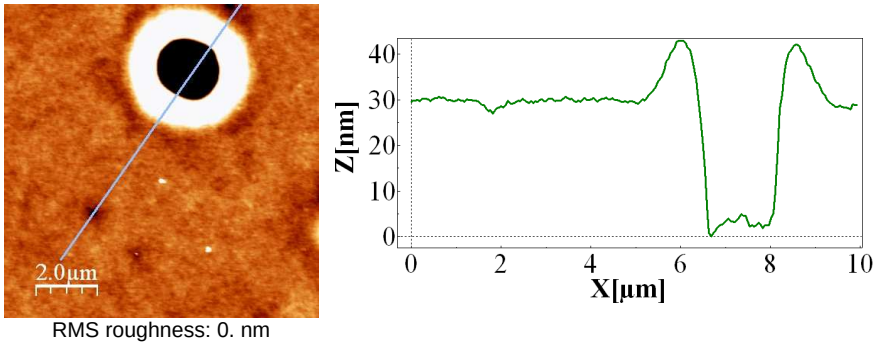


Fig. 4.14 A PS/PMMA film (64 ± 3 nm) annealed at 140 °C for 64 hr show a pit and a hole from surface and bulk phase separation and dewetting respectively.

Another interesting result is that, some indications for surface crystals were observed in the 31 nm films annealed at 140 ℃ for 2 hr and 130 ℃ for 16 hr, as displayed in F ig. 4.15. These narrow ridges are a few 100 nm long with height around 10-15 nm. Given these dimensions they are very likely to be the new-born crystal lamellae. As the pure PMMA films are only able to form some peaks at a higher T_a (Fig. 4.9), e.g. over 160 ℃, these ridges are assigned to PS crystallization. However, no similar “surface crystals” were found in other PS/PMMA samples prepared using the same PS and PMMA. A possible explanation is the low crystallinity of the system: since, any initial nuclei that are formed might contribute directly to the phase separation, hence, the chance of forming lamellae crystals is low. This agrees well with the promotive effect of crystallization on phase separation discussed in section 4.3.2.2.

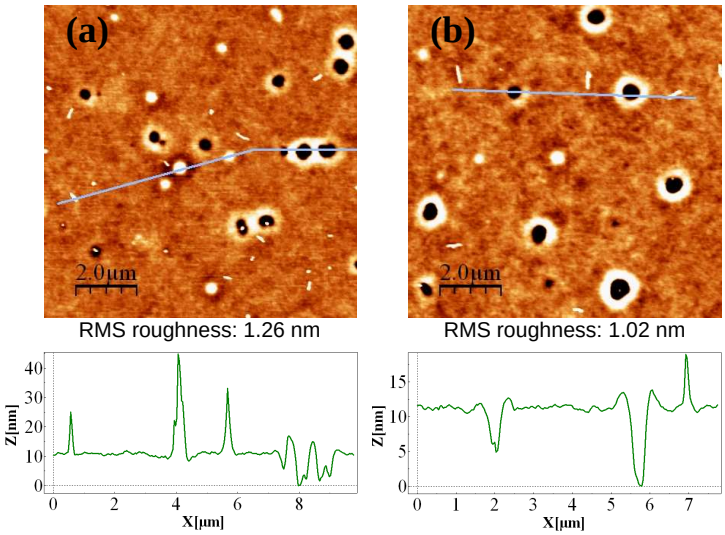


Fig. 4.15 AFM height images of PS/PMMA films (31 ± 4 nm) annealed at (a) 140 °C for 2 hr and (b) 130 ℃ for 16 hr. Indications for surface crystals are presented.

4.3.2 Effects of Crystallization

For polymers with bulky side groups, e.g. PS, crystallizability depends heavily on the tacticity of the polymer chains. Although the PS used in this project has controlled molecular weight, the tacticity of PS possibly varied between batches resulting in different crystallizability. In this section, results from samples involving higher crystallinity PS (PS2), which is likely a result of isotactic or syndiotactic blocks in the chains, are discussed. All the films investigated have as-spin-cast thickness around 64 nm.

4.3.2.1 Crystallization in PS films

- *Surface crystallization and crystalline aggregation*

The crystallization of the PS was confirmed directly by the observations of surface crystals in thin films of pure PS2. Two hours of annealing was shown to be a suitable period for investigation of surface crystallization in polyesters [28]. In PS/PMMA samples annealed at 110 ℃ for 2 hr, aggregations with height less than 10 nm were discovered (Fig. 4.16b). This is believed to be the initial stage of PS crystallization, most likely forming in the near-surface region since the annealing temperature is only just above the bulk T_g of PS. A few big peaks with height over 70 nm were also found, which are attributed to the easy crystallization or aggregation around the as-spin-cast features, the white dots in Fig. 4.16a. When T_a increased to 120 ℃, some irregular aggregations (or crystals) could be observed (Fig. 4.16c). They have height around 8 nm and should be the initial stage of typical surface-specific crystals as they were observed in different areas of the sample rather than the features due to the as-spin-cast morphology. Still clearer “irregular” surface-specific crystals were generated at 130 ℃ with a similar height (Fig. 4.16d). Again, there are also peaks tens of nanometres height observed, assigned to the nuclei of crystalline aggregations from the as-spin-cast features. At a slightly enhanced T_a, e.g. 135 ℃ (Fig. 4.16e), instead of forming advanced surface crystals, only bulky peaks, around 50 nm high, were observed. A similar situation has also been found in a sample

annealed at 130 ℃ for extended time, e.g. 65 hr (F ig. 4.16f).

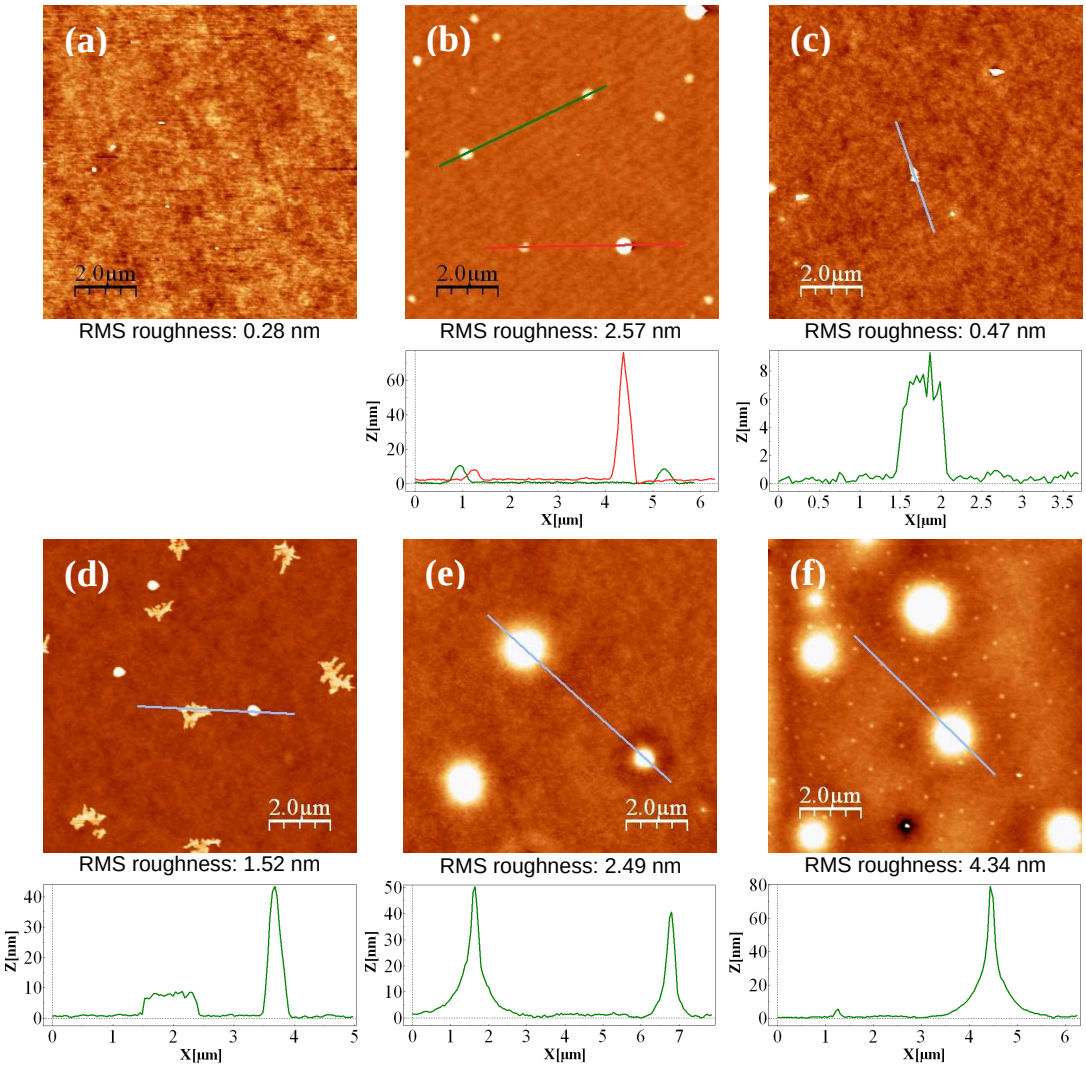
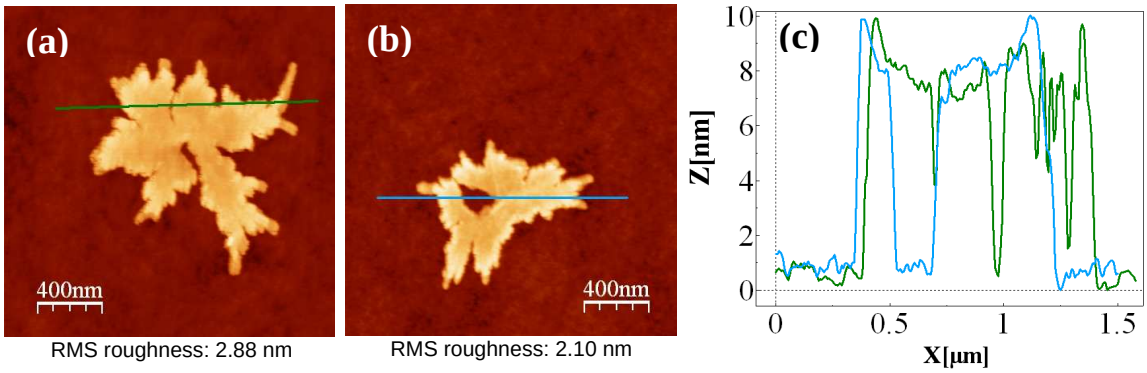


Fig. 4.16 Morphological development of PS films (66 ± 3 nm) on annealing. (a) as-spin-cast, (b) 110 °C 2 hr, (c) 120 °C 2 hr, (d) 130 °C 2hr, (e) 135 °C 2 hr, and (f) 130 °C 65 hr.

The AFM results displayed in Fig. 4.16 clearly suggest that, as expected for all crystalline polymers, crystalline PS is able to form surface-specific crystals as well as crystals in the bulk. In PS, surface crystallization can only apparently occur in a very narrow temperature range, even narrower than that observed in polyesters [28]. In polyesters, the onset of surface-specific crystallization was observed at temperatures around the bulk T_g (significantly lower than the onset of bulk crystallization). For 2 hr annealing, the onset temperature for PS surface crystallization, around 130 ℃, is much higher than the bulk T_g of PS (99.3 ℃), perhaps due to the bulky side grou ps limiting chain mobility, meaning that

the 2 hr annealing time was insufficient for surface-specific crystals to form at lower temperatures. However, Fig. 4.16f shows that longer annealing times at 130 ℃ allows the formation of the large aggregates, leaving no trace of any surface crystals formed after 2 hr annealing, even in the spaces between the large aggregations. Moreover, this surface crystallization of the PS was not observed in all samples imaged. The tendency to form crystalline aggregations is more prevalent in samples than clear surface crystallization, which is confirmed, for example, by the observation of crystalline aggregations at a lower T_a, 110 ℃, and the bulky aggregations that easily de veloped at different annealing temperatures after different annealing times (e.g. Fig. 4.16e&f). This is possibly due to the high surface energy of the crystal's fold surface (the surface of the flat-on PS crystals). The tacticity of the PS is uncontrolled, which means there will be a variation in crystallinity between different samples. It is probable that regions with only short sections of stereoregular PS tend to produce crystalline aggregations rather than surface crystals on annealing, whereas a greater length of ordering is required to produce the well-defined morphologies of the surface-specific crystal lamellae. This explains why no such apparent surface crystals displayed in Fig. 4.16d were found in the lower-crystallizability PS (PS1) discussed in section 4.3.1. Another possible reason for the variability between samples is the variation of "impurities" (e.g. catalyst residues, surfaces, and low molar mass PS chains) or nano-particles in as-spin-cast films. The nuclei for flat-on PS surface crystals are assigned to a pseudo-homogeneous nucleation where "impurities" interact weakly with PS, while the crystalline aggregations are developed through a heterogeneous nucleation arising directly from "impurities".

- *Diffusion-limited surface crystallization of PS*



RMS roughness: 2.88 nm RMS roughness: 2.10 nm

Fig. 4.17 Morphology of PS surface crystals with corresponding depth profile.

Examples showing details of the PS surface crystals are presented in Fig. 4.17. In contrast to PET, PEN, PVOH and PA12 and 6 films (tens of nanometres thick), where surface-specific crystals appear to be edge-on crystals in the forms of lamellar sheaves or 2D spherulites, the PS surface crystals appear in the shape of compact seaweed, a typical flat-on structure. The flat-on crystal structure normally exists in an ultrathin film or a monolayer, where the diffusion of polymer chains is significantly limited [126]. Therefore, the surface crystallization in PET, PEN, PVOH and PA thin films is surface-nucleation controlled, while the surface crystallization of PS is a diffusion-limited process, perhaps due to the low concentration of stereoregular sequences in the sample. Fractal seaweed shaped crystals with much larger size (several microns) has been reported previously in an iPS film around several nanometres (below the lamellar thickness, around 8 nm) thick after melting and recrystallization at 180 ℃ [168], Fig. 2.22. Simulating the growth of diffusion-limited aggregation, Tao *et al*. [283] concluded that a compact growth shape would be formed in the early stages and a fractal shape would be formed at a later stage. This indicates that the PS surface crystals obtained here are at the early stage of crystallization and would have the potential to grow into fractal crystals if sufficient crystallisable material could diffuse to the growth front. Also, the comparison implies that this PS surface crystallization, as displayed in Fig. 4.17, is limited to a near-surface layer with thickness less than the lamellar thickness, 8 nm (Fig. 4.17c). In this case, as

suggested by Taguchi *et al*. [168], the diffusion rate of PS chains is affected by entanglement, which means that if the degree of entanglement is too high, surface crystallization is restricted and crystalline aggregation become a better choice. That is in good agreement with the observation that surface crystallization does not apply to all PS samples. Although, the effects of entanglement on surface crystallization in other polymers, e.g. PET, PEN and PVOH, are not clear, the results on PS discussed above indicate an upper limitation to degree of entanglement for surface crystallization. The irregular growth shape of the PS crystals (Fig. 4.16d&4.17a&b), however, indicates a relatively high anisotropy of surface tension.

4.3.2.2 Effects of PS crystallization on PS/PMMA phase separation

Using the higher-crystallizability PS (PS2), the morphology of PS/PMMA films on annealing could be different, however, since the surface T_g of the polymers remains similar, a comparable development of phase separation from surface to bulk as discussed in section 4.3.1 might be expected. This is confirmed by the morphological evolution of these films annealed at different temperatures for 2 hr (Fig. 4.18): surface pits at lower T_a and bulk phase separation and dewetting at higher T_a, which is consistent with the results of mixtures with lower-crystallinity PS (Fig. 4.5).

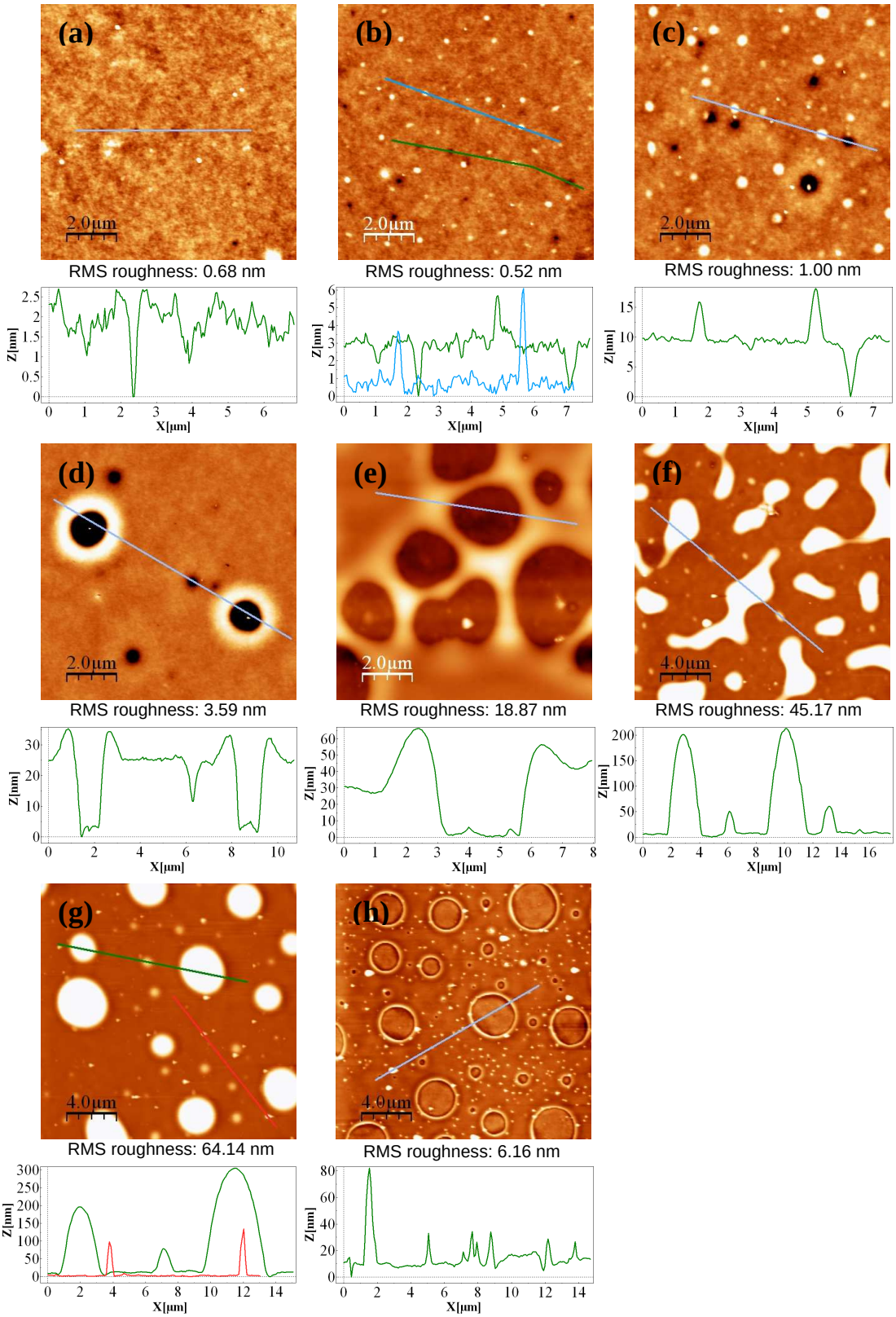


Fig. 4.18 Crystallization associated phase separation in PS/PMMA films annealed at different temperatures for 2 hr: (a) 130 ℃, (b) 140 ℃, (c) 150 ℃, (d) 155 ℃, (e) 160 ℃, (f) 170 ℃, and (g) 190 ℃. (h) is the morphology of (g) after the removal of PS by a 10-min cyclohexane etching.

Height profiles in Fig. 4.18 show that when T_a is elevated from 130 ℃ to 140 ℃, the depth of the pits has only a slight increase approximately from 2 nm to 3 nm, while the depth value reaches 10 nm when T_a increases to 150 ℃, which is recognized as the transition point between surface and bulk behaviours. As T_a continues to increase, from 155 ℃ to 190 ℃, bulk phase separation and dewetti ng of PS/PMMA takes place forming dewetting rings (Fig. 4.18d), PS network (Fig. 4.18e) and islands or droplets (Fig. 4.18f&g) (The PS contribution is proved by solvent etching, Fig. 4.18h). In addition to the growth of pits, the generation of crystalline-aggregates was observed during the surface phase separation, which is believed to be surface crystallization: a special form of phase separation. These aggregations appear when T_a is around 140 ℃ and have heights of a few nanometres (Fig. 4.18b). The origin of these surface aggregations is assigned to the PS crystallization as, for 2 hr annealing, a pure PMMA film with similar thickness needs a T_a of around 180 ℃ to produce such aggregations (Fig . 4.9b).

Comparing the results in Fig. 4.5 and 4.18, it can be found that, with the higher-crystallizability PS, the PS/PMMA phase separation (especially the bulk phase separation) is promoted, with similar morphologies observed at around 10 K lower temperatures for the PS2/PMMA mixture than the PS1/PMMA mixture. This is because of the lower T_g of the PS2, and the PS2 chains with higher regularity (crystallizability) have a higher self-aggregation ability. Meanwhile, hindered by PMMA chains, the T_a required for the onset of PS crystallization increases dramatically in the blend, from roughly 110 ℃ in the pure PS2 sample (Fig. 4.16b) to 140 ℃ (4.18b) for the PS2/PMMA blend. Also, in the mixtures, the diffusion distance of PS chains in the near-surface region is further decreased, hence, no PS flat-on surface-specific crystals were observed on annealing.

Phase separation in the PS/PMMA films containing the higher-crystallizability PS proves that although crystallization may change the morphology of phase separation, e.g. a more obvious formation of aggregations, the blend is still able to show surface phase behaviour at lower T_a and bulk phase behaviour as T_a is increased. The free surface effect is still

applied to the situation where crystallization and phase separation interplay.

- *Bulk aggregations on annealing*

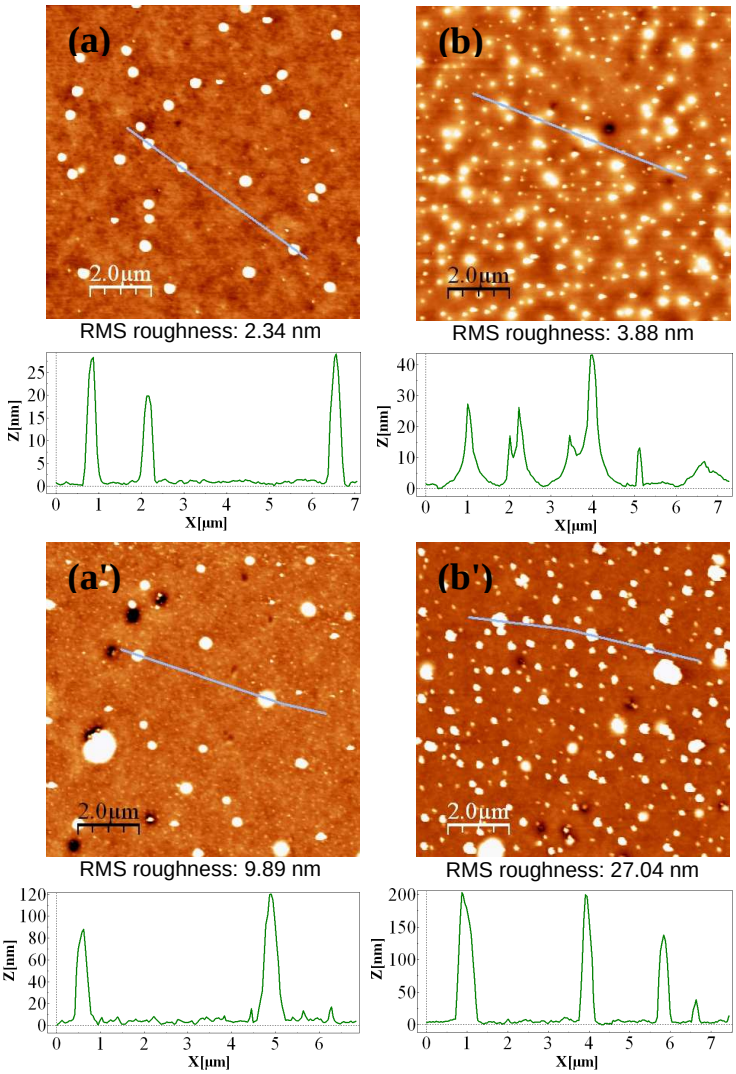


Fig. 4.19 PS/PMMA films (with the higher-crystallinity PS) annealed at 130℃ for (a) 3 hr and (b) 64 hr; corresponding images of samples after immersion in cyclohexane for 10 min (a'&b').

Since 130 ℃ is about 20 K higher than the bulk T_g of the two polymers, rather than showing surface phase separation after a 2 hr anneal (Fig. 4.18a), sufficient annealing at 130 ℃ can lead to bulk aggregation (or peak) formi ng in the blends containing high crystallizability PS (Fig. 4.19a&b) as in the case for the lower crystallizability materials (Fig. 4.6f&4.13b). Numerous aggregations were generated after a 64 hr anneal (Fig. 4.19b).

In contrast to the surface aggregations, the bulk aggregations involve both PS and PMMA. This is revealed by the film morphology after immersion in cyclohexane for 10 min (Fig. 4.19a'&b''). Depth profiles show that aggregations with greatly increased dimensions remained after etching. Comparing the morphologies before and after etching, it could be concluded that bulk aggregation at 130 ℃ involves a lateral phase separation forming PMMA aggregations, either crystalline or not, penetrating through the PS rich layer, reminiscent of the PMMA aggregations in thicker as-spin-cast films (Fig. 4.2a&4.3a). Thus, these bulk aggregations have PMMA inside and PS outside. The dimensions of the peaks after solvent-etching are actually larger than expected. This might be due to the swelling of residual PS chains as some of them might firmly attach to PMMA phase through entanglement. The swelling of PMMA in cyclohexane is also possible, but the degree of such swelling should be very small in 10 min.

- *Surface crystals in PS/PMMA films*

Occasionally, some typical surface crystals were observed in a PS/PMMA film annealed at 90℃ for 65 hr, examples of which are exhibited in Fig. 4.20a&b. These 2D crystals are mainly in the form of lamellar sheaves or fibrils (ridges) with thickness around a few nanometres (Fig. 4.20a''&b''). Since surface crystals have only been observed in PS films, it is very likely that these surface crystals are PS crystals as well. Again, this surface crystallization is not observed in most of the PS/PMMA films.

The generation of these surface crystals indicates a relatively high mobility of polymer chains, even higher than that in the near-surface region of a pure PS film, where under a similar annealing condition, only some aggregations with height around 10 nm were observed (Fig. 4.20d&d'). The super high chain mobility at this low T_a, which might be due to the low degree of chain entanglement, is also confirmed by the phase separation that has already occurred as displayed in Fig. 4.20c. AFM results in Fig. 4.20b&b' also show some aggregations of around 2-3 nm in height by phase separation. The reason for this

large scale phase separation at 90 ℃ is not very c lear. There is some danger that low molecular weight chains resulting from thermal degradation contribute to it. However, other facts may also explain for it, such as impurities which promote phase separation, or absorbed water molecules from environment which acts as plasticizer and greatly lower the surface T_g of the polymers.

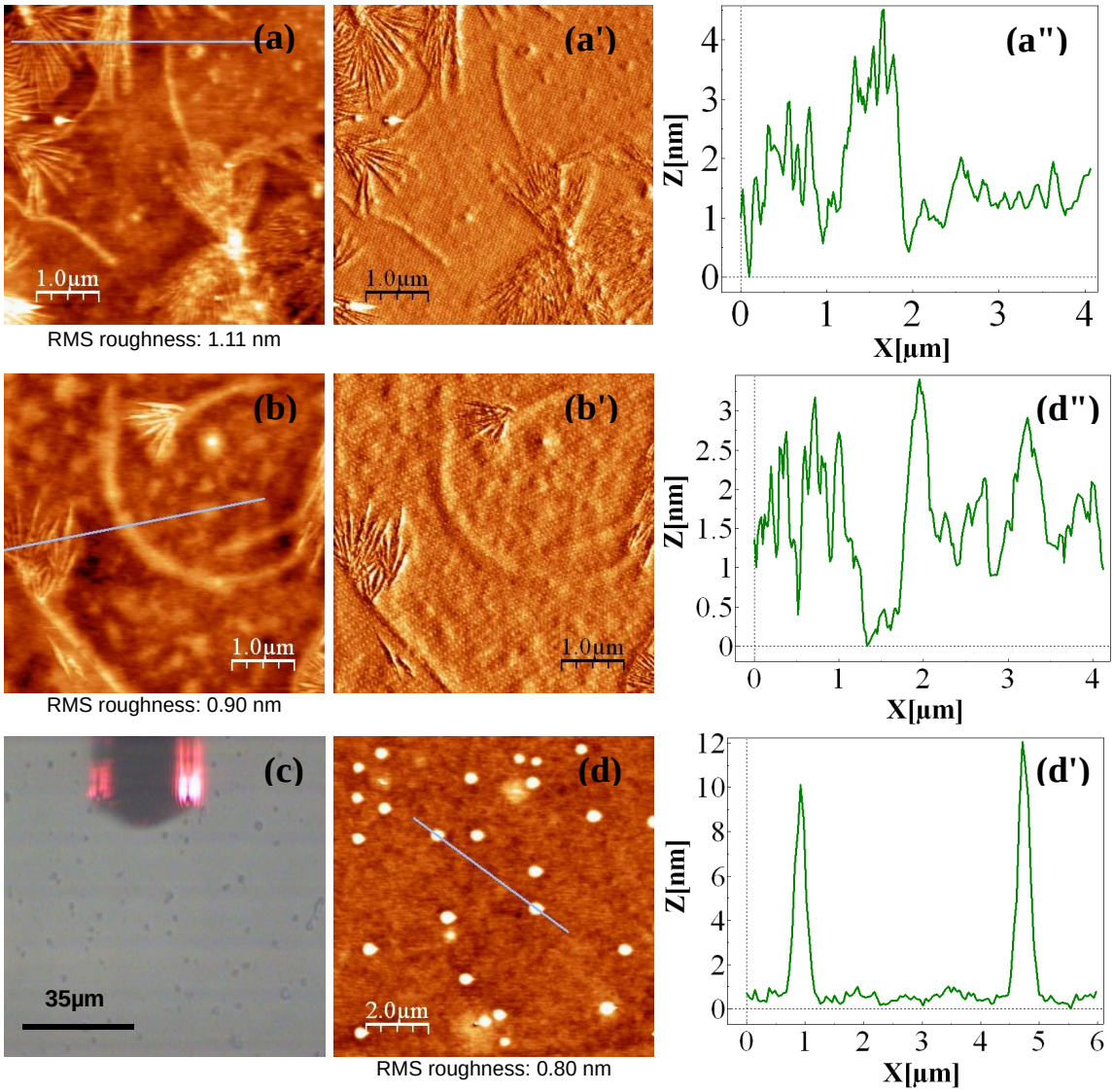


Fig. 4.20 Examples showing surface crystals in a PS/PMMA film (with the higher-crystallinity PS) annealed at 90 ℃ for 65 hr (a)(b) AFM height images , (a')(b') phase images, (a")(b") height profiles and (c) optical image of the sample; (d&d') AFM height image of the corresponding PS film annealed at 90 ℃ for 68 hr with its height profile .

4.4 CONCLUSIONS

Results on the immiscible PS/PMMA thin film system show that, due to lower T_g in the surface regions, a polymer blend is able to phase separate in the near-surface region at a much lower temperature than its bulk phase separation temperature, where polymer chains in the bulk of the film are still immobile. In the PS/PMMA thin films, the morphologies of surface phase separation observed include pits, undulations and aggregations. Investigation of the mixtures with a more easily crystallizable PS (which has a lower T_g) shows a promoted phase separation, compared with mixtures containing the lower-crystallizability PS, and a hindered crystallization compared with pure PS films. However, the observation of surface phase separation at a much lower T_a remains the same, showing a constant free surface effect regardless of the interplay between the crystallization and phase separation. This greater understanding of polymer phase separation behaviour is relevant to thin film applications, but, being a free surface effect, is pertinent to all phase separation systems with a free surface. This conclusion also agrees well with the surface-specific crystallization behaviour of polymers observed previously.

The observation of PS surface crystals turns out to be further evidence of the universality of the surface-specific crystallization phenomenon. However, PS surface crystals are only observed in a limited proportion of samples, which is likely due to the uncontrolled or variable tacticity of the PS. The flat-on structure of the PS crystals, rather than the edge-on surface crystals in PET, PEN, PVOH and PA, shows the vital influence of diffusion rate of polymer chains on the morphology or growth shape of surface crystals. Since, for films over a certain thickness, surface behaviours are independent of film thickness, the diffusion rate relies heavily on the degree of chain entanglement.

5 MICROSTRUCTURAL EVOLUTION IN HIGH HARD BLOCK CONTENT TPU THIN FILMS ON ANNEALING

Polymers in thin films are known to have distinct properties from those in the bulk. The influence of the free- and substrate- surfaces can modify phase behaviour and crystallization morphologies through the effect of surface and interfacial energies, and of chain confinement. In addition, the increased mobility of chains near the free surface gives rise to a lower surface T_g, and polymer surface crystallization, for example, has been shown to occur at a temperature much lower than the bulk T_c due to the lower surface T_g, as discussed in Chapter 3.

In this study, a block copolymer phase separation system that undergoes both phase separation and crystallization processes, in contrast to the polymer blend in chapter 4, is investigated in thin films. The system of choice is a series of linear TPUs with high HS content (70-100 wt%). These TPUs have EO-PPO-EO as the SS and a short diol chain-extended MDI as the HS. The chain extenders used are 2M13PD and 15PD. Replacements of BDO, one of the most commonly used chain extenders, with these diols lower the melting transition of the TPU, hence, allowing annealing studies at temperatures around melting without significant degradation, e.g. chain scission and recombination [38]. Previous work by co-workers from the University of Manchester, used scattering techniques and microscopy to investigate the crystallization and phase separation behaviour in bulk 2M13PD-extended TPUs and identified the origin of multiple endotherms observed by DSC. To extend and complement this study of the bulk phase behaviour, the crystallization and phase separation of these TPUs in thin films are presented here and compared to the bulk behaviour. Thin films, as well as their relevance for direct applications, and for studying surface and interfacial interactions, provide an additional way to directly image the morphological evolutions on annealing using AFM

techniques. Effects of annealing, HS content, film thickness and chain extender are extensively investigated.

5.1 BACKGROUND

Annealing can enhance mechanical and thermal properties of TPUs due to phase changes that can be characterized by the multiple endothermic peaks discovered in DSC traces, the subject of numerous previous investigations [38, 284-293]. Most of this work was carried out on TPUs with hard segments based on MDI extended by BDO, which is one of the most extensively investigated TPU classes. In general, three endotherms were reported in TPUs heated following an annealing treatment: a first endotherm, which is also known as the annealing endotherm (T_A) at roughly a few tens of Kelvin above the annealing temperature, and two high temperature endotherms, roughly within the range 120-200 ℃. Several phenomena have been proposed to explain the T_A including short range ordering of the HS [284, 285] or of HS over a critical block length (below which the HS is dissolved within the soft phase) [287, 289], enthalpy relaxation (physical aging) of amorphous HS [290] or interfacial materials [291], and the formation of fringed micelle-like crystals in the HS domains [293]. Early work attributed the intermediate endotherm to long range ordering of the HS [284, 285] or the onset of the formation of a homogeneous mixed phase [289], and the last endotherm to melting of crystalline HS domains. Recent work [38, 291, 292] incorporating scattering data, explained the two high temperature endotherms as melting of HS crystals followed by a HS/SS microphase mixing.

This brief review of previous work shows that the origin of annealing-induced structural evolution in TPUs is not fully understood and there has been little work on the annealing effect on TPUs in thin film situations. Hsu and co-workers [294, 295] reported that the phase separation of TPUs in thin films would be restricted when the films thickness is below 200 nm and this effect becomes more obvious when the thickness is around

100 nm. Later work by Kojio *et al.* [296] suggested that, below a certain film thickness, the crystallization of HS is confined in thin films, leading to a depression in the domain size of the hard and soft phases. However, the morphological evolution in TPU thin films is still largely uncharacterized.

Previous work [38, 291] indicated that, for melt-quenched 2M13PD-extended TPU (bulk) samples, a two-phase morphology, consisting of a “pure” HS phase and a HS/SS mixed phase (with a HS content of 65 wt%), is obtained when HS content is above 65 wt%, while only a mixed phase is produced when the HS content is less than 65 wt%. A schematic diagram of the two-phase morphology proposed for a TPU sample with continuous HS phase is presented in Fig. 5.1a. On annealing, a microphase separation in the mixed phase can take place forming microphase-separated mesophase domains (Fig. 5.1b) in a sample. A corresponding microphase mixing of HS and SS will take place within the mesophase domains when the annealed sample is heated to a certain temperature, the microphase mixing transition temperature (T_{MMT}).

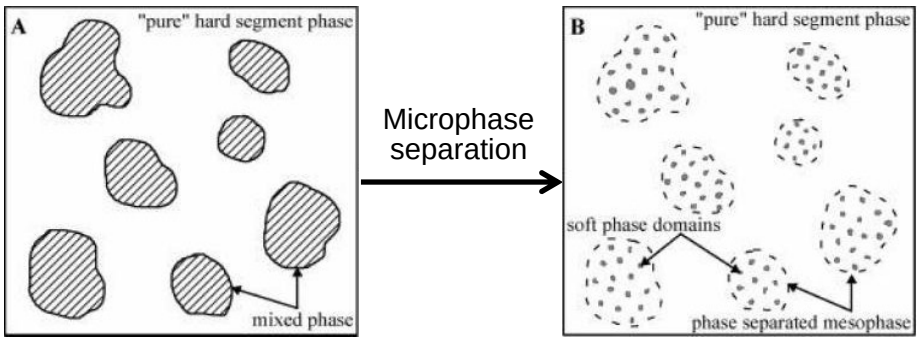


Fig. 5.1 Schematic diagrams showing the morphology of (a) melt-quenched 2M13PD-extended TPU samples with a continuous “pure” HS phase and (b) the one after microphase separation on annealing. Reproduced from [291] with permission of the copyright holder.

5.2 EXPERIMENTAL

All the TPUs were provided by collaborators from School of Materials, University of Manchester. TPU samples, which had been synthesized in a two-step process [38, 291, 292], are designated with the label of CE-XX where XX is the weight percentage of the HS, i.e. MDI plus CE. Molecular weights of the TPUs were obtained by gel permeation chromatography (GPC) (by Manchester) and are listed in Table 5.1.

Table 5.1 Molecular weights and polydispersities for polyurethanes involved.

CE used	HS wt%	M_w (g/mol)	M_n (g/mol)	M_w/ M_n
2M13PD	70	69730	19160	3.64
	80	59400	15550	3.82
	90	75770	23930	3.17
	100	77870	29390	2.65
15PD	70	109130	29936	3.65
	90	81515	30650	2.66
	100	106710	36090	2.96

TPU films were prepared from solutions of the TPUs in dimethylacetamide (DMAC) (Aldrich) by spin coating onto glass substrates. The solutions were normally stirred overnight for sufficient dissolution and were filtered with PTFE syringe filters with 200 nm pore size prior to deposition to remove any impurities or undissolved polymer particles, which might act as nuclei for crystallization or phase separation. The glass substrates were sonicated in detergent (several drops of Decon in 600 ml deionized water) and deionized water for 10 min each, and then in acetone and isopropanol for 5 min in turn at T_{room}. The samples were spin coated at room temperature for 1 min with a spin speed of 2000 rpm and an acceleration rate of 200 rpm/s. The as-spin-cast samples were then dried in vacuum for two days. Film thickness was controlled by solution concentration and was measured by a Dektak profilometer (Veeco), using a 1 mg stylus force and a scan rate of 150 μm/s.

The surface morphology of the TPU films was investigated using tapping mode AFM (Park Scientific Instruments) with both topography and phase images recorded at ambient conditions. As-spin-cast TPU films were annealed at temperatures ranging from 40 ℃ to

190 ℃ for various times. The as-spin-cast morpholo gy of each of the samples was characterized before annealing to ensure a constant starting point since some morphology developments discovered are slight and may be wrongly attributed to as-spin-cast morphology. Surface chemistry of some samples was also analysed by XPS (see Section 4.2).

DSC data of melt-quenched 2M13PD- and 15PD-extended TPUs were provided by co-workers from Manchester. Thermal analysis was performed by DSC Q100 (TA Instruments) with a scan rate of 20 ℃/min. These d ata (Table 5.2 and Fig. A1), showing the thermal behaviour of the TPUs in the bulk, are taken as a reference for thin film discussions.

TEM analysis was carried out using a JEOL 2010 LaB_6 microscope operated at 100 kV. Details of sample preparation are in the Section 3.2

Table 5.2 Transition temperatures indicated by DSC.

Melt-Quenched TPUs	T_g (°C)		T_c (°C)	T_{MMT} (°C)		ΔH_{total} (J/g)	
	1st heating	2nd heating		1st heating	2nd heating	1st heating	2nd heating
Melt-Quenched 2M13PD-70	41	33	121 (1st) 112(2nd)	176	175	21.52	16.98
Melt-Quenched 2M13PD-80	48	71	126	168	167	12.72	6.648
Melt-Quenched 2M13PD-90	55	85	-------	173	173	9.476	1.546
Melt-Quenched 2M13PD-100	78	94	-------	-------	-------	-------	-------
Melt-Quenched 15PD-70	26	-------	67	173	183	28.26	25.61
Melt-Quenched 15PD-80	43	79	88	172	170	27.96	24.00
Melt-Quenched 15PD-90	71	85	119	172	171	31.06	12.02
Melt-Quenched 15PD-100	69	83	138	168	167	12.69	1.300

5.3 RESULTS AND DISCUSSION

5.3.1 2M13PD-Extended TPU Thin Films

In contrast to the situation in melt-quenched 2M13PD-extended bulk TPU samples, AFM results showed that, for as-spin-cast TPU films around 72 nm thick, a “homogeneous” surface morphology was obtained as the HS content varies from 70 to 90 wt% (Fig. 5.2a-c). These TPU thin films all show a similar surface morphology with tiny granules and low surface roughness around 0.3 nm. Although this morphology is also very close to that of the polyurethane without SS (Fig. 5.2d), commensurate with it being from a single (or a HS/SS mixed) phase, the granule size and surface roughness in the 100 wt% HS polyurethane film is lower as it does not contain the more mobile soft segment. This is confirmed by the XPS results in Fig. 5.3 which indicate the presence of both HS and SS at the surface with the HS content in the surface regions increasing with the HS wt% in the polyurethane, implied by the decreased intensity of ether carbon.

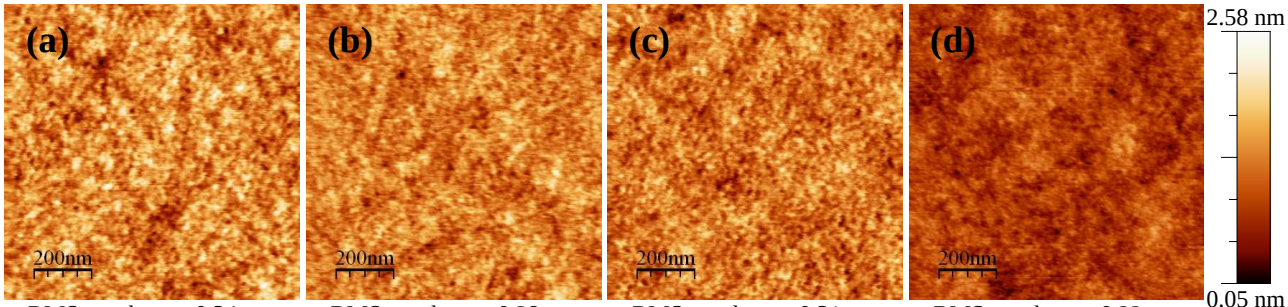


Fig. 5.2 AFM topographic images showing as-spin-cast morphology of 2M13PD extended TPU films with thickness around 72 nm and HS content: (a) 70 wt%, (b) 80 wt%, (c) 90 wt% and (d) 100 wt%.

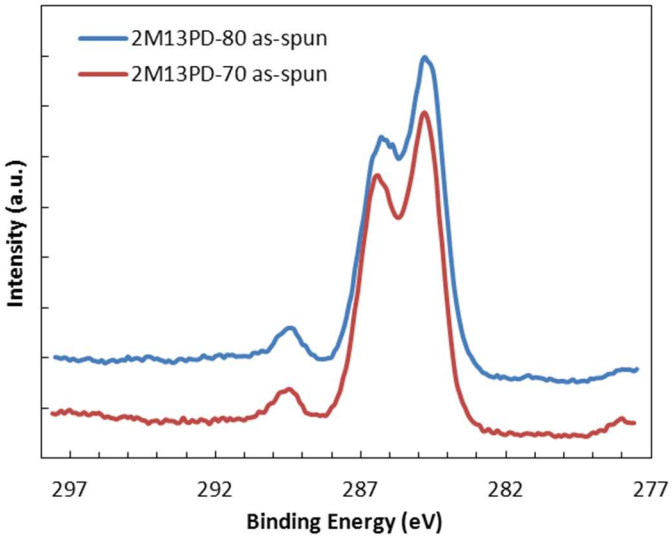


Fig. 5.3 XPS C1s spectra for thin films of 2M13PD-70 (morphology shown in Fig. 5.2a) and 2M13PD-80 (morphology shown in Fig. 5.2b). The peaks observed at 284.8, 286.4 and 289.4 eV are assigned to neutral (CC*C), ether (C*O) and urethane carbonyl (NHC*(=O)O) carbon respectively. As HS content increases from 70 to 80 wt%, the intensity for NHC*(=O)O stays approximately constant, while the intensity for C*O decreases, which indicates a decrease in SS content.

Compared to the melt-quenched samples, the significantly suppressed degree of phase separation in the as-spin-cast samples is due to the faster solvent-quenching rate than the melt-quenching rate and to molecular confinement from the film thickness. This effect of confinement agrees well with Hsu *et al.*'s work [294, 295] on polyurethanes in a restricted state.

5.3.1.1 Morphological evolution on annealing

Despite starting from a mixed phase in the thin films rather than the two-phase morphology of the bulk, the phase separation and crystallization processes corresponding to the various DSC endotherms still occur, but at different temperatures from the bulk due to the spatial confinement in very thin films. Here, 2M13PD-90 is taken as an example to illustrate the evolution of the surface morphology in 2M13PD-extended TPU thin films on annealing. AFM images of as-spin-cast 2M13PD-90 films around 73 nm thick annealed at

temperatures between 90 ℃ to 180 ℃ for 16 hr are displayed in Fig. 5.4, summarising the phase evolution.

According to previous work on 2M13PD-extended TPUs in the bulk [291], given sufficient time phase separation is able to occur at very low annealing temperatures, e.g. 2M13PD-80 at 25 ℃ for 96 hr, suggested by the observation of the endotherm in a subsequent DSC heating trace due to microphase mixing of HS and SS. Due to the plasticizing effect of the SS, ordering of HS in the mixed phase could even occur at T_a below the T_g of the hard phase (T_{gHP}), whereas the HS ordering in the "pure" HS phase requires an annealing temperature over T_{gHP}. The HS orderings in both the mixed phase and the HS phase are shown to have the same ordered form and result in the crystal melting endotherm (T_M) peak just below T_{MMT}.

In 2M13PD-90 thin films, any obvious surface morphology change was observed to require annealing over 90 ℃ (Fig. 5.4a) (for a 16 hr anneal), which is just above the T_{gHP} of bulk samples, 85 ℃ (Table 5.2, 2nd heating). The small aggregations observed with height around 10 nm (see the profile in Fig. 5.4a) are believed to be the beginning stage of phase separation and HS ordering in the mixed phase. With 10 wt% SS content, the HS have sufficient SS around to give them enough mobility to form an ordered phase. Still, at this temperature, the HS ordering is limited to the HS chains forming local small aggregations, observed in many places across the surface. When the T_a was increased to 100 ℃ (Fig. 5.4b), much larger peaks were discovered due to the greater mobility at this temperature, which leads to a larger phase separation and crystallization region around an aggregation centre and lowers the areal density of such peaks.

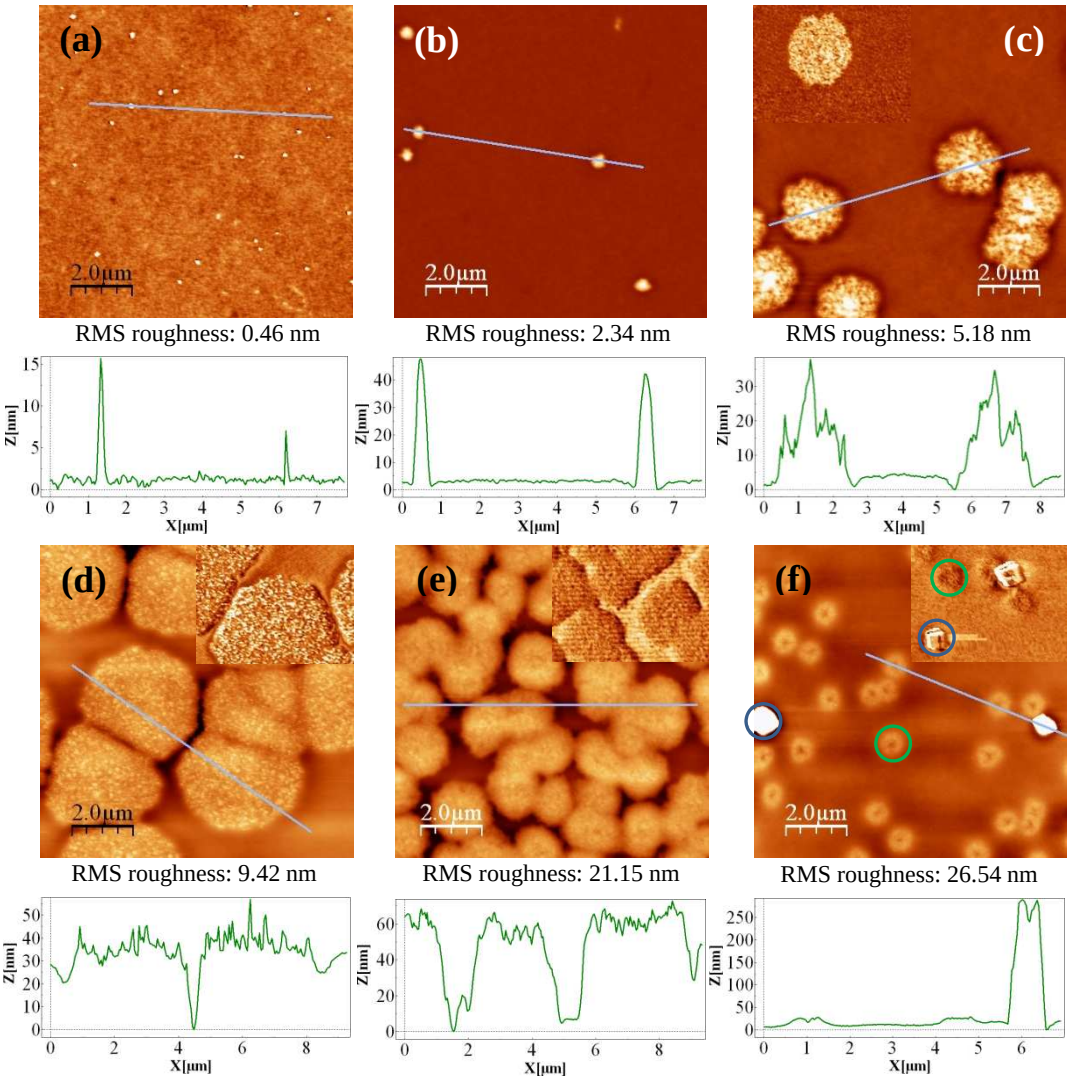


Fig. 5.4 Phase separation and crystallization on annealing. AFM height images of 2M13PD-90 films (73 ± 4 nm) annealed, after spin-casting, at different temperatures for 16 hr: (a) 90 ℃, (b) 100 ℃, (c) 120 ℃, (d) 140 ℃, (e) 150 ℃, (f) 160 ℃, wit h height profiles beneath. The inserts in (c), (d) (e) and (f) are the phase images of corresponding areas in the height images.

Distinct domains, a few microns across, were found in 2M13PD-90 films annealed at 120 ℃ and 140 ℃ for 16 hr. On annealing melt-quen ched bulk samples at 120 ℃, the mixed phase domains will undergo a microphase separation creating a phase-separated mesophase [292]. In the thin films these observed domains, with a height distribution between 20 nm and 40 nm show a similar morphology to that postulated for the so-called phase-separated mesophase in the bulk (Fig. 5.1b). The formation of these domains involves both lateral phase separation and vertical phase separation since the lateral

domains extend tens of nanometres above the surface of the matrix (more evidence for vertical phase separation is given by the XPS results of 2M13PD-80, Fig. 5.7a). Due to the HS ordering generated during phase separation, these domains exhibit a higher modulus manifested by the lighter colour in the phase image (insert in Fig. 5.4c), with the dimmer regions within the mesophase domains attributed to the soft segment phase. With this microphase-separated morphology, these domains can be recognized as the same phase-separated mesophase reported in bulk samples. This prompts the conclusion that, for 2M13PD-extended TPU thin films annealed at temperatures above T_{gHP}, the microphase-separated mesophase develops directly from the as-spin-cast HS/SS mixed phase without the initial formation of the two-phase stage indicated by the melt-quenched samples. Therefore, the HS content in the mesophase should be the same as that in the mixed phase domains obtained by melt-quenching the bulk, which is around 65 wt%, whereas the HS content in the continuous phase increases with the growth of the microphase-separated mesophase and a “pure” HS phase would ultimately be obtained.

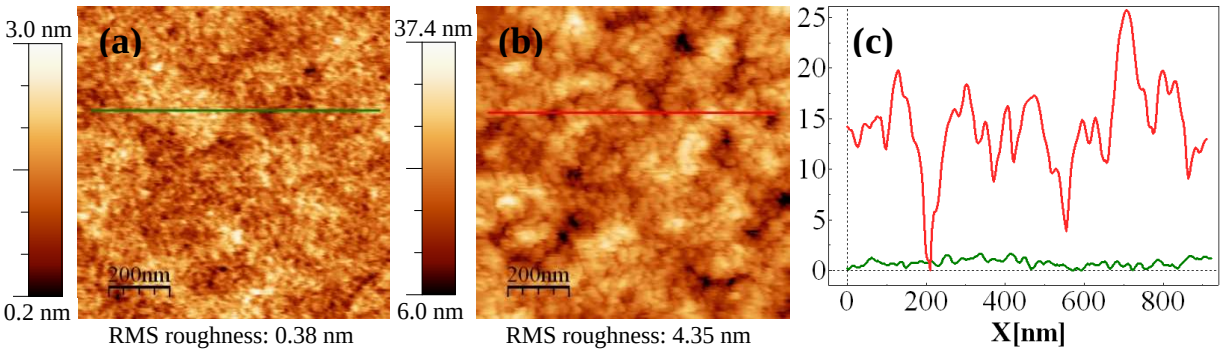


Fig. 5.5 AFM height images showing the continuous area (a) and the domain area (b) of a 2M13PD-90 film annealed at 120 °C for 16 hr with corresponding height profiles displayed in (c).

A comparison between the morphology of the continuous phase and the phase-separated mesophase at higher magnification is presented in Fig. 5.5. Annealing (at 120 ℃) has little effect on the morphology of the continuous region (compare Fig. 5.5a and Fig. 5.2c) with only a slight increase in surface roughness. The new-born mesophase regions formed by phase separation and crystallization have a significantly larger grain size

(Fig. 5.5b) with a significant greater height variation (around 25 nm) than the continuous phase (Fig. 5.5c), as would be expected for a microphase separated morphology.

The phase image of the sample annealed at 140 ℃ (Fig. 5.4d) shows that the regions between the mesophase domains are softer than the mesophase, even though these regions are expected to contain little SS at this point. By this stage of the phase separation, the continuous region contains nearly “pure” HS phase, the chain mobility is very low and, with a large proportion of the sample forming the mesophase domains, the residual materials between or below the domains form a much thinner film which greatly confined the mobility of the HS chains. Therefore, even after annealing at 140 ℃, the continuous hard phase is still amorphous and is softer than the mesophase with ordered HS.

The morphology in a sample annealed at 150 ℃ for 16 hr, however, suggests that there is HS ordering in the continuous phase, confirmed by the higher modulus than the mesophase indicated by the phase image (Fig. 5.4e). Compared to the domains formed at 140 ℃, the mesophase domains have a decreased size but increased number and height. This might be due to the hindered lateral mesophase growth rate by the now-crystalline surrounding hard phase. The mesophase now shows a clear spinodal pattern within the original phase when observed under optical microscopy (Fig. 5.6) rather than the isolated nucleation of mesophase regions observed at lower temperatures. In this case, it may be that spinodal decomposition occurs first, creating an elevated mixed phase, with a 65 wt% HS content, and a “pure” hard phase, as observed in melt-quenched samples, followed by the HS/SS phase separation and HS ordering within the mixed phase.

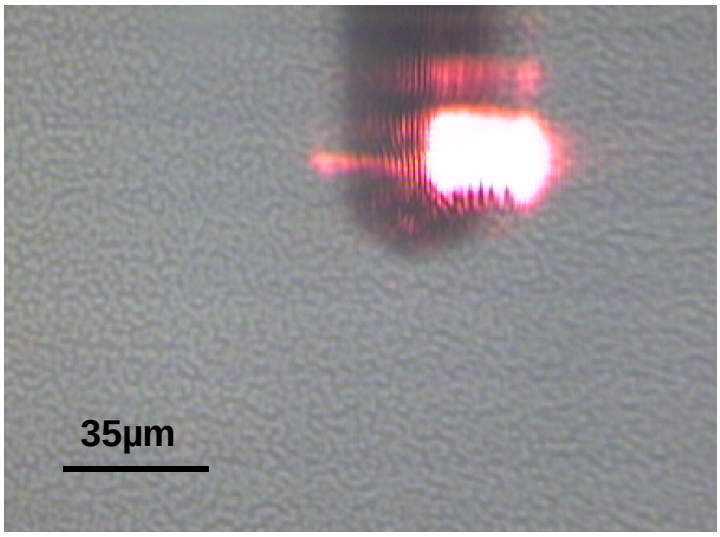


Fig. 5.6 Optical image of a 2M13PD-90 film (73 ± 4 nm) annealed at 150 ℃ for 16 hr.

AFM results of 2M13PD-90 films annealed at 160 ℃ reveal the generation of multilayer crystal blocks with height around 250 nm (in the blue circles in Fig. 5.4f) (these will be discussed in section 5.3.3) as well as the existence of some small domains with height only around 20 nm (in the green circles in Fig. 5.4f). These domains are believed to be the residue of the mesophase domains after a microphase mixing or melting process of a previously formed mesophase. Certainly there is a smooth connection between the continuous phase and the domains (see the profile in Fig. 5.4f). In other words, both the continuous phase and the residual domains should be a mixed phase with a HS content around 65 wt%, the HS content of the mesophase domains. This is also supported by the lack of contrast (Fig. 5.4f insert) between the two parts. The film now is expected to have a vertically phase-separated structure: a mixed phase at top and a “pure” hard phase at bottom, resulting from the previous mesophase formation and microphase mixing. This vertical pattern is substantially driven by the thermodynamics of wetting: the interfacial energy with the substrate and the air.

XPS results (Fig. 5.7a) of 2M13PD-80 films confirm this idea of a vertical phase segregation. There was a decrease in the HS/SS ratio in the surface region during the stages of mesophase forming and impinging, which was implied by the decreased intensity of urethane carbonyl carbon and the increased intensity of ether carbon.

Comparing Fig. 5.3 and 5.7a, the 2M13PD-80 sample annealed at 100 ℃ for 16 hr in fact shows a similar HS/SS ratio to that in the as-spin-cast 2M13PD-70 sample. This supports the conclusion that at elevated temperatures the polymer becomes sufficiently mobile to allow vertical phase segregation on annealing creating an upper phase-separated mesophase layer with a HS content close to 65 wt% and a "pure" hard phase underneath. The corresponding surface morphologies of 2M13PD-80 films annealed at 100 ℃ and 160 ℃ are revealed in Fig. 5.7b and 5.7c respectiv ely. The morphological evolution in the 2M13PD-80 films on annealing is similar to that observed in the 2M13PD-90 films, but requires lower T_a due to the higher SS proportion.

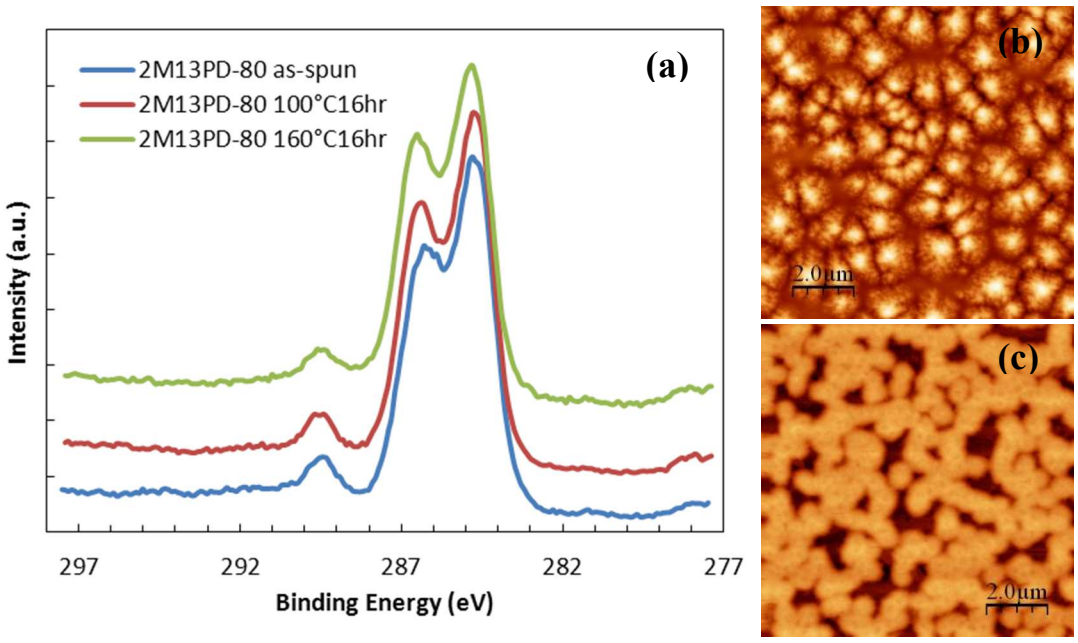


Fig. 5.7 (a) XPS C1s spectra for thin films of 2M13PD-80 (70 ± 2 nm) as-spin-cast, after 16 hr annealing at 100 ℃ (where phase-separated mesophase regions are obs erved by AFM (b)), and at 160 ℃, where the mesophase domains impinge (c) . Interpretations of the peaks are according to that in Fig. 5.3. With increasing annealing temperature, the C*O intensity increases, while the NHC*(=O)O intensity decreases. This implies a decreased HS content at the sample surface as annealing temperature increases.

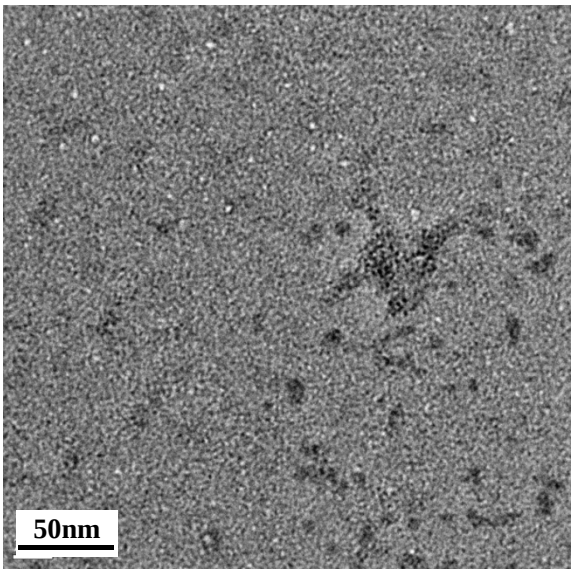


Fig. 5.8 TEM micrograph of 2M13PD-90 films (thickness 73 ± 4 nm), an area between the large-scale crystals showing the microphase-separated morphology.

Annealing at higher temperatures, e.g. 180 ℃, still revealed a morphology dominated by these large, blocky, crystals. A TEM image of the continuous region (Fig. 5.8) between these crystals shows the existence of soft phase domains (dark areas) less than 10 nm across in a harder phase matrix, which is similar to the morphology of the microphase-separated mesophase in bulk samples by TEM [292] but with a much lower soft phase proportion. This result indicates that the phase separated mesophase with HS around 65 wt% does not form on annealing at 180 ℃ for 16 hr and the continuous phase has a different HS content. As the T_a is above the T_{MMT} in this case, no such phase separation is to be expected. The tiny white dots in Fig. 5.8 are assigned to the ordered HS structures in the hard phase matrix. Both the soft phase domains and the ordered HS were expected to form during the sample cooling process as 180 ℃ is well above the T_M of the ordered HS and the T_{MMT}.

5.3.1.2 Influence of HS content

The microphase separation and crystallization in TPUs depend greatly on the proportion of HS and SS. The lower the SS content, the lower the HS mobility. DSC (Fig. A1a&b) traces of the 100% HS material indicated that without the presence of SS, crystallization of HS becomes difficult and no melting endotherms were detected. This agrees with the AFM results that, for 16 hr annealing, only when T_a is over 140 ℃ can a slight morphology change, e.g. small crystalline aggregations with height around 15 nm (Fig. 5.9), be detected in 2M13PD-100 films. The morphology developments of 2M13PD-70, -80 and -90 thin films (with thickness around 72 nm) on annealing (16 hr) are summarized in Fig. 5.10. In general, the TPU thin films undergo three main stages on annealing: (i) the generation of microphase-separated mesophase domains; (ii) formation of a complete impinged mesophase phase at the surface; (iii) formation of multilayer large crystals.

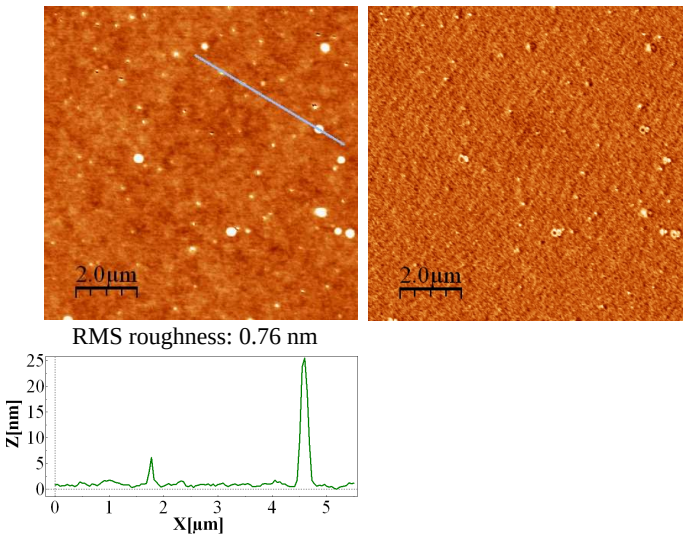


Fig. 5.9 AFM image of a 2M13PD-100 film (72 ± 2 nm) annealed at 140 ℃ for 16 hr: (a) topography, (b) phase.

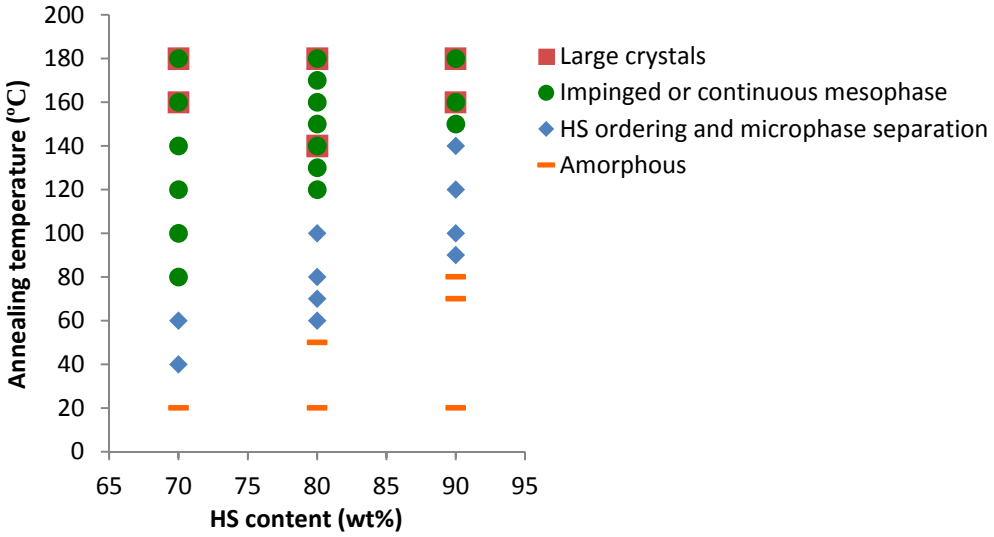


Fig. 5.10 Morphological evolution of 2M13PD-extended high HS content TPU thin films (around 72 nm thick) on annealing for 16 hr. T_{room} is assumed to be 20 ℃.

The first stage, at the lowest annealing temperatures, is the ordering of HS in the mixed phase in the form of small aggregations of several nanometres height. The lowest temperature where this occurs is consistent with the T_{gHP} of the corresponding bulk samples (Fig. A1b, Table 5.2) at each composition, increasing with the HS content due to the HS mobility increasing with SS content in the mixed phase. For 2M13PD-70 films, with high HS mobility, the HS aggregations densely cover the surface (Fig. 5.11) and there are many more nucleation centres formed in 2M13PD-70 films than the TPU films with higher HS content. This large density of HS aggregations means that no large phase-separated mesophase domains similar to those found in 2M13PD-90 films (Fig. 5.4c) were observed in 2M13PD-70 films, but ultimately only impinging aggregations (with a much higher density compared to Fig. 5.4b) were observed, a typical example of which is displayed in Fig. 5.11b.

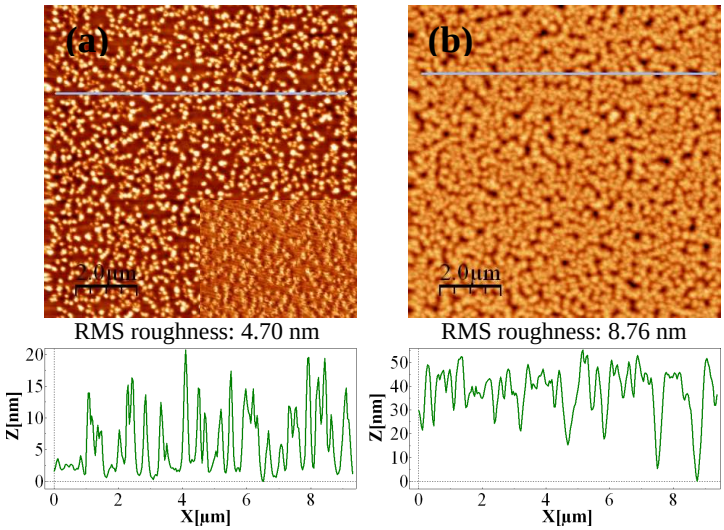
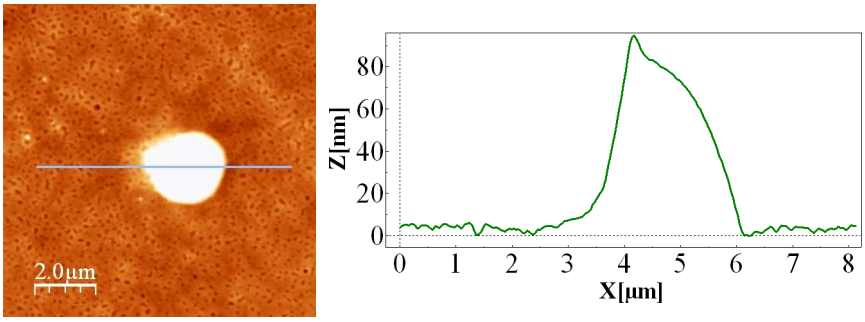


Fig. 5.11 Morphology of a 2M13PD-70 film (72 ± 6 nm) annealed at (a) 60 ℃ and (b) 80 ℃ for 16 hr with corresponding line profiles and phase image (insert).

With a similar HS/SS ratio in the mesophase, for instance 65/35, the mesophase formed in 2M13PD-90 will be around 29 wt% of the whole film, while the mesophase fractions in 2M13PD-80 and -70 films would be as high as 57 wt% and 86 wt% respectively. However, for all compositions there is vertical phase segregation, which means that the sample is tending towards a complete surface coverage with the mesophase. Once the annealing temperature is sufficiently high for the 'continuous mesophase' layer to form on the surface, the surface composition is thought to be a constant 65 wt% HS. For 2M13PD-70 and 2M13PD-80 films (around 72 nm thick), there are still gaps or holes in the continuous mesophase when the sample is annealed over 160 ℃ (e.g. Fig. 5.7c&5.19a). This formation of a near-continuous mesophase layer at the surface, however, is accompanied with the ordering of HS (at 160 ℃). With a higher SS content in the TPU (in the as-spin-cast state), a higher HS crystallinity could be obtained at an early stage in the annealing process, hindering the lateral growth of the mesophase (and any subsequent microphase mixing). Therefore, when annealing at 160 ℃, the mesophase-joining and microphase mixing process is much easier in a higher HS-content film, e.g. 2M13PD-90 film (Fig. 5.4f).

Because of this similar HS/SS ratio of the upper mesophase, there was no trend in the temperature at which the large crystals are first observed at these higher annealing temperatures. In the 2M13PD-80 films, the large crystals were observed at about 20 K lower than the other two compositions, but this is likely due to the much lower molecular weight of 2M13PD-80 compared to 2M13PD-70 and 2M13PD-90, as indicated in Table 5.1. DSC (Fig. A1, Table 5.2) also confirmed that T_{MMT} of 2M13PD-80 is lower than the other two polyurethanes. This lower T_{MMT} also explains why large crystals were difficult to find at higher T_a in this material, and when annealed at 180 ℃, onl y large aggregations (e.g. Fig. 5.12) rather that clearly defined crystallites were observed.



RMS roughness: 9.84 nm

Fig. 5.12 Morphology of a as-spin-cast 2M13PD-80 film (70 ± 2 nm) after a 16 hr anneal at 180 ℃ with a corresponding line profile.

Although, the HS content of the TPU has little effect on the temperature at which the large crystals first appear, it does influence their morphology (detailed in section 5.3.3.2).

5.3.1.3 Microphase mixing

Morphological development of 2M13PD-80 films (excluding the crystal blocks) around T_{MMT}, which is approximately 167 ℃ for melt-quenched s amples (Table 5.2), is presented in Fig. 5.13. After elevating T_a from 150 ℃ to 170 ℃ (Fig. 5.13a&b), the depth of gaps between the mesophase regions, a residue from mesophase impinging, significantly decreases (the deep ones decrease roughly from 60 nm to 30 nm). These gaps disappear leaving a slight undulation when T_a increases to 180 ℃ (Fig. 5.13c), suggesting a complete microphase mixing. The morphological evolution here shows that the melting of

the HS ordered regions and the subsequent microphase mixing process in the continuous regions between the large crystal blocks actually are in good agreement with the DSC results from bulk samples. The appearance of pits around several nanometres deep on annealing over 170 ℃, however, is attributed to a phase separation process during sample cooling as this apparent but tiny scale phase separation is not expected at a temperature over T_{MMT}. Since, the regions away from the bulky crystals have undergone the microphase mixing transition when T_a is above T_{MMT}, the HS content in these regions changes with the total HS content of the TPU. Thus this phase separation on cooling occurs more significantly in the materials with a greater proportion of SS, due to the greater chain mobility. In the case of 2M13PD-90 films, with a very high HS content, these pits are not observed.

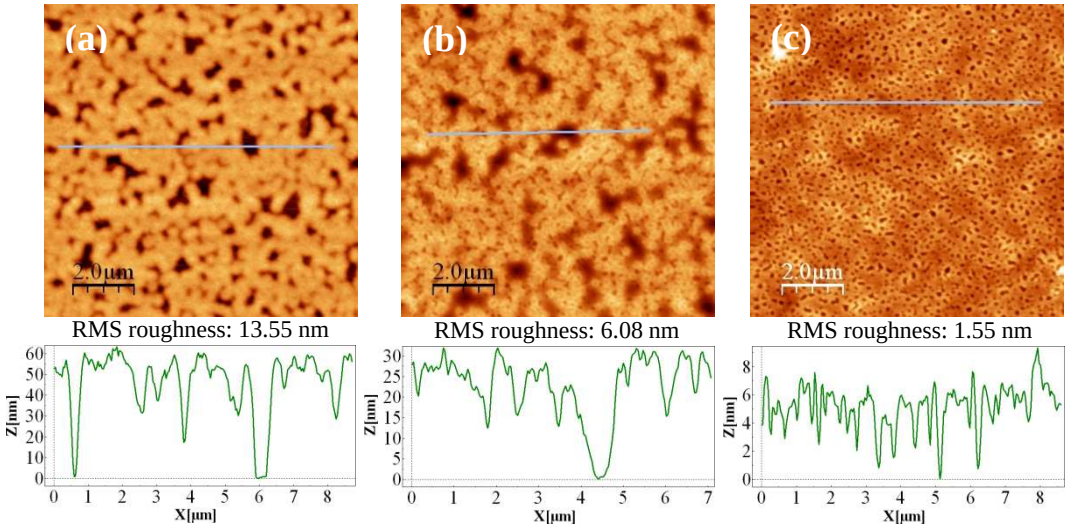


Fig. 5.13 AFM topography images of as-spin-cast 2M13PD-80 films (70 ± 2 nm) after 16 hr annealing at (a) 150 ℃, (b) 170 ℃ and (c) 180 ℃, with corresponding height profiles. The T_{MMT} of melt-quenched 2M13PD-80 by DSC is around 167 ℃.

5.3.1.4 Thickness effects

Increasing the film thickness accelerated and enlarged the various morphological developments. For example, in a 73 nm thick 2M13PD-90 film annealing at 90 ℃ for 16 hr only allows some small aggregations with height around 10 nm (Fig. 5.4a) to form, but in 127 nm and 363 nm thick films aggregations with height around 25 nm (Fig. 5.14a) and

30 nm (Fig. 5.14d) respectively can form. In samples annealed at 120 ℃ for 16 hr, separated mesophase domains are observed in 73 nm films (Fig. 5.4c), but they are beginning to impinge in 127 nm films (Fig. 5.14b), and almost completely cover the surface in 363 nm films (Fig. 5.14e). This implies that the mobility of polymer chains in 2M13PD-extended TPU thin films is confined in film thickness below a few hundred nanometres, which agrees with the suggestion of Hsu *et al*. [294, 295].

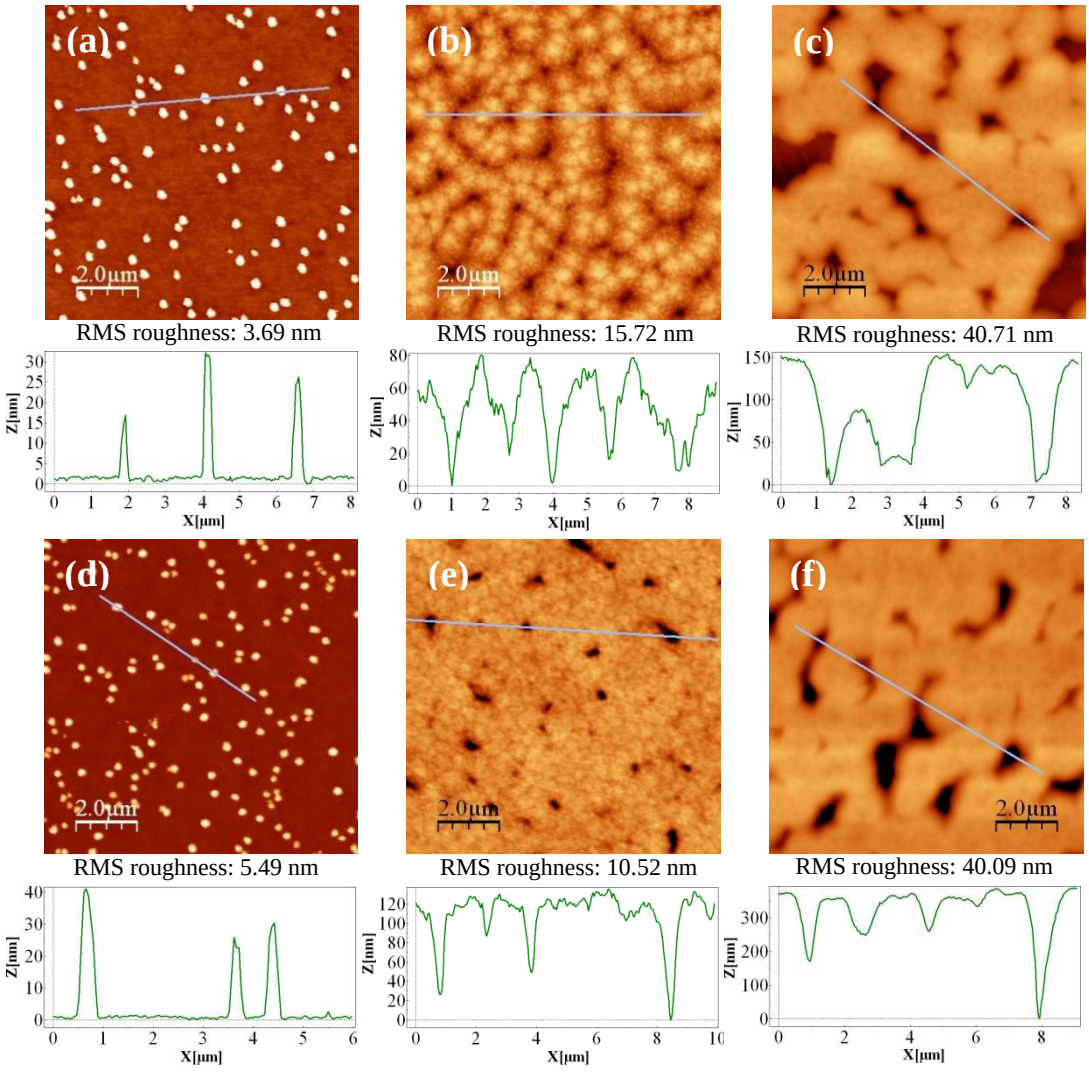


Fig. 5.14 AFM topography images of 2M13PD-90 films: (a-c) 127 ± 3 nm and (d-f) 363 ± 9 nm annealed at different temperatures for 16 hr: (a)(d) 90 ℃, (b)(e) 120 ℃ and (c)(f) 160 ℃ with corresponding height profiles beneath. Improved chain mobility with film thickness is indicated.

As work on PET indicated that surface-specific behaviour, e.g. crystallization, is confined by the film thickness only when film thickness is below a few tens of nanometres [27], the

morphological evolution, especially the formation of the nano-height aggregations at low T_a (Fig. 5.4a), is consistent with them being bulk behaviours of the whole TPU thin films rather than a surface-specific behaviour.

On annealing at 160 ℃, more advanced mesophase imp inging occurred in films with thickness around 127 nm and 363 nm (Fig. 5.14c&f). However, the large, multilayer crystals, which were observed in 73 nm thick 2M13PD-90 films annealed at 160 ℃ (Fig. 5.4f), were not found in the thicker films, where chain mobility should be higher. The failure to observe the lamellar crystal blocks in thicker films suggests that these crystal blocks are a phenomenon specific to thin films and their generation requires a film thickness below a certain value, approximately around 100 nm in the case of 2M13PD-extended TPUs.

5.3.2 15PD-Extended TPU Thin Films

By varying chain extenders, properties of the HS can be qualitatively modified. In contrast to the case in 2M13PD-extended TPU films (with thickness below 100 nm), where microphase separation and HS ordering occur at low T_a and large multilayer crystals are generated at temperatures around the T_{MMT} (as measured in bulk samples), it is principally crystallization processes that are observed in annealed 15PD-extended TPU films of similar thickness, and no formation of microphase-separated domains was observed. This is due to the significantly greater chain flexibility of 15PD compared to 2M13PD giving rise to an enhanced compatibility with SS, minimising phase separation between HS and SS. With HS/SS phase separation restricted, high HS content 15PD-extended TPU films, e.g. 15PD-70, 15PD-90, show a similar morphological evolution to that of pure HS films, 15PD-100, on annealing, which is shown in Fig. 5.15.

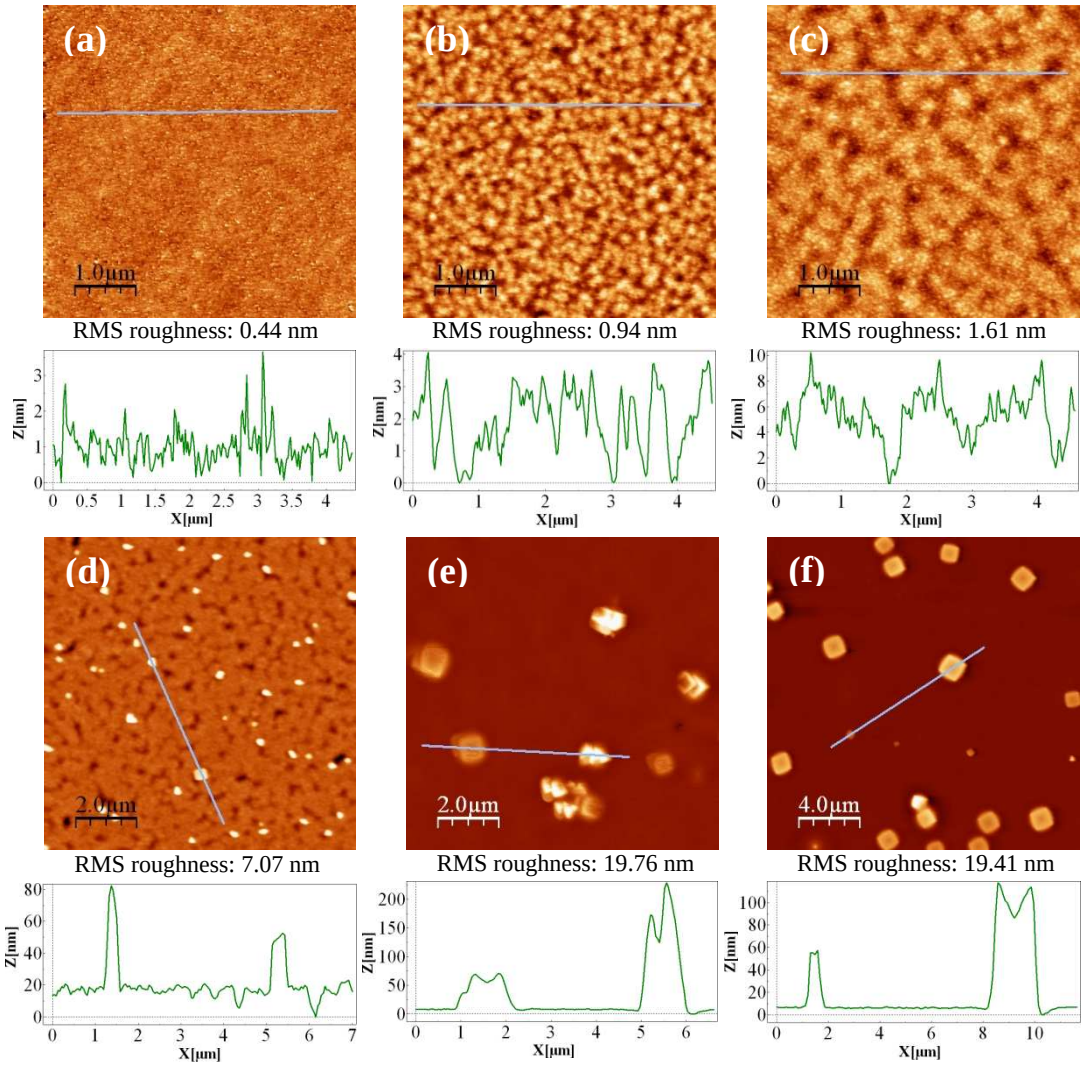


Fig. 5.15 AFM height images of as-spin-cast 15PD-100 films (69 ± 5 nm) after 16 hr annealing at (a) 80 ℃, (b) 100 ℃, (c) 130 ℃, (d) 150 ℃, (e) 170 ℃ and (f) 190 ℃, with corresponding height profiles beneath. Note the scale changes in images.

In 15PD-100 thin films (around 70 nm thick), the development of surface morphology begins with the appearance of tiny HS aggregations with height around a few nanometres (Fig. 5.15a) when annealed at 80 ℃ which is about 10 degrees more than the T_g of melt-quenched 15PD-100 (Table 5.2, 1st heating). As T_a increases, a significant growth was observed in these aggregations leading to impingement at 100 ℃ (Fig. 5.15b) and ultimately to rearrangement of the films producing surfaces with undulations (Fig. 5.15c&d). The development of surface morphology here resembles the morphology evolution in 2M13PD-70 films (Fig. 5.11), also associated with HS aggregations, however,

the aggregations have height variations around tens of nanometres in 2M13PD-70 films, while in 15PD-100 films the height profile undulates over only several nanometres (Fig. 5.15b-d), presumably because of the lack of any SS lending chain mobility. The undulations are lost as T_a increases to 170 ℃ (Fig. 5.15e&f), which is just above the T_M (167 ℃, Table 5.2) of bulk 15PD-100. In this tempe rature region, any small crystals or short-range order generated previously may start to melt (Fig. A1d). On annealing above 170 ℃, instead of forming short-range ordered regions, the HS prefer to arrange themselves into large multilayer crystals (Fig. 5.15e&f). This transition of crystal growth preference takes place when T_a is around 150 ℃, where the two crystalline morphologies coexist (Fig. 5.15d). In contrast to 2M13PD-100 thin films, 15PD-100 with the more flexible chain extender can form these crystals.

Similar crystals were formed in 15PD-90 at the same T_a where, in the presence of SS, the mobility of polymer chains is higher and crystals were better developed (discussed in section 5.3.3.2).

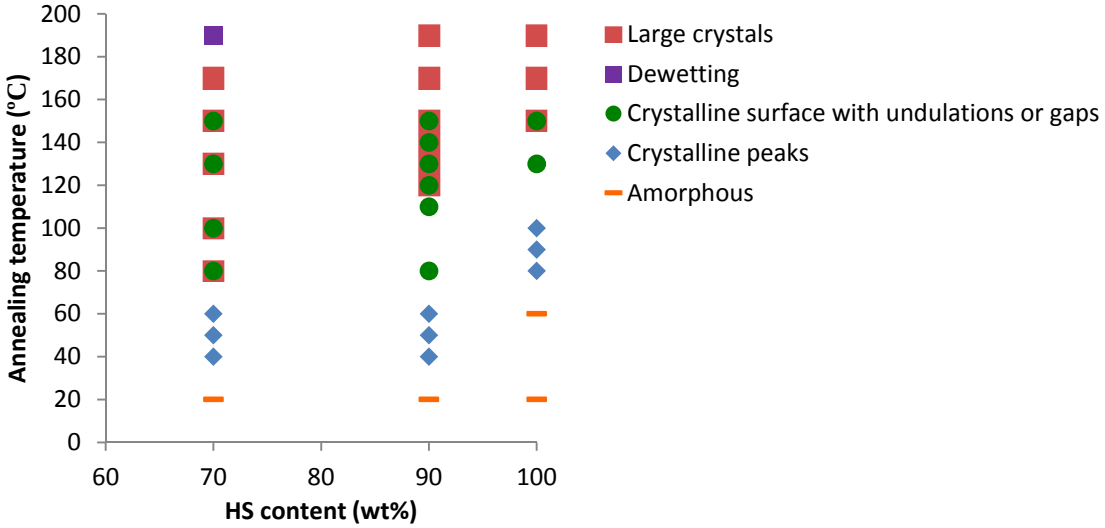


Fig. 5.16 Morphological evolution of 15PD-extended high HS content TPU thin films (70-80 nm) on annealing (16 hr). T_{room} is assumed to be 20 ℃.

The morphological developments of 15PD-extended high HS content TPU thin films on annealing (16 hr) are summarized in Fig. 5.16. Basically, there are two phase changes on

annealing. Firstly, there is formation of ordered HS structure which appears in the form of small peaks or aggregations at relatively low T_a and result in bulk crystallization of the whole film with undulations or gaps formed at the surface at higher T_a. This phase transition takes place when T_a is over T_{gHP}, which is higher for 100% HS material, and disappears when T_a approaches T_M of the ordered HS structures, which does not depend on the HS content (approximately in the range 150-170 ℃, Fig. 5.16). The results here are in good agreement with the DSC results (T_{gHP}, T_{MMT} or T_M) of melt-quenched bulk samples (Table 5.2). The other principal phase behaviour is the development of large crystal blocks. The lowest temperatures needed for the generation of these crystal blocks is around the T_c (just above T_c for 16 hr annealing) of the melt-quenched bulk 15PD-extended polyurethanes (Table 5.2). However, these crystals could even be generated at temperatures over T_{MMT} or T_M of bulk samples, which is around 170 ℃ (Table 5.2). They have not been observed in the previous bulk materials, experiments. With elevated T_a, the geometries of the crystal blocks changes and becomes more regular, which leads to multilayer crystals with a square shape in planar view at T_a above bulk T_{MMT} or T_M.

5.3.3 Multilayer Crystal Blocks

An intriguing phenomenon discovered in the high HS content TPU thin films is the generation of the large multilayer crystals reaching hundreds of nanometres above the surface of the sample, even greater than the average thickness of the films. It is clear from images of material with either chain extender (e.g. phase image of Fig. 5.4f, and Fig. 5.15e&f) that these large crystals are stacks of regular-shaped layers. It is the first time that such large multilayer crystal blocks have been observed in polymer thin films through cold crystallization. Since there are no such crystal blocks found in bulk samples

or films with thickness over 100 nm in these materials, this is a specific thin-film phenomenon induced by either free surfaces or spatial confinement (film thickness).

5.3.3.1 Crystal development

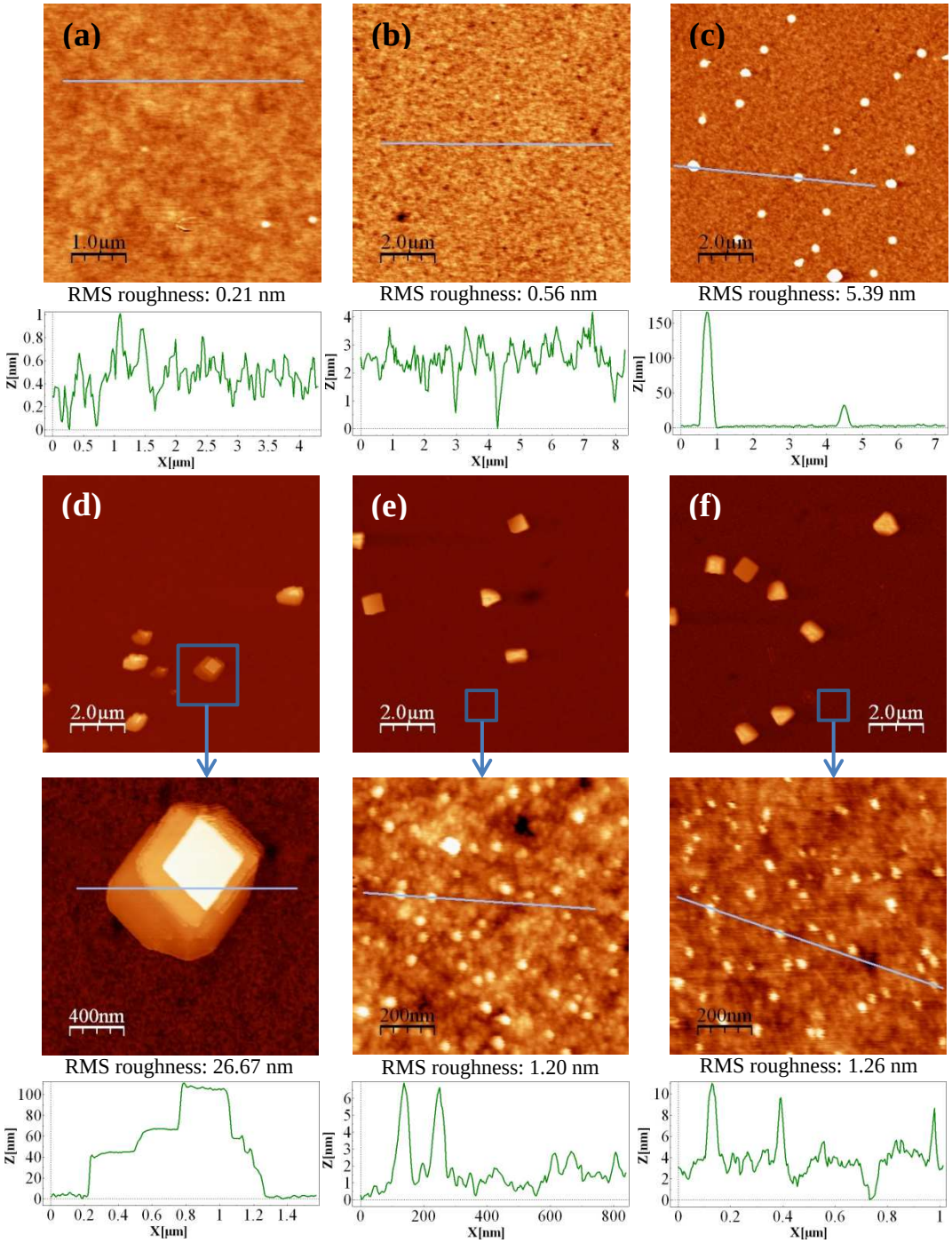


Fig. 5.17 Crystal development with time in 15PD-90 films (78 ± 8 nm) on annealing at 130 ℃: (a) as-spin-cast, (b) 4 hr, (c) 8 hr, (d) 16 hr, (e) 65 hr, (f) 125 hr. Crystalline aggregations form first and then develop into multilayer crystals.

The morphological development of as-spin-cast 15PD-90 films around 78 nm thick annealed at 130 ℃ for various times, Fig. 5.17, exemplified the development of large crystals. These AFM results allow us to have a better understanding of the growth of the crystal blocks in high HS-content polyurethane thin films. The annealing temperature was roughly 10 K over the bulk T_c of 15PD-90 (119 ℃, Table 5.2). At an early stage of annealing, e.g. after 4 hr annealing, ordering of the HS occurred resulting in surface pits with depth of one or two nanometres (Fig. 5.17b). Aggregations of heights between 20 nm and 160 nm were then observed after an 8 hr anneal (Fig. 5.17c), and after 16 hr annealing, only multilayer crystals with evident steps were found with similar heights to the earlier aggregations (Fig. 5.17d), suggesting they had developed from the preformed aggregations. This aggregation-crystallization process allows the polymer chains to arrange themselves into extraordinarily large lamellar crystal blocks with total thickness reaching hundreds of nanometres proud of the surface, because such ordering on this scale cannot occur within the thickness of these films. With more annealing time, the stepped crystals developed into crystal blocks and after 65 hr annealing developed no further (Fig. 5.17e&f).

On annealing for more than 65 hr, small aggregations were observed in the region between the large crystals and they gained a slight increase in height, roughly from 6 nm to 10 nm, as the annealing time increased from 65 hr to 125 hr (Fig. 5.17e&f). This might due to some degradation of polymer chains under long annealing. Previous work on 2M13PD-extended TPU samples [38] have indicated a substantial increase in the molecular weight and the molecular weight distribution after a 70 hr anneal at 160 ℃ due to the chain break and recombination. The annealing at 120 ℃ for such a long time or at 220 ℃ for a short time has little effect on the molecular weight. With a close melting temperature (Table 5.2), similar degradation is expected to occur in the 15PD-extended samples as well.

5.3.3.2 Crystal morphology

Large crystals of both a square and a “seaweed” morphology were observed in 2M13PD-90 thin films (73 ± 4 nm) annealed at 180 ℃ , a temperature greater than the T_M of the ordered HS structure and the T_{MMT} of bulk samples (Fig. A1, Table 5.2). These crystals can exist at a T_a above T_M presumably because they are so much larger than the ordered structures reported in bulk samples. Typical examples of such large crystals are shown in Fig. 5.18a-c, displaying substantial crystallites with both square blocks and seaweed morphology. The AFM height profile shows that the multilayer crystal blocks can now rise as high as 400 nm at this temperature, whereas the seaweed crystals rise approximately 100 to 200 nm from the surface. The seaweed morphology was more prevalent in this material with only a small proportion of square shaped crystals.

The multilayers of the 2M13PD-90 large crystals, with each “layer” or stage around 100 nm, are revealed by the height profile (Fig. 5.18a). It should be noted that AFM is not able to expose each individual crystalline lamella layer, which means that one stage could contain more than one crystal layer. Considering the rigidity of the MDI based HS, the formation of these large crystals is attributed to the plasticizing effect of the SS, which has a T_g around −73 ℃ [38]. With the ultrahigh mobility or fluidness of SS at a T_a around T_M or T_{MMT}, the HS/SS aggregation might be thought of as a good “solution” of HS in SS. In the aggregation-crystallization process, aggregations of HS/SS mixtures form first and then the crystallization of HS takes place promoting the irregular aggregations to a multilayer regular shaped crystal blocks. These regular-shaped crystals show a similarity to the multilayer single crystals of polymers, e.g. polyethylene, crystallized from dilute solution, with each lamellar layer typically 10 nm thick [41] (see section 2.1.2.2). The formation of the single crystals of a polymer from a dilute solution, however, requires the absence of chain entanglements. It could be conceived that the crystal blocks here are made up of HS single (or lamellar) crystal layers (flat-on arranged) with the SS existing between each layer (which act the role of a “good solvent” at T_a around T_M or T_{MMT}).

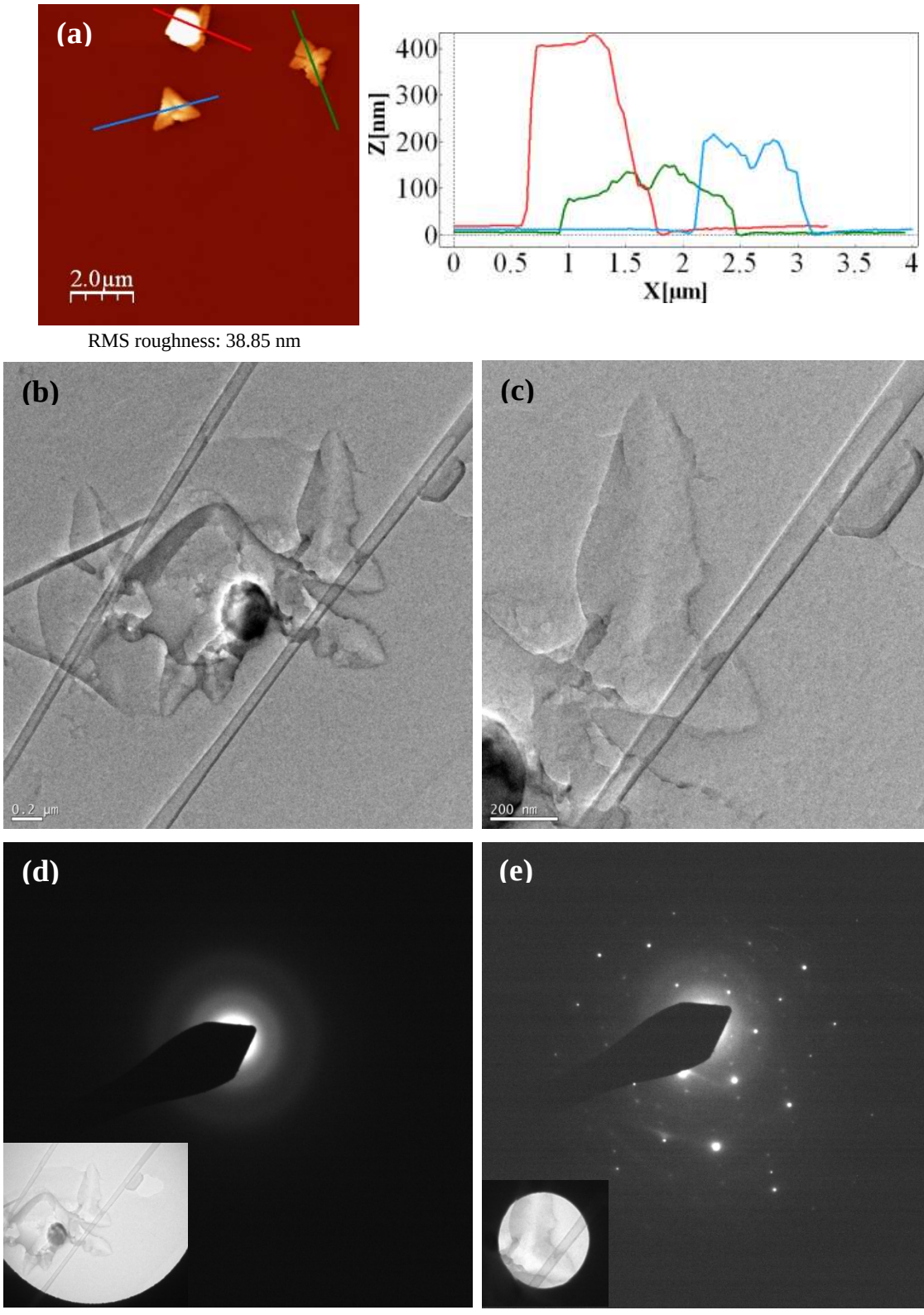


Fig. 5.18 Crystal morphology of 2M13PD-90 films (73 ± 4) annealed at 180 ℃ for 16 hr: (a) AFM height image with depth profile beside, (b)(c) large crystals, and (d)(e) selected-area diffraction pattern from (b)(c) respectively with the exact areas indicated in inserts.

Fig. 5.18b&c present TEM micrographs of the large crystals with corresponding electron diffraction patterns in Fig. 5.18d&e, respectively. The diffuse diffraction rings in Fig. 5.18d&e are associated with amorphous materials in the region between the large crystallites. When the diffraction area was selected to probe the seaweed crystals, diffraction spots were observed. This demonstrates the multiple crystalline orientations in these seaweed crystals as well. While the formation of the regular square crystal blocks is mainly the reorganisation of the HS and SS in aggregations generated at the early stage, the seaweed shape is thought to be a result of the lateral growth of the single crystals, e.g. initially started from the residual mesophase domains (as displayed Fig. 5.4f), a special kind of “HS/SS aggregations”. (Note that the HS/SS ration in the seaweed crystals could be different from that in the mesophase due to the crystal growth.) This compact seaweed morphology also implies a small anisotropy of the surface tension of surrounding mixture [186] at 180 ℃, which might be due to the incompat ibility between the HS and the SS.

- *Influence of chain extender*

In contrast to 2M13PD-extended TPU thin films, no seaweed flat-on crystals were observed in 15PD-extended TPU thin films of any composition with similar film thickness. This is probably because of the greatly increased HS/SS miscibility in 15PD-extended polyurethanes. In 2M13PD-extended TPU films (with some SS content), even over T_{MMT}, the miscibility between the HS and SS is low which might provide the small anisotropy of the surface tension of the surrounding materials required for seaweed crystal growth, whereas in the 15PD-extended TPU films good HS/SS miscibility at T_a over T_{MMT} or amorphous HS at T_a over T_M (for 15PD-100) gives rise to an isotropic surrounding medium to the nuclei which leads to the regular flat-on crystals only. Therefore, the choice of the chain extender affects not only the phase separation process but also the growth pattern of the large crystals.

- *Influence of soft block*

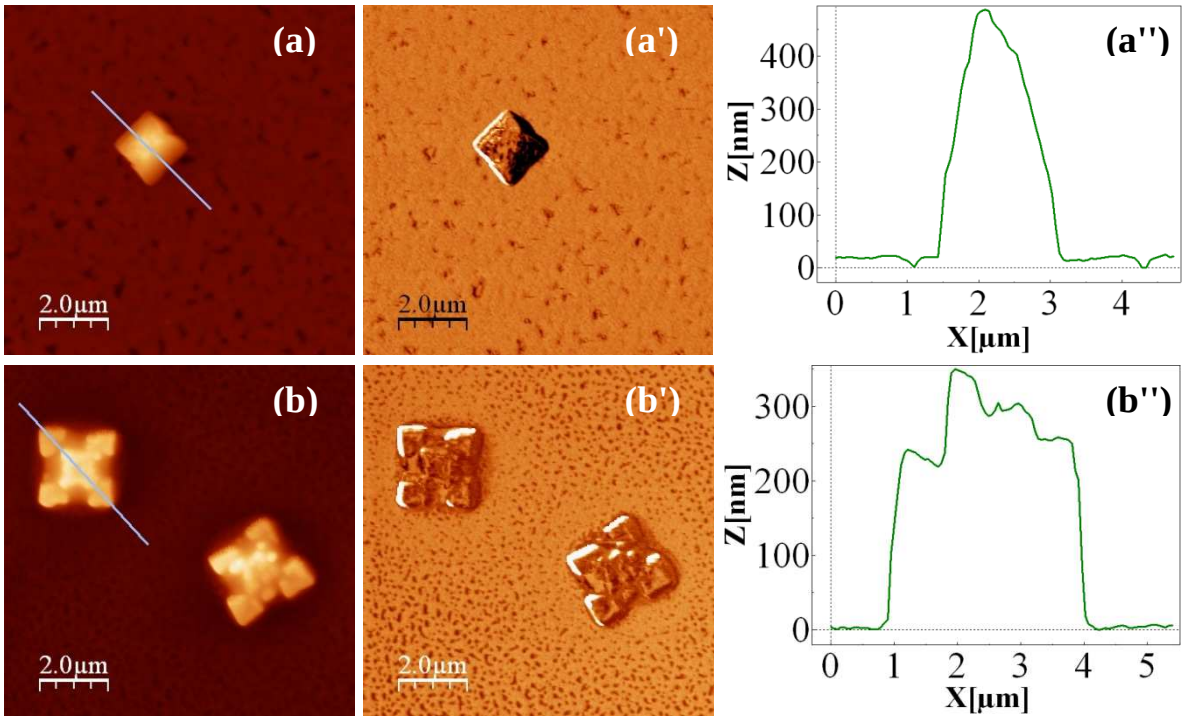


Fig. 5.19 Large crystals in 2M13PD-70 films (72 ± 6 nm) generated at (a) 160 ℃ and (b) 180 ℃ (16 hr) with corresponding phase images and height profile. These crystals are more “bulky” than these formed in 2M13PD-90 films (73 ± 4 nm) (Fig. 5.4f&5.17a).

No large crystals were found in the 2M13PD-100 (pure HS) sample on annealing, while large crystals were observed in the 15PD-100 sample. This implies a critical role for the soft segments in the case of 2M13PD-extended samples or the more flexible chain extender in 15PD-extended samples, in this crystallization. Indeed the morphology of the large crystals depends upon the composition of the TPU. For example, compared to the large crystals in 2M13PD-90 films (Fig. 5.4f&5.18a), those crystals obtained both at 160 ℃ and 180 ℃ in 2M13PD-70 films are more bulky (Fig. 5.19), with larger dimensions as presented in their height profiles and with less regularity. The morphological difference between the large crystals implies a different HS/SS ratio in the aggregations from that of the mesophase. For 2M13PD-70, it is the higher SS content in the aggregations that results in the less regularity and the more bulky morphology. When annealed at 180 ℃,

rather than forming seaweed crystals, only bulky crystals with subtly distinguished leaves were found in 2M13PD-70 films (Fig. 5.19b&b').

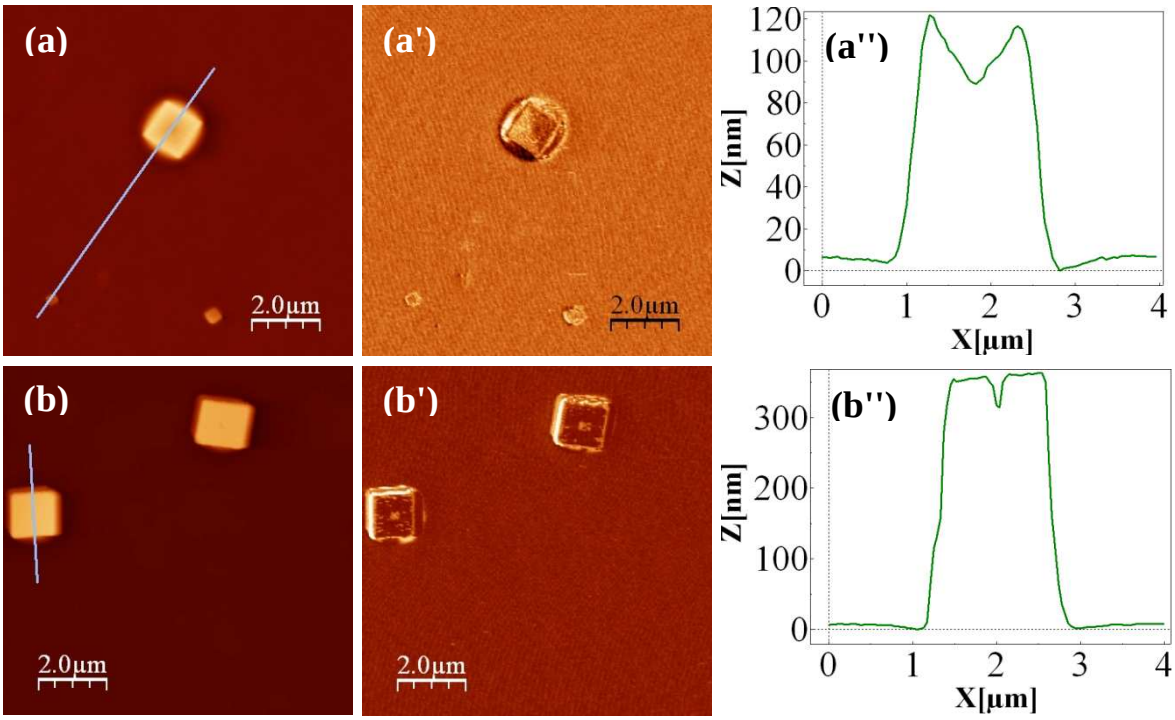


Fig. 5.20 Crystal blocks generated at 190 ℃ (16 hr) in film s of (a) 15PD-100 (69 ± 5 nm) and (b) 15PD-90 (78 ± 8 nm) with corresponding phase images and height profiles.

Bulky crystal blocks of 15PD-100 formed at 190 ℃ h ave perfect square shape in planar view (Fig. 5.15f&5.20a) but with an inverted pyramidal pit on the top, clearly indicated in phase image (Fig. 5.20a'). This specific morphology (only in the crystal blocks generated at 190 ℃) is not fully understood yet, however, a possible explanation is the ordering of materials towards the edges which causes the loss of the materials in the centre region of the block and leads to the pit. It is likely that the crystallization in regions close to the wall of the aggregations (precursor of the bulky crystals) where chain mobility is higher due to the free surface plays an important role. Yet, the crystallization within the aggregations may contribute as well since these aggregations might be considered a “good solution” of HS in SS. Further crystallization can decrease the size of the pits in the crystal blocks. This is what was found in 15PD-90 large crystals generated at the same T_a where, in the presence of SS, the mobility of polymer chains is much higher and the crystals were better

developed exhibiting a significant height enhancement (Fig. 5.20b, b'&b''). Height profiles of crystals in 15PD-100 and -90 films (Fig. 5.20a''&b'') show that, in a better developed crystallite, the side length of the pit is dramatically decreased, while the depth is similar.

- *Influence of interfaces*

The reason why these regular multilayer (flat-on) crystal blocks can reach such a high thickness, hundreds of nanometres, above the surface of the films is intriguing. Although the extraordinary aggregation-crystallization process explains the formation of these crystal blocks well, the large crystal blocks, e.g. these presented in Fig. 5.20b with height over 350 nm and side length around 2 μm, indicate a further crystal growth both in the lateral direction and upwards, out of the plane of the film. A typical example of the increase in crystal size with T_a can be obtained by comparing the crystals in 15PD-90 films generated at 170 ℃ (Fig. 5.21) and at 190 ℃ (Fig. 5.20b). It would seem that there are additional lamellar layers forming underneath the primary crystals (developed from the aggregations) and building up the very thick crystal blocks.

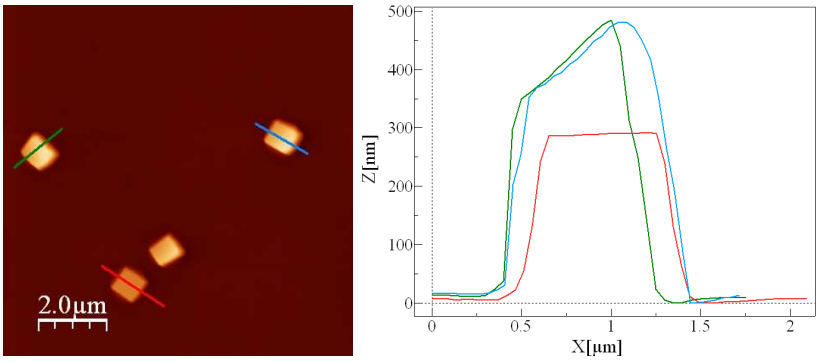


Fig. 5.21 Crystal blocks in a 15PD-90 (78 ± 8 nm) film annealed at 170 ℃ for 16 hr with corresponding height profiles

Wang *et al*. [127] reported that heterogeneous nucleation at the polymer-substrate interface lead to the generation of flat-on lamellae and at high temperatures, e.g. near T_m, and in very thin films these flat-on crystals can grow through the thickness direction and appear at the surface. This theory suggests that in the TPU thin films, it is possible that

the start of the flat-on crystalline orientation in the preformed aggregations (discussed in 5.3.3.1) is due to the flat-on crystals formed at the polymer-substrate interface. This explains why the multilayer crystal blocks were only found in films with thickness below 100 nm (section 5.3.1.3) since the growth of the flat-on lamellae originated at the polymer-substrate interface throughout the thickness direction requires a small film thickness. The further lateral growth of the multilayer crystals and the formation of the new lamellar crystal layers underneath the crystal blocks, however, are attributed to ultrahigh chain mobility induced by the free surface (the polymer-air interface) as the chain mobility in the bulk of the film or at the polymer-substrate layer is much lower.

- *Influence of annealing temperature*

AFM results (Fig. 5.15d-f) show that the growth and geometry of the 15PD-extended HS crystals rely much on the initial growth states of nuclei: some have lamellar layers roughly parallel to the polymer surface and the others have lamellar layers oblique to, crossing, the surface. Annealed at 150 ℃ (Fig. 5.15d), those crystals with lamellar layers parallel to the film surface were square-shaped with height around 35 nm, while the crystals with lamellar layers oblique to the surface appeared less regular and may be as high as 70 nm. This difference enlarged when the film was annealed at 170 ℃ (Fig. 5.15e). A possible explanation is the anisotropy of the polymer surface due to HS ordering, which is controlled by T_a. With the surrounding materials being amorphous and highly mobile at temperatures over T_M, a perfect square-shaped multilayer flat-on crystal is more likely to be generated, whereas at T_a below T_M, with ordered HS regions around the growth direction of formed lamellar layers is likely affected. That is why for even higher T_a, e.g. 190 ℃ (Fig. 5.15f), where no HS crystalline domains exist, all the large crystals show a perfect regular morphology.

The different thermodynamics for the development of the large crystals at various T_a have also been manifested by the different morphologies of crystals in 15PD-70 and -90 films

annealed at different temperatures. Examples from 15PD-90 films (around 78 nm thick) are presented in Fig. 5.21. For a 16-hr anneal, the large 15PD-90 crystals have a morphology with facets, e.g. pyramidal (Fig. 5.22a&a'), at 120 ℃, with steps at 130 ℃ (Fig. 5.17d), and start to have a square-shaped appearance by 140 ℃ (Fig. 5.22b&b'). They mainly exist in the form of square-shaped blocks at T_a over T_M (Fig. 5.22c&5.20b). Again, the results here clearly show that in the temperature region over T_M or T_{MMA}, the lamellar layers in the large crystals tend to lie parallel to the film surface, while in the lower temperature region, e.g. over T_c and below T_M, the lamellar layers can lie obliquely, crossing the surface or even be perpendicular to the surface.

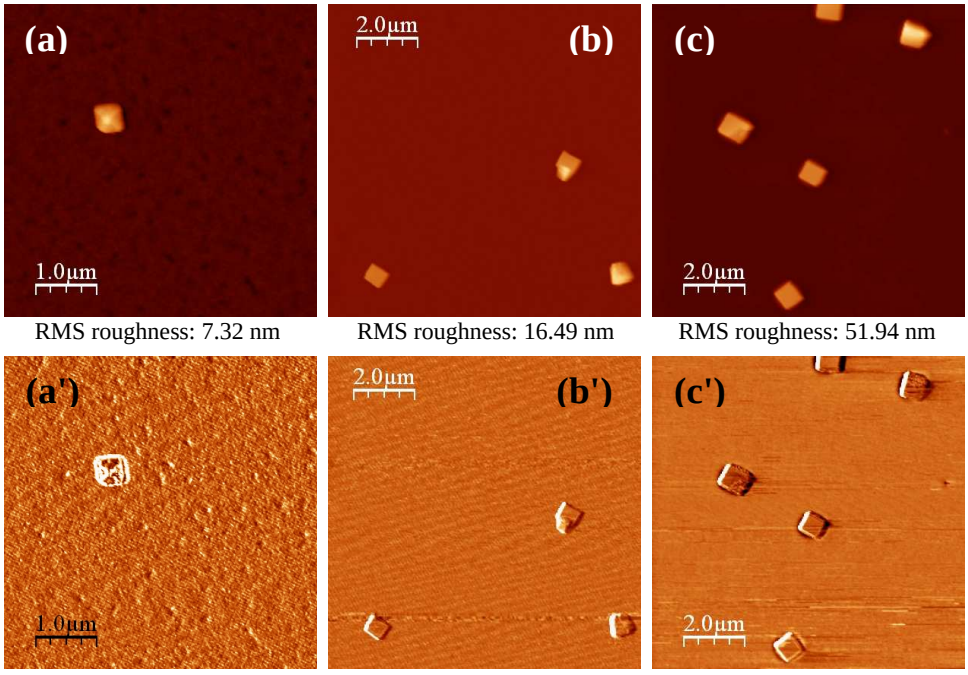


Fig. 5.22 AFM height images of as-spin-cast 15PD-90 films (78 ± 8 nm) after 16 hr annealing at (a) 120 ℃, (b) 140 ℃, and (e) 170 ℃, with corres ponding phase images beneath. Note the scale changes in images.

With a sufficiently long annealing time, e.g. 448 hr, aggregations can already be observed in 15PD-extended TPU thin (around 75 nm) annealed at temperatures as low as 100 ℃ (Fig. 5.23). This temperature is over the T_c of bulk 15PD-70, but in the temperature range T_g-T_c for bulk samples of 15PD-90 and 15PD-100 (Table 5.2). At this low a T_a, the crystallites in the 15PD-100 film are still in the form of aggregations with height in the

range 10-25 nm even after a 448 hr anneal (Fig. 5.23c) without rearranging themselves into regular-shaped crystals such as that in the sample annealed at 150 ℃ for 16 hr (Fig. 5.15d). This is due to the much lower chain mobility at 100 ℃. At the same annealing condition, both 15PD-70 and 15PD-90 films show a snowflake-like pattern made up of aggregations, which indicates the tendency to form aggregations at the growth front of primary aggregations. The large dimensions of the aggregation in the 15PD-70 and 15PD-90 films (line profiles in Fig. 5.23a&b), however, indicate a requirement for super high chain mobility, which could be possible due to the free surface effect. Results here show that T_a has a significant influence not only on the crystallization rate, but also on the crystalline morphology.

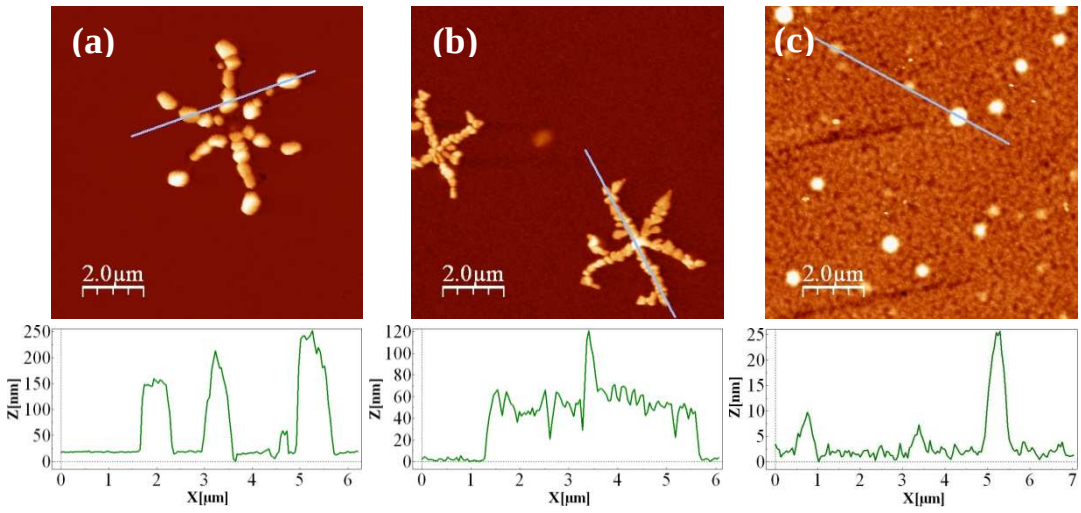


Fig. 5.23 AFM topography images of 15PD extended films annealed at 100 ℃ for 448 hr: (a) 15PD-70 (79 ± 4 nm), (b) 15PD-90 (78 ± 8 nm) and (c) 15PD-100 (69 ± 5 nm).

- *Influence of film thickness*

As indicated by the 2M13PD-extended TPU thin films, the generation of the multilayer large crystals requires a film thickness below around 100 nm. However, the confinement of chains in the film and possible substrate interactions reduces their mobility, meaning that a greater annealing temperature is required to induce aggregations and crystal formation. For instance, in 15PD-70 thin films around 79 nm thick aggregations form after

a 16 hr anneal at 80 ℃ (Fig. 5.24b), whereas for 3 6 nm thick films, such aggregations do not form until the film is annealed for 16 hr at 140 ℃ (Fig. 5.24a).

With increasing film thickness, HS/SS phase separation in 15PD-extended TPU films is likely to take place. As displayed in Fig. 5.24c, a 156 nm thick 15PD-90 film annealed at 160 ℃ for 16 hr shows some domains, whereas, for t he same annealing condition, multilayer crystal blocks are expected for a 15PD-90 film around 78 nm. The result here suggests that the restricted HS/SS phase separation in 15PD-extended thin films with thickness below 100 nm is not just due to the flexile 15PD but also a result of spatial confinement. This is consistent with bulk work on high HS content 15PD-extended TPUs where both crystallization and phase separation were found, indicated by the multiple melting endotherms in DSC traces (Fig. A1d&e).

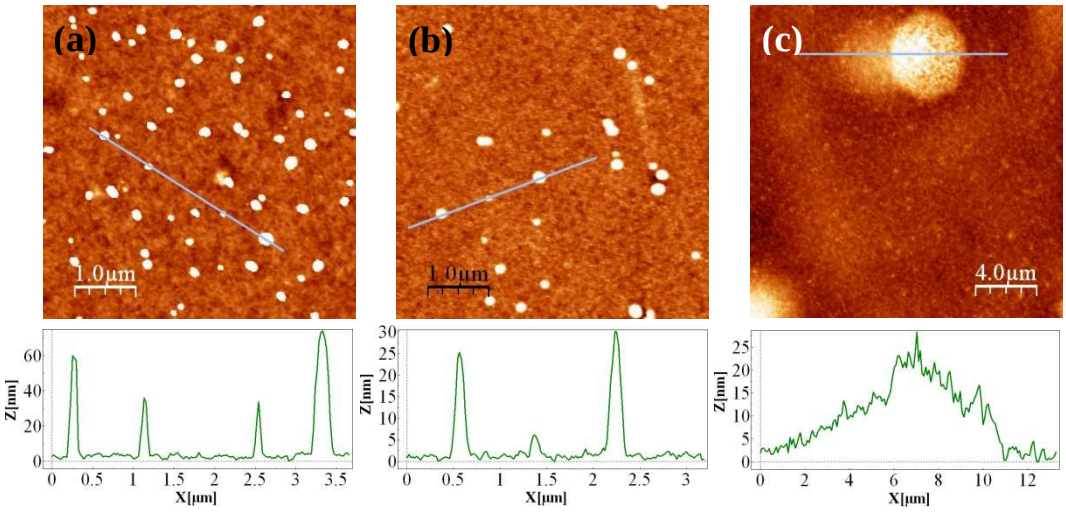


Fig. 5.24 AFM topography images of annealed (16 hr) 15PD-70 films (a) 36 ± 4 nm, T_a = 140 ℃, (b) 79 ± 4 nm, T_a = 80 ℃ and 15PD-90 films (c) 156 ± 4 nm, T_a = 160 ℃.

5.4 CONCLUSIONS

The morphological evolution in TPU thin films of high HS content (70-100 wt%) on annealing have been analysed and show many similarities with bulk behaviour. Rather than having a two-phase morphology in melt-quenched bulk 2M13PD-extended TPU samples, a single-phase morphology is obtained in as-spin-cast thin films. However, the HS ordering, the formation of a phase-separated mesophase domain, and the microphase mixing process detected in thin films on annealing agree well with the bulk results from DSC, scattering and TEM, despite the slight differences in transition temperatures due to spatial confinement. These thin-film observations are able to give a better insight into the bulk microstructures, e.g. by directly imaging the microphase-separated mesophase domains using AFM. Decreased HS content allows lower-temperature phase separation and crystallization, yet TPU films with various HS contents show a similar morphological evolution on annealing. Increasing the film thickness can accelerate and enlarge the various morphological developments. Extended by a more flexible diol, 15PD, the HS/SS compatibility is greatly enhanced. In annealed 15PD-extended TPU films of similar thickness, it is principally crystallization processes that are observed, and no formation of microphase-separated domains is detected.

Special multilayer flat-on crystal blocks were observed in annealed TPU thin films and could even be detected in samples annealed over T_M or T_{MMT} of bulk samples. These large crystals are a specifically thin-film phenomenon very likely induced by the free surface and the flat-on lamellae originated at the polymer-substrate interface (film thickness dependent), being only observed in thin films with thickness below 100 nm. The generation of these large crystals is based on an aggregation-crystallization process as revealed in 15PD-extended TPU thin films: aggregations form first and then the irregular aggregations transform into multilayer regular-shaped crystal blocks. The morphology of these crystals is influenced by the flexibility of the chain extender, the HS/SS ratio of the TPU, and the HS orderings in the surrounding matrix (which relies on T_a).

6 SUMMARY

In this project, three thin film systems were investigated including: polyamide thin films, PS/PMMA blend thin films, and high hard block content TPU thin films. It was the first time that the existence of surface-specific crystallization had been proven in polyamide systems, which crystallize readily. Also, with immiscible PS/PMMA thin films, the possibility of surface-specific phase separation in the near-surface region at a much lower temperature than the bulk phase separation temperature had been confirmed for the first time. The observation of the flat-on PS surface crystals was another interesting discovery, while before only edge-on surface-specific crystals had been found. Furthermore, the investigation of the TPU thin films, giving better insight into the bulk microstructures, was an important supplementary to the results from bulk samples. In addition, special multilayer flat-on crystal bocks with thickness over hundreds of nanometres were observed in annealed TPU thin films. It was the first time that such crystals were observed in polymer thin films.

The work on polyamide and PS/PMMA systems together showed that the free surface effect would lead to surface-specific crystallization or phase separation at much lower temperatures. This conclusion not only is significant in understanding the physical behaviours of polymers but also shows promising industrial applications, e.g. modify or pattern surface of polymers at a much lower temperature, which means energy saving and lower costs. Since no such surface-specific behaviour was observed in TPU thin films, the focus of this system is different. However, the free surface effect is believed to contribute to the formation of the large crystal blocks.

7 CONCLUSIONS

The main objective of this project is to investigate crystallization and phase separation in different polymer systems with particular interests in the effect of the free surface. To date surface-specific crystallization which can take place at temperatures well below bulk crystallization temperature has only been observed in a few polymers. The range of semicrystalline polymers in which this surface-specific crystallization occurs is yet to be established. Similar to crystallization, phase separation specific to the near-surface region, occurring at temperatures lower than the bulk phase separation temperature, is also expected. This work is also aimed to study the possibility of such surface-specific phase separation. The thin film behaviours of a block copolymer that undergoes both phase separation and crystallization are also the interests of this project.

7.1 SURFACE-SPECIFIC CRYSTALLIZATION

Polyamides represent a group of flexible-chained polymers with some degree of hydrogen bonding that crystallize readily. Spin-coating PA12 results in as-spin-cast 2D crystals with morphologies depending on solvent evaporation rate and film thickness. Two crystalline morphologies: shuttle-like and lamellar, were discovered both with a γ crystalline form, the most stable crystalline phase for PA12. In spite of the as-spin-cast crystals, the free surface allows a secondary surface crystallization process of PA12 at a T_a roughly 20 ℃ below the bulk crystallization temperature, which was confirmed by the significant change in surface morphology. While the secondary crystals in bulk samples are expected to be α or α' form [249, 272], the secondary surface crystals were indicated to be the γ form by the constant γ crystalline distribution of annealed PA12 film. This shows that surface crystals tend to be in the most stable crystalline phase of a polymer. A similar secondary surface

crystallization has also been observed in the PA6 films but at a higher T_a due to the higher T_g of PA6.

Surface-specific crystals have also been observed in the PS (semicrystalline due to the isotactic or syndiotactic composition), a polymer with bulky side groups. This supports the universality of the surface crystallization phenomenon. However, rather than the edge-on surface crystals in PET, PEN, PVOH and PA12 films (with a similar thickness), the PS surface crystals are flat-on oriented showing the important effect of side groups on the morphology or growth shape of surface crystals.

No such surface-specific crystallization was found in TPU (having EO-PPO-EO as the SS and 2M13PD or 15PD extended MDI as the HS) films, where the HS is crystalline, on annealing. This is possibly due to the molecular structure of the TPU. Nevertheless, special multilayer flat-on crystal blocks with total thickness reaching hundreds of nanometres proud of the surface were observed in annealed TPU thin films. These large crystals are only found in the thinner films and their large growth may depend heavily on the free surface.

The investigations of thin-films crystallization to date indicate that surface-specific crystallization is more likely to take place in a polymer that could form spherulites in the bulk, e.g. PET, PEN, PVOH and PA, or flat-on crystals in the ultrathin films (iPS or sPS), rather than small-scale crystalline aggregations, such as in the TPUs.

7.2 SURFACE-SPECIFIC PHASE SEPARATION

Using the immiscible PS/PMMA thin film system, it was confirmed that a polymer blend can have a surface-specific phase separation at a much lower temperature than its bulk phase separation temperature due to the lower T_g in the near-surface region. With a fast solvent quenching, it is possible to “freeze in” a two-phase morphology in the near-surface

region. Annealing at temperatures well above T_g, a PS/PMMA film undergoes bulk vertical phase separation and dewetting of PS to PMMA, forming holes, network structures and islands. Annealing around or just below the bulk polymer T_g, leads to surface-specific phase separation: pits, undulations and peaks confined to the near-surface region. This surface-specific phenomenon, being a result of the free surface, should be applied widely to phase separation systems with a free surface. An increase in crystallizability of PS was found to promote the phase separation process. However, the observation of surface-specific phase separation remains constant indicating that the free surface effect is not dependent on an interplay between the crystallization and phase separation.

7.3 CRYSTALLIZATION AND PHASE SEPARATION IN TPU THIN FILMS

The melt-quenched bulk 2M13PD-extended TPU of high HS content (above 70 wt%) has a two-phase morphology: a continuous hard phase and domains of mixed phase. On annealing there will be a microphase separation in the mixed phase forming microphase-separated mesophase domains. Plasticized by the SS, the HS in the mixed phase could crystallize at T_a below T_{gHP}, while the HS ordering in the hard phase requires T_a above T_{gHP}. A corresponding HS/SS microphase mixing takes place after the melting of the HS ordered regions [291].

In contrast to the bulk case, spin coating produces thin films with a single phase. On annealing, microphase-separated mesophase domains develop directly from the as-spin-cast mixed phase without the formation of the two-phase morphology indicated by the melt-quenched samples. The HS ordering, the formation of mesophase, the melting of HS ordered regions, and microphase mixing observed in thin films are consistent with the bulk results but with slightly different transition temperatures because of spatial confinement. With a softer chain extender, e.g. 15PD, the HS/SS phase separation is restricted. The thin film investigations allow a better understanding of the microstructural

evolution in these high hard block content TPUs on annealing by imaging the morphology directly.

Another phenomenon that is specific to thin films is the discovery of the large multilayer crystals in these TPU thin films initially developed from preformed aggregations. The appearance of these crystal blocks is believed to be the result of both the free surface effect and the significant substrate effect in thin films, e.g. with thickness below 100 nm.

The failure to observe surface-specific phase separation in these TPU thin films might be attributed to hindrance from the HS ordering.

7.4 FUTURE WORK

There are several questions worth exploration in the future. Firstly, for a better understanding of surface-specific crystallization or phase separation, it is necessary to clear the influence of entanglement, e.g. to compare the surface behaviours in polymers with molecular weight below and well above their critical entanglement molecular weight. In this project, surface-specific phase separation occurring at a lower temperature than bulk phase separation temperature was firstly confirmed using the immiscible PS/PMMA blend, which is a UCST system. Yet, the surface-specific phase separation in a LCST system, e.g. PS/PVME, where the blend is miscible at start is another interesting research topic. (This kind of system can have a homogeneous mixture at the surface, but observation of the very beginning of phase separation might have difficulties due to the weak repulsive interactions between the two polymers just after the transition from miscible to immiscible.) The possibility of surface-specific phase separation in block copolymer systems, e.g. block copolymers of PS and PMMA, is also a question, although no such surface-specific phase separation were observed in TPUs in this project. In addition, understanding the thermodynamic behind the formation of the large multilayer TPU crystals could be a next-stage investigation as well.

REFERENCES

[1] F. Pardos, *Plastic Films: Situation and Outlook: a Rapra market report*: Rapra Technology Limited, 2004.

[2] O. K. C. Tsui and T. P. Russell, *Polymer Thin Films*: World Scientific, 2008.

[3] P. J. Lemstra, "Materials Science: Confined Polymers Crystallize," *Science,* vol. 323, 2009.

[4] C. S. S. R. Kumar, *Nanomaterials for the Life Science Vol.5:Nanostructured Thin Films and Surfaces*: WILEY-VCH Verlag GmbH & Co. KGaA, Weinheim, 2010.

[5] H. E. Katz and J. Huang, "Thin-Film Organic Electronic Devices," *Annual Review of Materials Research,* vol. 39, pp. 71-92, 2009.

[6] B. Kippelen and J.-L. Bredas, "Organic Photovoltaics," *Energy & Evironmental Science,* vol. 2, pp. 251-261, 2009.

[7] J. Lewis, "Material Challenge for Flexible Organic Devices," *Materials Today,* vol. 9, pp. 38-45, 2006.

[8] R. A. Segalman, B. McCulloch, S. Kirmayer, and J. J. Urban, "Block Copolymers for Organic Optoelectronics," *Macromolecules,* vol. 42, pp. 9205-9216, 2009.

[9] M. J. Brown, A. R. Hillman, S. J. Martin, R. W. Cernosek, and H. L. Bandey, "Manipulation of Electroactive Polymer Film Viscoelasticity: the Roles of Applied Potential and Frequency," *Journal of Materials Chemistry,* vol. 10, pp. 115-126, 2000.

[10] J. H. Burroughes, D. D. C. Bradley, A. R. Brown, R. N. Marks, K. Mackay, R. H. Friend*, et al.*, "Light-Emitting Diodes Based on Conjugated Polymers," *Nature,* vol. 347, pp. 539-541, 1990.

[11] Q. Pei, G. Yu, C. Zhang, Y. Yang, and A. J. Heeger, "Polymer Light-Emitting Electrochemical Cells," *Science,* vol. 269, pp. 1086-1088, 1995.

[12] M. Granstrom, M. Berggren, and O. Inganas, "Micrometer- and Nanometer-Sized Polymeric Light-Emitting Diodes," *Science,* vol. 267, pp. 1479-1481, 1995.

[13] J. S. Lewis and M. S. Weaver, "Thin-Film Permeation-Barrier Technology for Flexible Organic Light-Emitting Devices," *IEEE Journal of Selected Topics in Quantum Electronics,* vol. 10, pp. 45-57, 2004.

[14] T. W. Kelley, D. V. Muyres, P. F. Baude, T. P. Smith, and T. D. Jones, "High Performance Organic Thin Film Transistors," *Materials Research Society Symposia Proceedings,* vol. 771, pp. L6.5.1-L6.5.11, 2003.

[15] H. Klauk, "Organic Thin-Film Transistors," *Chemical Society Reviews,* vol. 39, pp. 2643-2666, 2010.

[16] G. Dennler, C. Lungenschmied, H. Neugebauer, N. S. Sariciftci, M. Latreche, G. Gzeremuszkin*, et al.*, "A New Encapsulation Solution for Flexible Organic Solar Cells," *Thin Solid Films,* vol. 511-512, pp. 349-352, 2006.

[17] K. M. Coakley and M. D. McGehee, "Conjugated Polymer Photovoltaic Cells," *Chemistry of Materials,* vol. 16, pp. 4533-4542, 2004.

[18] W. U. Huynh, J. J. Dittmer, and A. P. Alivisatos, "Hybrid Nanorod-Polymer Solar Cells," *Science,* vol. 295, pp. 2425-2427, 2002.

[19] G. Yu, J. Gao, J. C. Hummelen, F. Wudl, and A. J. Heeger, "Polymer Photovoltaic Cells: Enhanced Efficiencies via a Network of Internal Donor-Acceptor Heterojunctions," *Science,* vol. 270, pp. 1789-1791, 1995.

[20] C. W. Frank, V. Rao, M. M. Despotopoulou, R. F. W. Pease, W. D. Hinsberg, R. D. Miller*, et al.*, "Structure in Thin and Ultrathin Spin-Cast Polymer Films," *Science,* vol. 273, pp. 912-915, 1996.

[21] C. B. Roth and J. R. Dutcher, "Glass Transition and Chain Mobility in Thin Polymer Films," *Journal of Electroanalytical Chemistry,* vol. 584, pp. 13-22, 2005.

[22] J. A. Forrest, K. Dalnoki-Veress, J. R. Stevens, and J. R. Dutcher, "Effect of Free Surfaces on the Glass Transition Temperature of Thin Polymer Films," *Physical Review Letters,* vol. 77, p. 2002, 1996.

[23] J. A. Forrest, K. Dalnoki-Veress, and J. R. Dutcher, "Interface and Chain confinement Effects on the Glass Transition Temperature of Thin Polymer Films," *Physical Review E,* vol. 56, pp. 5705-5716, 1997.

[24] J. S. Sharp and J. A. Forrest, "Free Surface Cause Reductions in the Glass Transition Temperature of Thin Polystyrene Films," *Physical Review Letters,* vol. 91, pp. 235701-1-4, 2003.

[25] A. M. Mayes, "Glass Transition of Amorphous Polymer," *Macromolecules,* vol. 27, pp.

3114-3115, 1994.
[26] A. N. Raegen, M. V. Massa, J. A. Forrest, and K. Dalnoki-Veress, "Effect of Atmosphere on Reductions in the Glass Transition of Thin Polystyrene Films," *The European Physical Journal E,* vol. 27, pp. 375-377, 2008.
[27] K. Shinotsuka, V. N. Bliznyuk, and H. E. Assender, "Near-surface Crystallization of PET," *Polymer,* vol. 53, pp. 5554-5559, 2012.
[28] K. Shinotsuka, "Crystallization in Thin Films of Polymers and Copolyesters," The Department of Materials, The University of Oxford, 2009.
[29] M. Thomas, "Surface Modification of Poly(vinyl Alcohol)," Department of Materials, University of Oxford, 2012.
[30] L. Xue, J. Zhang, and Y. Han, "Phase Separation Induced Ordered Patterns in Thin Polymer Blend Films," *Progress in Polymer Science,* vol. 37, pp. 564-594, 2012.
[31] L. Li, S. Sosnowski, C. E. Chaffey, S. T. Balke, and M. A. Winnik, "Surface Morphology of a Polymer Blend Examined by Laser Confocal Fluorescence Microscopy," *Langmuir,* vol. 10, pp. 2495-2497, 1994.
[32] C. Ton-That, A. G. Shard, R. Daley, and R. H. Bradley, "Effects of Annealing on the Surface Composition and Morphology of PS/PMMA Blend," *Macromolecules,* vol. 33, pp. 8453-8459, 2000.
[33] C. Ton-That, A. G. Shard, D. O. H. Teare, and R. H. Bradley, "XPS and AFM Surface Studies of Solvent-cast PS/PMMA Blends," *Polymer,* vol. 42, pp. 1121-1129, 2001.
[34] K. Tanaka, A. Takahara, and T. Kayiyama, "Film Thickness Dependence of the Surface Structure of Immiscible Polystyrene/Poly(methyl methacrylate) Blends," *Macromolecules,* vol. 29, pp. 3232-3239, 1996.
[35] C. Ton-That, A. G. Shard, and R. H. Bradley, "Surface Feature Size of Spin Cast PS/PMMA Blends," *Polymer,* vol. 43, pp. 4973-4977, 2002.
[36] S. Y. Heriot and R. A. L. Jones, "An Interfacial Instability in a Transient Wetting Layer Leads to Lateral Phase Separation in Thin Spin-Cast Polymer-Blend Films," *Nature Materials,* vol. 4, pp. 782-786, 2005.
[37] J. T. Koberstein and R. S. Stein, "Small-Angle X-Ray Scattering Studies of Microdomain Structure in Segmented Polyurethane Elastomers," *Journal of Polymer Science: Polymer Physics Edition,* vol. 21, pp. 1439-1472, 1983.
[38] A. Saiani, W. A. Daunch, H. Verbeke, J. W. Leenslag, and J. S. Higgins, "Origin of Multiple Melting Endotherms in a High Hard Block Content Polyurethane. 1. Thermodynamic Investigation," *Macromolecules,* vol. 34, pp. 9059-9068, Dec 2001.
[39] L. Mandelkern, *Crystallization of Polymers. Volume 1. Equilibrium Concepts*, Second ed. vol. 1: Cambridge University Press, 2002.
[40] F. W. Billmeyer, *Textbook of Polymer Science*, Third ed.: John Wiley & Sons, 1984.
[41] D. V. Rees and D. C. Bassett, "The Texture of Crystalline Polymers: A Brief Review," *Journal of Materials Science,* vol. 6, pp. 1021-1035, 1971.
[42] M. Muthukumar, "Commentary on Theories of Polymer Crystallization," *The European Physical Journal E,* vol. 3, pp. 199-202, 2000.
[43] J. M. G. Cowie and V. Arrighi, *Polymers: Chemistry and Physics of Modern Materials*, Third ed.: CRC Press, 2008.
[44] K. A. Jackson, *Kinetic Processes: Crystal Growth, Diffusion, and Phase Transitions in Materials*: Wiley-VCH, 2004.
[45] R. S. Stein and J. Powers, *Topics in Polymer Physics*: Imperial College Press, 2006.
[46] A. Sharples, *Introduction to Polymer Crystallization*: Edward Arnold Ltd., 1966.
[47] U. W. Gedde, *Polymer Physics*: Chapman & Hall, 1995.
[48] W. M. D. Bryant, "Polythene Fine Structure," *Journal of Polymer Science,* vol. 2, pp. 547-564, 1947.
[49] P. J. Flory, "Thermodynamics of Crystallization in High Polymers. IV. A Theory of Crystalline States and Fusion in Polymers, Copolymers, and Their Mixtures with Diluents.," *The Journal of Chemical Physics,* vol. 17, pp. 223-240, 1949.
[50] R. Jaccodine, "Observations of Spiral Growth Steps in Ethylene Polymer," *Nature,* vol. 176, pp. 305-306, 1955.
[51] A. Keller, "A Note on Single Crystals in Polymers: Evidence for a Folded Chain Configuration," *Philosophical Magazine,* vol. 2, pp. 1171-1175, 1957.
[52] P. H. Till, "The Growth of Single Crystals of Linear Polyethylene," *Journal of Polymer Science,* vol. 24, pp. 301-306, 1957.
[53] D. H. Reneker and P. H. Geil, "Morphology of Polymer Single crystals," *Journal of Applied*

Physics, vol. 31, pp. 1916-1925, 1960.
[54] P. J. Flory, "On the Morphology of the Crystalline state in Polymers," *Journal of the American Chemical Society,* vol. 84, pp. 2857-2867, 1962.
[55] C. W. Bunn and T. C. Alcock, "The Texture of Polythene," *Transactions of the Faraday Society,* vol. 41, pp. 317-325, 1945.
[56] G. R. Strobl, *The Physics of Polymers: Concepts for Understanding Their Structures and Behaviour*, Second ed.: Springer-Verlag, 1997.
[57] M. A. Kotnis and M. Muthukumar, "Entropy-induced Frozen Morphology in Unstable Polymer Blends," *Macromolecules,* vol. 25, pp. 1716-1724, 1992.
[58] J. A. Manson and L. H. Sperling, *Polymer Blends and Composites*: Plenum Press, 1976.
[59] F. S. Bates, "Polymer-Polymer Phase Behavior," *Science,* vol. 251, pp. 898-905, 1991.
[60] D. R. Paul and C. B. Bucknall, *Polymer Blends Volume 1: Formulation*: John Wiley & Sons, 2000.
[61] P. J. Flory, "Thermodynamics of High Polymre Solutions," *Journal of Chemical Physics,* vol. 10, pp. 51-61, 1942.
[62] M. L. Huggins, "Some Properties of Solutions of Long-chain Compounds," *The Journal of Physical Chemistry,* vol. 46, pp. 151-158, 1942.
[63] R. Koningsveld, W. H. Stockmayer, and E. Nies, *Polymer Phase Diagrams: A Text Book*: Oxford University Press, 2001.
[64] A. Karim and S. Kumar, *Polymer Surfaces, Interfaces and Thin Films*: World Scientific, 2000.
[65] R. Jones, "The Dynamics of Thin Polymer Films," *Current Opinion in Colloid & Interface Science,* vol. 4, pp. 153-158, 1999.
[66] Z. Fakhraai, "Dynamics of Polymer Thin Films and Surfaces," Doctor of Philosophy, University of Waterloo, 2007.
[67] J. A. Forrest and Dalnoki-Veress, "The Glass Transition in Thin Polymer Films," *Advances in Colloid and Interface Science,* vol. 94, pp. 167-196, 2001.
[68] M. Alcoutlabi and G. B. McKenna, "Effects of Confinement on Material Behaviour at the Nanometre Size Scale," *Journal of Physics: Condensed Matter,* vol. 17, pp. R461-R524, 2005.
[69] G. Reiter, "Mobility of Polymers in Films Thinner than Their Unperturbed Size," *Europhysics Letters,* vol. 23, pp. 579-584, 1993.
[70] B. Frank and A. P. Gast, "Polymer Mobility in Thin Films," *Macromolecules,* vol. 29, pp. 6531-6534, 1996.
[71] K. C. Tseng, N. J. Turro, and C. J. Durning, "Molecular Mobility in Polymer Thin Films," *Physical Review E,* vol. 61, pp. 1800-1811, 2000.
[72] H. Liem, J. Cabanillas-Gonzalez, P. Etchegoin, and D. D. C. Bradley, "Glass Transition Temperatures of Polymer Thin Films Monitored by Raman Scattering," *Journal of Physics: Condensed Mater,* vol. 16, pp. 721-728, 2004.
[73] C. L. Jackson and G. B. McKenna, "The Glass Transition of Organic Liquids Confined to Small Pores," *Journal of Non-Crystalline Solids,* vol. 131-133, pp. 221-224, 1991.
[74] J. L. Keddie, R. A. L. Jones, and R. A. Cory, "Size-Dependent Depression of the Glass Transition Temperature in Polymer Films," *Europhysics Letters,* vol. 27, 1994.
[75] J. L. Keddie, R. A. L. Jones, and R. A. Cory, "Interface and Surface Effects on the Glass-Transition Temperature in Thin Polymer Films," *Faraday Discussions,* vol. 98, pp. 219-230, 1994.
[76] J. L. Keddie and R. A. L. Jones, "Depression of the Glass Transition Temperature in Ultra-Thin, Grafted Polystyrene Films," *MRS Proceedings,* vol. 366, pp. 183-188, 1995.
[77] O. Prucker, S. Christian, H. Bock, J. Ruhe, C. W. Frank, and W. Knoll, "On the Glass Transition in Ultrathin Polymer Films of Different Molecular Architecture," *Macromolecular Chemistry and Physics,* vol. 199, pp. 1435-1444, 1998.
[78] J. H. Kim, J. Jang, and W. C. Zin, "Estimation of the Thickness Dependence of the Glass Transition Temperature in Various Thin Polymer Films," *Langmuir,* vol. 16, pp. 4064-4067, 2000.
[79] S. Herminghaus, K. Jacobs, and R. Seemann, "The Glass Transition of Thin Polymer Films: Some Questions, and a Possible Answer," *The European Physical Journal E,* vol. 5, pp. 531-538, 2001.
[80] Y. Grohens, L. Hamon, G. Reiter, A. Soldera, and Y. Holl, "Some Relevant Parameters Affecting the Glass Transition of Supportd Ultra-Thin Polymer Films," *The European Physical Journal E,* vol. 8, pp. 217-224, 2002.

[81] L. Singh, p. J. Ludovice, and C. L. Henderson, "Influence of Molecular Weight and Film Thickness on the Glass Transition Temperature and Coefficient of Thermal Expansion of Supported Ultrathin Polymer Films," *Thin Solid Films,* vol. 449, pp. 231-241, 2004.
[82] P. G. de Gennes, "Glass Transitions in thin Polymer Films," *The European Physical Journal E,* vol. 2, pp. 201-205, 2000.
[83] K. Fukao and Y. Miyamoto, "Glass Transitions and Dynamics in Thin Polymer Films: Dielectric Relaxation of Thin Films of Polystyrene," *Physical Review E,* vol. 61, pp. 1743-1754, 2000.
[84] O. K. C. Tsui and T. P. Russell, "Effect of Interfacial Interactions on the Glass Transition of Polymer Thin Films," *Macromolecules,* vol. 34, pp. 5535-5539, 2001.
[85] Y. Grohens, J. Sacristan, L. Hamon, H. Reinecke, C. Mijangos, and J. M. Guenet, "Glass Transition of Ultra-Thin Films of Modified PVC," *Polymer,* vol. 42, pp. 6419-6423, 2001.
[86] J. H. Kim, J. Jang, and W. C. Zin, "Thickness Dependence of the Glass Transition Temperatue in Thin Polymer Films," *Langmuir,* vol. 17, pp. 2703-2710, 2001.
[87] S. Kawana and R. A. L. Jones, "Character of the Glass Transition in Thin Supported Polymer Films," *Physical Review E,* vol. 63, pp. 021501-1-5, 2001.
[88] V. N. Bliznyuk, H. E. Assender, and G. A. D. Briggs, "Surface Glass Transition Temperature of Amorphous Polymers. A New In sight with SFM," *Macromolecules,* vol. 35, pp. 6613-6622, 2002.
[89] T. Miyazaki, K. Nishida, and T. Kanaya, "Thermal Expansion Behavior of Ultrathin Polymer Films Supported on Silicon Substrate," *Physical Review E,* vol. 69, pp. 061803-1-6, 2004.
[90] J. H. Kim and J. Jang, "Thickness and Composition Dependence of the Glass Transition Temperature in Thin Homogeneous Polymer Blend Films," *Macromolecules,* vol. 35, pp. 311-313, 2002.
[91] O. K. C. Tsui, T. P. Russell, and C. J. Hawker, "Effect of Polymer-Substrate Interactions on the Glass Transition of Polymer Thin Films," *AIP Conference Proceeding,* vol. 708, pp. 598-600, 2004.
[92] J. Q. Pham and P. F. Green, "The Glass Transition of Thin Film Polymer/Polymer Blends: Interfacial Interacions and Confinement," *Journal of Chemical Physics,* vol. 116, pp. 5801-5806, 2002.
[93] L. Hamon, Y. Grohens, and Y. Holl, "Thickness Dependence of the Glass Transition Temperature in Thin Films of Partially Miscible Polymer Blends," *Langmuir,* vol. 19, pp. 10399-10402, 2003.
[94] W. E. Wallace, J. H. v. Zanten, and W. L. Wu, "Influence of an Impenetrable Interface on a Polymer Glass-Transition Temperature," *Physical Review E,* vol. 52, pp. R3329-R3332, 1995.
[95] J. H. van Zanten, W. E. Wallace, and W. Wu, "Effect of Strongly Favorable Substrate Interactions on the Thermal Properties of Ultrathin Polymer Films," *Physical Review E,* vol. 53, pp. R2053-R2056, 1996.
[96] J. S. Sharp, J. H. Teichroeb, and J. A. Forrest, "The Properties of Free polymer Surfaces and Their Influence on the Glass Transition Temperature of Thin Polystyrene Films," *The European Physical Journal E,* vol. 15, pp. 473-487, 2004.
[97] G. B. DeMaggio, W. E. Frieze, D. W. Gidley, M. Zhu, H. A. Hristov, and A. F. Yee, "Interface and Surface Effects on the Glass Transition in Thin Polystyrene Films," *Physical Review Letters,* vol. 78, p. 1524, 1997.
[98] Y. Zhang, J. Zhang, Y. Lu, Y. Duan, S. Yan, and D. Shen, "Glass Transition Temperature Determination of Poly(ethylene terephthalate) Thin Films using Reflection-Absorption FTIR," *Macromolecules,* vol. 37, pp. 2532-2537, 2004.
[99] W. Cheng, R. Sainidou, P. Burgardt, N. Stefanou, A. Kiyanova, M. Efremov*, et al.*, "Elastic Properties and Glass Transition of Supported Polymer Thin Films," *Macromolecules,* vol. 40, pp. 7283-7290, 2007.
[100] C. B. Roth, K. L. McNerny, W. F. Jager, and J. M. Torkelson, "Elimination the Enhanced Mobiliy at the Free Surface of polystyrene: Fluorescence Studies of the Glass Transition Temperature in Thin Bilayer Films of Immiscible polymers," *Macromolecules,* vol. 40, pp. 2568-2574, 2007.
[101] Y. Fujii, K. Akabori, K. Tanaka, and T. Nagamura, "Chain Conformation Effects on Molecular Motions at the Surface of Poly(methyl methacrylate) Films," *Polymer Journal,* vol. 39, pp. 928-934, 2007.
[102] J. Erichsen, K. Dolgner, V. Zaporojtchenko, and F. Faupel, "Glass Transition Temperature in Thin Polymer Films Determined by Thermal Discharge in X-ray Photoelectron

Spectroscopy," *Macromolecules,* vol. 37, pp. 8813-8815, 2004.
[103] M. Erber, U. Georgi, J. Muller, K. J. Eichhorn, and B. Voit, "Polystyrene with Different Topologies: Study of the Glass Transition Temperature in Confined Geometry of Thin Films," *European polymer Journal,* vol. 46, pp. 2240-2246, 2010.
[104] Z. Fakhraai and J. A. Forrest, "Probing Slow Dynamics in Supported Thin Polymer Films," *Physical Review Letters,* vol. 95, pp. 025701-1-4, 2005.
[105] G. Beaucage, R. Composto, and R. S. Stein, "Ellipsometric Study of the Glass Transition and Thernal Expansion Coefficients of Thin Polymer Films," *Journal of Polymer Science: Part B: Polymer Physics,* vol. 31, pp. 319-326, 1993.
[106] K. Dalnoki-Veress, J. A. Forrest, C. Murray, C. Gigault, and J. R. Dutcher, "Molecular Weight Dependence of Reductions in the Glass Transition Temperature of Thin, Freely Standing Polymer Films," *Physical Review E,* vol. 63, pp. 031801-1-10, 2001.
[107] S. Peter, H. Meyer, and J. Baschnagel, "Thickness-Dependent Reduction of the Glass-Transition Temperature in Thin polymer Films with a Free Surface," *Journal of Polymer Science: Part B: Polymer Physics,* vol. 44, pp. 2951-2967, 2006.
[108] A. R. C. Baljon, S. Williams, N. K. Balabaew, F. Paans, D. Hudzinskyy, and A. V. Lyulin, "Simulated Glass Transition in Free-Standing Thin Polystyrene Films," *Journal of Polymer Science: Part B: Polymer Physics,* vol. 48, pp. 1160-1167, 2010.
[109] T. Kerle, Z. Lin, H. Kim, and T. P. Russell, "Mobility of Polymers at the Air/Polymer Inerface," *Macromolecules,* vol. 34, pp. 3484-3492, 2001.
[110] B. Frank, A. P. Gast, T. P. Russell, H. R. Brown, and C. Hawker, "Polymer Mobility in Thin Films," *Macromolecules,* vol. 29, pp. 6531-6534, 1996.
[111] D. B. Hall, R. D. Miller, and J. M. Torkelson, "Molecular Probe Techniques for Studying Diffusion and Relaxation in Thin and Ultrathin polymer Films," *Journal of Polymer Science: Part B: polymer Physics,* vol. 35, pp. 2795-2802, 1997.
[112] Z. Fakhraai and J. A. Forrest, "Measuring the Surface Dynamics of Glassy Polymers," *Science,* vol. 319, pp. 600-604, 2008.
[113] Z. Yang, Y. Fujii, C.-H. Lam, and O. K. C. Tsui, "Glass Transition Dynamics and Surface Layer Mobility in Unentangled Polystyrene Films," *Science,* vol. 328, pp. 1676-1679, 2010.
[114] G. Reiter, "Dewetting of Highly Elastic Thin Polymer Films," *Physcial Review Letters,* vol. 87, pp. 186101-1-4, 2001.
[115] F. Saulnier, E. Raphael, and P. G. Gennes, "Dewetting of Thin Polymer Films Near the Glass Transition," *Physical Review Letters,* vol. 88, pp. 196101-1-4, 2002.
[116] H. V. Melick, A. V. Dijken, J. D. Toonder, L. Govaert, and H. Meijer, "Near-Surface Mechanical Properties of Amorphous Polymers," *Philosophical Magazine A,* vol. 82, pp. 2093-2102, 2002.
[117] R. D. Priestley, C. J. Ellison, L. J. Broadbelt, and J. M. Torkelson, "Structural Relaxation of Polymer Glasses at Surfaces, Interfaces, and In Between," *Science,* vol. 309, pp. 456-459, 2005.
[118] R. Inoue, T. Kanaya, K. Nishida, I. Tsukushi, M. T. F. Telling, B. J. Gabrys*, et al.*, "Glass Transition and Molecular Mobility in Polymer Thin Films," *Physical Review E,* vol. 80, pp. 031802-1-4, 2009.
[119] J. A. Zasadzinski, "Scanning Force Microscopy: New Instrumentation and Applications," *Current Opinion in Colloid and Interface Science,* vol. 1, pp. 264-269, 1996.
[120] S. N. Magonov and D. H. Reneker, "Characterization of Polymer Surfaces with Atomic Force Microscopy," *Annual Review of Materials Science,* vol. 27, pp. 175-222, 1997.
[121] M. Radmacher, R. W. Tillmann, and H. E. Gaub, "Imaging Viscoelasticity by Force Modulation with the Atomic Force Microscopy," *Biophysical Journal,* vol. 64, pp. 735-742, 1993.
[122] V. M. De Cupere and P. G. Rouxhet, "Surface Crystallization of Poly(ethylene terephthalate) Studied by Atomic Force Microscopy," *Polymer,* vol. 42, pp. 5571-5576, 2002.
[123] J. K. Hobbs, O. E. Farrance, and L. Kailas, "How Atomic Force Microscopy has Contributed to our Understanding of Polymer Crystallization," *Polymer,* vol. 50, pp. 4281-4292, 2009.
[124] D. Drechsler, A. Karbach, and H. Fuchs, "Morphology and In Situ Deformation of Polyamide Films Investigated with Scanning Force Microscopy," *Surface and Interface Analysis,* vol. 25, pp. 537-542, 1997.
[125] L. Kuutti, J. Peltonen, P. Myllarinen, O. Teleman, and P. Forssell, "AFM in Studies of Thermoplastic Starches during Ageing," *Carbohydrate Polymers,* vol. 37, pp. 7-12, 1998.
[126] Y.-X. Liu and E.-Q. Chen, "Polymer Crystallization of Ultrathin Films on Solid Substrates,"

Coordination Chemistry Review, vol. 254, pp. 1011-1037, 2010.
[127] Y. Wang, C.-M. chan, K.-M. Ng, and L. Li, "What Controls the Lamellar Orientation at the Surface of Polymer Films During Crystallization," *Macromolecules,* vol. 41, pp. 2548-2553, 2008.
[128] Y. Ma, W. Hu, and G. Reiter, "Lamellar Crystal Orientations Biased by Crystallization Kinetics in Polymer Thin Films," *Macromolecules,* vol. 39, pp. 5159-5164, 2006.
[129] Y. Wang, M. Rafailovich, J. Sokolov, D. Gersappe, T. Araki, Y. Zou*, et al.*, "Substrate Effect on the Melting Temperature of Thin Polyethylene Films," *Physical Review Letters,* vol. 96, pp. 028303-1-4, 2006.
[130] H. Schonherr and C. W. Frank, "Ultrathin Films of Poly(ethylene oxides) on Oxidized Silicon. 2. In Situ Study of Crystallization and Melting by Hot Stage AFM," *Macromolecules,* vol. 36, pp. 1199-1208, 2003.
[131] H. Schonherr and C. W. Frank, "Ultrathin Films of Poly(ethylene oxides) on Oxidized Silicon. 1. Spectroscopic Characterization of Film Structure and Crystallization Kinetics," *Macromolecules,* vol. 36, pp. 1188-1198, 2003.
[132] A. J. Lovinger and H. D. Keith, "Elecron Diffraction Investigation of a High-Temperature Form of Poly(vinylidene fluoride)," *Macromolecules,* vol. 12, pp. 919-924, 1979.
[133] Z. Bartczak, A. S. Argon, R. E. Cohen, and T. Kowalewski, "The Morphology and Orientation of Polyethylene in Films of Sub-Micron Thickness Crystallized in Contact with Calcite and Rubber Substrates," *Polymer,* vol. 40, pp. 2367-2380, 1999.
[134] Y. K. Godovsky and S. N. Magonov, "Atomic Force Microscopy Visualization of Morphology and Nanostructure of an Ultrathin Layer of Polyethylene during Melting and Crystallization," *Langmuir,* vol. 16, pp. 3549-3552, 2000.
[135] J. K. Hobbs, A. D. L. Humphris, and M. J. Miles, "In-Situ Atomic Force Microscopy of Polyethylene Crystallization. 1. Crystallization from an Oriented Backbone," *Macromolecules,* vol. 34, pp. 5508-5519, 2001.
[136] O. Mellbring, S. Kihlman Øiseth, A. Krozer, J. Lausmaa, and T. Hjertberg, "Spin Coating and Characterization of Thin High-Density Polyethylene Films," *Macromolecules,* vol. 34, pp. 7496-7503, 2001.
[137] J. K. Hobbs, "In Situ Atomic Force Microscopy of the Melting of Melt-Crystallized Polyethylene," *Polymer,* vol. 47, pp. 5566-5573, 2006.
[138] K. Jeon and R. Krishnamoorti, "Morphology Behavior of Thin Linear Low-Density polyethylene Films," *Macromolecules,* vol. 41, pp. 7131-7140, 2008.
[139] X. Wang, W. Hou, J. Zhou, L. Li, Y. Li, and C. C-M., "Melting Behavior of Lamellae of Isotactic Polypropylene Studied Using Hot-Stage Atomic Force Microscopy," *Colloid and Polymer Science,* vol. 285, pp. 449-455, 2007.
[140] F. J. Padden, Jr., and H. D. Keith, "Crystallization in Thin Films of Isotactic Polypropylene," *Journal of Applied Physics,* vol. 37, pp. 4013-4020, 1966.
[141] H. Schonherr, R. M. Maymouth, and C. W. Frank, "Nucleation and Crystallization of Low-Crystallinity Polypropylene Followed in Situ by Hot Stage Atomic Force Microscopy," *Macromolecules,* vol. 36, pp. 2412-2418, 2003.
[142] D. C. Bassett and A. S. Vaughan, "On the Lammelar Morphology of Melt-Crystallized Isotactic Polystyrene," *Polymer,* vol. 26, pp. 717-725, 1985.
[143] O. Greis, Y. Xu, T. Asano, and J. Petermann, "Morphology and Structure of Syndiotactic Polystyrene," *Polymer,* vol. 30, pp. 590-594, 1989.
[144] S. J. Sutton, K. Izumi, H. Miyaji, Y. Miyamoto, and S. Miyashita, "The Morphology of Isotactic polystyrene Crystals Grown in Thin Films: the Effect of Substrate Material," *Journal of Materials Science,* vol. 32, pp. 5621-5627, 1997.
[145] R. Pearce and G. J. Vancso, "Imaging of Melting and Crystallization of Poly(ethylene oxide) in Real-Time by Hot-Stage Atomic Force Microscopy," *Macromolecules,* vol. 30, pp. 5843-5848, 1997.
[146] K. E. Strawhecker and E. Manias, "AFM of Poly(vinyl alcohol) Crystals Next to an Inorganic Surface," *Macromolecules,* vol. 34, pp. 8475-8482, 2001.
[147] Y. Sakai, M. Imai, K. Kaji, and M. Tsuji, "Growth Shape Observed in Two-Dimensional Poly(ethylene terephthalate) Spherulites," *Macromolecules,* vol. 29, pp. 8830-8834, 1996.
[148] M. Durell, J. E. Macdonald, D. Trolley, A. Wehrum, P. C. Jukes, R. A. L. Jones*, et al.*, "The Role of Surface-Induced Ordering in the Crystallisation of PET Films," *Europhysics Letters,* vol. 58, pp. 844-850, 2002.
[149] H. G. Haubruge, R. Daussin, A. M. Jonas, and R. Legras, "Morhpology Study of Melt-Crystallized Poly(ethylene terephthalate): B. Thin Films," *Polymer,* vol. 44, pp. 8053-8059,

2003.
[150] E. L. Bedia, M. Tsuji, M. Tosaka, M. Ohara, and S. Kohjiya, "Morhpologies of Melt-Crystallized Thin Films of Nylon-6, Nylon-6,6, and Their Blends as Revealed By Transmission Electron Microscopy," *Journal of Macromolecular Science, Part B,* vol. 40, pp. 1079-1096, 2001.
[151] T. Elzein, M. Brogly, and J. Schultz, "Crystallinity Measurement of Polyamides Adsorbed as Thin Films," *Polymer,* vol. 43, pp. 4811-4822, 2002.
[152] Y. Kikkawa, H. Abe, M. Fujita, T. Iwata, Y. Inoue, and Y. Doi, "Crystal Growth in Poly(L-lactide) Thin Film Revealed by In Situ Atomic Force Microscopy," *Macromolecular Chemistry and Physics,* vol. 204, pp. 1822-1831, 2003.
[153] Y. Yuryev, P. Wood-Adams, M.-C. Heuzey, C. Dubois, and J. Brisson, "Crystallization of Polylactide Films: An Atomic Force Microscopy Study of the Effects of Temperature and Blending," *Polymer,* vol. 49, pp. 2306-2320, 2008.
[154] V. H. Mareau and R. E. Prud'homme, "In-Situ Hot Stage Atomic Force Microscopy Study of Poly(ε-caprolactone) Crystal Growth in Ultrathin Films," *Macromolecules,* vol. 38, pp. 398-408, 2005.
[155] W.-K. Lee and C.-S. Ha, "Miscibility and Surface Crystal Morphology of Blends Containing Poly(vinylidene fluoride) by Atomic Force Microscopy," *Polymer,* vol. 39, pp. 7131-7134, 1998.
[156] O. E. Farrance, R. A. L. Jones, and J. K. Hobbs, "The Observation of Rapid Surface Growth During the Crystallization of Polyhydroxybutyrate," *Polymer,* vol. 50, pp. 3730-3738, 2009.
[157] Y. Wang, S. Ge, M. Rafailovich, J. Sokolov, Y. Zou, H. Ade*, et al.*, "Crystallization in the Thin and Ultrathin Films of Poly(Ethylene-vinyl acetate) and Linear Low-Density Polyethylene," *Macromolecules,* vol. 37, pp. 3319-3327, 2004.
[158] L. Li, C.-M. Chan, K. L. Yeung, J.-X. Li, K.-M. Ng, and Y. Lei, "Direct Observation of Growth of Lamellae and Spherulites of a Semicrystalline Polymer by AFM," *Macromolecules,* vol. 34, pp. 316-325, 2001.
[159] Y.-G. Lei, C.-M. Chan, J.-X. Li, K.-M. Ng, and Y. Wang, "The Birth of an Embryo abd Development of the Founding Lamella of Spherulites As Observed by Atomic Force Microscopy," *Macromolecules,* vol. 35, pp. 6751-6753, 2002.
[160] Y. Jiang, D.-D. Yan, X. Gao, C. C. Han, X.-G. Jin, and L. Li, "Lamellar Branching of Poly(bisphenol A-co-decane) Spherature AFM," *Macromolecules,* vol. 36, pp. 3652-3655, 2003.
[161] Z.-L. Cheung, K.-M. Ng, L.-T. Weng, C.-M. Chan, and L. Li, "Crystallization-Driven Migration of the Low Surface Energy Segment of a Copolymer to the Bulk," *Polymer,* vol. 47, pp. 3164-3170, 2006.
[162] D. A. Ivanov, B. Nysten, and A. M. Jonas, "Atomic Force Microscopy Imaging of Single Polymer Spherulites During Crystallization: Application to a Semi-Crystalline Blend," *Polymer,* vol. 40, pp. 5899-5905, 1999.
[163] F. Zhang, J. Liu, H. Huang, B. Du, and T. He, "Branched Crystal Morphology of Linear Polyethylene Crystallized in a Two-Dimensional Diffusion-Controlled Growth Field," *The European Physical Journal E,* vol. 8, pp. 289-297, 2002.
[164] L. Kaias, C. Vasilev, J.-N. Audinot, H.-N. Migeon, and J. K. Hobbs, "A Real-Time Study of Homogeneous Nucleation, Growth, and Phase Transformations in Nanodroplets of Low Molecular Weight Isotactic Polypropylene Using AFM," *Macromolecules,* vol. 40, pp. 7223-7230, 2007.
[165] V. V. Tsukruk and D. H. Reneker, "Surface Morphology of Syndiotactic Polypropylene Single Crystals Observed by Atomic Force Microscopy," *Macromolecules,* vol. 28, pp. 1370-1376, 1995.
[166] Z. Bu, Y. Yoon, R.-M. Ho, W. Zhou, I. Jangchud, R. K. Eby*, et al.*, "Crystallization, Melting, and Morphology of Syndiotactic Polypropylene Fractions. 3. Lamellar Single Crystals and Chain Folding," *Macromolecules,* vol. 29, pp. 6575-6581, 1996.
[167] K. Taguchi, H. Miyaji, K. Izumi, A. Hoshino, Y. Miyamoto, and R. Kokawa, "Growth Shape of Isotactic Polystyrene Crystals in Thin Films," *Polymer,* vol. 42, pp. 7443-7447, 2001.
[168] K. Taguchi, H. Miyaji, K. Izumi, A. Hoshino, Y. Miyamoto, and R. Kokawa, "Crystal Growth of Isotactic Polystyrene in Ultrathin Films: Film Thickness Dependence," *Journal of Macromolecular Science, Part B: Pysics,* vol. 41, pp. 1033-1042, 2002.
[169] K. Taguchi, A. Toda, and Y. Miyamoto, "Crystal Growth of Isotactic Polystyrene in Ultrathin Films: Thickness and Temperature Dependence," *Journal of Macromolecular Science, Part*

B: Physics, vol. 45, pp. 1141-1147, 2006.
[170] V. H. Mareau and R. E. Prud'homme, "Crystallization of Ultrathin Poly(ε-caprolactone) Films in the Presence of Residual Solvent, An In Situ Atomic Force Microscopy Study," *Polymer,* vol. 46, pp. 7255-7265, 2005.
[171] G. Reiter and J.-U. Sommer, "Polymer Crystallization in Quasi-Two Dimensions. I. Experimental Results," *Journal of Chemical Physics,* vol. 112, pp. 4376-4383, 2000.
[172] J.-U. Sommer and G. Reiter, "Polymer Crystallization in Quasi-Two Dimensions. II. Kinetic Models and Computer Simulations," *Journal of Chemical Physics,* vol. 112, pp. 4384-4393, 2000.
[173] D.-S. Zhu, Y.-X. Liu, A.-C. Shi, and E.-Q. Chen, "Morphology Evolution in Superheated Crystal Monolayer of Low Molecular Weight Poly(ethylene oxide) on Mica Surface," *Polymer,* vol. 47, pp. 5239-5242, 2006.
[174] L. Jin, G. Zhang, X. Zhai, Z. Ma, P. Zheng, and W. Wang, "Macromolecular Effect on Crystal Pattern Formation in Ultra-Thin Films: Molecular Segregation in a Binary Blend of PEO Fractions," *Polymer,* vol. 50, pp. 6157-6165, 2009.
[175] B. C. Okerberg, H. Marand, and J. F. Douglas, "Dendritic Crystallization in Thin Films of PEO/PMMA Blends: A Comparison to Crystallization in Small Molecule Liquids," *polymer,* vol. 49, pp. 579-587, 2008.
[176] V. Ferreiro, J. F. Douglas, J. A. Warren, and A. Karim, "Nonequilibrium Pattern Formation in the Crystallization of Polymer Blend Films," *Physical Review E,* vol. 65, pp. 042802-1-4, 2002.
[177] V. Ferreiro, J. F. Douglas, J. Warren, and A. Karim, "Growth Pulsations in Symmetric Dendritic Crystallization in Thin Polymer Blend Films," *Physical Review E,* vol. 65, pp. 051606-1-16, 2002.
[178] N. Grozev, I. Botiz, and G. Reiter, "Morphological Instabilities of Polymer Crystals," *The European Physical Journal E,* vol. 2008, pp. 63-71, 2008.
[179] Y. Huang, X.-B. Liu, H.-L. Zhang, D.-S. Zhu, Y.-J. Sun, S.-K. Yan*, et al.*, "AFM Study of Crystallization and Melting of a Poly(ethylene oxide) Diblock Copolymer Containing a Tablet-like Block of Poly{2,5-bis[(4-methoxyphenyl)oxycarbonyl]styrene} in Ultrathin Films," *Polymer,* vol. 47, pp. 1217-1225, 2006.
[180] Z. Hu, F. Zhang, B. Du, H. Huang, and T. He, "Morphology and Structures of Self-Assembled Symmetric Poly(di-n-alkylsilanes)," *Langmuir,* vol. 19, pp. 9013-9017, 2003.
[181] Z. Hu, H. Huang, F. Zhang, B. Du, and T. He, "Thickness-Dependent Molecular Chain and Lamellar Crystal Orientation in Ultrathin Poly(di-n-hexylsilane) Films," *Langmuir,* vol. 20, pp. 3271-3277, 2004.
[182] A. J. Lovinger and R. E. Cais, "Structure and Morphology of Poly(trifluoroethylene)," *Macromolecules,* vol. 17, pp. 1939-1945, 1984.
[183] R. Nisman, P. Smith, and G. J. Vancso, "Anisotropic Friction at the Surface of Lamellar Crystals of Poly(oxymethylene) by Lateral Force Microscopy," *Langmuir,* vol. 10, pp. 1667-1669, 1994.
[184] B. Lotz and S. Z. D. Cheng, "Polymer Crystallization Processes as Seen from the Growth Front's perspective," *Polymer Journal,* vol. 40, pp. 891-899, 2008.
[185] E. Brener, H. Muller-Krumbhaar, and D. Temkin, "Kinetic Phase Diagram and Scaling Relations for Stationary Difusional Growth," *Europhysics Letters,* vol. 17, pp. 535-540, 1992.
[186] E. Brener, H. Muller-Krumbhaar, and D. Temkin, "Structure Formation and the Morphology Diagram of Possible Structures in Two-Dimensional Diffusional Growth," *Physical Review E,* vol. 54, pp. 2714-2722, 1996.
[187] E. Brener, H. Muller-Krumbhaar, D. Temkin, and T. Abel, "Morphology Diagram of Possible Structures in Diffusional Growth," *Physica A,* vol. 249, pp. 73-81, 1998.
[188] M. M. Despotopoulou, C. W. Frank, R. D. Miller, and J. F. Rabolt, "Kinetics of Chain Organization in Ultrathin Poly(di-n-hexylsilane) Films," *Macromolecules,* vol. 29, pp. 5797-5804, 1996.
[189] S. Sawamura, H. Miyaji, K. Izumi, S. J. Sutton, and Y. Miyamoto, "Growth Rate of Isotactic Polystyrene Crystals in Thin Films," *Journal of the Physical Society of Japan,* vol. 67, pp. 3338-3341, 1998.
[190] M. Furukawa, K. Kojio, S. Kugumiya, Y. Uchiba, and Y. Mitsui, "Microphase Separation of Bulk and Ultrathin Films of Polyurethane Elastomers," *Macromolecular Symposia,* vol. 267, pp. 9-15, 2008.
[191] G. Wen, X. Li, Y. Liao, and L. An, "Surface Phase Separations of PMMA/SAN Blends

Investigated by Atomic Force Microscopy," *Polymer,* vol. 44, pp. 4035-4045, 2003.
[192] K. Kojio, S. Kugumiya, Y. Uchiba, Y. Nishino, and M. Furukawa, "The Microphase-separated Structure of Polyurethane Bulk and Thin Films," *Polymer Journal,* vol. 41, pp. 118-124, 2009.
[193] R. S. McLean and B. B. Sauer, "Tapping-Mode AFM Studies Using Phase Detection for Resolution of Nanophases in Segmented Polyurethanes and Other Block Copolymers," *Macromolecules,* vol. 30, pp. 8314-8317, 1997.
[194] C. T. Black and K. W. Guarini, "Structural Evolution of Cylindrical-Phase Diblock Copolymer Thin Films," *Journal of Polymer Science: Part A: Polymer Chemistry,* vol. 42, pp. 1970-1975, 2004.
[195] J. J. M. Halls, C. A. Walsh, N. C. Greenham, E. A. Marseglia, R. H. Friend, S. C. Moratti*, et al.*, "Efficient Photodiodes from Interpenetrating Polymer Networks," *Nature,* vol. 376, pp. 498-500, 1995.
[196] P. Vanlaeke, A. Swinnen, I. Haeldermans, G. Vanhoyland, T. Aernouts, D. Cheyns*, et al.*, "P3HT/PCBM Bulk Heterojunction Solar Cells: Relation Between Morphology and Electro-Optical Characteristics," *Solar Energy Materials and Solar Cells,* vol. 2006, pp. 2150-2158, 2006.
[197] W.-H. Baek, T.-S. Yoon, H. H. Lee, and Y.-S. Kim, "Composition-Dependent Phase Separation of P3HT:PCBM Composites for High Performance Organic Solar Cells," *Organic Electronics,* vol. 11, pp. 933-937, 2010.
[198] A. Bernasik, J. Rysz, A. Budkowski, K. Kowalski, J. Camra, and J. Jedlinski, "Three-Dimensional Information on the Phase Domain Structure of Thin Films of Polymer Blends Revealed by Secondary Ion Mass Spectrometry," *Macromolecular Rapid Communications,* vol. 22, pp. 829-834, 2001.
[199] E. Moons, "Conjugated Polymer Blends: Linking Film Morphology to Performance of Light Emitting Diodes and Photodiodes," *Journal of Physics: Condensed Matter,* vol. 14, pp. 12235-12260, 2002.
[200] M. Wendlandt, T. Kerle, M. Heuberger, and J. Klein, "Phase Separation in Thin Films of Polymer Blends: The Influence of Symmetric Boundary Conditions," *Journal of Polymer Science: Part B: Polymer Physics,* vol. 38, pp. 831-837, 2000.
[201] A. Karim, T. M. Slawecki, S. K. Kumar, J. F. Douglas, S. K. Satija, C. C. Han*, et al.*, "Phase-Separation-Induced Surface Patterns in Thin Polymer Blend Films," *Macromolecules,* vol. 31, pp. 857-862, 1998.
[202] D. Slep, J. Asselta, M. H. Rafailovich, J. Sokoloc, D. A. Winesett, A. P. Smith*, et al.*, "Phase Separation of Polystrene and Bromo-Polystyrene Mixtures in Equilibrium Structures in Thin Films," *Langmuir,* vol. 14, pp. 4860-4864, 1998.
[203] H. Wang and R. J. Composto, "Understanding Morphology Evolution and Rougheding in Phase-Separation Thin-Film Polymer Blends," *Europhysics Letters,* vol. 50, pp. 622-627, 2000.
[204] H. Wang and R. J. Composto, "Thin Film Polymer Blends Undergoing Phase Separation and Wetting: Identification of Early, Intermediate, and Late Stages," *Journal of Chemical Physcis,* vol. 113, pp. 10386-10397, 2000.
[205] H. Wang, R. J. Composto, E. K. Hobbie, and C. C. Han, "Multiple Lateral Length Scales in Phase-Separating Thin-Film Polymer Blends," *Langmuir,* vol. 17, pp. 2857-2860, 2001.
[206] P. Muller-Buschbaum, J. S. Gutmann, R. Cubitt, and M. Stamm, "Probing the In-Plane Composition of Thin Polymer Films with Grazing-Incidence Small Angle Neutron Scattering and Atomic Force Microscopy," *Colloid and Polymer Science,* vol. 277, pp. 1193-1199, 1999.
[207] S. H. Anastasiadis, T. P. Russell, S. K. Satija, and C. F. Majkrzak, "The Morphology of Symmetric Diblock Copolymers as Revealed by Neutron Reflectivity," *The Journal of Chemical Physics,* vol. 92, pp. 5677-5691, 1990.
[208] P. Muller-Buschbaum, J. S. Gutmann, and M. Stamm, "Influence of Blend Composition on Phase Separation and Dewetting of Thin Polymer Blend Films," *Macromolecules,* vol. 33, pp. 4886-4895, 2000.
[209] K. Dalnoki-Veress, J. A. Forrest, J. R. Stevens, and J. R. Dutcher, "Phase Separation Morphology of Thin Films of Polystyrene/Polyisoprene Blends," *Journal of Polymer Science: Part B: Polymer Physics,* vol. 34, pp. 3017-3024, 1996.
[210] K. Dalnoki-Veress, J. A. Forrest, J. R. Stevens, and J. R. Dutcher, "Phase Separation Morphology of Spin-Coated Polymer Blend Thin Film," *Physica A,* vol. 239, pp. 87-94, 1997.

[211] S. Walheim, M. Boltau, J. Mlynek, G. Krausch, and U. Steiner, "Structure Formation via Polymer Demixing in Spin-Cast Films," *Macromolecules,* vol. 30, pp. 4995-5003, 1997.
[212] E. Kumacheva, L. Li, M. A. Winnik, D. M. Shinozaki, and P. C. Cheng, "Direct Imaging of Surface and Bulk Structures in Solvent Cast Polymer Blend Films," *Langmuir,* vol. 13, pp. 2483-2489, 1997.
[213] J. S. Gutmann, P. Muller-Buschbaum, and M. Stamm, "Complex Pattern Formation by Phase Separation of Polymer Blends in Thin Films," *Faraday Discussion,* vol. 112, pp. 285-297, 1999.
[214] J.-S. Kim, P. K. H. Ho, C. E. Murphy, and R. H. Friend, "Phase Separation in Polyfluorene-Based Conjugated Polymer Blends Lateral and Vertical Analysis of Blend Spin-Cast Thin Films," *Macromolecules,* vol. 37, pp. 2861-2871, 2004.
[215] J. Raczkowska, P. Cyganik, A. Budkowski, A. Bernasik, J. Rysz, I. Raptis*, et al.*, "Composition Effects in Polymer Blends Spin-Cast on Patterned Substrates," *Macromolecules,* vol. 38, pp. 8486-8493, 2005.
[216] T. Liu, R. Ozisik, and R. W. Siegel, "Phase Separation and Surface Morphology of Spin-Coated Films of Polyetherimide/Polycaprolactone Immiscible Polymer Blends," *Thin Solid Films,* vol. 515, pp. 2965-2973, 2007.
[217] S. Walheim, E. Schaffer, J. Mlynek, and U. Steiner, "Nanophase-Separated Polymer Films as High-Performance Antireflection Coatings," *Science,* vol. 283, pp. 520-522, 1999.
[218] H. Hou, E. Wang, J. Bergqvist, B. V. Andersson, Z. Wang, C. Muller*, et al.*, "Lateral Phase Separation Gradients in Spin-Coated Thin Films of High-Performance Polymer:Fullerene Photovoltaic Blends," *Advanced Functional Materials,* vol. 21, pp. 3169-3175, 2011.
[219] L. Yan and F. Yang, "Prediction and Phase Segregation in Thin-Film of Conjugated Polymer Blends," *Journal of Polymer Science: Part B: Polymer Physics,* vol. 43, pp. 1382-1391, 2005.
[220] P. F. Green and R. Limary, "Block Copolymer Thin Films: Pattern Formation and Phase Behavior," *Advances in Colloid and Interface Science,* vol. 94, pp. 53-81, 2001.
[221] Q. Zong, Z. Li, and X. Xie, "Inversion of Phase Morphology in Polymer-Blend Thin Films on Glass Substrates," *Macromolecular Chemistry and Physcis,* vol. 205, pp. 1116-1124, 2004.
[222] M. Harris, G. Appel, and H. Ade, "Surface Morphology of Annealed Polystyrene and Poly(methyl methacrylate) Thin Film Blends and Bilayers," *Macromolecules,* vol. 36, pp. 3307-3314, 2003.
[223] S. Reich and Y. Cohen, "Phase Separation of Polymer Blends in Thin Films," *Journal of Polymer Science: Polymer Physics Edition,* vol. 19, pp. 1255-1267, 1981.
[224] Y. Liao, J. You, T. Shi, L. An, and P. K. Dutta, "Phase Behavior and Dewetting for Polymer Blend Films Studied by In Situ AFM and XPS: From Thin to Ultrathin Films," *Langmuir,* vol. 23, pp. 11107-11111, 2007.
[225] H. Ogawa, T. Kanaya, K. Nishida, and G. Matsuba, "Phase Separation and Dewetting in Polymer Blend Thin Films," *The European Physcial Journal Special Topics,* vol. 141, pp. 189-192, 2007.
[226] H. Ogawa, T. Kanaya, K. Nishida, and G. Matsuba, "Phase Separation and Dewetting in Polystyrene/Poly(vinyl methy)," *Polymer,* vol. 49, pp. 254-262, 2008.
[227] J. T. Garrett, J. Runt, and J. S. Lin, "Microphase Separation of Segmented Poly(urethane urea) Block Copolymers," *Macromolecules,* vol. 33, pp. 6353-6359, 2000.
[228] S. Hild, O. Marti, F. Hollmann, and B. Rieger, "Effects of the Chain Microstructure on the Properties of Polyketones Terpolymers Characterized by Scanning Force Microscopy," *European Polymer Journal,* vol. 40, pp. 905-916, 2004.
[229] B. M. D. O'Driscoll, R. Oren, and I. W. Hamley, "Phase Separation in Thin Films of End-Grafted Block Copolymers," *Polymers for Advanced Technologies,* vol. 22, pp. 924-932, 2011.
[230] A. Wolinska-Grabczyk, J. Zak, J. Muszynski, and A. Jankowski, "Surface Morphology of the Polyurethane-Based Prevaporation Membranes Studied by Atomic Force Microscopy. I. Effects of Polyurethane molecular Structure," *Journal of Macromolecular Science Part A-Pure and Applied Chemistry,* vol. 40, pp. 225-237, 2003.
[231] T. Kajiyama, K. Tanaka, N. Satomi, and A. Takahara, "Surface Relaxation Process of Monodisperse Polystyrene Film Based on Lateral Force Microscopic Measurements," *Macromolecules,* vol. 31, pp. 5150-5151, 1998.
[232] X. Li, Y. Han, and L. An, "Surface Morphology Control of Immiscible Polymer-Blend Thin Films," *Polymer,* vol. 44, pp. 8155-8165, 2003.
[233] X. Li, R. Xing, Y. Zhang, Y. Han, and L. An, "Molecular Weight Effects on the Phase

Morphology of PS/P4VP Blend Film on Homogeneous SAM and Heterogeneous SAM/Au Substrates," *Polymer,* vol. 45, pp. 1637-1646, 2004.
[234] M. Boltau, S. Walheim, J. Mlynek, G. Krausch, and U. Steiner, "Surface-Induced Structure Formation of Polymer Blends on Patterned Substrates," *Nature,* vol. 391, pp. 877-879, 1998.
[235] L. Rockford, Y. Liu, P. Mansky, T. P. Russell, M. Yoon, and S. G. J. Mochrie, "Polymers on Nanoperiodic, Heterogeneous Surfaces," *Physical Review Letters,* vol. 82, pp. 2602-2605, 1999.
[236] K. A. Barnes, A. Karim, J. F. Douglas, A. I. Nakatani, H. Gruell, and E. J. Amis, "Suppression of Dweting in Nanoparticle-Filled Polymer Films," *Macromolecules,* vol. 33, pp. 4177-4185, 2000.
[237] Y. A. Akpalu, A. Karim, S. K. Satija, and N. P. Balsara, "Suppression of Lateral Phase Separation in Thin Polyolefin Blend Films," *Macromolecules,* vol. 34, pp. 1720-1729, 2001.
[238] H. J. Chung, A. Taubert, R. D. Deshmukh, and R. J. Composto, "Mobile Nanoparticles and Their Effect on Phase Separation Dynamics in Thin-Film Polymer Blends," *Europhysics Letters,* vol. 68, pp. 219-225, 2004.
[239] D. U. Ahn, Z. Wang, I. P. Campbell, M. P. Stoykovich, and Y. Ding, "Morphological Evolution of Thin PS/PMMA Films: Effects of Surface Energy and Blend Composition," *Polymer,* vol. 53, pp. 4187-4194, 2012.
[240] T. Fujiwara, M. Miyamoto, and Y. Kimura, "Crystallization-Induced Morphological Changes of a Poly(L-lactide)/Poly(oxyethylene) Diblock Copolymer from Sphere to Band via Disk: A Novel Macromolecular Self-Organization Process from Core-Shell Nanoparticles on Surface," *Macromolecules,* vol. 33, pp. 2782-2785, 2000.
[241] F. Zhang, Y. Chen, H. Huang, Z. Hu, and T. He, "Boundary Effect of Relief Structure on Crystallization of Diblock Copolymer in Thin Films," *Langmuir,* vol. 19, pp. 5563-5566, 2003.
[242] F. Zhang, H. Huang, Z. Hu, Y. Chen, and T. He, "Crystallization of Weakly Segregated Poly(styrene-b-ε-caprolactone) Diblock Copolymer in Thin Films)," *Langmuir,* vol. 19, pp. 10100-10108, 2003.
[243] Y. S. Hu, A. Hiltner, and E. Baer, "Improving Oxygen Barrier Properties of Poly(ethylene terephthalate) by Incroporating Isophthalate. II. Effect of Crystallization," *Journal of Applied Polymer Science,* vol. 98, pp. 1629-1642, 2005.
[244] J. Fu, B. Luan, C. Pan, B. Li, and Y. Han, "Early Stage Interplay of Microphase Separation and Crystallization in Crystalline-Coil Poly(L-lactic acid)-block-polystyrene Thin Films," *Macromolecules,* pp. 5118-5127, 2005.
[245] D. Chen, Y. Gong, and T. He, "Effect of Crystallization on the Lamellar Orientation in Thin Films of Symmetric Poly(styrene)-b-poly(L-lactide) Diblock Copolymer," *Macromolecules,* vol. 39, pp. 4101-4107, 2006.
[246] S. Dasgupta, W. B. Hammond, and W. A. Goddard, "Crystal Structures and Properties of Nylon Polymers from Theory," *Journal of the American Chemical Society,* vol. 118, pp. 12291-12301, Dec 1996.
[247] T. Ishikawa, S. Nagai, and N. Kasai, "The γ → α partial transformation in nylon 12 by drawing," *Makromolekulare Chemie-Macromolecular Chemistry and Physics,* vol. 182, pp. 977-988, 1981.
[248] C. Ramesh, "Crystalline Transitions in Nylon 12," *Macromolecules,* vol. 32, pp. 5704-5706, Aug 1999.
[249] L. B. Li, M. H. J. Koch, and W. H. de Jeu, "Crystalline Structure and Morphology in Nylon-12: A Small- and Wide-angle X-ray Scattering Study," *Macromolecules,* vol. 36, pp. 1626-1632, Mar 2003.
[250] X. N. Yang, S. S. Tan, G. Li, and E. Zhou, "Dependence of the Brill Transition on the Crystal Size of Nylon 10 10," *Macromolecules,* vol. 34, pp. 5936-5942, Aug 2001.
[251] D. Y. Yan, Y. J. Li, and X. Y. Zhu, "Brill Transition in Nylon 10 12 Investigated by Variable Temperature XRD and Real time FT-IR," *Macromolecular Rapid Communications,* vol. 21, pp. 1040-1043, Oct 2000.
[252] S. S. Nair, C. Ramesh, and K. Tashiro, "Crystalline Phases in Nylon-11: Studies using HTWAXS and HTFTIR," *Macromolecules,* vol. 39, pp. 2841-2848, Apr 2006.
[253] V. Ferreiro, Y. Pennec, R. Seguela, and G. Coulon, "Shear Banding in Polyamide 6 Films as Revealed by Atomic Force Microscopy," *Polymer,* vol. 41, pp. 1561-1569, 2000.
[254] V. Ferreiro and G. Coulon, "Shear Banding in Strained Semicrystalline Polyamide 6 Films as Revealed by Atomic Force Microscopy: Role of the Amorphous Phase," *Journal of*

Polymer Science: Part B: Polymer Physics, vol. 42, pp. 687-701, 2004.
[255] V. Ferreiro, C. Depecker, J. Laureyns, and G. Coulon, "Structure and Morphologies of Cast and Plastically Strained Polyamide 6 Films as Evidenced by Confocal Raman Microspectroscopy and Atomic Force Microscopy," *Polymer,* vol. 45, pp. 6013-6026, 2004.
[256] N. S. Murthy, S. A. Curran, S. M. Aharoni, and H. Minor, "Premelting Crystalline Relaxations and Phase Transitions in Nylon 6 and 6,6," *Macromolecules,* vol. 24, pp. 3215-3220, 1991.
[257] C. Ramesh and E. B. Gowd, "High-Temperature X-ray Diffraction Studies on the Crystalline Transitions in the α- and γ-Forms of Nylon-6," *Macromolecules,* vol. 34, pp. 3308-3313, 2001.
[258] T. D. Fornes and D. R. Paul, "Crystallization Behaviour of Nylon 6 Nanocomposites," *Polymer,* vol. 44, pp. 3945-3961, 2003.
[259] C. J. Lawrence, "The Mechanics of Spin Coating of Polymer Films," *Physics of Fluids,* vol. 31, pp. 2786-2795, 1988.
[260] I. Horcas, R. Fernandez, J. M. Gomez-Rodriguez, J. Colchero, J. Gomez-Herrero, and A. M. Baro, "WSXM: A Software for Scanning Probe Microscopy and A Tool for Nanotechnology," *Rev. Sci. Instrum.,* vol. 78, p. 013705, 2007.
[261] F. A. Novillo, M. Fujita, M. Tsuji, and S. Kohjiya, "Preferential Orientation of Poly(ethylene 2,6-naphthalate) Melt-crystallized on the Friction Transfer Layer of PTFE," *Sen-I Gakkaishi,* vol. 54, pp. 544-549, Oct 1998.
[262] P. Yang and Y. C. Han, "Crystal Growth Transition from Flat-On to Edge-On Induced by Solvent Evaporation in Ultrathin Films of Polystyrene-b-Poly(ethylene oxide)," *Langmuir,* vol. 25, pp. 9960-9968, Sep 2009.
[263] J. E. Stamhuis and A. J. Pennings, "Crystallization of Polyamides under Elevated Pressure: 6.Pressure-induced Crystallization from the Melt and Annealing of Folded-chain Crystals of Nylon-12, Polylaurolactam under pressure," *Polymer,* vol. 18, pp. 667-674, 1977.
[264] T. Ishikawa, S. Nagai, and N. Kasai, "Effect of Casting Conditions on Polymorphism of Nylon-12," *Journal of Polymer Science Part B-Polymer Physics,* vol. 18, pp. 291-299, 1980.
[265] Matsubar.I, Y. Itoh, and Shinomiy.M, "Lower-Frequency Infrared Spectra (800-200 CM-1) and Structures of Polyamides," *Journal of Polymer Science Part B-Polymer Letters,* vol. 4, pp. 47-53, 1966.
[266] J. D. Hoffman and J. I. Lauritzen, "Crystallization of Bulk Polymers With Chain Folding: Theory of Growth of Lamellar Spherulites," *Journal of Research of the National Bureau of Standards,* vol. A 65, pp. 297-336, 1961.
[267] T. Konishi, W. Sakatsuji, K. Fukao, and Y. Miyamoto, "Polymer Crystallization Mechanism through a Mesomorphic State," *Physical Review B,* vol. 84, Oct 2011.
[268] A. Keller, M. Hikosaka, S. Rastogi, A. Toda, P. J. Barham, and G. Goldbeckwood, "An Approach to the Formation and Growth of New Phases with Application to Polymer Crystallization: Effect of Finite Size, Metastability, and Ostwald's Rule of Stages," *Journal of Materials Science,* vol. 29, pp. 2579-2604, May 1994.
[269] K. Tashiro, K. Imanishi, Y. Izumi, M. Kobayashi, K. Kobayashi, M. Satoh*, et al.*, "Cocrystallization and Phase Segregation of Polyethylene Blends between the D and H Species. 7. Time-Resolved Synchrotron-Source Small-Angle X-ray Scattering Measurements for Studying the Isothermal Crystallization Kinetics: Comparison with the FTIR Data," *Macromolecules,* vol. 28, pp. 8477-8483, Dec 1995.
[270] G. Strobl, "From the Melt via Mesomorphic and Granular Crystalline Layers to Lamellar Crystallites: A Major Route Followed in Polymer Crystallization?" *European Physical Journal E,* vol. 3, pp. 165-183, Oct 2000.
[271] G. Strobl, "Colloquium: Laws Controlling Crystallization and Melting in Bulk Polymers," *Reviews of Modern Physics,* vol. 81, pp. 1287-1300, Jul-Sep 2009.
[272] N. Dencheva, T. G. Nunes, M. J. Oliveira, and Z. Denchev, "Crystalline Structure of Polyamide 12 as Revealed by Solid-state C-13 NMR and Synchrotron WAXS and SAXS," *Journal of Polymer Science Part B-Polymer Physics,* vol. 43, pp. 3720-3733, Dec 2005.
[273] T. Ishikawa, S. Nagai, and N. Kasai, "Thermal Behavior of α Nylon-12," *Journal of Polymer Science Part B-Polymer Physics,* vol. 18, pp. 1413-1419, 1980.
[274] P. Wang and J. T. Koberstein, "Morphology of Immiscible Polymer Blend Thin Films Prepared by Spin-Coating," *Macromolecules,* vol. 37, pp. 5671-5681, 2004.
[275] K. Tanaka, J. Yoon, A. Takahara, and T. Kajiyama, "Ultrathinning-Induced Surface Phase Separation of Polystyrene/Poly(vinyl methyl ether) Blend Film," *Macromolecules,* vol. 28,

pp. 934-938, 1995.
[276] D. G. H. Ballard, G. F. Wignall, and J. Schelten, "Measurement of Molecular Dimensions of Polystyrene Chains in the Bulk Polymer by Low Angle Neutron Diffraction," *European Polymer Journal,* vol. 9, pp. 965-969, 1973.
[277] T. P. Russell, R. P. Hjelm Jr., and P. A. Seeger, "Temperature Dependence of the Interaction Parameter of Polystyrene and Poly(methyl methacrylate)," *Macromolecules,* vol. 23, pp. 890-893, 1990.
[278] A. D. F. Dunbar, P. Mokarian-Tabari, A. J. Parnell, S. J. Martin, M. W. A. Skoda, and R. A. L. Jones, "A Solution Concentration Dependent Transition from Self-stratification to Lateral Phase Separation in Spin-cast PS:d-PMMA Thin Films," *The European Physical Journal E,* vol. 31, pp. 369-375, 2010.
[279] W. W. Graessley and S. F. Edwards, "Entanglement Interactions in Polymers and the Chain Contour Concentration," *Polymer,* vol. 22, pp. 1329-1334, 1981.
[280] R. Xie, A. Karim, J. F. Douglas, C. C. Han, and R. A. Weiss, "Spinodal dewetting of thin polymer films," *Physical Review Letters,* vol. 81, pp. 1251-1254, Aug 1998.
[281] M. Tolan, O. H. Seeck, J. P. Schlomka, W. Press, J. Wang, S. K. Sinha*, et al.*, "Evidence for Capillary Waves on Dewetted Polymer Film Surfaces: A Combined X-ray and Atomic Force Microscopy Study," *Physical Review Letters,* vol. 81, pp. 2731-2734, 1998.
[282] X. Li, Y. Han, and L. An, "Annealing Effects on the Surface Morphologies of Thin PS/PMMA Blend Films with Different Film Thickness," *Applied Surface Science,* vol. 230, pp. 115-124, 2004.
[283] R. Tao, M. A. Novotny, and K. Kaski, "Diffusion-Limited Aggregation with Surface Tension," *Physical Review A,* vol. 38, pp. 1019-1026, 1988.
[284] R. W. Seymour and S. L. Cooper, "Thermal Analysis of Polyurehtane Block Polymers," *Macromolecules,* vol. 6, pp. 48-53, 1973.
[285] J. W. C. Van Bogart, D. A. Bluemke, and S. L. Cooper, "Annealing-Induced Morphological Changes in Segmented Elastomers," *Polymer,* vol. 22, pp. 1428-1438, 1981.
[286] J. T. Koberstein and A. F. Galambos, "Multiple Melting in Segmented Polyurethane Block Copolymers," *Macromolecules,* vol. 25, pp. 5618-5624, 1992.
[287] J. T. Koberstein, A. F. Galambos, and L. M. Leung, "Compression-Molded Polyurethane Block Copolymers. 1. Microdomain Morphology and Thermomechanical Properties," *Macromolecules,* vol. 25, pp. 6195-6204, 1992.
[288] J. T. Koberstein and L. M. Leung, "Compression-Molded Polyurethane Block Copolymers. 2. Evaluation of Microphase Compositions," *Macromolecules,* vol. 25, pp. 6205-6213, 1992.
[289] L. M. Leung and J. T. Koberstein, "DSC Annealing Study of Microphase Separation and Multiple Endothermic Behavior in Polyether-Based Polyurethane Block Copolymers," *Macromolecules,* vol. 19, pp. 706-713, 1986.
[290] T. K. Chen, T. S. Shieh, and J. Y. Chui, "Studies on the First DSC Endotherm of Polyurethane Hard Segment Based on 4,4'-Diphenylmethane Diisocyanate and 1,4-Butanediol," *Macromolecules,* vol. 31, pp. 1312-120, 1998.
[291] A. Saiani, A. Novak, L. Rodier, G. Eeckhaut, J. W. Leenslag, and J. S. Higgins, "Origin of Multiple Melting Endotherms in a High Hard Block Content Polyurethane: Effect of Annealing Temperature," *Macromolecules,* vol. 40, pp. 7252-7262, Oct 2007.
[292] A. Saiani, C. Rochas, G. Eeckhaut, W. A. Daunch, J. W. Leenslag, and J. S. Higgins, "Origin of Multiple Melting Endotherms in a High Hard Block Content Polyurethane. 2. Structural Investigation," *Macromolecules,* vol. 37, pp. 1411-1421, Feb 2004.
[293] Y. Yanagihara, N. Osaka, S. Murayama, and H. Saito, "Thermal Annealing Behavior and Structure Development of Crystalline Hard Segment Domain in a Melt-Quenched Thermoplastic Polyurethane," *Polymer,* vol. 54, pp. 2183-2189, 2013.
[294] C. W. Meuse, X. Yang, D. Yang, and S. L. Hsu, "Spectroscopic Analysis of Ordering and Phase-Separation Behavior of Model Polyurethanes in a Restricted Geometry," *Macromolecules,* vol. 25, pp. 925-932, 1992.
[295] H. J. Tao, C. W. Meuse, X. Yang, W. J. MacKnight, and S. L. Hsu, "A Spectroscopic Analysis of Phase Separation Behavior of Polyurethane in Restricted Geometry: Chain Rigidity Effects," *Macromolecules,* vol. 27, pp. 7146-7151, 1994.
[296] K. Kojio, Y. Uchiba, Y. Mitsui, M. Furukawa, S. Sasaki, H. Matsunaga*, et al.*, "Depression of Microphase-Separated Domain Size of Polyurethanes in Confined Geometry," *Macromolecules,* vol. 40, pp. 2625-2628, 2007.

APPENDIX

Appendix 1 GPC results for as-cast and annealed PS and PMMA measured by the School of Chemistry, University of Manchester.

Table A1 GPC results for PS and PMMA as cast and annealed at 140 ℃ for 2 hr in air. The as cast data obtained shows a slight broader molecular weight distribution compared to the data from the manufacturer. However, results here show a very slight change in molecular weight on annealing indicating a good stability of polymers on annealing.

PS-as cast

Conventional Calibration - Homopolymers : Results

Peak RV - (ml)	18.478	27.187
Mn - (Daltons)	66,393	0
Mw - (Daltons)	94,403	0
Mz - (Daltons)	106,955	0
Mp - (Daltons)	109,222	0
Mw / Mn	1.422	0.000
Percent Above Mw: 0	0.000	0.000
Percent Below Mw: 0	0.000	0.000
Mw 10.0% Low	24,016	0
Mw 10.0% High	146,293	0
RI Area - (mvml)	61.78	17.69
UV Area - (mvml)	0.00	0.00

PMMA-as cast

Conventional Calibration - Homopolymers : Results

Peak RV - (ml)	18.563	27.142
Mn - (Daltons)	61,499	0
Mw - (Daltons)	85,696	0
Mz - (Daltons)	98,381	0
Mp - (Daltons)	99,327	0
Mw / Mn	1.393	0.000
Percent Above Mw: 0	0.000	0.000
Percent Below Mw: 0	0.000	0.000
Mw 10.0% Low	23,082	0
Mw 10.0% High	140,129	0
RI Area - (mvml)	28.12	21.38
UV Area - (mvml)	0.00	0.00

PS-140°C 2hr

Conventional Calibration - Homopolymers : Results

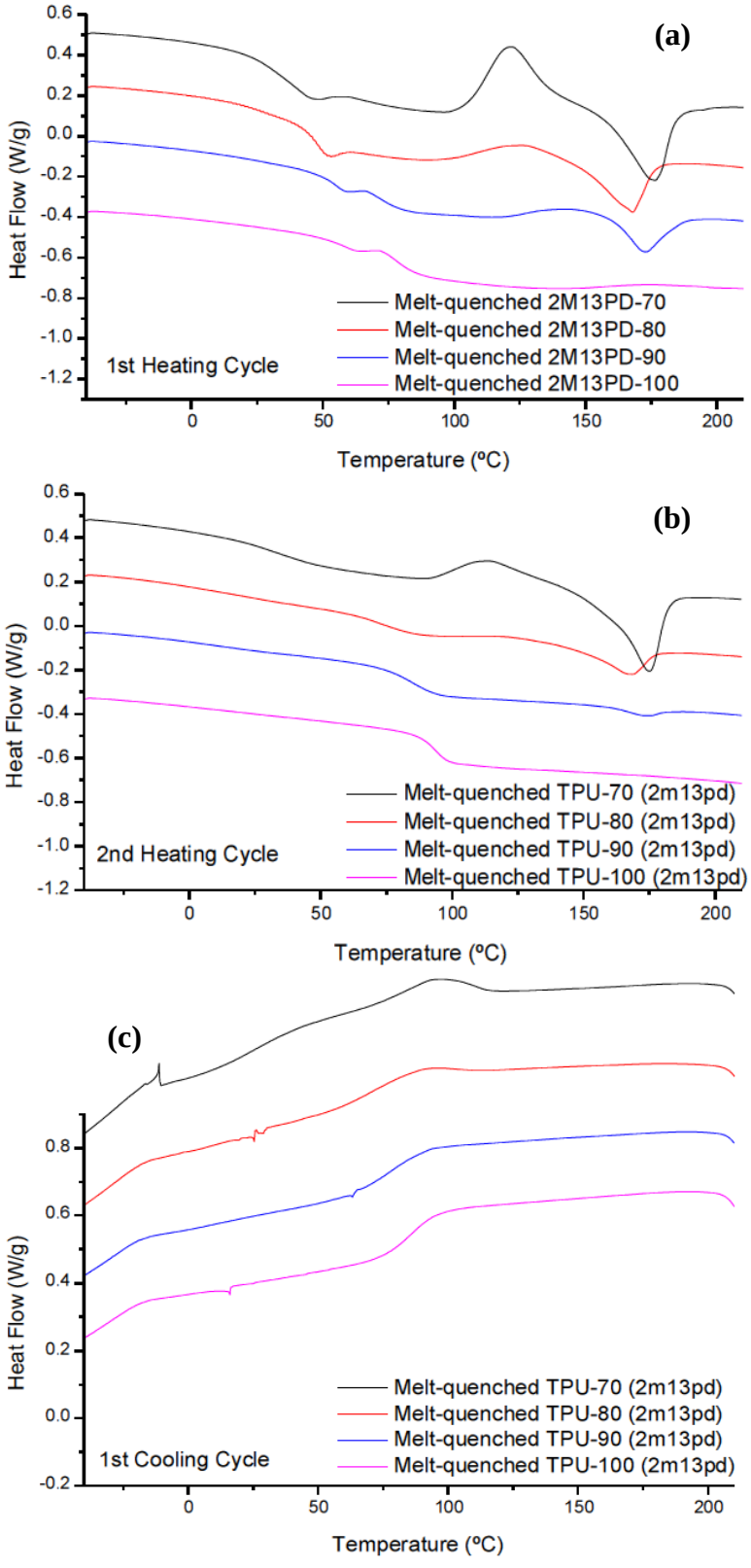
Peak RV - (ml)	18.518	27.254
Mn - (Daltons)	65,941	0
Mw - (Daltons)	93,781	0
Mz - (Daltons)	106,458	0
Mp - (Daltons)	109,365	0
Mw / Mn	1.422	0.000
Percent Above Mw: 0	0.000	0.000
Percent Below Mw: 0	0.000	0.000
Mw 10.0% Low	23,197	0
Mw 10.0% High	146,629	0
RI Area - (mvml)	138.15	27.06
UV Area - (mvml)	0.00	0.00

PMMA-140°C 2hr

Conventional Calibration - Homopolymers : Results

Peak RV - (ml)	18.563	27.187
Mn - (Daltons)	62,685	0
Mw - (Daltons)	86,124	0
Mz - (Daltons)	98,603	0
Mp - (Daltons)	100,360	0
Mw / Mn	1.374	0.000
Percent Above Mw: 0	0.000	0.000
Percent Below Mw: 0	0.000	0.000
Mw 10.0% Low	23,959	0
Mw 10.0% High	140,617	0
RI Area - (mvml)	58.01	20.99
UV Area - (mvml)	0.00	0.00

Appendix 2 DSC graphs of melt-quenched 2M13PD and 15PD extended TPUs provided by co-workers from Manchester.



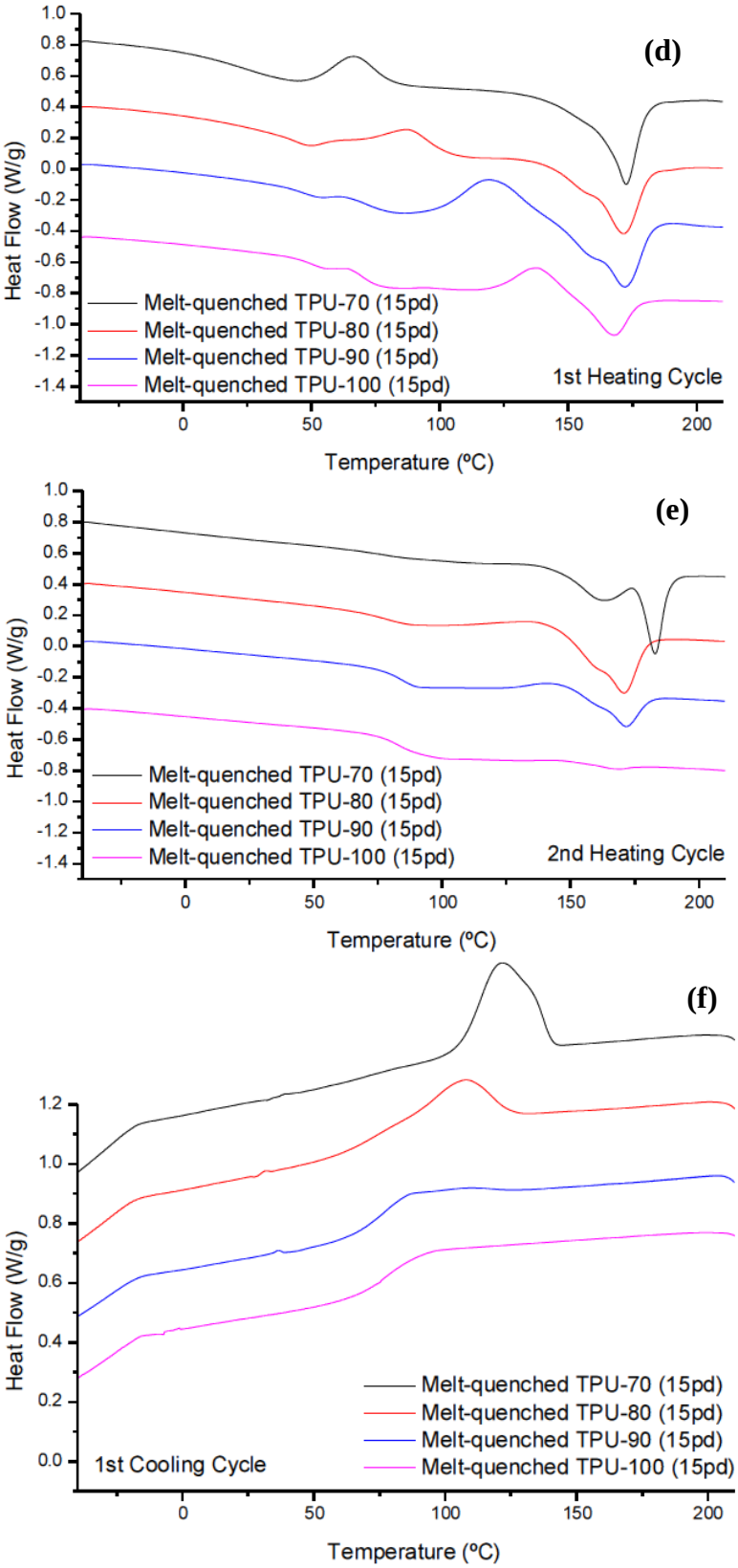


Fig. A1 1st heating (a), 2nd heating (b) and 1st cooling (c) DSC cycles of melt-quenched 2M13PD TPUs and 1st heating (d), 2nd heating (e) and 1st cooling DSC (f) cycles of melt-quenched 15PD TPUs.